TECHNISCHE UNIVERSITÄT MÜNCHEN
Lehrstuhl für Kognitive Systeme

From a Multi-modal Intelligent Cell to a Self-organizing Robotic Skin – Realizing Self and Enriching Robot Tactile Interaction

Dipl.-Ing. Univ. Philipp Mittendorfer

Vollständiger Abdruck der von der Fakultät für Elektrotechnik und Informationstechnik der Technischen Universität München zur Erlangung des akademischen Grades eines

Doktor-Ingenieur (Dr.-Ing.)

genehmigten Dissertation.

Vorsitzender:		Univ.-Prof. Paolo Lugli, Ph.D.
Prüfer der Dissertation:	1.	Univ.-Prof. Gordon Cheng, Ph.D.
	2.	Prof. Giorgio Cannata, Università di Genova, Italien
	3.	Prof. Eiichi Yoshida, Ph.D., Tokyo University of Agriculture and Engineering, Japan

Die Dissertation wurde am 24.09.2014 bei der Technischen Universität München eingereicht und durch die Fakultät für Elektrotechnik und Informationstechnik am 28.04.2015 angenommen.

Abstract

Human skin provides numerous inspirations for robots, supplying the whole body surface with multi-modal tactile sensitivity. Unlike a robot purely relying on joint information or vision, a robot equipped with artificial skin has a much richer information set. Challenges to efficiently deploy, organize and utilize a high number of distributed multi-modal sensors have so far prevented an effective utilization of artificial skin technology in robotics. In this thesis, we introduce a novel approach to create multi-modal artificial skin and a novel approach to self-organize the body representation of a robot. Our modular artificial skin is built by placing similar skin cells side-by-side into a flexible carrier material. Every skin cell is a self-contained system with a variety of sensors, signal conversion, processing and communication capabilities. The advantage of our modular approach is its robustness, scalability and transferability to various robotic systems. We developed various self-organizing features to automatically handle a potentially high number of skin cells on a large surface area. Automatic networking algorithms explore available skin cells and connections, distribute unique identifiers and provide robust and adaptive real-time communication. Mounted on a robot, our framework systematically explores and models the robot's body schema – inferring the robot's own kinematic and volumetric model from an egocentric perspective. In order to speed up the process, and to omit potentially harmful contacts, we only utilize low-range, open-loop motions of the robot and accelerometers embedded in our skin cells. A first algorithm explores the kinematic dependencies of body parts and joints, allocating actuators to joints and skin cells to body parts. A 3D reconstruction algorithm then computes the volumetric surface model of each body part, utilizing relative rotation estimates based on gravity and a topographic map inferred from the cell-2-cell connections. Turning skin patches into active visual markers, those distributed surface models can be visually combined into one homogeneous body representation – additionally joining tactile and visual space. A kinematic calibration algorithm finally estimates the parameters of the self-assembled kinematic model. In completion, we show exemplary applications of the prototype skin on industrial robot arms and the upper body of a humanoid robot. These examples demonstrate the benefits of an artificial skin for human robot interaction, multi-modal contact control, safety and object manipulation.

Kurzfassung

Die Berührungsempfindlichkeit der menschlichen Haut, liefert zahlreiche Inspirationen für die Robotik. Robotern, die bisher lediglich mit Gelenksensoren und Kameras ausgestattet sind, kann eine künstliche Haut eine Fülle von neuen Informationen zur Verfügung stellen. Die Herausforderungen eine hohe Anzahl unterschiedlicher Sensoren effizient zu verteilen, zu organisieren und zu verwenden, verhinderten bisher einen nennenswerten Einsatz künstlicher Haut in der Robotik. In dieser Doktorarbeit wurden neue Ansätze erarbeitet, um eine multi-modale künstliche Haut für Roboter zu realisieren und das Körperschema eines Roboters selbständig zu organisieren. Hierfür wurde ein neuartiges, modulares System aus Hautzellen entwickelt, die nebeneinander platziert und vernetzt werden können. Jede Hautzelle ist ein eigenständiges System und verfügt über eine Reihe unterschiedlicher Sensoren, Signalverarbeitungs- und Kommunikationsfähigkeiten. Durch diese Modularität erreichen wir eine hohe Flexibilität, Robustheit und Skalierbarkeit, und können unsere künstliche Haut sehr schnell auf neuen Robotern einsetzen. Weiterhin entwickelten wir Methoden um eine hohe Anzahl an Hautzellen auf großen Oberflächen automatisch zu organisieren. Netzwerkalgorithmen stellen automatisch die Anzahl der zu Verfügung stehenden Zellen und Verbindungen fest, verteilen neue Identifikationsnummern und leiten Informationen robust und in Echtzeit zum Computer-Gehirn des Roboters weiter. Im nächsten Schritt benützen wir unser System um das Körperschema des Roboters, sein volumetrisches und kinematisches Modell, aus einer egozentrischen Perspektive zu erlangen. Um diesen Prozess zu beschleunigen und sicherer zu gestalten, benützen wir lediglich minimale Bewegungen des Roboters im freien Raum und Beschleunigungssensoren in den Hautzellen. Zuerst analysiert ein Algorithmus die kinematische Abhängigkeit zwischen Gelenken mit Drehachsen und Körperteilen mit Hautzellen. Anschließend benutzen wir das Erdgravitationsfeld und die Netzwerktopologie um die Oberfläche der Körperteilen in 3D zu rekonstruieren. Diese lokalen Rekonstruktionen können dann in optische Marker überführt und mit Hilfe einer monokularen Kamera in einer homogene 3D Darstellung des Körpers vereint werden. Zuletzt schätzt ein Algorithmus die Parameter eines automatisch erzeugten kinematischen Models. Abschließend präsentieren wir beispielhafte Anwendungen unserer künstlichen Haut auf industriellen Roboterarmen und einem humanoiden Roboter. Diese Beispiele verdeutlichen den Vorteil einer künstlichen Haut hinsichtlich Mensch-Maschine Interaktion, Kontaktregelung, Sicherheit und Objektmanipulation.

Acknowledgements

No one can whistle a symphony. It takes a whole orchestra to play it.

(H.E. Luccock)

I would like to thank all the people that have been supporting me during the last years. My special thanks go to my supervisor **Gordon Cheng** for setting me onto the topic of artificial skin, mentally and financially supporting me during my PhD. I also would like to thank my wife, **Stephanie**, for tolerating academic working hours and keeping my life in balance. I am very grateful for all the help of my **colleagues**, for their input and neat-less organization of everyday working life. My special thanks go to my proof readers **Florian Bergner**, **Emmanuel Dean** and **Alexander Schmitz**. Many thanks also to the countless **visitors**, for asking questions and such giving way to new points of view – especially **David Vernon**. My special thanks go to the **Joint Robotics Lab** at AIST in Tsukuba Japan, for hosting me 3 month as a visiting researcher – especially to **Eiichi Yoshida** and to **Thomas Moulard**. Last but not least, I would like to acknowledge the direct contributions of all **students** that have been working with me: **Erhard Wieser**, **Nora Martiny**, **Andre Richter**, **Byron Lim-Steffan**, **Stephan Holzhauser**, **Nilesh Bajaj**, **Stephan Ries**, **Alexander Diewald**, **Lola Garcia**, **Markus Breunig**, **Marco Marder**, **Tobias Brennich**, **Frederik Ebert** and **Wolfgang Burger**. I hope to have been a good teacher, but also a good learner.

This work was supported in parts by: the DFG cluster of excellence Cognition for Technical Systems (**CoTeSys**); the Institute for Cognitive Systems (**ICS**), Technische Universität München; the European Commission under grant agreement PITN-GA-2012-317488 (**CONTEST**); and the European Community's 7th Framework Programme (FP7/2007-2013) under grant agreement n°609206 (**Factory-in-a-Day**).

Munich, September 2014 Philipp Mittendorfer

List of Publications

Parts of the thesis "*From a Multi-modal Intelligent Cell to a Self-organizing Robotic Skin – Realizing Self and Enriching Robot Tactile Interaction*" have been published in:

2014 **P. Mittendorfer**, E. Dean and G. Cheng, "3D Spatial Self-organization of a Modular Artificial Skin", IEEE/RSJ International Conference on Intelligent Robots and Systems (IROS), pp. 3969-3974, September 2014, [Mittendorfer *et al.*, 2014a]

P. Mittendorfer, E. Yoshida and G. Cheng, "Realizing Whole-Body Tactile Interactions with a Self-organizing, Multi-modal Artificial Skin on a Humanoid Robot", RSJ Advanced Robotics Journal, vol. 29, no. 1, pp. 51-67, [Mittendorfer *et al.*, 2015]

P. Mittendorfer, E. Dean and G. Cheng, "Automatic Robot Kinematic Modeling with a Modular Artificial Skin", IEEE-RAS International Conference on Humanoid Robots (Humanoids), pp. 749-754, November 2014, [Mittendorfer *et al.*, 2014b]

M. Kaboli, **P. Mittendorfer**, V. Hugel, G. Cheng, "Humanoids Learn Object Properties From Robust Tactile Feature Descriptors via Multi-Modal Artificial Skin", IEEE-RAS International Conference on Humanoid Robots (Humanoids), pp. 187-192, November 2014, [Kaboli *et al.*, 2014]

2013 **P. Mittendorfer**, E. Yoshida, T. Moulard and G. Cheng, "A General Tactile Approach for Grasping Unknown Objects with a Humanoid Robot", IEEE/RSJ International Conference on Intelligent Robots and Systems (IROS), pp. 4747-4752, November 2013, [Mittendorfer *et al.*, 2013]

R. S. Dahiya, **P. Mittendorfer**, M. Valle, G. Cheng, V. J. Lumelsky, "Directions Toward Effective Utilization of Tactile Skin: A Review", IEEE Sensors Journal, vol. 13, no. 11, pp. 4121-4138, November 2013, [Dahiya *et al.*, 2013]

P. Mittendorfer and G. Cheng, “From a Multi-modal Intelligent Cell to a Self-organizing Robotic Skin”, IEEE-RAS International Conference on Robotics and Automation (ICRA), workshop on electronic skin, May 2013, [Mittendorfer and Cheng, 2013]

P. Mittendorfer, “Capacitive Force Sensor and Fabrication Method”, European patent, EP 12 172 602.0, filed 19.06.2012 and issued 25.12.2013, [Mittendorfer, 2013]

2012 **P. Mittendorfer** and G. Cheng, “Integrating Discrete Force Cells into Multi-modal Artificial Skin”, IEEE-RAS International Conference on Humanoid Robots (Humanoids), pp. 847-852, December 2012, [Mittendorfer and Cheng, 2012b]

P. Mittendorfer and G. Cheng, “3D Surface Reconstruction for Robotic Body Parts with Artificial Skins”, IEEE/RSJ International Conference on Intelligent Robots and Systems (IROS), pp. 4505-4510, October 2012, [Mittendorfer and Cheng, 2012a]

P. Mittendorfer and G. Cheng, “Uniform Cellular Design of Artificial Robotic Skin”, German Conference on Robotics, pp.145-149, May 2012, [Mittendorfer and Cheng, 2012d]

P. Mittendorfer and G. Cheng, “Open-loop Self-calibration of Articulated Robots with Artificial Skins”, IEEE-RAS International Conference on Robotics and Automation (ICRA), pp. 4539-4545, May 2012, [Mittendorfer and Cheng, 2012c]

2011 **P. Mittendorfer** and G. Cheng, “Self-Organizing Sensory-Motor Map for Low-Level Touch Reactions”, IEEE-RAS International Conference on Humanoid Robots (Humanoids), pp. 59-66, October 2011, [Mittendorfer and Cheng, 2011b]

E. Wieser, **P. Mittendorfer** and G. Cheng, “Accelerometer based Robotic Joint Orientation Estimation”, IEEE-RAS International Conference on Humanoid Robots (Humanoids), pp. 67-74, October 2011, [Wieser *et al.*, 2011]

P. Mittendorfer and G. Cheng, “Humanoid Multi-Modal Tactile Sensing Modules”, IEEE Transactions on Robotics (T-RO) - Special Issue on Robotic Sense of Touch, vol. 27, pp. 401-410, June 2011, [Mittendorfer and Cheng, 2011a]

Contents

List of Figures

List of Tables

List of Algorithms

Notations

Abbreviations

3D	3 Dimensional
ASIC	An Application-specific Integrated Circuit
CAD	Computer Aided Design
CAN	Controller Area Network
CTMU	Charge Time Measurement Unit
DoF	Degree(s) of Freedom
dB	Decibel
EMC	Electromagnetic Compability
ESD	Electrostatic Discharge
EMI	Electromagnetic Interference
FPGA	Field Programmable Gate Array
F/T	Force/Torque
IR	Infrared
ID	Identifier
LED	Light Emitting Diode
LVDS	Low Voltage Differential Signaling
MEMS	Microelectromechanical System
OS	Operating System
PVDF	Polyvinylidenfluorid
PCB	Printed Circuit Board
PLL	Phase Locked Loop
PC	Personal Computer
QTC	Quantum Tunneling Composite
RGB	Red, Green and Blue
SNR	Signal to Noise Ratio
SC	Skin Cell
SoF	Start of Frame
SVD	Singular Value Decomposition
SMD	Surface Mounted Device
TSU	Tactile Section Unit
TTL	Transistor Transitor Logic
UART	Universal Asynchronous Receiver and Transmitter
UDP	User Datagram Protocol
SME	Small and Medium-sized Enterprises

Symbols

linear acceleration	$\boldsymbol{a}$
tangential acceleration	${}_{\tan}\boldsymbol{a}$
centripetal acceleration	${}_{\mathrm{cp}}\boldsymbol{a}$
rotational position	θ
rotational velocity	ω
rotational acceleration	α
rotational jerk	ζ
joint axis	$\boldsymbol{j}$
rotation matrix	$\mathbf{R}$
homogeneous transformation	$\mathbf{T}$
identity matrix	$\mathbf{I}$

Conventions

Scalars, Vectors and Matrices

scalar	s
vector	$\boldsymbol{v}$
matrix	$\mathbf{M}$

Operators

dot product	$\boldsymbol{a} \cdot \boldsymbol{b}$
matrix product	$\mathbf{A} \cdot \mathbf{B}$
cross product	$\boldsymbol{a} \times \boldsymbol{b}$
time derivative	$\frac{\mathrm{d}}{\mathrm{d}t}(.)$ or $\dot{(.)}$
euclidean norm	$\lVert . \rVert$
absolute value	$\lvert . \rvert$
summation sequence	$\sum\limits_{n=1}^{N} f(n)$
product sequence	$\prod\limits_{n=1}^{N} f(n)$
transposed	$(.)^T$
inverse	$(.)^{-1}$
Hadamard multiplication	$(.) \circ (.)$
logical comparisons	$>, <, ==$

Functions

time continuous function	$f(t)$
time discrete function	$f[n]$
multi-dimensional function	$\boldsymbol{f}(.)$
sinus	$\sin(.)$
cosinus	$\cos(.)$
exponential	$\exp(.)$ or $e^{(.)}$
maximum	$\max(.)$
minimum	$\min(.)$
minimization in x	$\min\limits_{x} f(x)$
common logarithm (base 10)	$\log(.)$
sign copy function	$\mathrm{copysign}(value, sign)$
find index function	$\mathrm{find}(.)$
determinant	$\det(.)$
signum function	$\mathrm{sign}(.)$
singular value decomposition	$\mathrm{svd}(.)$
rotation matrix from axis angle	$\mathrm{vrrotvec2mat}(axis, angle)$

Sub- and Superscripts

vector in u coordinate frame	${}^{u}\boldsymbol{v}$
transformation from b to a coordinates	${}^{a}\mathbf{T}_{b}$
scalar indices	$s_{x,y}$
vector indices	$\boldsymbol{v}_{x,y}$
special indices (e.g. names or directions)	x_{text} or ${}_{\text{text}}x$

CHAPTER 1

Introduction

> Brave men are all vertebrates; they have their softness on the surface and their toughness in the middle.
>
> *(Gilbert K. Chesterton)*

In this chapter, we would like to motivate the reader with the potential impacts of artificial skin. We continue with an introduction of the challenges to create and organize a whole-body, multi-modal artificial skin. Then, we state the contribution of this thesis, solving those challenges with our novel self-organizing, cellular skin approach. We conclude this chapter with an outline of the thesis.

1.1. Motivation

1.1.1. Skin for Robots

Visual Presence Whole Body Interaction Social Interaction

Body Monitoring Classification Contact Control

FIGURE 1.1. The figure visualizes the utilization of sensitive skin in everyday life.

Biological skin provides numerous inspirations for robots, deploying high resolution and multi-modal sensitivity over the whole (soft/compliant) body surface. Due to its localization on the body surface, sensitive skin provides a rich and direct feedback of all close-contact interactions with the world. Sensitive skin delivers locatable, qualitative and quantitative measurements of all these close encounters. Additionally, skin provides information about contacts with the own physical body. Those self-sensations help to create knowledge about the own sensory-motor embodiment – the body schema. Along with the proprioceptive, the tactile sense is a key component to self-acquire a kinematic and volumetric body model. In comparison to a robot purely relying on joint information (position/currents/torques) and visual feedback (2D/3D), a robot equipped with sensitive skin has a much richer and more direct information set. Joint level sensing looses information in multi-contact scenarios and requires precise kinematic and dynamic robot models to separate internal from external effects. Vision reaches its limit in occlusive environments and close contact. Future robots sharing our environment, or taking over close contact tasks, must be enhanced with artificial skin. Skin's multi-modal capability is beneficial for classifying or controlling various contact properties, while willingly or accidentally touching surfaces. Different receptors modalities measure light contact, normal and shear forces, vibration, temperature and nociception. Multi-modal skin can be applied for a variety of tasks, like for body monitoring, for contact control and for object/touch classification (see Fig. 1.1). Although sensitive skin is one of the most important sensors for vertebrate life, lack of tactile sensing often results in severe injuries, it is not yet well-represented in robotics (refer to Sec. 2). In this thesis, we provide an easy to use, modular solution to equip robots with artificial skin, along with algorithms to automatically acquire the complete kinematic and volumetric body model without any a-priori knowledge.

1.1.2. Potential Impacts

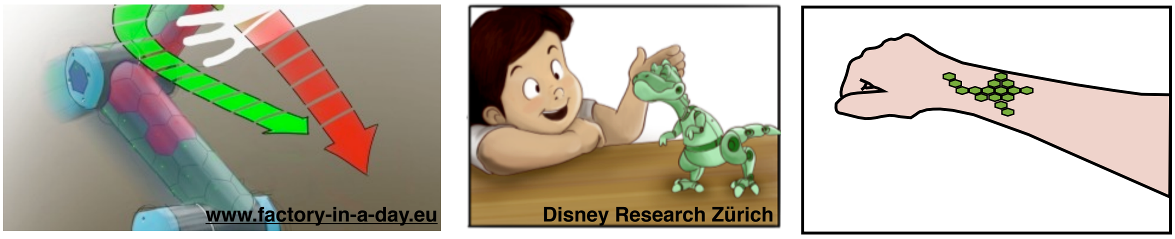

Industrial Robots **Entertainment** **Health Care**

FIGURE 1.2. The figure visualizes potential impacts of artificial skin across multiple domains.

Providing low-cost, reliable and easy to use artificial skin would have major technical, economical and societal impacts. Potential application scenarios range across multiple domains, from industrial environments to health care and entertainment (see Fig. 1.2).

Industrial Robots: Industrial robots equipped with a safety-rated artificial skin could work in close contact with humans. Collaborative robots are essential for the next generation of factory automation, where skilled workers are working in assistance with robots e.g. to lower unhealthy manipulation forces, speed up tasks or enhance quality. The benefit of an artificial skin, in comparison to e.g. joint level force sensing, is that existing robots can be easily upgraded with a clip-on solution and the size/weight of the robot does not interfere with the skin sensation – even allowing powerful robots to safely help humans. Artificial skin also does not require precise kinematic and dynamic models in order to separate internal from external forces. In comparison to vision, sensitive skin does not suffer from occlusion and provides direct multi-modal contact measurements. The multi-modality of skin, and the large area that can be covered with skin, offer novel ways of human-robot interaction. Expert teach pendants could be replaced with direct tactile interaction e.g. tactile gestures and tactile kinesthetic teaching. Active visual elements in the skin could serve as full body touch screens, and visualize the state and motion intention of the robot. Industrial robots equipped with sensitive skin could also manipulate objects with their whole body instead of limiting contacts to the end-effectors, e.g. in order to handle large and heavy objects by distributing the load. In summary, artificial skin is a prerequisite for the coming robotic age, introducing robots into everyday life.

Health Care: Medical applications for artificial skin are numerous. In the same form as with industrial scenarios, medical robots should be equipped with sensitive skin to enhance and simplify their interaction with the environment and human. Surgical robots could use touch sensitivity to omit collisions between staff and robots in the constrained operative workspace, while direct tactile interaction could reduce the required robot control panels to a minimum. Endoscopic robots could automatically avoid tissue damages, automatically avoiding high forces or delivering feedback about potential harm to the operator. Care-taking robots must be equipped with sensitive skin to be able to deal with unstructured environments and handle close contacts with patients. Physical contact could also play an important role in the emotional acceptance of those robots. Besides robots, prosthetic devices could be equipped with artificial skin. The skin could give patients or the prosthesis control feedback of distributed contacts on the artificial body part. For a prosthetic controller, the demand for tactile feedback will grow, in order to adequately react in a variety of situations. Feedback to the patient could be delivered via a neuronal implant or rerouted with tactile displays to other areas of the body. This could help the patients to better incorporate the artificial limb into their own body schema (refer to Sec. 6.3). Tactile feedback could also be applied to patients with tactile impairments, e.g. to prevent that patients are harming themselves. Another cost intensive application area is rehabilitation. Currently trained staff is mainly visually monitoring exercises, e.g. hip stabilization while sitting. An artificial skin could monitor those exercises, provide staff and patients with additional information and deliver extended autonomous training for patients. Tactile monitoring of patient behavior could also be used for enhanced diagnosis, e.g. in order to trace back the cause for a severe back pain to wrong sitting positions at work. Artificial skin could be enhanced with additional sensors, e.g. skin resistivity, EEG/EMG or biomedical probes. Those sensors could be embedded into sensing suits, plasters (see Fig. 1.2) or hospital beds, offering novel ways of real-time monitoring of patients.

Object Monitoring The ability of an artificial skin to monitor the surface of objects could be another interesting application for industry and consumer products. Prototypes equipped with distributed sensors could be utilized to enhance the performance of a product design, e.g. the air resistance of cars with a real-time measurement of the force profile. Monitoring products on the market could be used for event logging and emergency prevention, e.g. the surveillance of the integrity of an airplane surface or car frame for damages. Insurances could make use of event logging to analyze liabilities, e.g. the responsibility for damages on a shared car.

Sports: Applications for artificial skin technology in sport range from quantify-yourself-movements to professional athletes. Artificial skin on sports equipment could be used to initially fit equipment to the user, as well as monitoring the proper utilization during the product life. This would not only serve the demands of the growing quantify-yourself-community, but also have medical benefits when preventing mis-utilization, e.g. providing on-line feedback about a wrong running style with sensitive shoes. Contact monitoring in close or non-contact sports, could be utilized to support referee judgment and automated statistics, e.g. fouls in soccer or punch strength in boxing.

Entertainment: Artificial skin could largely be utilized in entertainment. In theme parks, robots equipped with artificial skin could be involved in close contact interaction with visitors. For those type of robots contact safety, as well as the ability to respond to tactile stimuli is important. Inadequate contacts or pain should be avoided by those robots, while pleasant interaction should be fostered. Surface sensation could enhance the interactivity of toys in general, providing visual feedback and tactile input on large surface areas.

1.2. Challenges

The challenges of artificial skin are due to its decentralized nature – covering large and arbitrary 3D surfaces with multi-modal sensitivity. On the one hand, the efficient implementation of a high number of multi-modal sensors on large surface areas poses technological challenges. The amount of sensors ranges from a few thousand to a couple of million, while the sensitive area reaches from a couple of square centimeter to square meters. All of these sensors have to be supplied, their signals converted and processed, and the resulting information extracted and transfered to a control system. In order to feature reactive control, e.g. to withdraw from undesired contacts, real time constraints apply. Regarding safety, important factors such as redundancy and conformity to standards and norms are have to be considered. Skin has to be soft and flexible in order to passively absorb impacts and to spread and shape the contact area between the robot and external objects. At the same time, sensitive skin has to be efficient to manufacture, transferable between multiple robotic systems and easy to deploy. Artificial skin has to be sensitive, but robust and reliable, since it is in constant interaction with the external world. Skin is exposed to mechanical stress, e.g. wear, tear and impacts, but also to chemicals like human sweat and the environment. Due to its electronic nature, electromagnetic compatibility plays an important role. Electrostatic discharges will be surged into the skin. Its sensor signals are objective to electromagnetic interference on their long pathways to the central processing system and electromagnetic emission plays an important role in medical, industrial or consumer applications. Skin should neither consume much power nor weigh much. Finally, skin should also be aesthetically pleasing and deliver a friendly, natural and appealing look and feel. On the other hand, the effective setup, maintenance and utilization of a high number of distributed sensors poses significant challenges. A variable and high number of sensors on an arbitrarily shaped surface need to be identified, labeled, routed and processed. Skin has to organize and adapt its own processing and communication infrastructure to the number of present sensors. In the scope of sensory-motor control, the location and orientation of each sensor on the 3D surface and within the kinematic chain has to be provided to the control algorithm. Manually providing this knowledge would be time consuming and error prone. Since every motor action results in skin sensations, even the own individual interaction (self-touch, skin kinesthesis), skin can capture knowledge about the own sensory-motor embodiment – the robot uses its own sensors to learn about itself. This is especially interesting when an artificial sensor skin is not designed for a single robot, but easily applicable across multiple robotic systems. Self-organization is also useful to automatically accommodate hardware failure during life time – which is likely as skin is exposed to every (potentially harmful) contact. All those challenges have to be addressed in a single systematic approach.

1.3. Contribution

This thesis contributes a novel approach to create a self-organizing, multi-modal, whole-body artificial skin for robots and other potential applications. Unlike existing approaches, we solve common problems i.e. wiring, failure tolerance and processing, with a modular approach. Multi-modal skin cells form a scalable surface sensor network that can be easily enhanced with new sensors and can be transfered to other robots or domains. The self-organizing network of skin cells automatically adapts to changes in the topology, e.g. recovers from wiring failures using redundant cell-2-cell connections. Besides this framework to automatically organize and acquire data from a variable number of distributed skin cells, we provide algorithms to acquire their physical embodiment on the surface of a robot in a short time and with low-ranging, open-loop motions. We provide an approach to acquire the 3D volumetric surface and an approach to explore, model and calibrate the kinematic model of a robot. In order to achieve those results, we have implemented cross-modal sensor fusion for tactile, visual and proprioceptive senses. We demonstrate the feasibility of our approach with various different applications. These applications include the first industrial robot arm with an intuitive, multi-modal, whole-body tactile interface and distributed visual feedback and the first multi-modal, whole body tactile grasping approach on a full-sized humanoid robot. This thesis presents the first multi-modal, whole-body skin and the first completely self-organizing skin system. Our solution provides a larger flexibility than any other existing artificial skin. We believe that the presented work will have a long lasting impact on the design, organization and utilization of artificial skin in robotics and beyond.

1.4. Thesis Outline

The remaining parts of this thesis are divided into five chapters: Chapter 2 gives a concise overview of the related works on biological skin, artificial skin technology, body schema in robotics and utilization of artificial skin. Chapter 3 introduces our novel modular approach to create artificial skin from multi-modal skin cells, and explains our prototype implementation based on standard technologies. Chapter 4 introduces our novel approach to automatically reconstruct the 3D surface of body parts equipped with our artificial skin and a novel method to visually combine distributed tactile representations. Chapter 5 explains our different approaches to acquire kinematic knowledge for robots equipped with our skin system. These approaches include the acquisition of a local, inverse Jacobian like mapping, the exploration of the kinematic dependencies and a full kinematic model estimation. Finally, Chapter 6 shows exemplary applications of our artificial skin system: e.g. enhancing the interaction capabilities of industrial robots or enabling a full-sized humanoid to grasp unknown objects with the upper body only using tactile feedback.

CHAPTER 2

Related Work

If I have seen further, it is by standing on the shoulders of giants.

(Bernard of Chartres)

In this chapter, we would like to give a concise overview of the related work. In order to complete the biological motivation, we first introduce human skin and the biological notion of body schema. The remaining parts are split i.e. into creation of artificial skin, body schema in robotics and the application of tactile sensing in robotics and related fields.

2.1. Biological Inspiration

As an organized/distributed system, each biological body is centered on the concepts of specialization and division of work. The cell is the basic structural and functional unit of living organisms – the building block of life. Organization is necessary to drive those numerous cells towards the collective goal, the generation of a new global entity – the body itself. In biological systems, self-organization is a process where some form of global order or coordination arises from local interactions between the individual components [Camazine *et al.*, 2001]. For an embodied cognitive system, this coordination is centralized towards the brain [Llinas, 2002]. According to Llinas an embodied cognitive system requires at least three capabilities: 1) sensors to receive information about the surrounding environment; 2) actuators to realize effects in the environment; 3) a centralized nervous system to internalize the external world, predict and select appropriate actions. However before any external action is taken, the own body has to be built and organized. Why should we take inspiration from biological skin to develop an artificial skin system? – Because no artificial skin system yet comes close to the overall performance of the biological archetype. We can learn from this beautifully designed system and find answers to questions occurring during our own technical system design.

2.1.1. Sensitive Skin

Sensitive skin covers the complete body surface ($\approx 2\,\mathrm{m}^2$) with a few million discrete receptors [Myles and Binseel, 2007] (see Fig. 2.1). The size of these receptors range from a few µm with free nerve endings, to 1 mm with the largest receptor: the Pacinian corpuscle [Hubbard, 1974]. It is consequently possible to realize sensitive skin with small discrete sensor elements. Skin receptors are classified into mechano-, thermal- and noci-receptors [McGlone and Reilly, 2010]. The purpose of nociceptors (pain receptors), is to protect the body against actual or potential damage resulting from intense intense mechanical, thermal or polymodal (e.g. chemical, mechanical, thermal) stimuli [Kandel *et al.*, 2012]. The absence of an encapsulation also renders nociceptors susceptible to intrinsic (and extrinsic) chemical agents [McGlone and Reilly, 2010]. Thermal hot- and cold-receptors encode deviations from a homeostatic setpoint around 35 °C. There are five times as many cold-points as warm-points [McGlone and Reilly, 2010]. Maybe human thermal object classification is biased towards cooling effects, as humans are commonly warmer than the environment (which is similar for robots). It seems also more important for a biochemical system to prevent cold than warmth, since cooling is be easily achieved with sweat evaporation (with robots the opposite is the case – heat dissipation is a major issue). The utilization of slow C (0.4-2.0 m/s) and $A\delta$ (4-36m/s) fibers

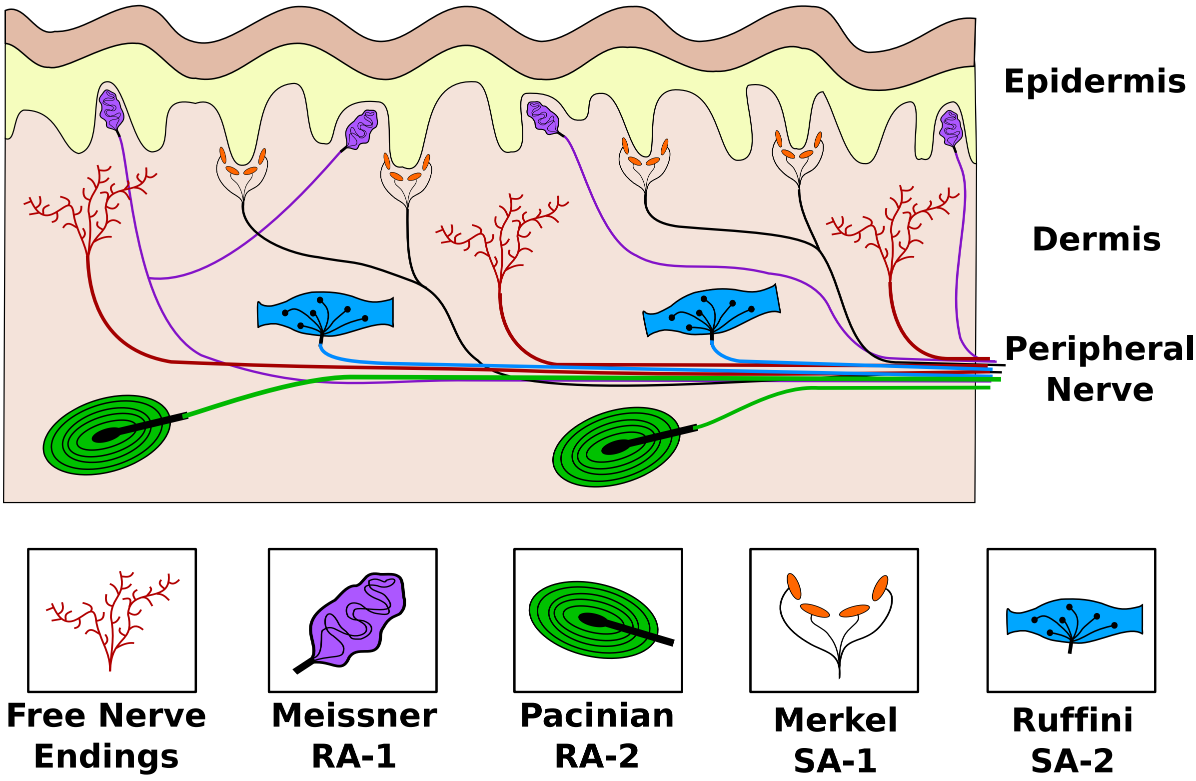

FIGURE 2.1. The figure shows the layers and mechano-receptors of human skin.

[Kandel *et al.*, 2012], conducting the sensory signals of thermal sensation and nociception from the sensor site to the brain, shows the minor relevance of latency and bandwidth for both modalities. Thermal receptors do not require fast transmissions as thermal sensation itself has a high time constant. The slow transmission of nociceptor signals can only be explained by a binary response to pain – painful stimuli must be detected, but there is no need to regulate or accurately classify pain. Mechano-receptors instead utilize myelinated (coated) fibers with large diameters and high conduction speeds, like $A\beta$ (36-72 m/s) and $A\alpha$ (72-120 m/s) fibers [Kandel *et al.*, 2012]. Those fibers conduct signals at high bandwidth and only a small delay, allowing fast control and a high resolution. The location of the mechano-receptors in the skin is essential to promote their functionality [Maeno *et al.*, 1998]. Especially the structure of the epidermal ridges and papillae, structures in the upper level of the skin, act as mechanical filters to shape the transmission of stimuli to the receptors [Cauna, 1954] [Dandekar *et al.*, 2003]. Type 1 mechano-receptors, in particular the Merkel cell (SA1) or the Meissner corpuscle (RA1), are located at the epidermal/dermal boundary, 0.5-1.0 mm below the skin surface [Kandel *et al.*, 2012]. Type 2 mechano-receptors, in particular the Ruffini ending (SA2) or the Pacinian corpuscle (RA2), are located 2-3 mm below the skin surface in the dermal layer [Kandel *et al.*, 2012]. Consequently the mechanical receptive field is smaller and the spatial accuracy of sensors of Type 1 is higher than for Type 2. This also explains why there are about 100 Merkel and 150 Meissner receptors per cm^2 on the fingers, but only about 20 Pacinian and 20 Ruffini receptors per cm^2 [Johnson, 2001]. On the contrary, Type 2 sensors are always innervated only by a single fiber, while with Type 1 only one fiber innervates multiple receptors nearby [Kandel *et al.*, 2012]. With Type 1 receptors, large amount of spatial information is fused at the receptor level. The fast adapting (FA) types only respond to the on- and off-set of a stimulus, while the slow adapting (SA) persistently respond to constant stimulation. The Pacinian corpuscle for example, embeds three levels of filtering: 1) the mechanical filter of the onion-like capsule; 2) the electromechanical filter of the membrane; and 3) the electrochemical spike-train encoder [Bell and Holmes, 1992]. This filtering is performed locally at the receptor level and helps with the efficient encoding of the tactile signals, for example in manipulation tasks [Johansson and Flanagan, 2009]. In general, every mechano-receptor has a measurement specialty: a) Pacinian corpuscles are very sensitive to high frequent vibrations and largely applied for tool and object manipulation; b) Ruffini endings monitor stretch of skin, useful to detect skin deformation, e.g. when conforming to an object or on own motions (kinesthetic sensing [Edin, 2004]); c) Merkel cells give precise feedback about tactile patterns such as points, edges and curvatures; and d) Meissner corpuscles react to low frequent, but sudden force changes, e.g. onset of slip or making and breaking of contacts [Johnson, 2001] [Johansson and Flanagan, 2009]. Hair root receptors react to very low forces and are enhancing the touch sensing ability of skin by a few millimeters above the skin surface [Kandel *et al.*, 2012]. Slow conducting CT afferents, preferentially reacting to low force and slow moving mechanical stimuli, are said to posses limbic functionality towards the emotional aspects of touch [McGlone and Reilly, 2010]. Moreover, biological skin is very bendable, but limited to a maximum stretch of about 30% [Hendriks, 2005]. The ability of skin to span across joints is a consequence of its ability to bend, not to stretch, which allows it to wrinkle and fold.

2.1.2. Human Body Schema

"*The mechanisms underlying the working and development of body schema (and body image) in animals and humans are still far from clear.*" [Hoffmann *et al.*, 2010]. According to [de Vignemont, 2010], a growing consensus denotes at least two distinct types of body representations – body schema and body image. De Vignemont defines the body schema as a cluster of sensori-motor representations that are action-oriented and represent the body as the effector and as the goal of the action. The body image instead groups all the representations about the body that are not used for action, whether they are perceptual, conceptual or emotional. According to Macaluso *et al.* [Macaluso and Maravita, 2010], the body representations

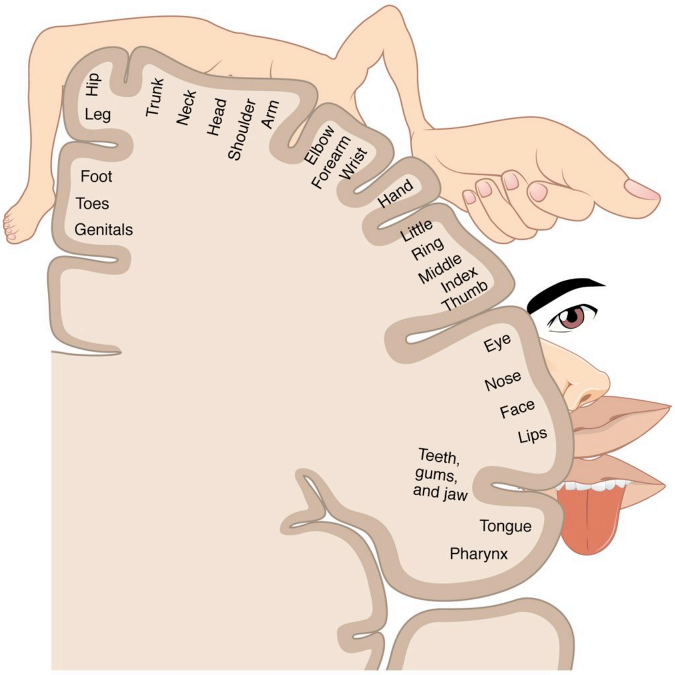

FIGURE 2.2. The figure shows the cortical sensory homunculus, a visualization of the spatial representation of tactile sensor locations in the human brain [Fig. by OpenStax College[1]].

also extend to the peri-personal space and are dominated by spatial, cross-modal links between visual, tactile and proprioceptive senses. "*Rather, the body schema and peri-personal space are emergent properties of a network of interacting cortical and sub-cortical centres. Each centre processes multi-sensory information in a reference frame appropriate to the body part concerning which it receives information, and with which responses are to be made.*" [Holmes and Spence, 2004]. An instantiation of the spatial relationships can be seen with the sensory homunculus in the primary somato-sensory cortex (see Fig. 2.2). The sensory homunculus shows that sensors in close physical vicinity on the physical body are represented in a similar spatial relationship in the somato-sensory cortex. In [Medina and Coslett, 2010] Medina *et al.*, presented arguments that this first somato-topical representation should be accompanied by a second body form (size and shape) representation that allows to locate tactile sensations on the skin surface, and a third postural representation that localizes the body in external space in various egocentric frames of reference. The answer how the body infers those relationships is found in the design of the human system [Kandel *et al.*, 2012], as well as in its cognitive development [Rochat, 1998]. With the tactile mechano-receptors, spatial relationships are exploited at the cellular level (see Fig. 2.1), combining multiple receptors to receptive

---

[1] Fig. 14.23 in Anatomy & Physiology, OpenStax College, published on 25th April 2013, can be downloaded for free at `http://cnx.org/content/col11496/latest/`.

fields [Kandel *et al.*, 2012]. Afferent fibers from the same areas are then routed by similar pathways through the multiple stages of the central nervous system. Topological maps, are already established all the way up to the cortex. Different exploration methods, as depicted in [Rochat, 1998], serve to establish and calibrate the missing links. Rochat *et al.* explain that infants have an early ability to discriminate environmental (single-touch) from self-stimulation (double-touch). According to Rochat *et al.*, this serves to develop the ecological self. The perceptual monitoring of own actions serves as training data for the inter-modal calibration between tactile, visual and proprioception. As this process is split into short-term versus long-term body representations, the body schema is plastic in time [de Vignemont, 2010]. This representation involves primarily visual, somatosensory and proprioceptive modalities, operates in body part-centred reference frames [Holmes and Spence, 2004], thus demonstrating significant plasticity.

2.2. Artificial Skin

In the early 1980s, Leon D. Harmon conducted a survey about the requirements and potential impacts of tactile sensing for researchers and industry [Harmon, 1982]. Some of his findings are: "*Approximately 90% of the respondents felt strongly that tactile sensing is needed. Touch sensing was seen as an essential concomitant of vision. ... Artificial skin should have high sensitivity, fast response, and continuous-variable output, and it should require little power and be cheap and durable. ... Some sort of peripheral preprocessing of tactile sensory data seemed imperative to most respondents. ... It would be imperative to pre-process the great flow of transducer signals at or near the skin surface. ... a manufacturer is obliged to offer complete systems; users are unwilling and/or unable to cope with specialized installations. Standard systemintegration, data-processing software packages will undoubtedly be essential to future systems. ... A somatotopic (skin-surface) map (similar to a retinal map in vision) is desirable; some central representation of the patterns impinging on the sensory surface is essential to intelligent processing. ... In the more general and interesting case of a relatively unstructured environment, a robot arm or hand must have advance warning of impending contact at all times. ... The touch-transducer response time needs to be small compared to that for the loop cycle. ... Reaction time of 1-10 ms is desirable for the entire automaton, according to some respondents, and should range up to 300 ms according to others. ... In general, software was seen as the major problem. This worry was most sharply focused on data processing and control algorithms. The integration of many sensors was felt to be quite difficult. ... Very likely, some of the really high-payoff applications will not demand high speed and/or high resolu-*

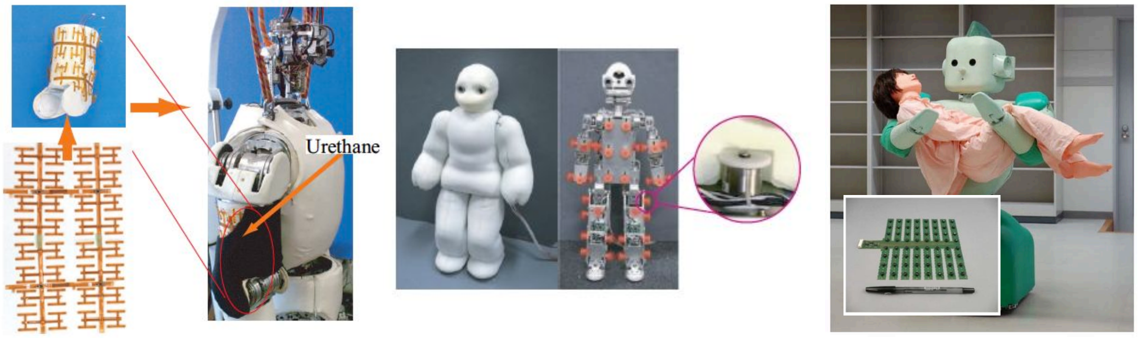

Ohmura et al. 2006 **Yoshikai et al. 2007** **Mukai et al. 2008**

Alirezaei et al. 2009 **Göger et al. 2009** **Iwata et al. 2009**

Takashi et al. 2011 **Kumagai et al. 2012** **Maiolino et al. 2013**

FIGURE 2.3. The figure shows a collection of related work artificial skin systems.

tion during early, evolutionary years. ... Much more consultation between manufacturers and robot designers was urged. Likewise, the need to implement considerably more laboratory-to-real-world transfer was noted. ... As robotics matures and automata get smarter, more versatile, and more numerous, machine-human interfacing will increase ... Safety looms as a large problem and an obviously acute concern. Robots are powerful and stupid. Proximity devices and overload systems can fail. Extraordinarily fail-safe protective measures will have to be part of robotic systems of the future, as people and machines work side by side in increasing numbers and complexity of interactions.” [Harmon, 1982]. About 30 years later, tactile sensing still does not play this envisioned role [Lee, 2000]. A couple of recent reviews from different authors [Dahiya *et al.*, 2010] [Lucarotti *et al.*, 2013] [Howe, 1994] [Lee and Nicholls, 1999] [Yousef *et al.*, 2011] unveil that the implementation of artificial skin has so far largely been biased towards the technological implementation of sensors [Dahiya *et al.*, 2008], while a complete system is desired. Together with Dahia *et al.*, we have recently summarized challenges towards the effective utilization of artificial skin [Dahiya *et al.*, 2013]. In the following, we are giving a short review on the different aspects of artificial skin technology in the related work (see Fig. 2.3).

Sensing Modalities: Examination of sensing modalities in human, speak for a distinguished set of sensors to encode different phases in contact handling [Johansson and Flanagan, 2009]. Pressure/Force is the overall choice if only a single modality is integrated [Tawil *et al.*, 2009] [Ulmen and Cutkosky, 2010] [Maheshwari and Saraf, 2006]. Using only a single modality simplifies signal handling as it is not necessary to convert, transmit and process orthogonal sensor signals, and homogeneous skin structures can be used. Nevertheless, the additional costs for implementing multiple modalities seem to pay off on the processing side and provide a greater range of applications. Slippage and surface roughness can be classified by sensing vibrations [Göger *et al.*, 2009] [Edwards *et al.*, 2008]. Temperature changes help to distinguish between different materials [Fishel *et al.*, 2009] and compensate thermal drift for all other mechanical sensors [Maiolino *et al.*, 2013]. Shear stress sensors support the detection of edges [Chorley *et al.*, 2009] or skin kinesthesia [Vogt *et al.*, 2013], but shear forces can also be calculated from normal deflection [Fearing, 1990]. Proximity sensors enable a reaction prior to touch, which is especially useful in motion control [Lumelsky *et al.*, 2001].

Transduction Methods: Most physical principles [Dahiya and Valle, 2013] have been exploited to convert excitations, mainly normal forces, into measurable signals. These range from resistive [Weiß and Woern, 2005] and piezoelectric principles [Göger *et al.*, 2009], to optical [Persichetti *et al.*, 2009] and capacitive effects [Cannata *et al.*, 2008]. The cost driving touch screen market, along with the low power consumption and high versatility [Sato *et al.*, 2012] [Rocha *et al.*, 2006], make capacitive touch sensing technologies a promising choice. Force sensitive resistors are commonly used in the form of thin film layers [Papakostas *et al.*, 2002], conductive elastomers [Weiss and Woern, 2004], wire stitched [Shimojo *et al.*, 2004] or segmented fabrics [Buescher *et al.*, 2012] or QTC segments [Stiehl and Breazeal, 2006]. Although, these materials provide excellent spatial resolution, they suffer from continuous force calibration problems, lack of long term robustness, temperature dependencies and a limited transduction bandwidth (temporal or force range). New materials, such as a mixture of carbon nano-tubes with liquid crystals, can be used to on-line tune the force sensitive range [Lai *et al.*, 2011] and eliminate those limitations. Capacitance to digital converters do not only detect conductive materials, e.g. human tissue, but it is possible to coat them with a conductive material and use them as force sensors [Ulmen and Cutkosky, 2010] [Cannata *et al.*, 2008] [Biggio *et al.*, 2010]. A combination of light emitter and detector senses light reflected on an approaching object [Lumelsky *et al.*, 2001], in a cavity [Hellard and Russell, 2002] or within foam material [Fujimori *et al.*, 2009] compressed by force. A method to measure the effect of shear and lateral force on cross coupling between multiple optical pairs is proposed in [Kadowaki *et al.*, 2009]. Using optical fiber systems, as in [Hasegawa *et al.*, 2008], decouples the location of sensation and conversion. The same applies to hydraulic skin, where fluid channels collect the overall deformation of areas, and convey the fluid pressure [Fishel *et al.*, 2009] or electrical resistance [Park *et al.*, 2010] [Tseng *et al.*, 2008] [Noda *et al.*, 2010] as an output. Piezoelectric materials, e.g. PVDF, show good vibrational sensitivity [Choi *et al.*, 2005] [Yamada *et al.*, 2002b], but lack constant excitation capabilities. MEMS sense different modalities such as orientation [Hoshi and Shinoda, 2008], shear and lateral force [Ascari *et al.*, 2007], vibration [Scheibert *et al.*, 2009] [Sukhoy *et al.*, 2009] and hardness [Shimizu *et al.*, 2002]. All in all, MEMS accelerometers have shown effective for sensing vibration and orientation in one package – a low-cost and easy to use sensor. Temperature is sensed with PTCs or NTCs in the form of custom wire patterns [Castelli, 2002] or chips [Yang *et al.*, 2008].

Coverage and Wiring Complexity: Only a few projects have attempted to largely cover robots with sensitive skin. Here, we would like to highlight: 1) The european *Roboskin* project that developed flexible, triangular units with a conductively coated silicone layer to provide large area capacitive force sensing [Cannata *et al.*, 2008]; 2) The robot *TwendyOne* at Waseda university that has been equipped with multiple distributed tactile pads[Iwata and Sugano, 2009]; 3) Kuniyoshi and Ohmura *et al.* developed flexible optical and resistive cut and paste wire comb patches to estimate contact forces on a humanoid [Ohmura *et al.*, 2006], on a human body [Fujimori *et al.*, 2009] and on human hands [Sagisaka *et al.*, 2011]; 4) Kadowaki *et al.* [Kadowaki *et al.*, 2009] developed an optical shear and normal force sensitive element that was applied by Kumagai *et al.* [Iori Kumagai *et al.*, 2012] on large areas of HRP-2. Most other projects only equipped parts of the robot with sensors, for example the finger tips [Beccai *et al.*, 2009] [Schmitz *et al.*, 2010] [Biggio *et al.*, 2010] and hands [Schmitz, 2011], or parts for the expected interaction areas [Mukai *et al.*, 2008] [Göger *et al.*, 2006]. The most obvious way is to connect each sensor directly, leading to a high wiring cost (e.g. space, weight, complexity, interference with motions). Several techniques attempt to overcome these shortfalls: *Matrix structures* for instance try to reduce the wires by arranging sensors in rows and columns [Yang *et al.*, 2008] [Someya *et al.*, 2004]. This technology is dependent on the speed and robustness of the multiplexing pathways. *Boundary scanning* methods inject currents [Alirezaei *et al.*, 2009] or light pulses [Rothmaier *et al.*, 2008] from the outside of a skin patch. As with computer tomography, the state of the monitored area is estimated from external sensor information. With this method, only a single modality has yet been introduced [Heo *et al.*, 2005]. *Digital bus systems* [Cannata *et al.*, 2008] [Fujimori *et al.*, 2009] are less sensitive to interference than analogue signal transmissions, but rely on the cooperation of every node. *Wireless* solutions based on radio [Chigusa *et al.*, 2007] [Cartaa *et al.*, 2009] or optical transmission [Yamada *et al.*, 2002a] suffer from low bandwidth and require a complex supporting structure.

Skin Materials: The actual skin material has large effects on its function [Shimojo, 1997] and aesthetics. Stretchability and bendability can be an inherent feature of the sensor [Alirezaei *et al.*, 2009] and supportive material [Kim *et al.*, 2008] [Ohmura *et al.*, 2006] or introduced at the interconnection of rigid patches[Perez, 2006] [Lacour *et al.*, 2005] or taxels [Lin and Jain, 2009] [Wakuda and Suganuma, 2011]. Special materials elongate the life time and robustness [Strohmayr, 2012] of the skin system and modify the look [Yoshikai *et al.*, 2007] of the overall robot. New, self healing materials [Hou *et al.*, 2013] [Toohey *et al.*, 2007] automatically repair small injuries. Surface structures can act as a mechanical filter for the sensation [Cutkosky *et al.*, 1987] [Gerling and Thomas, 2005] [Yamada *et al.*, 2002b]. For a force sensitive skin, the design of the mechanical conversion mechanism, the sensor and its cover materials [Vasarhelyi *et al.*, 2006] play a key role. Different materials, like urethane foam [Ohmura *et al.*, 2006] or silicone [Persichetti *et al.*, 2009], and micro-structures like domes [Tseng *et al.*, 2008] or cantilevers [Oddo *et al.*, 2009], have been utilized to convert forces into measurable displacement. Instead of discrete elements [Yang *et al.*, 2010], integrated organic semiconductors (plastic electronics) will become important in the future [Someya *et al.*, 2005]. Although those materials allow miniaturization, the thickness of artificial skin has an important mechanical contribution, e.g. provides passive (in addition to active) safety [Fritzsche *et al.*, 2011] [Sugaiwa *et al.*, 2008] [Park *et al.*, 2011].

Processing: Processing tactile data usually entails algorithms dealing with spatial [Göger *et al.*, 2009] or temporal [Edwards *et al.*, 2008] [Göger *et al.*, 2009] [Sukhoy *et al.*, 2009] information extraction. Since tactile data is strongly coupled to its sensor location, the robot can implement direct actions, e.g. protective reflexes in response to the excitation of a certain body area [Dahl and Palmer, 2010]. One of the most effective ways to process tactile data is to local analogue to digital conversion and preprocessing. This approach increases the data transmission integrity and reduces the necessary transmission bandwidth and high-level processing power [Perez, 2006] [Hakozaki *et al.*, 2001] [Richardson *et al.*, 2004]. It also explains the long existing demand for a self-contained system on a chip [Dahiya *et al.*, 2013].

2.3. Body Schema in Robotics

"*Like natural agents, artificial agents can acquire sensori-motor representations of their own bodies and use them to guide actions.*" [Hoffmann *et al.*, 2010]. We concur with a number of statements made by Hoffmann *et al.*, in their recent review on body schema in robotics. It is desirable that robots automatically develop, calibrate and adapt their own body models (e.g. coordinate transformations), in order to lower the cost for building and maintaining those models. A body model consists of two components: 1) relationships between sensor modalities; and 2) relationships between sensor and motor representations. Body models are beneficial e.g. when executing feed-forward control or predicting the expected sensory feedback. Models can not be replaced with reflex-like couplings, when planning and monitoring whole action sequences, especially in complex systems as humanoid robots. In comparison to implicit, explicit models are easier to debug and assess, easy to link to a common control theory and provide valid data also in previously unseen situations. So far, the work on body models in robotics has been heavily biased toward manipulator arms observed by a camera, which is lacking the integration of multiple modalities (e.g. proprioception, vision and tactile) as demonstrated by biological agents. We first focus on spatial tactile calibration (see Fig. 2.4) and then move on to kinematic calibration methods (see Fig. 2.5).

2.3.1. Spatial Tactile Calibration

"*The problem of robot skin calibration has been defined in [Cannata* et al.*, 2010c] as the automated process of determining the location of taxels with respect to a known reference frame, after the taxels have been actually fixed on a robot body link.*" [Cannata *et al.*, 2010b]. We agree with Cannata *et al.*, and add that not only the location, but also the orientation of taxels is important. It is for example essential to know the location and orientation of a shear force sensor to act in the right direction. Manually providing those 6 parameters for a high number of tactile sensors would be error prone and cumbersome. Nevertheless, manual calibration is a very prominent solution. In the following, we summarize related work to automatically acquire a spatial tactile calibration (see Fig. 2.4). In [Fuke *et al.*, 2007] a simulated robot first visually learns the local kinematics of its hand (see Fig. 2.4). It then probes the position of tactile sensors on its face through the known hand position. This approach is limited to the reachable body parts and the accuracy of the local kinematics. [Prete *et al.*, 2011] utilize a force/torque sensor in the upper arm of an iCub robot, and a completely initialized kinematic chain, in order to estimate the location of taxels on the lower arm or hand (see Fig. 2.4). The problems of self-reachability and self-contact control are omitted by touching the robot with an external point probe. This approach fails when there is no F/T sensor, preceding the body part under evaluation. In [Yoshikawa *et al.*, 2002] a cross-modal map is learned among joint, vision, and tactile sensor spaces by associating different pairs of sensor values when they are activated simultaneously (see Fig. 2.4). When no visual input is available this learning method misinterprets the given situation. In [Kuniyoshi *et al.*, 2004] a simulated baby body performs random movements in water, extracting only topological structures with spatio-temporal cor-

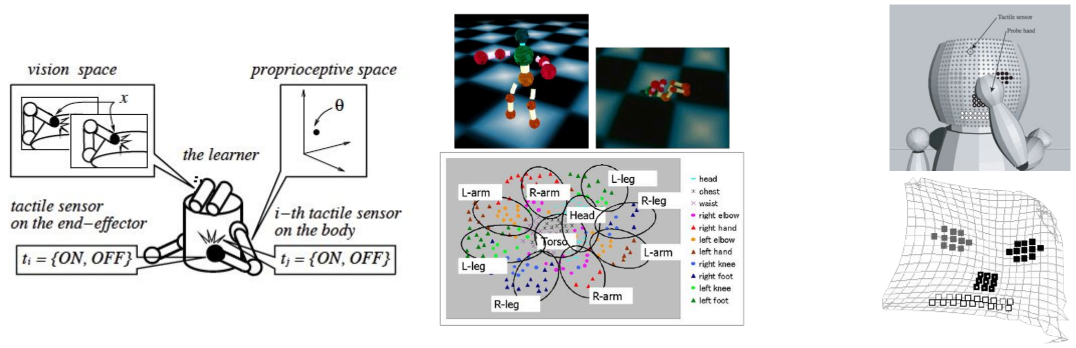

Yoshikawa et al. 2002 **Kuniyoshi et al. 2004** **Fuke et al. 2007**

Hoshi and Shinoda 2008 **Modayil 2010** **Prete et al. 2011**

FIGURE 2.4. The figure shows the spatial calibration results of related works.

relations (see Fig. 2.4). This approach has been extended to provide 3D sensor position estimates in [Modayil, 2010]. Modayil uses high correlations, limited to k-nearest neighbors, to establish local distance constraints. Then, a global optimization algorithm unfolds the 3D space, maximizing the unconstrained sensor distances. Implicitly given a global shape, the estimate only vaguely resembles the original (see Fig. 2.4). Hoshi *et al.*, utilize a fixed lattice structure of rigid links (see Fig. 2.4), equipped with triaxial accelerometers, to reconstruct the shape of cloth-like sheets [Hoshi and Shinoda, 2007]. Since the missing yaw angles are only estimated from assumptions on the elemental loops of the lattice, this accelerometer based approach suffers from singular configurations. In [Hoshi and Shinoda, 2008], Hoshi *et al.* extend the sensing capabilities of each link by a triaxial magnetometer, which is considered infeasible for an artificial skin on a robot. Metallic structures and the electromagnetic noise distort the magnetic field close to every robot. The fixed lattice grid also does not account for the flexibility of placing skin in arbitrary shapes on robots.

2.3.2. Kinematic Modeling

"*Articulated models ... based on state variables (such as manipulator joint angle positions) that interact according to the laws of dynamics and mechanics ... come closer to the notion of body schema as we know it from biology. This time, however, the variables have to be measured by the robot's own sensors.*", [Hoffmann *et al.*, 2010]. Kinematic models are commonly acquired with superficial, highly precise external metro-logy systems. However, it would be more interesting and important, e.g. to support life-long adaption and error recovery, to automatically acquire those models with internal sensors only. Commonly, an explicit kinematic model acquisition involves two steps: 1) the synthesis of an articulated model from a self-explored robot's topology; 2) the calibration of the kinematic parameters of the model.

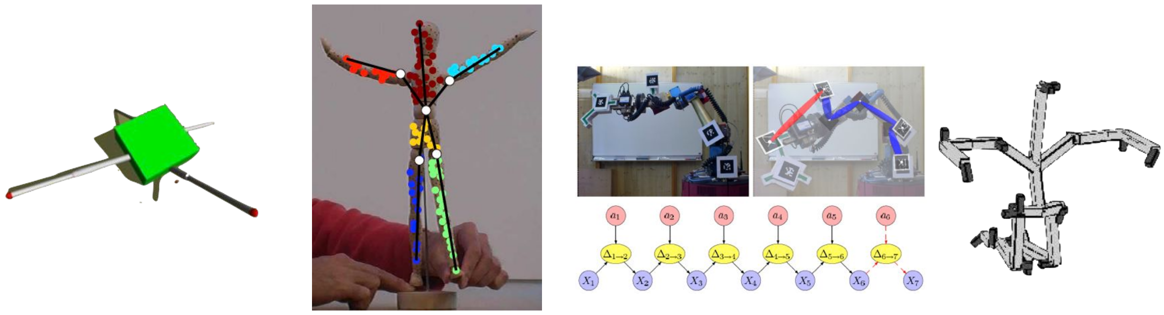

Bongard et al. 2006 **Yan and Pollefeys 2006** **Sturm et al. 2008** **Hersch et al. 2008**

FIGURE 2.5. The figure shows the kinematic modeling with related works.

The second step is well known as kinematic calibration e.g. with industrial robots. As described in [Hollerbach and Wampler, 1996], calibration approaches are divided into open- and closed-loop methods. With open-loop methods, a precise external metrology system measures the pose (only the end-effector or all body parts) of the robot under motion. Their precision stands and falls with the external metrology system. In the closed-loop approaches, the kinematic chain is closed with a mechanical constraint and the remaining mobility used with joint level sensing (positions and/or forces) to generate the required input for the estimation. Closed loop measurements profit from the accuracy of the fixation point to the environment or another manipulator. Their precision stands and falls with this fixation accuracy and the remaining mobility. With over-constrained closed loops additional sensors have to be provided, e.g. a force torque sensor at the endpoint [Bennett *et al.*, 1992]. A detailed overview of the *fundamentals of manipulator calibration* is denoted in a book by Mooring *et al.* [Mooring *et al.*, 1991]. Using a special form of open-loop motion, called Circle Point Analysis (CPA), moving only one joint axis at a time, the kinematic parameters can be computed analytically [Hollerbach and Wampler, 1996]. An example of this CPA approach, which is closely related to our work, has been presented in [Canepa *et al.*, 1994]. Canepa *et al.* utilize a 3-axis accelerometer on the end effector to conduct a Circle Point Analysis. However, their approach is based on a first order integration of the accelerometer data and large movements. This requires high integrity of the accelerometer data, which is normally only achieved with large and expensive high grade devices. Their approach also requires a large, collision free workspace for fast movements of the uncalibrated robot. Motion capture systems, have often been used to automatically build and estimate kinematic models. Most systems track active [Ude *et al.*, 2000] or passive [Yan and Pollefeys, 2006] visual markers/features (see Fig. 2.5). Such approaches are extremely fast and can also robustly adapt to structural changes, e.g. utilizing Bayesian networks [Sturm *et al.*, 2008] (see Fig. 2.5). Magnetic motion capture systems perform better when occlusion is a problem [O'Brien *et al.*, 2000], but would fail on metallic robots. All former approaches rely on a globally accurate and calibrated external sensor system, and the availability of robust tracking of markers or features. In [Hersch *et al.*, 2008] (see Fig. 2.5), an algorithm is presented to visually learn the subjective body schema of a HOAP-3 robotic platform from a partial internal view on the end-effectors or subsequent body parts. The model takes advantage of *a-priori* information on the arrangement of joints and cannot learn any new body structures. It also uses a calibrated stereo-vision system that provides reliable position input. Inertial motion capture systems, like the XSens MVN [Roetenberg *et al.*, 2008], come with a underlying body model on which several parameters have to be given manually and others are found by matching known postures, e.g. the T-pose). The difficulties to explore the topology and estimate the kinematic parameters from an egocentric perspective, using other than visual sensors, can be seen in [Bongard *et al.*, 2006a] and [Bongard *et al.*, 2006b] (see Fig. 2.5).

2.4. Utilization

Artificial skin is useful for a variety of tasks in robotics (see Fig. 2.6), from classification [Sukhoy *et al.*, 2009] to contact control [Cannata *et al.*, 2010a]. Providing tactile sensors, the required object knowledge can be relieved – the manipulation (e.g. a grasp) becomes reactive [Hsiao *et al.*, 2009]. As demonstrated in [Romano *et al.*, 2011], manipulation sequences can be separated into discrete states, activated e.g. by tactile events. In [Mukai *et al.*, 2011], tactile sensors are utilized to control the balancing contacts between a human-like object and the arms of a nursing robot, while carrying it. In [Ohmura and Kuniyoshi, 2007], tactile feedback and additional contact points enable a humanoid to lift heavy objects – we assume that tactile feedback serves here to switch between pre-computed procedures. In [Noda *et al.*,

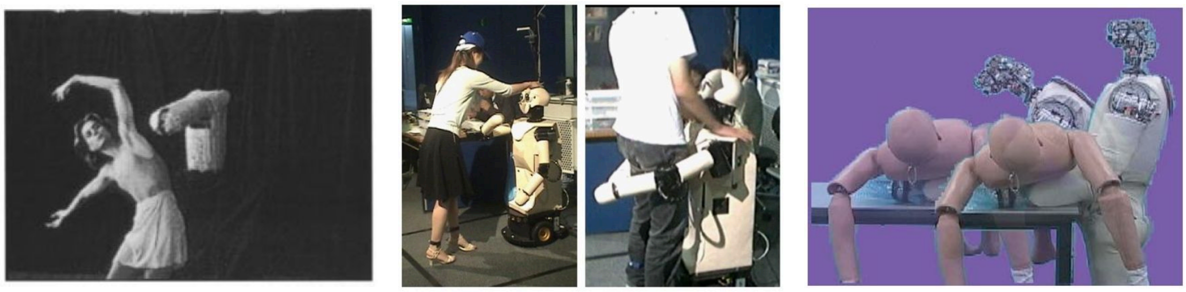

Lumelsky et al. 2001 **Noda et al. 2007** **Ohmura et al. 2007**

Argall et al. 2010 **Mukai et al. 2011** **Kumagai et al. 2012**

FIGURE 2.6. The figure shows the exemplary utilization of artificial skin in related works.

2007], tactile sensor signals have been used to classify types of interaction, like hugging or hand-shaking by a human with a real robot, while in [lori Kumagai *et al.*, 2012] whole-body contact states between the robot and an object are monitored. A survey by Argall *et al.* [Argall and Billard, 2010] on tactile human robot interaction shows the potential of this new interface – so far, the authors implemented an approach of tactile guidance for policy refinement [Argall *et al.*, 2010b] and tactile correction [Argall *et al.*, 2010a]. In [Iwata and Sugano, 2006], tactile recognition serves to identify a set of contact states (e.g. pulling, hitting, stroking) between human and robots. Finger sensors in [Göger *et al.*, 2009] detect slippage during manipulation and contact profiles [Schmid *et al.*, 2008] to open doors along with visual cues and joint-level F/T sensing. Instantaneous movements in response to a sensory stimulus provide touch triggered reflexes for safer robots, as in [Dahl and Palmer, 2010] and [Battaglia *et al.*, 2009]. This type of behavior has also been used for interactive real-time guidance [Lumelsky *et al.*, 2001] and reactive grasping [Schmidt *et al.*, 2006]. Before grasping, objects can be globally localized via touch as shown in [Petrovskaya and Khatib, 2011]. Once localized, those objects can be recognized by fusion of tactile and kinesthetic features [Navarro *et al.*, 2012] [Schmitz *et al.*, 2014]. Both papers show the symbiotic relationship of the tactile and kinesthetic sensing modalities. During manipulation, tactile information can evaluate the stability and allow in hand manipulation [Kojima *et al.*, 2013].

2.5. Summary

In this chapter, we summarized the related works on the creation and self-organization of artificial skin, from the biological inspiration to robotic implementations. We started with an overview of the multiple mechano-receptors in human skin, showing its multi-modal sensitivity and its distributed nature (e.g. conversion, processing, communication). We then stated the abilities of the human body to self-organize and calibrate its own sensory-motor body representation – the body schema. We continued introducing various artificial skin solutions and their contributions to the design and implementation of numerous multi-modal sensors on a large surface area. We then introduced the notion of body schema in robotics, from the spatial calibration of a highly distributed sensor system to classical and recent methods to model and calibrate the kinematic representations of robots.

We extend this related work by providing a multi-modal, modular artificial skin with a distributed nature like biological skin (refer to Chapter 3). We then utilize sensor fusion across visual, proprioceptive and tactile senses to build an ego-centric robotic body schema. We provide a method to accurately acquire the spatial tactile calibration (location and orientation of taxels) with distributed body frames (refer to Sec. 4.2), and a method to visually combine those distributed frames into a centralized body representation (refer to Sec. 4.3). Sensor fusion across the proprioceptive and tactile sense enable us to explore the kinematic topology (refer to Sec. 5.2) and calibrate the kinematic parameters with internal sensors only (refer to Sec. 5.4). We finally provide utilization examples that serve for laboratory-to-real-world transfer, e.g. enhancing the human-machine interface and safety of robots with contact and pre-contact sensing (refer to Chapter 6).

CHAPTER 3

Creating Artificial Skin

> Think how lucky you are that the skin you live in,
> so beautifully holds the "You" who's within.
>
> *(Michael Tyler:* The Skin You Live In*)*

This chapter introduces the novel artificial skin system we developed. In the first section, we introduce a modular approach to create artificial skin from the same building block, a multi-modal skin cell, along with a prototype with standard electronics. In the second section, we provide details about the novel force sensor that has been integrated into the skin cell.

3.1. Introduction

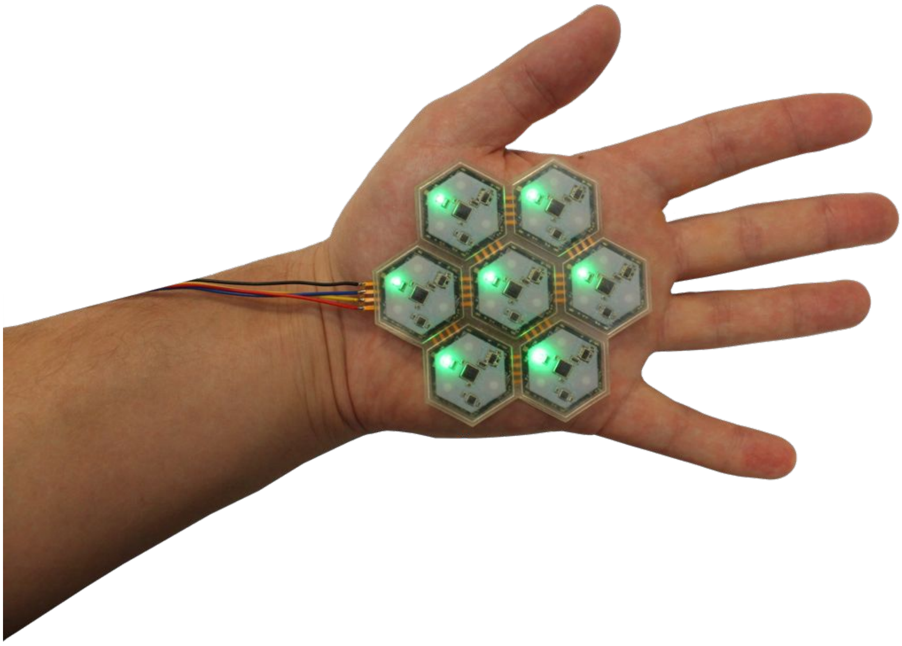

FIGURE 3.1. The figure shows a patch of CellulARSkin^{TM} on a human hand.

Every interaction of an embodied agent, with itself or the environment, is grounded on its surface. Sensitive skin provides a rich and direct feedback on these interactions, making it a key technology for future robots. Multi-modal awareness of distributed contacts will give robots, commonly only relying on vision and joint force/torque sensors, additional information – e.g. when handling large/unknown objects, classifying contacts or dealing with cluttered and occlusive environments. With a set of multiple sensor modalities, a variety of sensations is supported. Skin is able to feel the own body motion, thermal effects, contact forces, vibrations and painful stimuli. With an artificial skin those sensations can be meaningfully extended, e.g. by a sense of approaching objects to improve safety. The first step towards those aims, the creation of a large area, multi-modal artificial skin, poses many technical challenges. A large number of distributed sensors have to be implemented, their signals converted and processed, the resulting information extracted and transfered to the control system. Sensitive skin has to be efficient to manufacture, transferable between multiple robotic systems and easy to implement. Artificial skin has to be sensitive, but robust and reliable, as it is in constant interaction with the external world. A variable number of sensors on an arbitrary surface shape need to be identified, labeled, routed and processed. In this chapter, we provide solutions to these challenges, creating an easily transferable, scalable cellular artificial skin (see Fig. 3.1).

3.2. CellulARSkin™

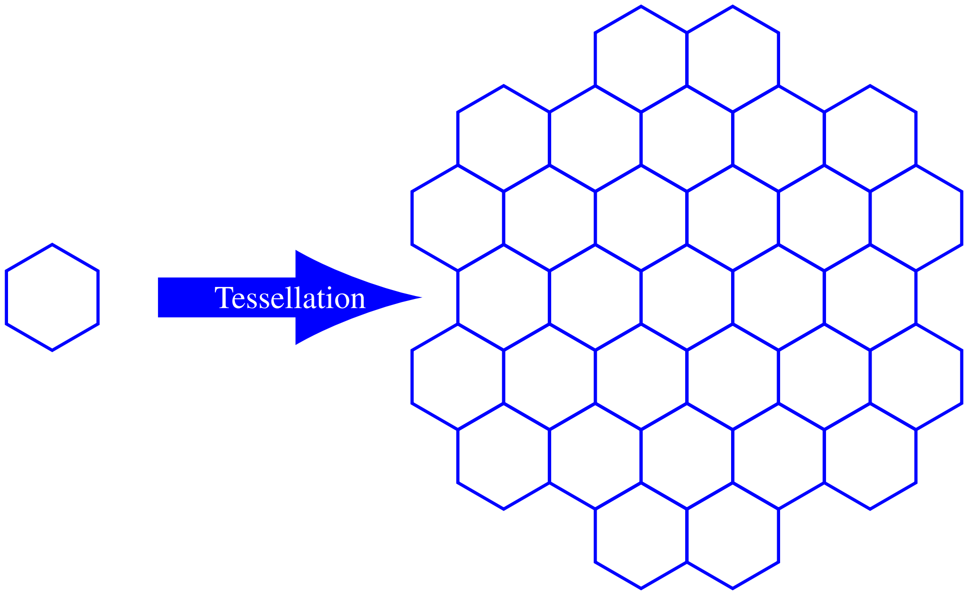

FIGURE 3.2. The figure shows a dense tessellation of a flat surface with hexagonal skin cells.

In this section, we introduce the concepts behind a cellular artificial skin, including its prototype realization[1]. Why should artificial skin be built from elementary cells? – Because following this biological inspiration is favorable for many technical advantages. First of all, building a high number of similar cells, is in favor of efficient mass production – one design is optimized and then replicated as many times as needed (see Fig. 3.2). Since each cell is a self-contained entity, it is neither dependent on a central system nor on its neighbors. Every cell provides its own sensing, processing, power and communication capabilities. Although the repetition of functional elements might be seen as a waste of resources, it highly contributes to the simplicity and robustness of the system. In the context of artificial skin, a highly distributed and parallelized system is much more robust than a centralized and serialized one. Failures, either the death of a complete cell or only partial loss of functions, are isolated at the smallest cellular level. The simplicity increases as all cells are functionally independent building blocks. The artificial skin is created by placing as many elements next to each other as fit the 3D surface to be sensitized. Since every cell brings its own infrastructure, little additional centralized infrastructure for power and communication is necessary. Combining local sensing and processing, largely increases the information content of signals fed into a system. Since those signals are digital, they are very well protected from external and internal influ-

---

[1] The work in this section has been published in [Mittendorfer and Cheng, 2011a][Mittendorfer and Cheng, 2012d][Mittendorfer and Cheng, 2013].

ences on the long communication pathways to the central processing system. In fact, digital repetition strengthens signals in technical as well as biological systems. Having a small, self-contained entity also eases organization. Connections, memories and processing are managed at cell level and *in-situ* modified to the available active elements. Control algorithms are able to take advantage of the smallest building block, creating system behavior through local rules. Self-organization, as a paradigm in biological systems, helps the creation of large and complex global systems. In engineering, this approach is known as *divide and conquer* paradigm.

3.2.1. Cellular Sensor Network

3.2.1.1. Economy of Scale of a Modular Solution

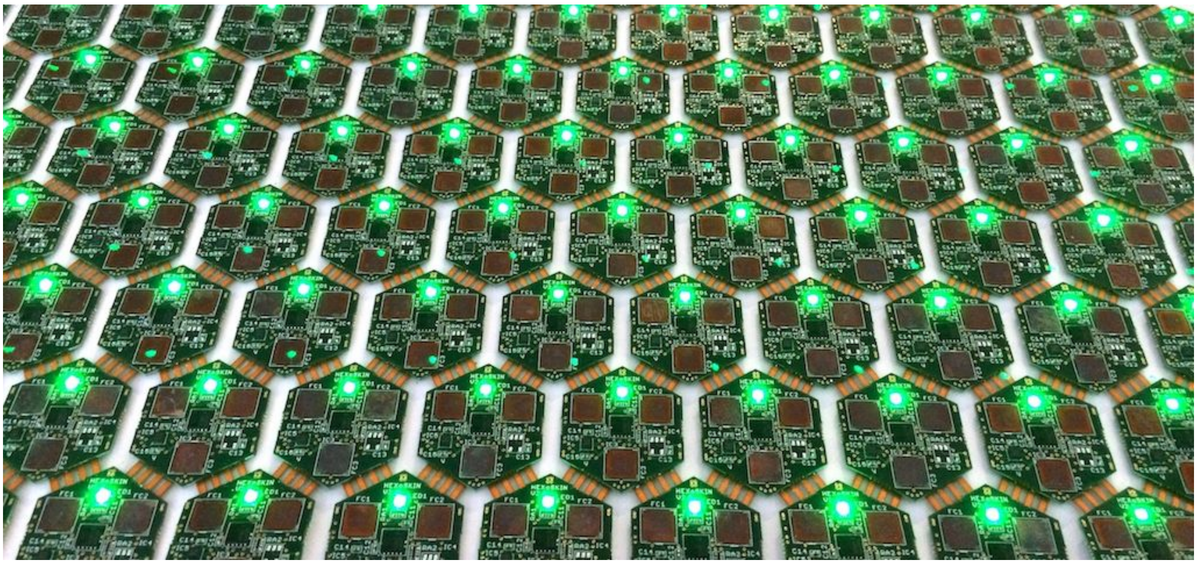

FIGURE 3.3. The figure shows a large array of CellulARSkin^{TM} electronic boards – the core of the cellular artificial skin.

An artificial skin solution should not be focused on a single robot and be easily applicable to other domains, e.g. health care or consumer products. Every solution has to be intrinsically transferable and scalable. In order to offer an economically attractive solution, for a manifold of potential customers, the costs have to be controlled. This goal is only achievable with a highly modular solution, where the expensive and complex part is similar and can be mass produced (see Fig. 3.3). The success of such a business model has not only been shown in automotive industry, but also is currently introduced into robotics – e.g. by Universal Robots. At the same time, the complexity of integrating customer specific solutions has to be minimal, e.g. reduced to a cut & paste process, while the design and production process of a customer specific solution has to be an easy subject for automation. An intense testing of the main module is justified by its potentially large production volume. Being able to specify and verify systematic behavior of a multi-module system, it should not be necessary to proof the conformity to international standards (e.g. CE, ISO, FCC) for every customer implementation. Using CellulARSkin$^{\mathrm{TM}}$ (see Fig. 3.3) we have demonstrated the economy of scale of a modular solution. We have been able to apply our solution to different robots and have been able to lower the production costs in every cycle by a factor of two, even in small series production.

3.2.1.2. Current and Future Integration Technologies

The available technologies are the pillars to build an artificial skin system on. However, the concept behind should be technology independent and applicable to current, as well as future technologies. In the case of CellulARSkin$^{\mathrm{TM}}$, we implemented a prototype with standards electronics – sensors from the growing smart phone market, standard Printed Circuit Boards (PCBs) and silicon chips (see Fig. 3.3). Those standard technologies clearly limit the capabilities of our artificial skin regarding sensor density, manufacturing costs and the ability to conform to arbitrary 3D surfaces. However, the conceptual design of the skin cell itself is independent of technologies. Explored concepts and algorithms can be easily transferred between current and upcoming technologies. We expect that the next step will allow hybrid solutions, between small and fast silicon interfacing chips and low-cost, densely printed organic sensors. In the future, we expect to be able to completely print cells in flexible organic electronics. It is possible to shrink the size of the skin cell within each technology limit, easing the integration on arbitrarily curved surfaces. Given a miniature skin cell, it is irrelevant if the cell element is rigid or flexible, as long as the embedding substrate exhibits those features. In order to be able to handle a growing number of distributed elements and sensor signals, self-organization features and local processing will become more and more important.

3.2.1.3. The Optimal Cell Shape

One of the first questions, when tessellating/parqueting a surface with the same element, is its shape. The 2D shape has an influence on how dense cells can be arranged next to each other. Optimally there should be little insensitive space left between elements. Cells overlapping or penetrating each other are not feasible. The 2D shape influences the number and contact faces to the neighboring cells. Optimally, there is space for physical bonds to many neighbors. The 2D shape of the rigid element with flex-rigid designs has an important influence on the flexibility. Optimally, there are many flexible connections in multiple directions. Only three

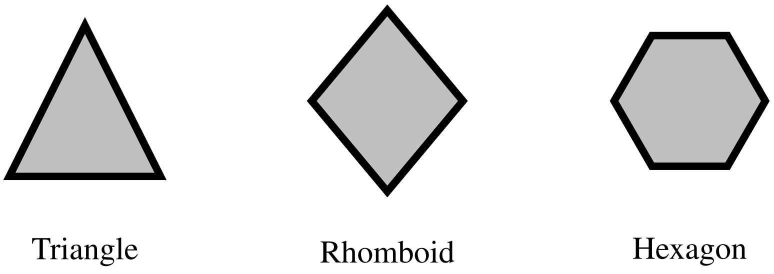

FIGURE 3.4. The figure shows potential regular skin cell shapes that tessellates a 2D surface without gaps.

regular geometrical shapes tessellate a plane without gaps: triangles, rhomboids and hexagons (see Fig. 3.4). We consider the hexagonal shape to be optimal due to the following arguments (see Fig. 3.5): 1) Every hexagon is connected to all of its neighbors (close/far) by an edge; these edges are utilized to establish physical (e.g. wired, optical, RF) data and power connections to every neighbor, offering a high number of potential links for redundancy or flexibility in parqueting; 2) The distance of same points on aligned neighboring hexagons is equal for all neighbors; This natural triangulation of sensor positions is best for circular symmetric kernels – amongst them edge detectors [He and Jia, 2005]; 3) The high density (close to the optimal circle) of the hexagon offers space for large standard components; This compactness is especially important for a flex-rigid solution. The benefits of hexagonal pixels, regarding sampling

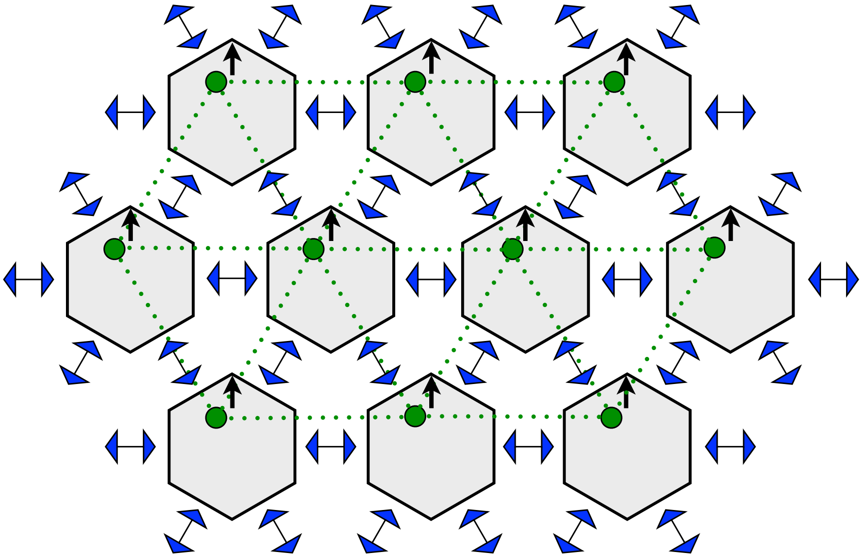

FIGURE 3.5. Advantages of the hexagonal skin cell shape in a dense grid: dense shape; natural sensor triangulation; edges to all neighbors.

and processing, have also been discussed in vision [He and Jia, 2005][Petersen, 1962]. He *et al.* argument that the main problem limiting the utilization of hexagonal image structures, is the lack of hardware for capturing and displaying hexagonal-based images. With our artificial skin system, we have the freedom to choose this optimal shape. Additionally, we wish to point out that the closest packing of identical circles and one of the closest packing for identical spheres (e.g. cells or atoms) is the hexagonal arrangement. This is the reason why hexagonal grids are often found in nature.

3.2.1.4. Conformation to Arbitrary 3D Surfaces

FIGURE 3.6. The figure shows a skin patch with 143 skin cells mounted on the first tube like link of an UR-5 robot arm. The tube like shape is approximated with a (tridecagon) regular polygon with a bending angle of 27.7°.

Artificial skin must conform to the arbitrary 3D surface it is put on. It also needs to partially conform to the arbitrary surface of the object it is making contact with, enlarging the mutual contact surface. In order to achieve this, skin requires mechanical flexibility. There are multiple options to realize this flexibility: 1) a completely flexible design, with flexible connections, sensors and logic; 2) a flex-rigid solution, with flexible connections, but rigid sensors and logic; 3) a hybrid design with flexible connections and sensors, but rigid logic. Although all flexible solutions are the ultimate goal, their practical implementation is not yet mature. On the one hand, flexible electronics are still much more expensive and not yet commercially available. On the other hand, technical problems occur when sensors, connections and active elements are bent, e.g. due to piezoelectric effects. Regrading sensors, it is also be extremely difficult to subtract flexure from desired effects, e.g. temperature induced changes vs. stretching of a resistive finger structure. The speed and integration complexity of organic electronics is still comparably low. With the existing technologies, an organic electronic skin would have a much lower bandwidth and higher latency compared to an inorganic electronic skin. In our case, we opt to use a flex-rigid solution with flexible interconnects, but (quasi-)rigid sensors and logic. This approach has multiple benefits: 1) mechanical stress is shifted from critical core elements to (redundant) interconnects; 2) standard rigid electronics and technologies can be applied; 3) sensors are affected less by flexing the skin. Reducing the size of the rigid elements increases the number of flexible interconnects and such the overall flexibility/bendability of the skin (see to Fig. 3.7). While the surface approximation quality of the skin is becoming better, the local bending angle of the flexible connection is becoming less. Another option to conform to the given surface is to leave skin cells from the initial regular grid, allowing higher bending angles and preventing overlaps. In summary, we can say that a high flexibility can be easily achieved with small rigid elements which are connected flexibly as demonstrated in parts with CellulARSkin^{TM} (see Fig. 3.6).

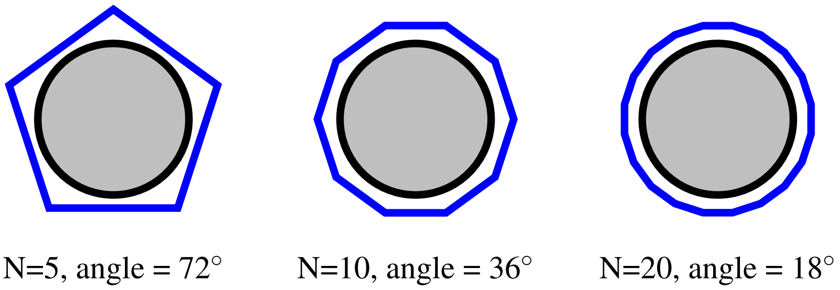

FIGURE 3.7. The figure shows a regular, piecewise linear approximation of a circle for different lengths of the linear element. The required bending angle decreases with 1/N.

3.2.1.5. Skin Layers

Biological skin features multiple layers, which can not be replicated with a thin electronic film on a rigid surface (refer to Sec. 2.1). The mechanical properties of the epidermal layer play a major role regarding contact properties, e.g. friction and micro-compliance and provide mechanical protection against wear and tear, physical and chemical abuse. The subcutaneous layer is essential for bonding to the supporting structure and provides compliance. Skin receptors are placed at different depth of the skin to enhance their mechanical sensation, e.g. to amplify light stimuli with papillary ridges [Cauna, 1954] or to broaden receptive fields with sensors in the lower skin layers [Shimojo, 1997]. CellulARSkin^{TM} uses multiple, specifically designed layers (see Fig. 3.8). The top elastomer cover is a material mix composed of a soft surface and soft encapsulation of the sensors, but hard epidermal layer with papillae like

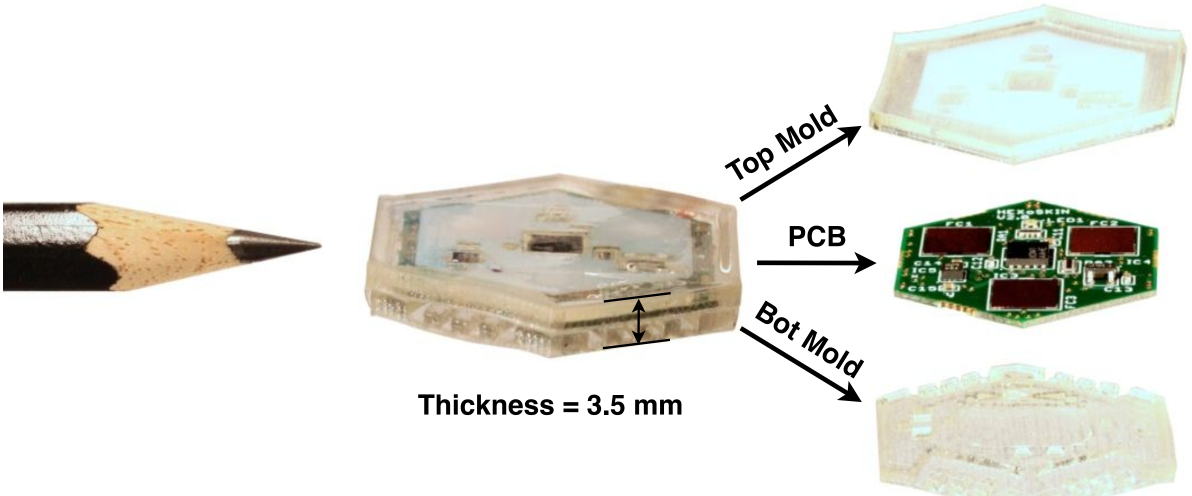

FIGURE 3.8. The figure shows the different layers of the artificial skin CellulARSkin$^{\mathrm{TM}}$.

structures on top of the force sensors. This design protects the sensors from impacts, provides a surface with high grip and acts as a spatial mechanical filter that collects and focuses forces onto the mechanical sensors. The dermal layer of our skin, the electronics board, holds multiple sensor modalities at various heights, e.g. the temperature sensor close to the surface for best thermal coupling and the force sensors deeper in the skin for spatial filtering. The subcutaneous layer provides compliance and protects the infrastructure. We either 3D print the skin material with an elastomer called Tango Plus and Vero White from OBJET, a rapid prototyping material that is printed drop by drop with a resolution of 16 µm, or we mold and assemble the top and bottom layers from silicone and plastic. Using rapid prototyping materials provides a number of advantages: 1) we can directly add micro structures made of different material mixtures into the skin; 2) a skin layout for a robot can quickly be designed in a CAD process and printed within a couple of hours. Molded materials instead, are long term stable, more robust against wear & tear and can be produced at lower costs at higher quantities.

3.2.1.6. Digital Cell-2-Cell Communication

One challenge of a large area artificial skin is the acquisition of sensor signals from distributed, multi-modal sensors. Sensor signals must not only be transfered over a potentially large distance, but also acquired from a high number of spatially distributed sensor locations. In order to change pre-processing parameters, every skin cell must be reachable by a central control unit. In comparison to analog, digital signal transmission offers many benefits in this application. Digital signals are easily transmitted from cell-2-cell and repeated with minimal hardware and no additional noise (only statistic errors). Embedding redundancy, digital signal errors can be detected and in many cases corrected. Especially for artificial skin, on a large surface area and in a noisy robotic environment (e.g. electric motors and computers), signal integrity plays a major role. Given local memory, digital signals are easy to store or delay – enabling static or dynamic scheduling algorithms for transmission. Dynamic routing algorithms provide means to transmitting critical data, e.g. safety related detections, with a higher priority, in order to minimize reaction delays. It is easy to transfer multi-modal data with digital data packets. Direct, bidirectional data connections between neighboring skin cells have multiple advantages. Significantly below the communication wavelength, impedance matching is not critical. In this way, cheaper and smaller hardware can be utilized e.g. simple TTL digital logic instead of LVDS differential signals with large analog drivers. The small antenna effect also reduces noise emission and admission. Forwarding data from neighboring cells, every cell behaves like a network repeater, which further increases signal integrity. Corrupted transmissions are eliminated at an early stage. Connection failures can be isolated, using alternative routing pathways. Every skin cell is able to utilize its own generation rate. There is no need to synchronize the data generation, unlike with a bus or matrix system. Cell-2-Cell communication also provides the ability to find adjacencies in the network and infer them to distances in the real world, enabling self-organization methods as shown in Sec. 4.2.

3.2.1.7. A Self-organizing Artificial Skin Network

An artificial skin has a potentially high number of distributed sensors, numerous parallel and serial communication pathways, and a unknown spatial topology. Manually setting up and maintaining the skin network is consequently not feasible and should be replaced with automated routines. In a cellular skin, every skin cell must only know two elementary settings: 1) its own unique ID, to be able to discriminate the origin of a packet in the network; 2) one out of the available neighbor connections to forward its own and received packets to. Additional information about the connection of the skin cells can be used to optimize this initial network or infer spatial distances for self-organizing methods (refer to Sec 4.2). In CellulARSkin^{TM} these settings are determined by a network exploration algorithm, which is part of the startup code. The self-organization is initiated and controlled by the interface, but unfolds with local rules on the skin cells. The number of interface connections to the skin cell network, as well as the topology of the network itself, is not limited. In the case of CellulARSkin^{TM}, the network organization is split into 4 phases (see Fig. 3.9). The organization starts with a broadcast of a synchronization command from the interface. This token initiates a search for bidirectionally active connections and synchronizes all skin cells after startup. Active connections are detected by a question and answer principle in both directions. Inactive connections are turned

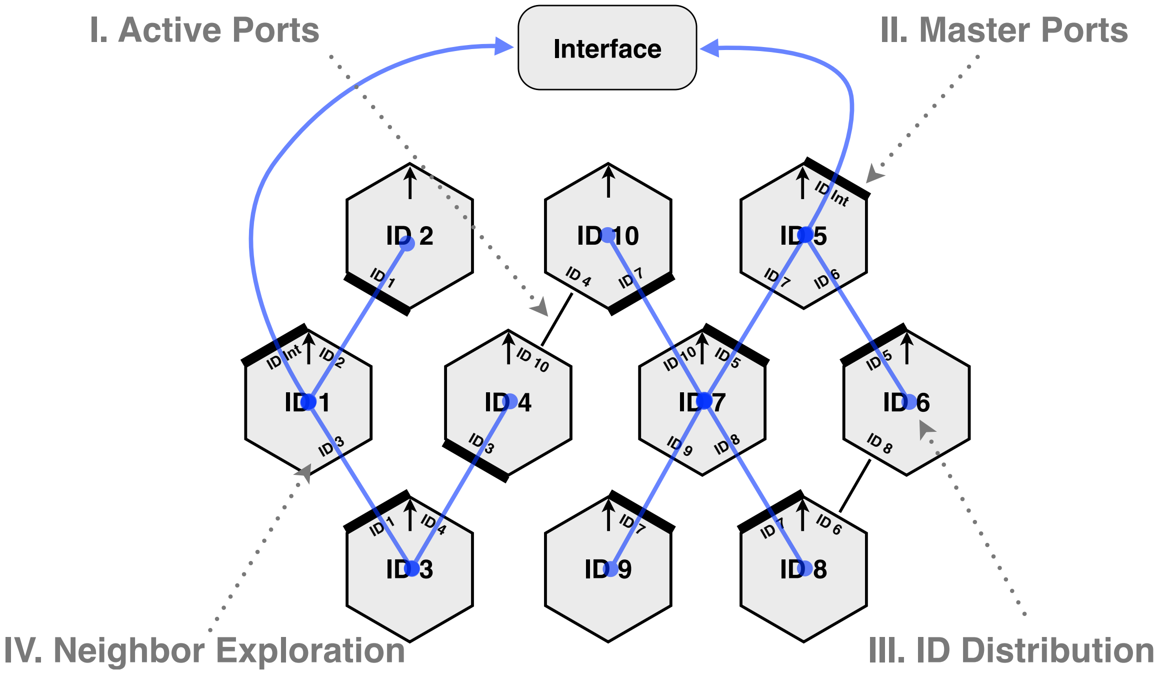

FIGURE 3.9. The figure shows an exemplary network self-organization result: detected active ports (I), set master ports (II), distributed IDs (III) and detected neighbors (IV).

off. Next, every interface port simultaneously injects a path exploration token. The connection of a skin cell at which this token is received first, is set as the master port, the others as slave ports. Every skin cell forwards this token once to all of its slave ports. Master and slave ports consequently build a directed communication path in the form of a communication tree. Every root of the tree is one port of an interface (see Fig. 3.9). This communication pathway is implicitly based on an optimization of the forwarding delay, from the interface ports to the skin cells. It is not necessarily optimal to relay sensor data vice versa. Algorithms such as the Capacitated Minimum Spanning Tree (CMST) algorithm can optimize this network based on the acquired network graph (neighbor exploration) and upload new master ports for every cell. In a next step, each tree like structure is utilized to distribute IDs by a Depth First Search algorithm, incrementing and setting IDs every time a new skin cell is reached. Every time the token is returned to an interface port, it is sent to the next interface port – until all active interface ports have been served. Finally, every skin cell queries the ID of its nearest neighbors and forwards this adjacency information to the computer. The artificial skin network then continues with normal operation. A minimum algorithm to reach and read from every cell (like for the boot-loader) only incorporates step I and II. As the ID distribution algorithm is not deterministic, skin cells have to memorize their IDs locally. The network exploration algorithm scales linear in time with an increasing number of cells. Connection and skin cell failure are handled with a quick re-exploration.

3.2.2. The Skin Cell

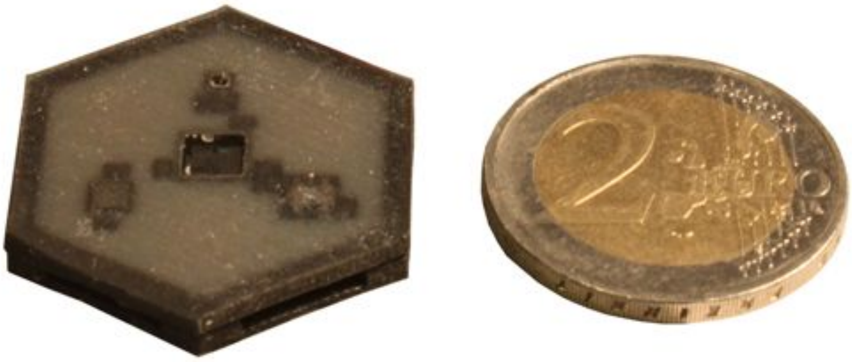

FIGURE 3.10. The figure shows the size of skin cell version 2.0 compared to a 2 EUR coin.

The skin cell (see Fig. 3.10) is the building block of our artificial skin. It is the carrier of sensor modalities and provides local infrastructure to acquire, pre-process and communicate sensor signals. In this subsection, we explain its functional elements and capabilities (please also refer to Table 3.1).

number of modalities	4	discrete sensors	6
cell input voltage	3.0-5.5 V	max cell power	16 mA/3.0 V
weight per cell	< 3.0 g	skin thickness	3.3 mm
cell-2-cell bandwidth	4 Mbit/s	cell-2-cell protocol	custom
cell-2-cell data packets	20 bytes	cell-2-cell commands	4 or 20 bytes
ports per cell	4	wires per port	4
data packet routing	active	data packet scheduler	round robin
min. cell-2-cell data delay	50 µs	1 cycle cell-2-cell data delay	200 µs
supply routing	passive, resistive	compensated voltage drop	< 2.5 V

TABLE 3.1. The table shows the general specifications of skin cell version 2.0.

3.2.2.1. Local Infrastructure

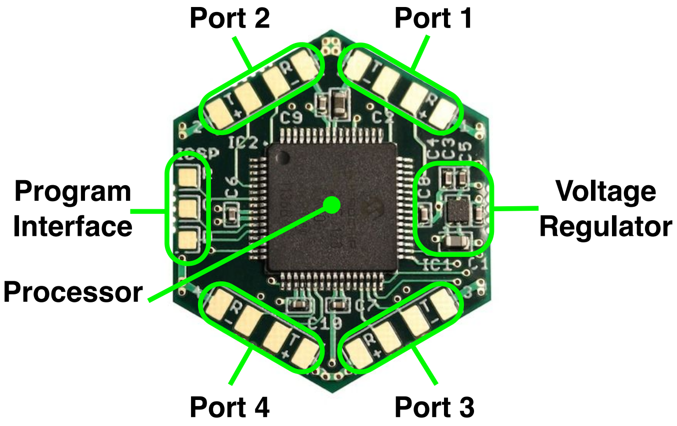

FIGURE 3.11. The figure shows the local infrastructure of the skin cell version 2.0.

The back side (see Fig. 3.11) of the skin cell features its local infrastructure: 1) the combined data & power ports to connect it to neighboring cells; 2) the processor for sampling and processing the sensor signals and communication; 3) the voltage regulator for local power stabilization; and 4) distributed devices for energy buffering, EMI and ESD protection.

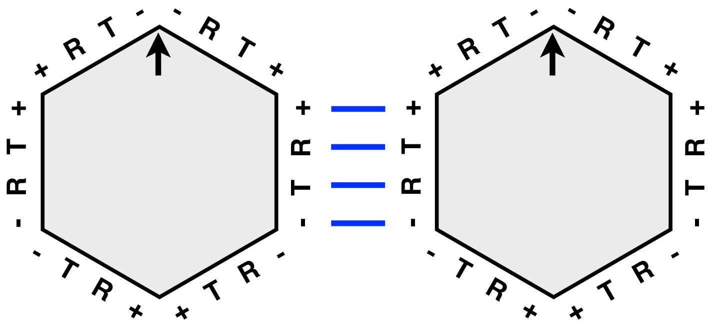

FIGURE 3.12. The figure shows a port pattern allowing direct cell-2-cell connections - (R)eception, (T)ransmission, (+) and (-) power.

Cell-2-Cell Ports: The cell-2-cell ports establish power and communication connections between neighboring cells or cells and the interface. With the hexagonal shape, up to six cell-2-cell connections can be established. In order to keep the wiring simple, only 4 non-crossed wires are utilized to transfer bidirectional data and power. Therefore we developed a specific pattern to allow direct connections between aligned neighboring cells (see Fig. 3.12). These connections must be bendable to allow the skin structure to conform to the surface. Up to 5 of 6 connections per hexagon can fail (currently only 4 connections are implemented), which introduces the necessary redundancy for a non-healing skin solution. In future, we would like to replace the wires with short ranging wireless solutions (e.g. capacitive or inductive coupling), simplifying the skin production process and improving the mechanical reliability and flexibility of the connections.

	Reg.	PIC24F	BMA250	VCNL4010	pull-ups	LM71	LED	Total
Active	0.2 mA	6.9 mA	0.2 mA	3.8 mA	1.3 mA	0.6 mA	3.0 mA	$\approx 16\,\mathrm{mA}$
Saving	2 µA	80 µA	7 µA	2 µA	-	-	-	$\approx 91\,\mu\mathrm{A}$

TABLE 3.2. The table shows the current consumption of each components of skin cell version 2.0 for a fully active and power saving standby mode (values from the data sheets).

Power Management: Every skin cell needs a small quantity of local energy storage and options to efficiently handle power consumption. Without local energy buffers, energy intensive events, e.g. an active sensor emission or increase in processing activity, can cause insufficient energy supply on a single cell. When power instabilities leave the boundaries of a single cell, they affect the signal quality or stability of the surrounding cellular network. We use a linear voltage regulator circuit to compensate the power network voltage drop (up to 2V), stabilize analog and digital supply rails (to 3V), provide a small energy buffer (16 mA for 600 us) and reject incoming and outgoing power noise (75 dB). Power management is necessary to cut down the overall power consumption. Power intensive active sensors should only be activated only for infinitesimal short times. We currently use a built in functionality of the proximity sensor (VCNL4010) to modulate its emitter current. Table 3.2 shows the consumption of specific components in fully active and power saving modes. The large contribution of the controller (PIC24F) can be reduced by lowering its frequency and entering idle modes – at the cost of higher latencies in the signal communication. The potential of power saving is consequently bound by the required sensors and latencies within a given application.

Local Controller: The local controller handles all multi-modal sensors, acquires digital sensor values or converts analog signals to the digital domain. It then pre-processes the digital signals and assembles the results into communication packets. Those packets are forwarded, from one skin cell to the next, towards one of the interface connections. Thus, the local controller requires AD conversion, processing and communication capabilities. A major part of the signal processing can be done locally. Local time based filters (e.g. median, low-pass, high-pass) significantly reduce the required sampling rates (Nyquist sampling theorem). Oversampling in combination with digital filters, e.g. delta-sigma converters, replaces complicated analog filters. Local spatial filters significantly reduce the dimensionality of the transfered data. For example, it is possible to temporarily average 3 linear force signals into a single output signal. Value based filters, such as thresholding or level detectors, completely suppress the transfer of signals when specific conditions are not met and the signals do not contain new pieces of information. This is especially interesting for artificial skin, since most areas of the skin are not excited or in constant excitation. Efficient pre-processing methods largely decrease the demand to transmit, decode and process informations throughout the entire processing chain. In consequence, a local controller leads to a more efficient and slender system design. In our design, we use the functionality of a common PIC24FJ128GA306 micro-controller to achieve the above properties. Beyond common controller features, the PIC24F features multiple high speed Universal Asynchronous Receiver and Transmitter (UART) peripherals and a multi-channel Direct Memory Access (DMA) controller to realize fast cell-2-cell communications, an Analog to Digital Converter (ADC) with a Charge Time Measurment Unit (CTMU) to realize capacitive sensing functionality and an internal Phase Locked Loop (PLL) with an embedded Resistor/Capacitor (RC) oscillator to generate a local high speed clock. Future designs can use a specialized ASIC for this purpose.

ESD/EMI Protection: Protection against Electrostatic Discharges (ESD) and Electromagnetic Interferences (EMI) are important topics for an artificial skin. Residing on a large surface area, artificial skin is especially prone to emission and immission, e.g. due to antenna effects or direct contact. Human (or robots) for example, accumulate charges when walking or moving due to tribocharging or electrostatic induction, leading to voltage differences as high as 25 kV. Electromagnetic compatibility (EMC) is not only a regulatory demand for applications in industrial and medical environments, it is also a core interest to reduce the Signal to Noise Ratio (SNR) and reliability of a sensor system. ESD incidents can not only destroy sensors or skin cells, but also change sensor behavior unnoticed. If not contained locally, ESD will also spread in a skin network and finally affect whole areas. In our skin cells, we implemented some preliminary measures against ESD. All components feature their local ESD protection circuits, providing a baseline of protection. Large areas of the surface of the skin cell are directly connected to a highly conductive ground plane beneath the surface. Distributed vias and the elevated grounded force sensor caps provide a direct connection to this ground plane, acting like lightning rods. Several distributed, low-inductive ceramic capacitors bypass and consume some of the transient voltage energy. The remaining energy is spread via the power network to neighboring cells and/or interfaces. Future designs will incorporate specialized ESD elements to further protect each cell. EMI take pathways that emit interferences, also for imission. In the case of artificial skin on robots there is a magnitude of potential imission sources – e.g. computers, motors, control boards and wireless transceivers. For example close to the joints, artificial skin is exposed to alternating magnetic fields from electric actuators, supply noise and RF noise from other sensor and communication systems. In our skin cells, we implemented some preliminary local measure against EMI. Every skin cell has a large ground plane providing a low-impedance ground connection. This also minimizes antenna effects for the return path of signal lines. The analog capacitive force sensor is shielded with ground from both sides. Power noise is rejected with a high attenuation by the voltage regulation circuit. The digital and analog power rails are separated in order to gain a higher SNR with sensors. The local analog to digital conversion and sensor handling allow to use very short tracks, minimizing the chance to catch interference. This also applies to the short distance of the cell-2-cell communication.

3.2.2.2. Multi-modal Sensors

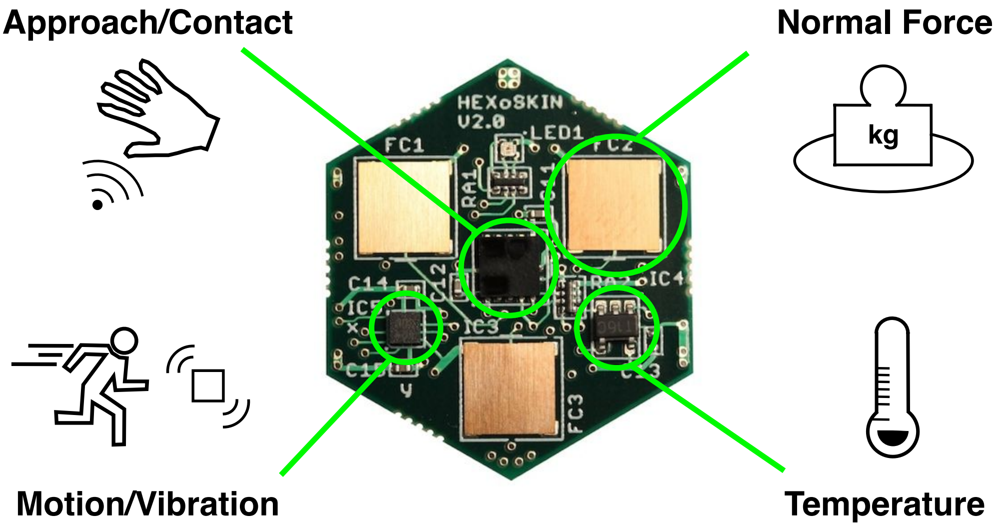

FIGURE 3.13. The figure shows the multi-modal sensors of the skin cell version 2.0.

The skin cell is a carrier platform for multiple sensor modalities (see Table 3.3 and Fig. 3.13). New sensor modalities can be easily integrated with future versions. The current set of four modalities is designed to meet human skin sensation, as well as provide useful extra functionality for robotic skins. The latest skin cell provides: 1) a proximity sensor – to detect light touch and approaching objects; 2) a 3-axis accelerometer – to sense indirect impacts, motion and vibration; 3) three normal force cells – to measure force along the surface normal; and 4) a temperature sensor – to measure the absolute skin temperature and changes (see Fig. 3.13).

sensor	VCNL4010	BMA250	LM71	custom
modality	pre-touch	acceleration	temperature	normal force
size in mm	4.0x4.0x0.8	2.0x2.0x1.0	3.0x3.0x1.0	6.0x6.0x0.1
resolution	16 bit non-linear	10 bit 3.91 mg	14 bit 0.03 °C	> 8 bit non-linear
range	1-200 mm	± 2/8/16 g	-40 to 150 °C	$>$ 0-3 N
bandwidth	0-250 Hz	0-1 kHz	0-7 Hz	0-33 kHz
per cell	1	1	1	3

TABLE 3.3. The table shows the multi-modal sensor specifications of skin cell version 2.0.

Proximity Sensor: Human skin senses the lightest touch, through mechano-receptors at the hair roots or in the epidermal layer of the skin. In our system, we emulate this light touch sensation with a proximity sensor. A sense for approaching contacts can also enhance safety and interaction capabilities of robots, enabling them to react prior to contact. Various methods are available on the market e.g. optical, capacitive, ultrasonic or inductive. We decided to use a reflective optical sensor, since there are small and low-cost solutions available. Reflective optical sensors measure the amount of light reflected from an object, which is dependent on the type of reflection (specular/diffuse), the reflectivity of the surface, the shape of the surface and naturally the distance of the object. Theoretically, this type of sensor comes to a limit with ideal transparent objects or black bodies. Practically, most visually transparent objects are not transparent in the infrared spectrum and ideal black bodies do not exist. Due to the measurement of the amount of reflected light, the returned value is not an accurate distance measure, but an indicator for the presence of an object. The sensor also does not distinguish where the object is in its angle of view. We started with an analog GP2S60 from SHARP with version 1.1, but switched over to the digital VCNL4010 from VISHAY in version 2.0 (refer to Sec. A.4). The VCNL4010 has dedicated hardware to modulate the emitter and demodulate its own signal from the photo-receptor. This way, it distinguishes between its own and other sources of light, does not saturate with sunlight and cuts down power consumption. Many skin cells can be operated close to or opposing each other without interference. In order to make the skin cell water & dust proof, an IR transparent window can be set on top of the sensor. Currently, we only provide an aperture for the sensor to avoid double reflections.

Accelerometer: Impact sensation, slip detection and contact roughness can be inferred from vibration signals (refer to Chapter 2). We opted to use an accelerometer to emulate the human vibration cue, as it provides additional motion sensing functionality. This motion sensing functionality is a key sense for our self-organizing features introduced in Chapter 4 and 5. The utilized Bosch BMA250 is a cost effective, small size and low power digital tri-axial accelerometer with an additional temperature sensor for temperature compensation. We utilize some of the built in monitoring functionalities, e.g. the tap detection to detect impacts.

Temperature Sensor: Temperature sensing plays an important part in the human tactile system, potentially because human features a very narrow biochemical operating range. Since robots have a much wider range, temperature sensing might not appear as important. However, this is a wrong assumption, since all mechano-receptors are affected by temperature and would such differ in performance due to the large variation of temperature on a robot surface. For instance, we have measured temperature differences up to 70 Kelvin on a KUKA light weight robotic arm. Due to the common temperature difference between skin and the environment, a sense of temperature can also be used to measure thermal transfers, e.g. wind-chill (see Sec. 6.4). Although the BMA250 accelerometer provides a temperature sensor, the low resolution of 0.5 degrees Celsius is far from human performance of 0.1 degrees [Dahiya *et al.*, 2010]. We therefore added a high resolution (0.03 °C) temperature sensor, the LM71 from National. In order to be sensitive, the thermal coupling between the skin surface and the temperature sensor is very important. We placed a comparably high/big sensor close to the surface and maximized the contact surface between the encapsulating elastomer and the sensor lead contacts, connected to its sensitive die.

Force Sensor: In completion to detecting touch (CellulARSkin^{TM} detects touch with the proximity sensor) an artificial skin should be able to quantify applied forces. Since miniature and low-cost force sensors have not been available on the market, we developed a custom normal force sensor. This normal force sensor measures the quantity of force applied along the surface normal in its receptive field. Due to its discrete nature, it can be integrated side-by-side with other sensor modalities. The receptive field of the discrete sensor is widened by specifically designed properties of the encapsulating skin material. Instead of common Force Sensing Rubber (FSR) materials, we utilize a metallic spring design. With this design, we have been able to achieve outstanding sensor behavior regarding dynamics, hysteresis, temperature effects and robustness. Please refer to Sec. 3.3 for further information.

3.2.2.3. Skin Cell Software

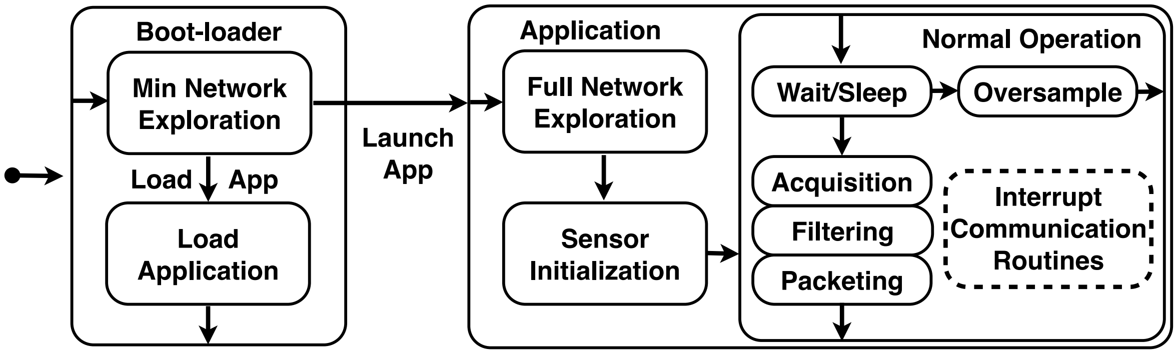

FIGURE 3.14. The figure shows the main parts and states of the skin cell software.

Software dictates the skin cell behavior. The software is divided into a boot-loader and an application code (see Fig. 3.14). With the boot-loader, new application code is simultaneously uploaded to all skin cells in the network. The boot-loader only provides a minimalistic network exploration functionality to be able to broadcast new code packets to the network. With a new application code, additional functionality can be implemented at the skin cell level, e.g. new filter functions or routing algorithms. The current application code is separated into a sensor initialization, a full network exploration and a normal operation phase. The current normal operation phase splits into a cyclic timer driven sensor acquisition and an event driven communication part.

Sensor Acquisition: The sensor acquisition is driven by two timers. One timer runs at a high oversampling rate and acquires the analog sensor signals for enhanced digital filtering. The other timer runs at the packet generation rate and acquires the remaining digital sensor signals. All sensor signals are then filtered and (e.g. offset-) compensated with values stored in local memory. In an operation mode where all sensor signals are forwarded to the processing system, the sensor results are put in a packet and sent to the transmission stack of the skin cell. We utilize controller internal timers to be bounded only by one critical component – the controller. For digital sensors, which are running on their own asynchronous clock, this approach may lead to an increased latency between conversion and transmission. If a sensor does not reply, safe default values are filled into the packet. Events from digital sensors are collected over one timer interval.

Network Exploration: For the skin cell it is only important to know: 1) the master port it is supposed to forward packets to and the slave ports to broadcast control messages; 2) its own ID to react on ID specific commands and assemble its own sensor data packets; 3) inactive ports to turn them off; and 4) all neighbors to assemble a neighbor information packet. For a full explanation of the network exploration method, please refer to Sec. 3.2.1.7.

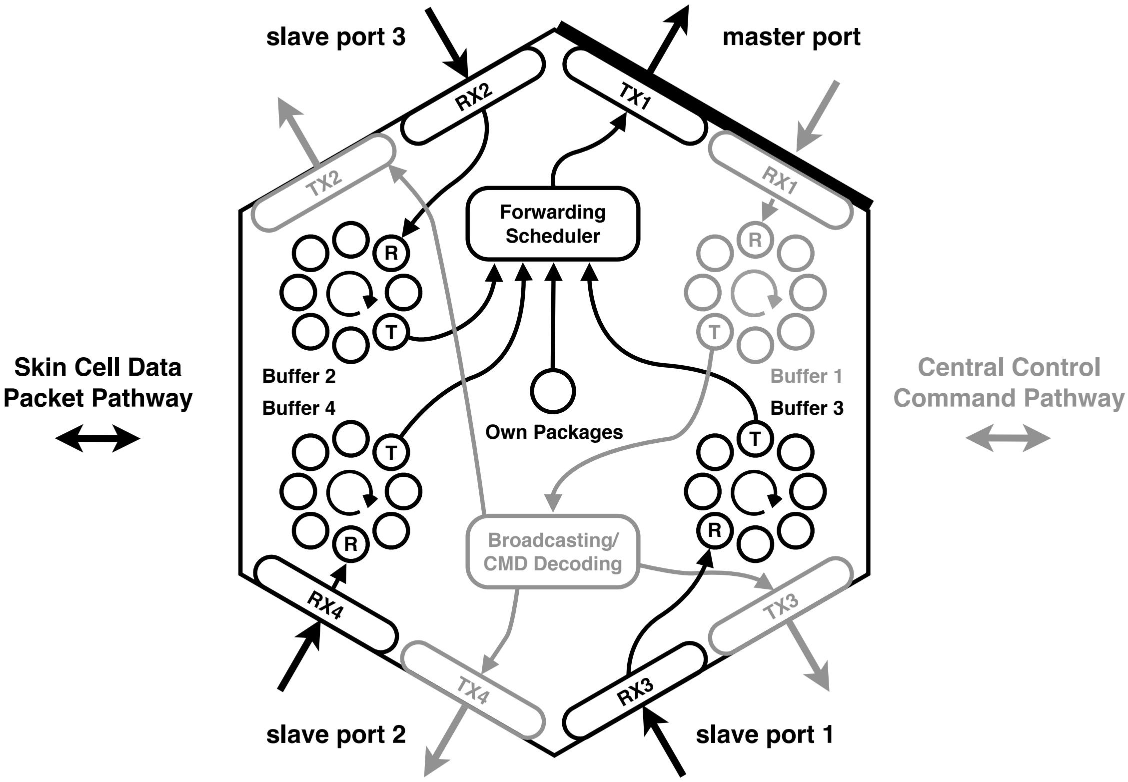

FIGURE 3.15. The figure shows a simplified data flow diagram for communication packets in each skin cell. Ring buffers receive the packets and (e.g. round robin) schedulers handle the forwarding, broadcasting and/or decoding.

Communication: The communication in the artificial skin is bidirectional – the central processor sends messages to the skin cells and vice versa. Fig. 3.16 shows an example of a 20 byte data packet. Each packet contains a clear end of frame (EoF) and start of frame (SoF) delimiter to be able to find packets in an asynchronous data stream. SoF and EoF bytes are marked with a logical one at the most significant bit (MSB), while data bytes carry a MSB set to logical zero. This fixed pattern serves to quickly identify transmission errors, as well as to identify SoFs and EoFs for re-synchronization, with only a 10% overhead. The type of packet is embedded as a command in the SoF. ID specific packets, like sensor packets, contain an ID of either the recipient or the origin. Skin cells receive packets with the UART peripherals and

	BIT<7>	BIT<6>	BIT<5>	BIT<4>	BIT<3>	BIT<2>	BIT<1>	BIT<0>
BYTE<0>	1	1	CMD<5>	CMD<4>	CMD<3>	CMD<2>	CMD<1>	CMD<0>
BYTE<1>	0	ID<13>	ID<12>	ID<11>	ID<10>	ID<9>	ID<8>	ID<7>
BYTE<2>	0	ID<6>	ID<5>	ID<4>	ID<3>	ID<2>	ID<1>	ID<0>
BYTE<3>	0	PROX<15>	PROX<14>	PROX<13>	PROX<12>	PROX<11>	PROX<10>	PROX<9>
BYTE<4>	0	PROX<8>	PROX<7>	PROX<6>	PROX<5>	PROX<4>	PROX<3>	PROX<2>
BYTE<5>	0	AccX<9>	AccX<8>	AccX<7>	AccX<6>	AccX<5>	AccX<4>	AccX<3>
BYTE<6>	0	AccY<9>	AccY<8>	AccY<7>	AccY<6>	AccY<5>	AccY<4>	AccY<3>
BYTE<7>	0	AccZ<9>	AccZ<8>	AccZ<7>	AccZ<6>	AccZ<5>	AccZ<4>	AccZ<3>
BYTE<8>	0	AccTmp<7>	AccTmp<6>	AccTmp<5>	AccTmp<4>	AccX<2>	AccX<1>	AccX<0>
BYTE<9>	0	AccTmp<3>	AccTmp<2>	AccTmp<1>	AccTmp<0>	AccY<2>	AccY<1>	AccY<0>
BYTE<10>	0	free	free	PROX<1>	PROX<0>	AccZ<2>	AccZ<1>	AccZ<0>
BYTE<11>	0	FCELL1<11>	FCELL1<10>	FCELL1<9>	FCELL1<8>	FCELL1<7>	FCELL1<6>	FCELL1<5>
BYTE<12>	0	free	free	FCELL1<4>	FCELL1<3>	FCELL1<2>	FCELL1<1>	FCELL1<0>
BYTE<13>	0	FCELL2<11>	FCELL2<10>	FCELL2<9>	FCELL2<8>	FCELL2<7>	FCELL2<6>	FCELL2<5>
BYTE<14>	0	free	free	FCELL2<4>	FCELL2<3>	FCELL2<2>	FCELL2<1>	FCELL2<0>
BYTE<15>	0	FCELL3<11>	FCELL3<10>	FCELL3<9>	FCELL3<8>	FCELL3<7>	FCELL3<6>	FCELL3<5>
BYTE<16>	0	free	free	FCELL3<4>	FCELL3<3>	FCELL3<2>	FCELL3<1>	FCELL3<0>
BYTE<17>	0	TEMP<13>	TEMP<12>	TEMP<11>	TEMP<10>	TEMP<9>	TEMP<8>	TEMP<7>
BYTE<18>	0	TEMP<6>	TEMP<5>	TEMP<4>	TEMP<3>	TEMP<2>	TEMP<1>	TEMP<0>
BYTE<19>	1	0	1	0	1	0	1	0

FIGURE 3.16. The figure shows an exemplary skin cell data packet containing raw sensor data, packet delimiters, an originating ID and a command (here 0x3F for raw data).

load them with DMA channels into local buffers (see Fig. 3.15). Once a packet is completely received, a fast interrupt routine increments the ring buffer pointer for ongoing reception and decides what to do with the received packet. Currently, packets received at the slave ports are immediately entering a round robin scheduler for transmission on the master port. Packets received on the master port, are decoded and forwarded once to every slave port. The decoded packets are analyzed for commands from the central controller. Currently, we feature commands to change the local LED color, memorize offsets of the proximity and force sensors, memorize the own ID or change the update rate.

3.3. Normal Force Sensor

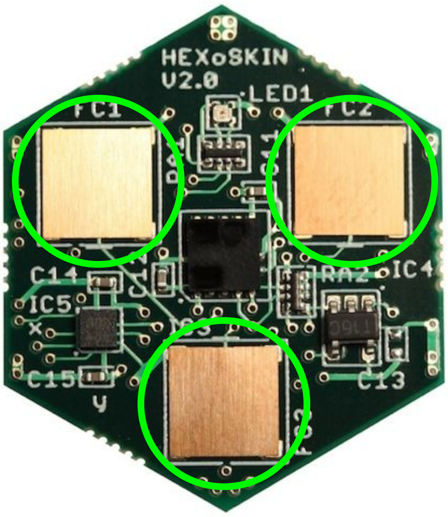

FIGURE 3.17. The figure shows the custom made force sensors on skin cell version 2.0.

In this section, we introduce our custom made discrete force sensor[2] (see Fig. 3.17). Whenever possible, we made use of sensors from the global electronics market, in order to speed up our development process and to lower the production costs (refer to Sec. 3.2.2.2). Since we were not able to find a commercial force sensor that fit all of our requirements (e.g. low-cost, robust, easy to implement, high dynamic range, low hysteresis, low temperature dependency, little analog electronics), we decided to develop our own force sensor. Our force sensor measures the force-induced deformation of a circular cavity, etched into a thin copper beryllium (CuBe2) plate, by means of capacitance (see Fig. 3.19). These caps are placed on any quasi-plane, quasi-rigid piece of a substrate material, e.g. a flex-rigid or rigid PCB (see Fig. 3.18). In comparison to rubber based sensors, this mechanism has significantly better characteristics, due to the behavior of the metal spring. In comparison to state-of-the-art MEMS sensors, our force sensor is easy to manufacture and low-cost. On excessive loads, the cavity settles into a well defined overload protection state. We also invented a self-adjusting design, in order to minimize the production and thus behavioral differences between a multitude of skin cells [Mittendorfer, 2013]. Substrate and cap are joined in a standard pick&place and reflow soldering process for automated mass production. Our design is scalable to support different sizes and/or force ranges (refer to Sec. A.6). Currently, we combined three force sensors on one of

---

[2] The work in this section has been published in [Mittendorfer and Cheng, 2012b] and [Mittendorfer, 2013].

our skin cells (see Fig. 3.17). In order to support force sensing, we enhanced the elastomer cover on top of every skin cell with a harder micro-structure (see Fig. 3.21 and 3.22). This structure collects forces acting on the surface, focuses the excitation on the three discrete force sensors and serves as a protection layer for the embedded electronics.

3.3.1. Mechatronic Design

3.3.1.1. Parts

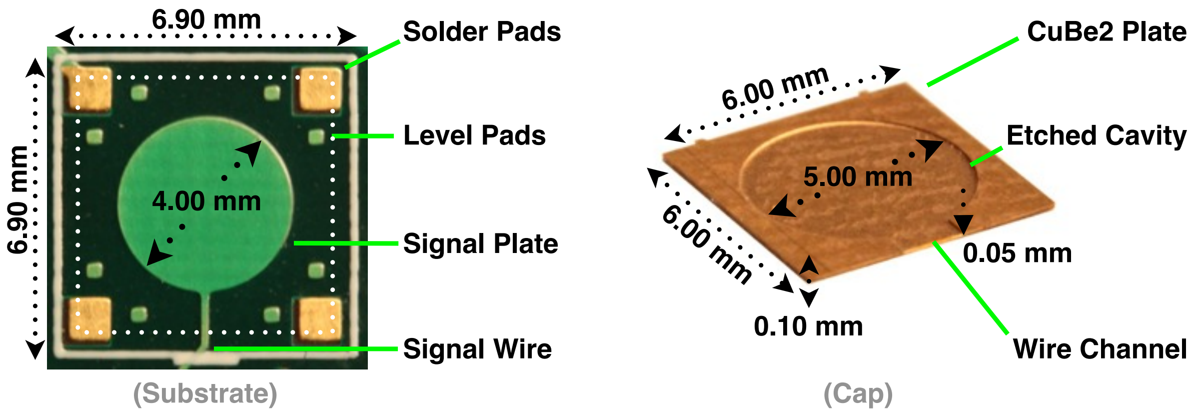

FIGURE 3.18. The figure shows the main parts of the custom made force sensor: the substrate and the cap. Placing the cap on the substrate builds a circular cavity which deforms on applied normal forces.

The discrete force sensor consists of two main components (see Fig. 3.18): 1) a conductive, thin and deformable cap with a micro-structured cavity; 2) a plane and rigid substrate with a conductive plate. The cap is made from a ($t_{\text{plate}} = 100\,\mu\text{m}$) thick CW101C-R1060 copper beryllium (CuBe2) sheet, in a fast and low-cost lithographic etching process. CuBe2 has excellent spring properties, high corrosion resistance, low creep and good conductivity. It is commonly used for spring contacts or high precision instruments. CuBe2 can be joined with common copper pads on a PCB in a common electronic soldering process. We are able to utilize an initially hardened alloy which does not change characteristics during the solder process, due to the low stress exerted on the material during the etching process. The substrate consists of an ordinary ($t_{\text{subs}} = 0.85\,\text{mm}$) thick FR4 PCB which, compared to the cap, is quasi-plane and -rigid. The actual capacitive sensor element builds from two conductive plates - a circular pad on the PCB and the overlaying part of the metal cap (see Fig. 3.19).

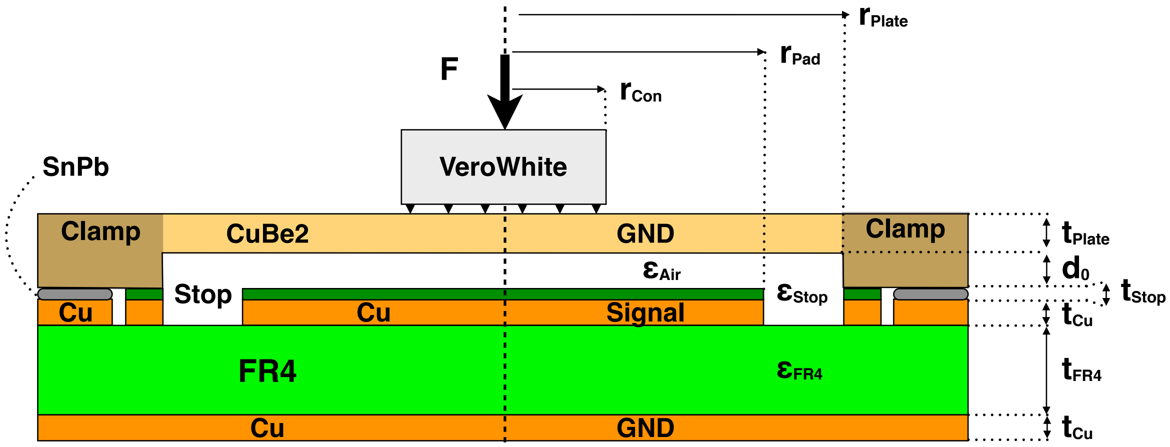

FIGURE 3.19. The figure shows an axial cut through a simplified, rotatory symmetric force sensor model.

3.3.1.2. Assembly

Our goal was to integrate the novel force cell into the automated fabrication process of the skin cells - utilizing pick & place machines and a reflow soldering process. Therefore, we invented[3] a special design. In this form, the cap self-aligns relative to the substrate, during the soldering step. This is important as the mechanical pick & place joining process is much less accurate than the chemical/lithographic manufacturing processes for the substrate and the cap. The self-alignment is based on capillary effects, acting in between the cap and the solder pads through the liquid solder. This serves to reduce two sources of uncertainty: 1) to align the cavity and the wire channel horizontally above the signal plate and the signal wire; 2) to minimize the vertical offset of the capacitor plate. For the second purpose, we added level pads to minimize lifting effects by the liquid solder (see Fig. 3.18). In comparison to the uncovered solder pads, the signal plate and the level pads are covered with a thin solder resist layer ($t_{\text{stop}} \approx 30\,\mu\text{m}$) on top of the copper. This thin isolation layer is important to prevent short circuits with the capacitive sensor. Otherwise both conductors would directly touch each other in case of a high load condition. The thickness of the solder resist layer ideally also defines the thickness of the solder joints in between the CuBe2 cap and the solder pads (see Fig. 3.19).

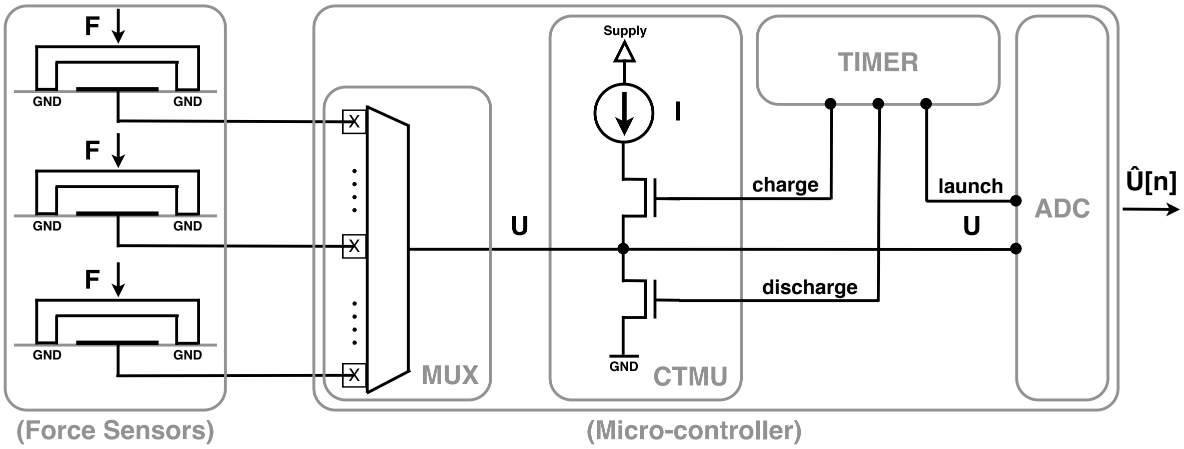

FIGURE 3.20. The figure shows the electronic components of PIC24F that are utilized to read the custom made force sensor: An analog multiplexer, a charge time measurement unit, a timer and an analog to digital converter.

3.3.1.3. Electronics

In order to reduce components, we only use electronics built into the micro-controller. The utilized PIC24F features a capacitive touch sensing module, called Charge Time Measurement Unit (CTMU). The CTMU provides a programmable and switchable constant current source, directly linked to a timer and an Analog to Digital Converter (ADC) (see Fig. 3.20). The CTMU allows to generate a constant current I, the timer to accurately gate the charge time T and the ADC to measure the final voltage value U. The CTMU can be multiplexed to any of the 16 available analog inputs and measure the capacitance of attached capacitors. Given that the capacitor has been completely discharged before the charging cycle, the total capacitance can be directly calculated:

$$C_{\text{total}} = \frac{Q}{U} = \frac{I \cdot T}{U} \tag{3.1}$$

We use the maximum current $I_{\text{max}} = 55\,\mu\text{A}$, allowing the highest update rates and giving to the parasitic resistive effects least time to interfere. The maximum voltage $U_{\text{max}} = 3.0\,\text{V}$ is limited by the supply voltage and the ADC range. The maximum voltage is measured in case of an unloaded sensor. Once the capacitor plates are forced together, the capacitance increases. Keeping the charge Q constant, the voltage U decreases. A range optimization algorithm can maximize the charging time in the unloaded case - generating custom values T_{cust} for each force sensor. Here, we utilize a heuristic default time $T_{\text{def}} = 2.5\,\mu\text{s}$, for both charging and discharging times, in order to easily compare raw signals from different cells. The initial capacitance of the force sensor in parallel to all parasitic capacitors, such as of the

---

[3] European Patent EP 12 172 602.0 [Mittendorfer, 2013]

pin or ADC, thus sum up to a value of $C_{\text{init}} = 46\,\text{pF}$. With a sample rate of 200 kHz at 12 bit resolution, one analog to digital conversion approximately takes $T_{\text{ADC}} \approx 5\,\mu\text{s}$. A complete force measurement approximately takes $T_{\text{force}} \approx T_{\text{ADC}} + 2 \cdot T_{\text{def}} \approx 10\,\mu\text{s}$. A skin cell can sample all three force sensors with an update rate of $f_{\text{max}} = 33\,\text{kHz}$. We currently use a sample rate of $f_{\text{samp}} = 2.5\,\text{kHz}$, and filter and decimate the signals to a lower update rate of $f_{\text{udr}} = 250\,\text{Hz}$. The digital filter in combination with the oversampling rate serves two purposes: I) as a low-pass filter to obey Nyquist sampling theorem; II) to filter uncorrelated noise and to increase the signal to noise ratio. For us, filtering in the digital domain is more effective. We save analog components, reduce costs and parasitic effects, are able to re-program the filter and achieve steeper filter curves. Filtering in closed-loop control systems is troublesome due to the inherent phase shifts. Nevertheless, utilizing unfiltered data, unwanted aliasing and spikes can occur. In consequence, we decided to utilize a non-linear median filter on the last $N = 10$ samples. Median filters do not degrade edges, but efficiently reduce outliers. In our case with $N = 10$ and a following decimation by the same factor, the worst case phase shift for a step response is half of the update rate $\frac{1}{2 \cdot f_{\text{udr}}} = 2\,\text{ms}$. Computation wise, the median calculation[4] takes $T_{\text{med}} = 65\,\mu\text{s}$ for all three cells on the PIC24F. Since sampling is handled by a timer triggered, non-interrupt routine, small amounts of sample rate jitter occur. A reasonable amount of sample rate jitter is an effective measure against harmonic noise (refer to [Davison, 2010]).

3.3.1.4. Composite Skin

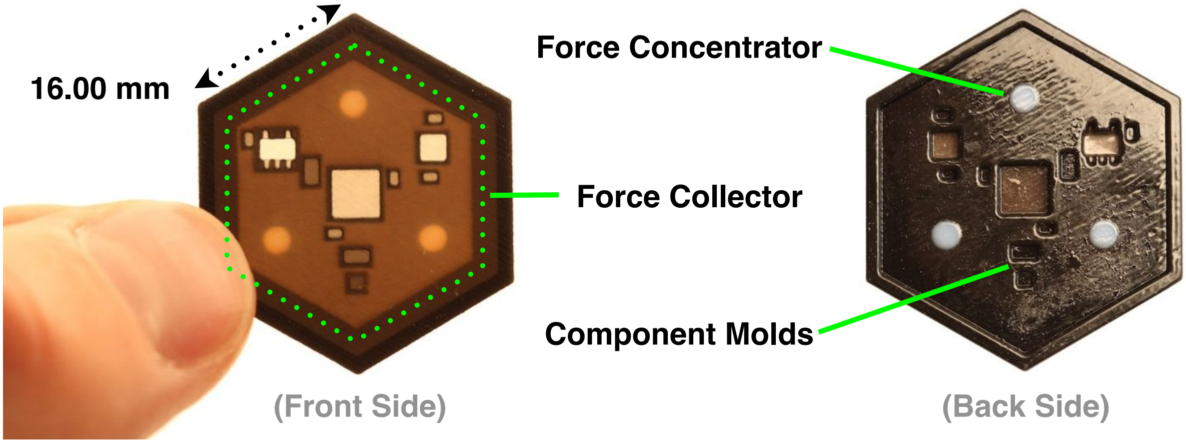

FIGURE 3.21. The figure shows the micro-structured top layer of the elastomer skin cover. The cover is made of soft TangoPlusBlack and hard TangoGrey material.

---

[4] kth_smallest(array[],10,5) by N. Wirth, implemented by N. Devillard

Composite skin is the material encapsulating the skin cells. The top layer (see Fig. 3.21) consists of two different materials, a soft TangoPlus Black/Transparent (TPT) rubber like and a hard Vero White/Grey (VW) ABS plastic like material (see Fig. 3.22). A hard VW layer of $t_{\text{dist}} = 500\,\mu\text{m}$ thickness, $t_{\text{over}} = 200\,\mu\text{m}$ below the TPT epidermal skin surface, acts as a collector of distributed pressure. The accumulated force is then concentrated by three pillars on the three available force sensors per skin cell. Three pillars are utilized to define a mechanically stable contact between the force collector and the sensors on the PCB. The pillars extend through the TPT and about $t_{\text{tpe}} = 100\,\mu\text{m}$ on top of the flat inner surface. All other sensor modalities have cutouts in the VW material that are filled with TPT to provide coupling to the skin and to reduce influence with the force cells. The measures given in Fig. 3.21 are dictated by the size of the off-the-shelf components and the minimal safe structure size (200 µm) with the 3D printer. They are also subject to ongoing improvements and changes in the production process (refer to Sec. A.5).

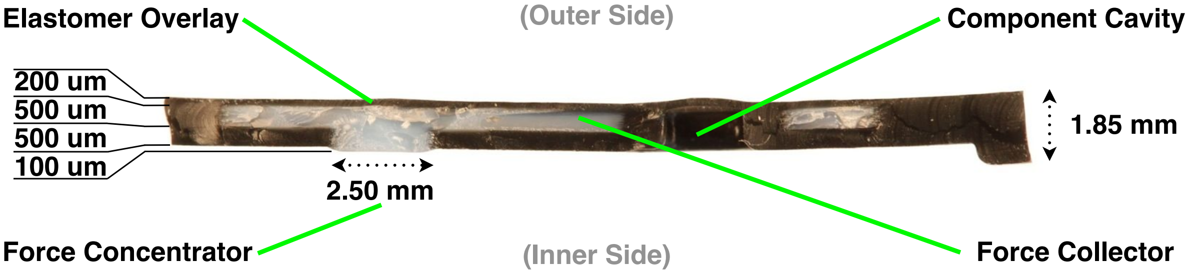

FIGURE 3.22. The figure shows a vertical cut through the top layer of the elastomer skin cover, at the center of a force collector pillar.

3.3.2. Evaluation

3.3.2.1. Test Stand

In order to evaluate the dynamic behavior of our force sensor, we designed a custom low-cost test stand. The core of our test stand (see Fig. 3.23) is a VM2836-180 linear Voice Coil Motor (VCM), converting current to force. A LMD18245 current driver converts arbitrary voltage signals from a signal generator, to a regulated current through the VCM. Our test stand currently generates forces between $0.12 - 3.12$N, constrained by the mass of the tip of 12 g and the VCM maximum current. We directly measure applied forces with a FSG-15N1A sensor at the end of the linear pusher and also utilize its flat, 5 mm diameter tip to press on the skin. The test stand can be extended with a TECB-1 peltier module to generate higher or lower skin cell temperatures.

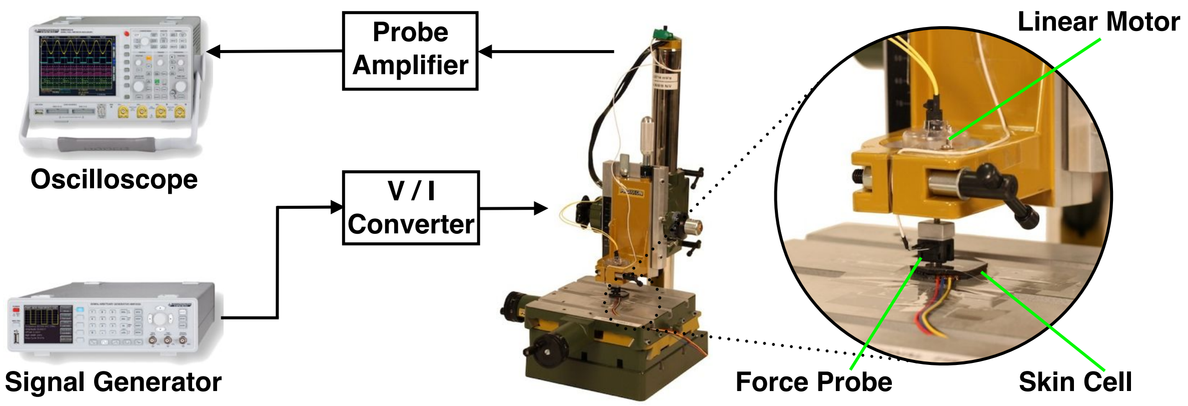

FIGURE 3.23. The figure shows the custom made dynamic force test stand.

3.3.2.2. Repetitive Signals

Fig. 3.24 shows the response towards a burst of sinusoidal or rectangular force pattern, directly applied on sensor 3. Offsets in between the three force sensors on the same skin cell are due to unavoidable differences in the production process, differences in signal wire length and stray capacitance. Permanent offsets are compensated in an automated calibration step. We were not able to discriminate cross coupling effects from the noise floor. In order to evaluate the sensor hysteresis, we plotted an overlay of the falling and rising flanks (see Fig. 3.25). No significant hysteresis was detected.

3.3.2.3. Step Response

Fig. 3.26 shows the response towards a rising and falling step with an amplitude of 3 N directly on force sensor 3 on a skin cell. From this data we have calculated mean values μ and standard deviations σ. In case of the excited sensor, we have picked the stable region with a window length of $N_{\text{win}} = 300$ samples. For sensor 1 and 2 we took all ($N_{\text{all}} = 3995$) samples into consideration. We then performed a Fourier analysis and plotted histograms for all mean free noise signals. Besides Gaussian white noise, there was no indication of spectral noise - especially harmonics of the micro-controller system clock or 50 Hz power net. We then calculated the system span δ, comparing the mean values in the unloaded μ_u and maximally loaded (test stand limit) μ_p state:

$$\delta = |\mu_u - \mu_p| \approx 312 \tag{3.2}$$

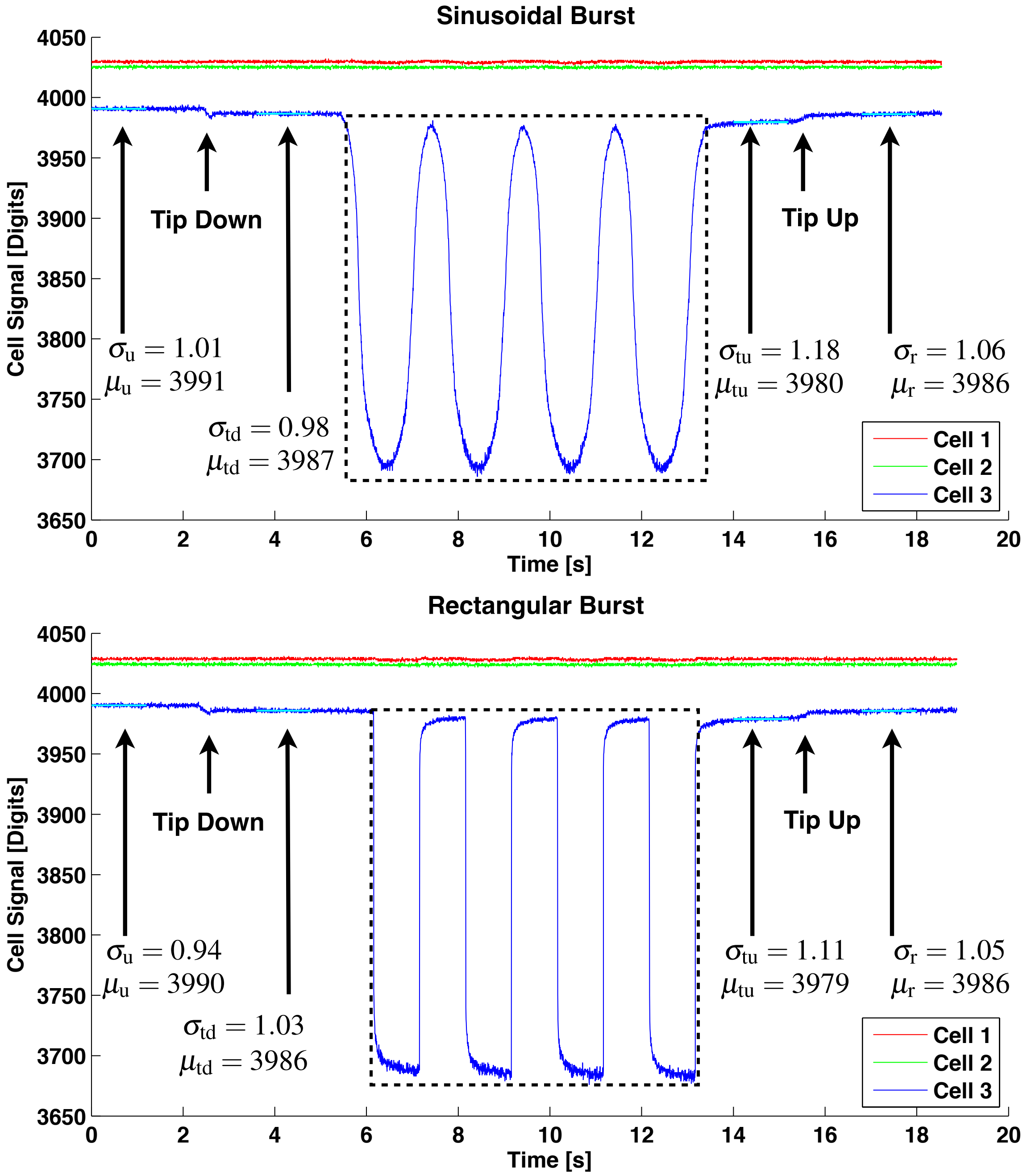

FIGURE 3.24. The figure shows the response of the force sensors on a skin cell on a burst of 4 sinusoidal or rectangular waves with a force of 0-3.12 N and a 2s period. Arrows are indicating the placement and removal of the force test stand tip with a weight of 12 gram.

The signal to noise ratio (SNR) is be calculated [Davison, 2010] as:

$$\mathrm{SNR} = \frac{\delta}{\sigma_u} \approx 315 \quad \text{or} \quad \mathrm{SNR}_{\mathrm{dB}} \approx 20 \cdot \log\left(\frac{\delta}{\sigma_u}\right) \approx 49.97\,\mathrm{dB} \tag{3.3}$$

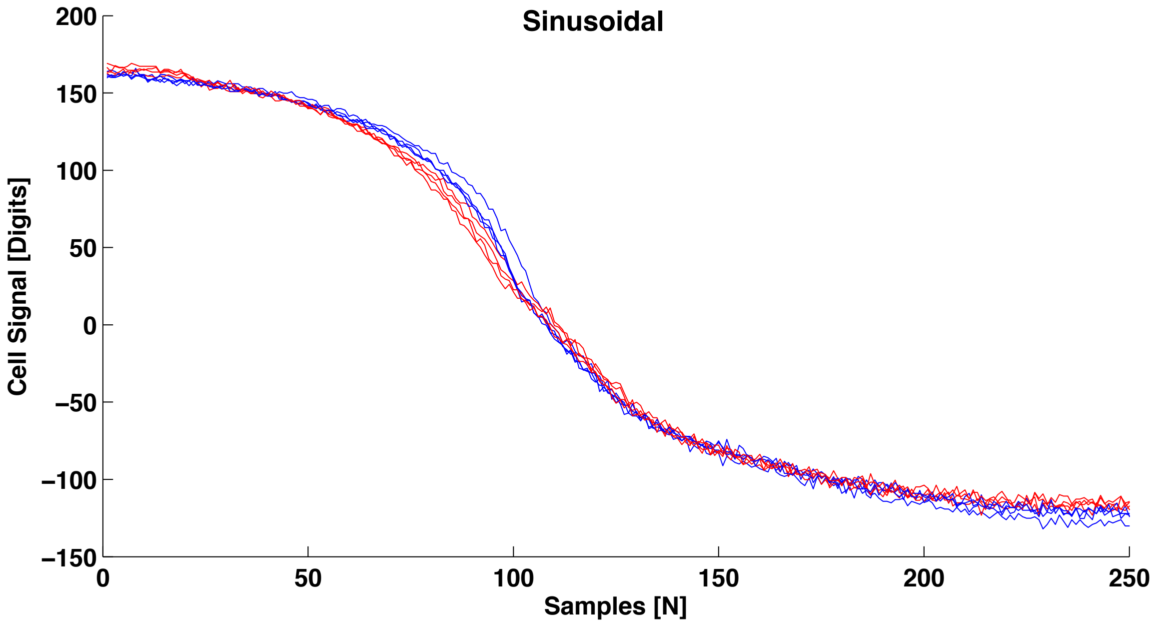

FIGURE 3.25. The figure shows an overlay plot of the sinusoidal signal flanks from Fig. 3.24 in order to evaluate the hysteresis of the force sensor.

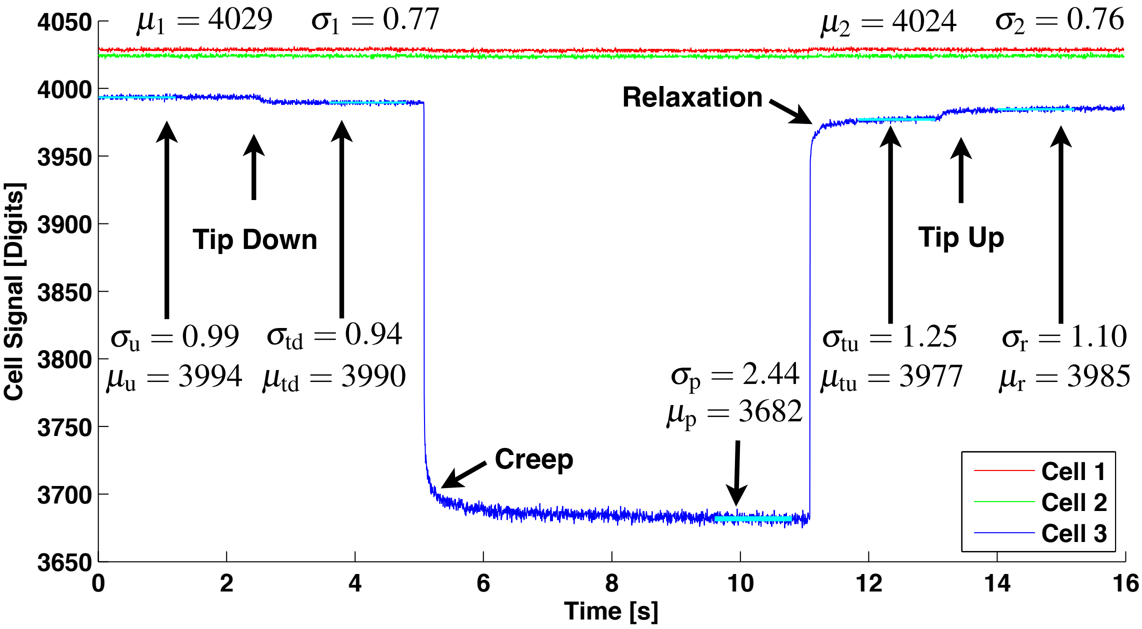

FIGURE 3.26. The figure shows the force sensor step response on a single pulse with a force of 0-3 N and a 6s period. Arrows indicate the placement and removal of the force test stand tip with a weight of 12 gram and regions of special interest.

Conservatively comparing the result to the dynamic range (random signal) or signal to noise ratio (sinusoidal signal) of an analog to digital converter, the sensor resolution is 8 bit. There is no detectable overshoot or ringing following a step. The sensor signal reaches 70% of the full step span δ within 1 sample period of $T_{s,70} = 4\,\mathrm{ms}$, 90% after $T_{s,90} = 8\,\mathrm{ms}$ and 95% after

$T_{s,95} = 36\,\mathrm{ms}$. The fast settling time is due to the specific design of the force sensor and the local median filter. A certain amount of creep and relaxation is inherently incorporated by the mixed composite skin, acting as a viscoelastic material. The difference between σ_u and σ_p can be explained by the vibrations originating from the voice coil motor (audible regulation noise). The difference between σ_u and σ_r is due to the slight long term relaxation of the difference in between μ_u and μ_r.

3.3.2.4. Curve Fitting

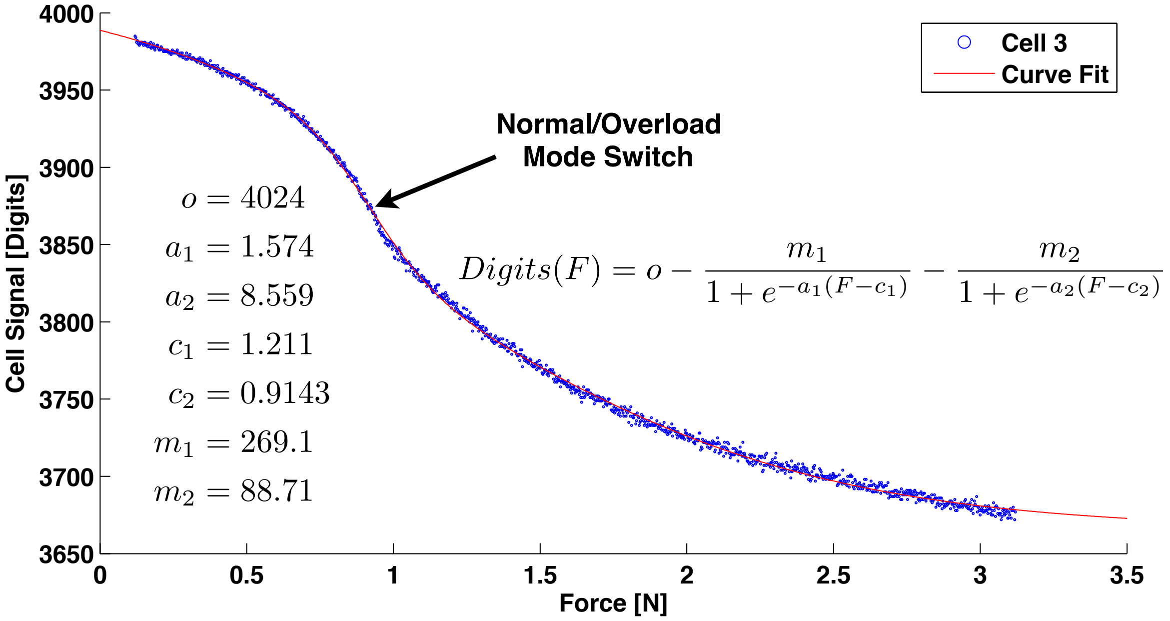

FIGURE 3.27. The figure shows a curve fitting for the input/output relation of the force sensor on applied forces.

Fig. 3.27 shows a functional regression model to compute the non-linear mapping in between readings of a force sensor and the originating force. A superposition of two sigmoid functions fits, as their properties match the sensor's behavior (also refer to Sec. A.6). Due to the two-split behavior (normal/overload), two sigmoid functions are necessary. Given this differentiable function, it is also possible to express the nonlinear sensitivity $S(F) = \frac{\mathrm{d}Digits(F)}{\mathrm{d}F}$, which reaches its absolute maximum of $-290\frac{Digits}{\mathrm{N}}$ at $F_{\mathrm{sw}} = 0.92\,\mathrm{N}$. At this force the sensor switches in between normal and overload mode. The switch occurs, when the CuBe2 cap first touches the incompressible solder resist layer of the signal plate (see Fig. 3.19), causing increasing resistance to any further deformation on an increasing force.

3.3.2.5. Chirp

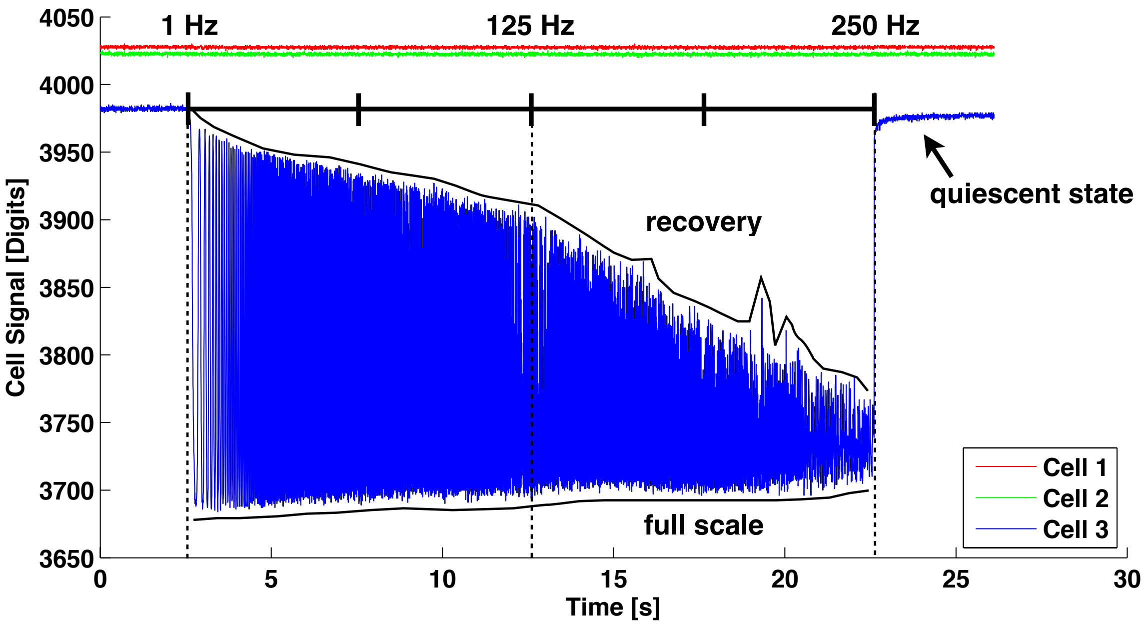

FIGURE 3.28. The figure shows the frequency response of one force sensor on a linear sinusoidal chirp from 1 Hz to 250 Hz, with a force of 0.12-3.12 N and a period of 20s.

Fig. 3.28 shows the response towards a linear, sinusoidal chirp between 1 and 250 Hz with a force of 0.12 to 3.12 N directly on one of the force sensors. The visible decay in amplitude is a superposition of the mechanical characteristics of the skin and the non-linear median filter. One has to keep in mind that median filters truncate sinusoidal waveforms dependent on their frequency, whereas they have less distortion effects on steps. It is also visible that the sensor almost reaches full scale values for all frequencies, but does not return to quiescent state for higher frequencies. This shows that the recovery time of the given system, including the mass of the force test stand tip, or any other object applying varying forces, is higher than the reaction time. The system settles close to full scale deflection, instead of mean or quiescent state. Such a behavior is advantageous for an artificial skin as it detects applied peak forces that can cause harm to objects under manipulation or the robot itself (please see 3.3.2.8). Outliers in the data are due to imperfections of the test stand, e.g. the excitation of harmonics in the voice coil motor linear mechanics.

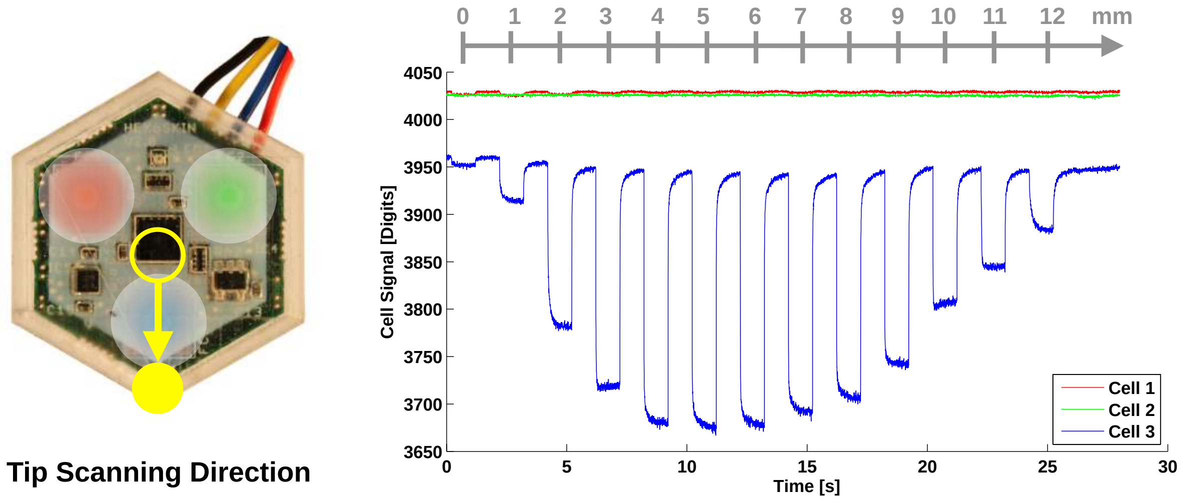

FIGURE 3.29. The figure shows the receptive field of the force sensors on a skin cell. A rectangular excitation, with a force between 0.12-3.12 N and a period of 2s, has been applied while shifting the excitation along the indicated direction during low force phases.

3.3.2.6. Receptive Field

Fig. 3.29 shows the measured receptive field of force sensor 3 on a skin cell. The receptive field was sampled, scanning with the tip of the force test stand along the indicated line over the surface of the skin cell. We applied a rectangular excitation of 0.12-3.12 N and shifted the position of the tip by one millimeter during each low force phase, making the field slightly asymmetric. Ideally the receptive fields of the three cells overlap such that no insensitive areas remain and every stimulus is sufficiently received by at least one receptor cell. Comparing the expansion of the receptive fields (see Fig. 3.29 red/green/blue circles), of approximately 12 mm, with the distance of the sensors, it is clear that there are still insensitive areas with the current design and object size (test stand tip). This puts a certain limit to the size and/or curvature radius of objects that can be detected. The final goal of completely overlapping receptive fields can be reached by increasing the thickness of the skin, stiffening the force distributor or by a denser set of smaller skin cells.

3.3.2.7. Temperature Dependency

Fig. 3.30 shows the deviation in response to the same force stimulus at different temperatures. In order to avoid bounding constraints, we reduced the CTMU charge time to $T_{\text{red}} = 1.875\,\mu\text{s}$. Thermal energy was sinked and sourced on the back side of the skin and measured with the LM71 temperature sensor in the upper layer. Such a setup produces temperature gradients, which is much more realistic than a homogeneous distribution. Condensation at low temper-

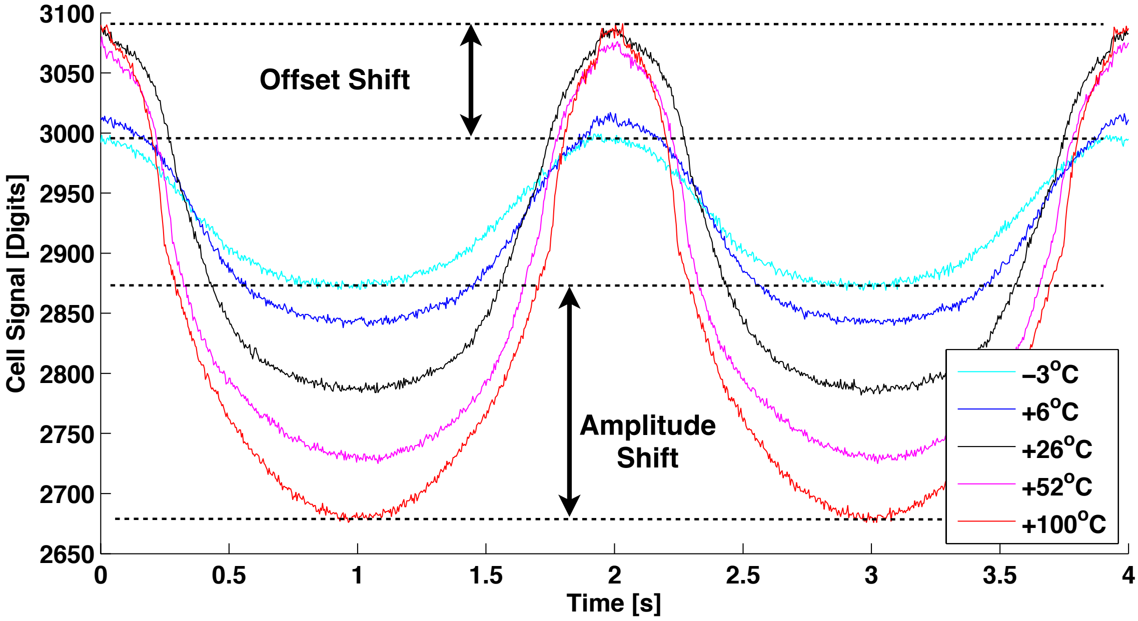

FIGURE 3.30. The figure shows the temperature dependency of the force sensor. We therefore applied a sinusoidal force between 0.12-3.12 N and a period of 2s, at different temperatures.

atures was prevented with a thin foil on top of the skin cell. The plot contains all possible effects, from the electronics, over thermal stress in the cap and PCB material, to the changing behavior of the composite skin. Significant offsets only occur with low temperatures, which can be explained with the change of elastomer stiffness at low temperatures. In this case, damping effects can no longer be neglected and relaxation offsets occur. The amplitude shift can be approximated (0.98 r-square goodness) with a linear model of $-1.9\frac{1}{^{\circ}\mathrm{C}}$ gain. One explanation is the thermal increase of capacitive area, explaining lower ADC readings with higher temperatures.

3.3.2.8. Robustness

Fig. 3.31 shows the reaction of a skin cell towards excessive loads and impacts generated by a human walking over, stomping or hammering on a skin cell lying on the floor. Due to the high stress, the sensor shows slightly more, but reversible relaxation effects. Permanent offsets were not experienced. Deviations in the quiescent state between Fig. 3.31 and e.g. Fig. 3.24 are due to the utilization of a different skin cell. The increased system span $\delta \approx 1000$ also indicates the existence of a third, ultra-high load mode, with a completely collapsed force cell.

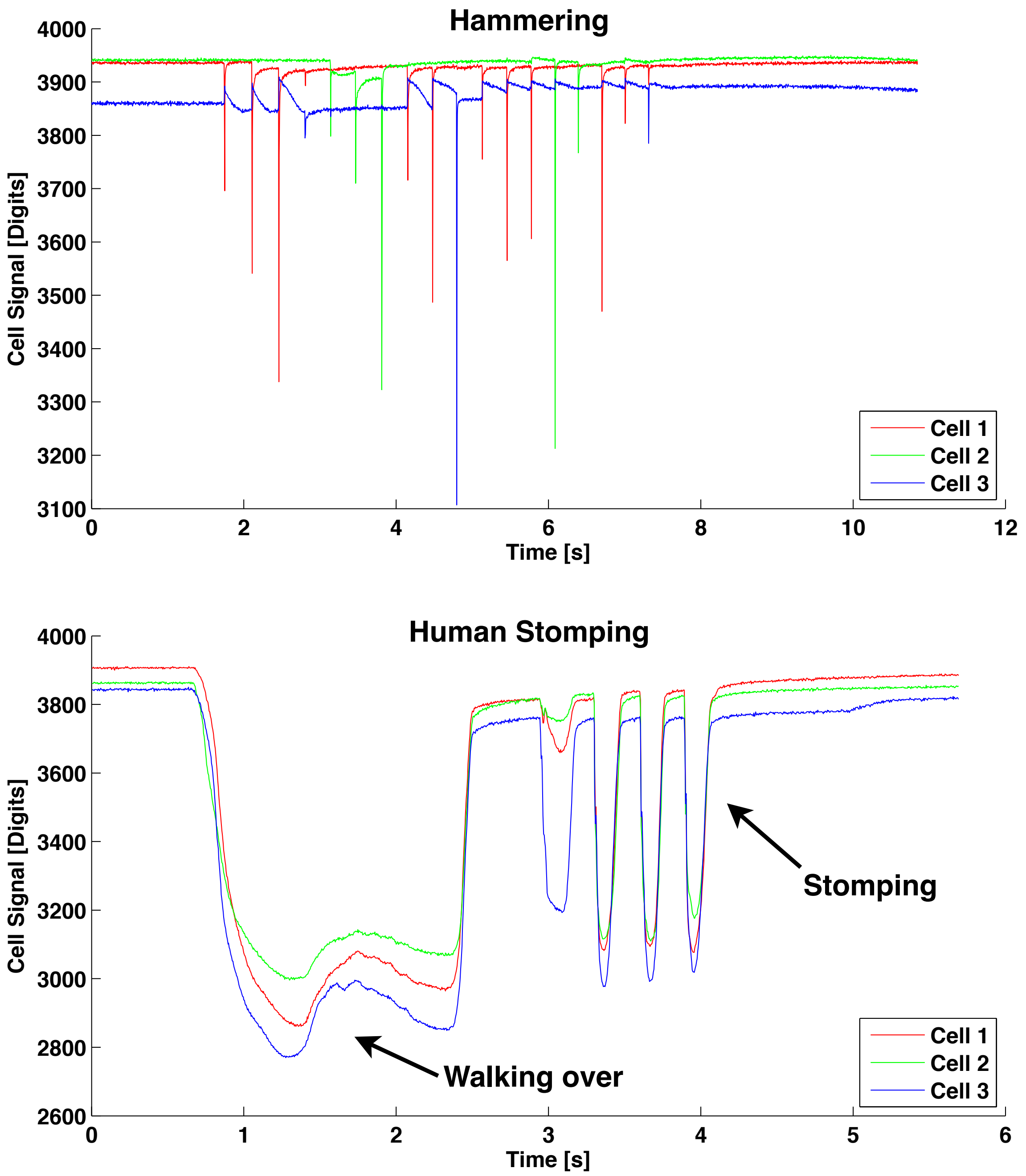

FIGURE 3.31. The figure shows recordings from one skin cell under excessive loads (80 kg human walking over and stomping on it) and impacts (hammering at different locations).

3.4. Summary

In this chapter, we introduced a modular artificial skin system, built from multi-modal skin cells. We showed that such a skin can not only be built with standard electronics, but has a lot of potential with future technologies. We discussed the selection of the optimal skin cell shape, the influence of multiple layers with an artificial skin and how an artificial skin made from a flex-rigid solution is able to conform to arbitrary 3D surfaces. We summarized the benefits of a digital cell-2-cell communication and introduced a self-organizing sensor network exploration method that is able to deal with varying topologies and partial failure. We then introduced a prototype skin cell to realize our novel concepts and a set of sensor modalities to emulate human and to enhance robot tactile sensation. We gave an overview of the required skin cell features, such as a local controller for communication and signal processing, and showed the essential skin cell behavior. Finally, we introduced our novel normal force sensor that is cost-effective, easy to manufacture and shows excellent sensing characteristics and robustness.

CHAPTER 4

Body Schema for Spatial Representation

> Something pretty ... that's just the surface.
>
> *(Jeanne Moreau)*

In this chapter, we first introduce a method to locally reconstruct the 3D shape of patches of artificial skin, e.g. body parts of the robot. We then provide a method to visually combine multiple of those locally reconstructed surfaces into one homogeneous body representation.

4.1. Introduction

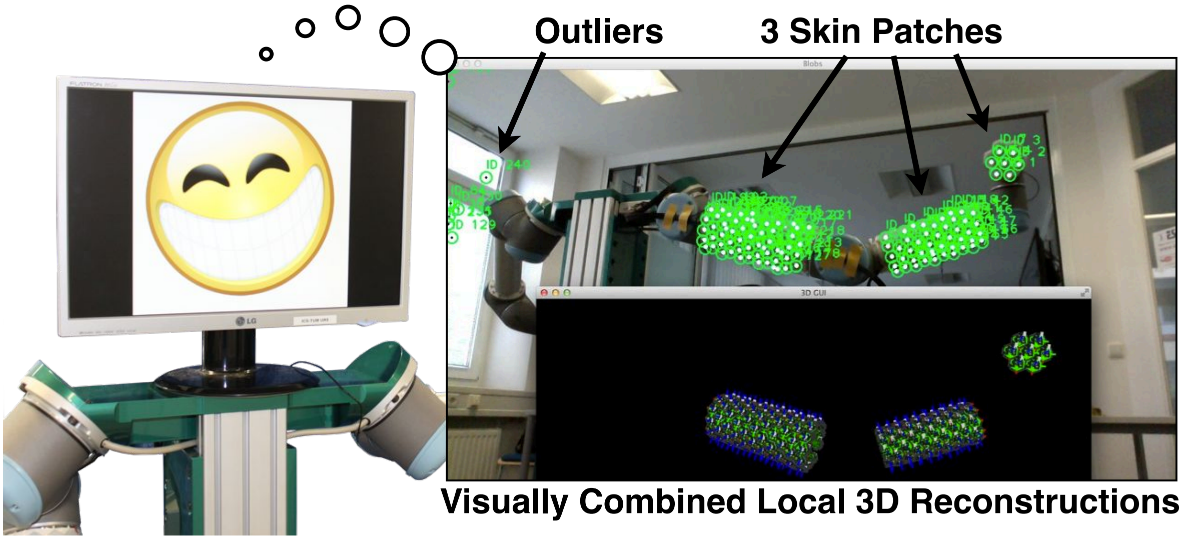

FIGURE 4.1. The figure shows a multi-body, 3D surface reconstruction with the robot TOM. Three skin patches, with 260 skin cells in total, have been individually 3D reconstructed and visually combined into a homogeneous body representation by our algorithms.

The 3D surface of our body shapes our tactile appearance, as every close-encounter must take place on it. Therefore, knowing the volumetric dimension of the own body, as well as the relative location and orientation of sensors on it, is important for many subsequent algorithms. For example, tactile patterns can only be extracted if the spatial relationship of sensors are known. The knowledge of the volumetric dimension of the own body, allows to plan motions without self- or environment collisions. It is consequently necessary to have a concise spatial representation of the 3D body surface and all sensors on it. It is not only important to know the position but also the orientation of every sensor, as e.g. normal and shear force sensors only differ in the sensing direction. Manually providing this 6D information for a high number of skin cells is cumbersome and erroneous. Robots should utilize their own sensors and actuators to build their own body models. In this chapter, we specifically introduce: 1) an algorithm (refer to Sec. 4.2) to relatively localize (position/orientation) all skin cells within a skin patch; 2) an algorithm (refer to Sec. 4.3) to estimate the transformations between multiple skin patches and to combine them in a homogeneous body representation. A skin patch is defined a closely connected set of skin cells on the same body part (see Fig. 4.15). The obtained result is the automatic calibration of the robot's volumetric surface model for areas equipped with artificial skin (see Fig. 4.1). The second algorithm also fuses visual and tactile coordinates, which has a strong biological background (refer to Sec. 2.1.2).

4.2. 3D Surface Reconstruction of Skin Patches

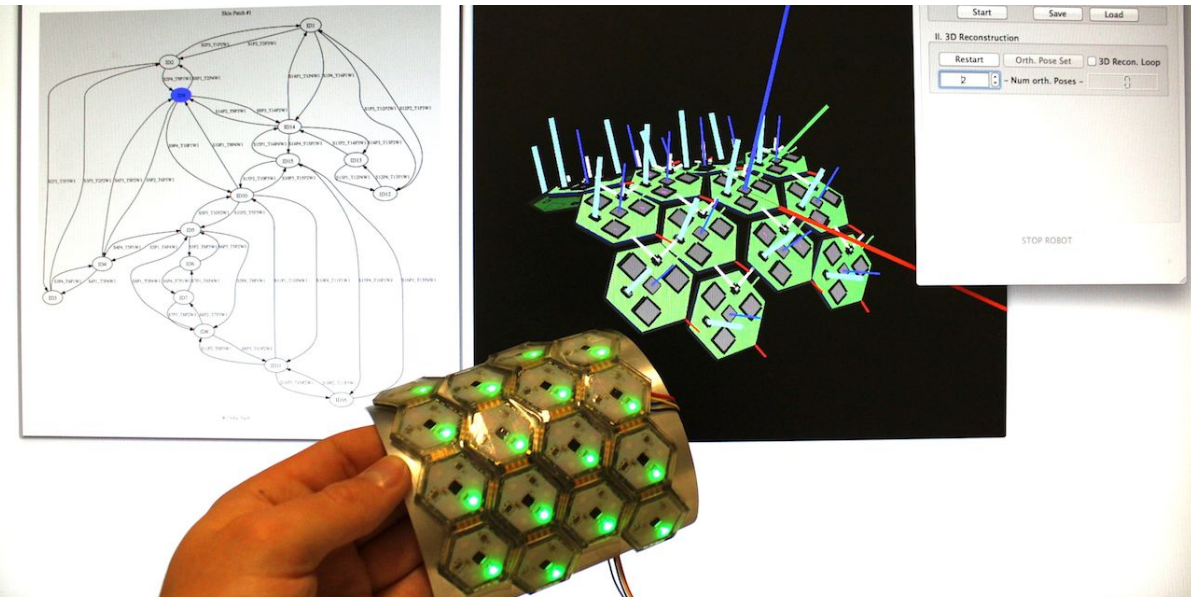

FIGURE 4.2. The figure shows the 3D reconstruction of a half-tube-like test shape equipped with 16 skin cells. The figure shows the real device, its 3D reconstruction in OpenGl and the transformation/network graph with Graphviz. The automatically chosen origin of the skin patch is highlighted in blue.

In this section, we present a new approach to reconstruct the 3D surface of robotic body parts equipped with artificial skin (please see Fig. 4.2) [1]. We achieve this by fusing static knowledge on the shape, size and tessellation capabilities of the skin cells, with dynamic knowledge about its neighbors and measurements from its orientation sensor – a 3-axis accelerometer. Our approach makes it possible to reconstruct the 3D surface of robotic body parts equipped with a patch of skin in a very short time, providing the location and orientation of every skin cell in a patch relative to an automatically chosen origin on the skin patch. This approach has been motivated by a paper from [Hoshi and Shinoda, 2007]. Our approach does not suffer from singularities in the rotation estimation. We sample a complementary set of gravity vectors, actively or passively driving the robotic body parts into a variable number of different poses, while the skin remains undeformed. Our approach explicitly makes use of the networking capabilities of our artificial skin, able to explore the connectivity between the nearest neighbors. Shifting the problem to graph theory and applying local, instead of global optimization the system can quickly adapt to changes, e.g. delete non-direct neighbor rela-

---

[1] Work in this section has been published in [Mittendorfer and Cheng, 2012a].

tions in the topological map when body structure information becomes available. Utilizing no external sensors, and only little robot independent a-priori knowledge, our method can be quickly transferred between robots. This touch-less skin calibration approach saves time and enables fast initial or re-calibration.

4.2.1. Formulation as Homogeneous Transformations

Our aim is to efficiently estimate the relative position and orientation of skin cells, distributed on the surface of robotic body parts, utilizing static a-priori and dynamically generated on-line knowledge.

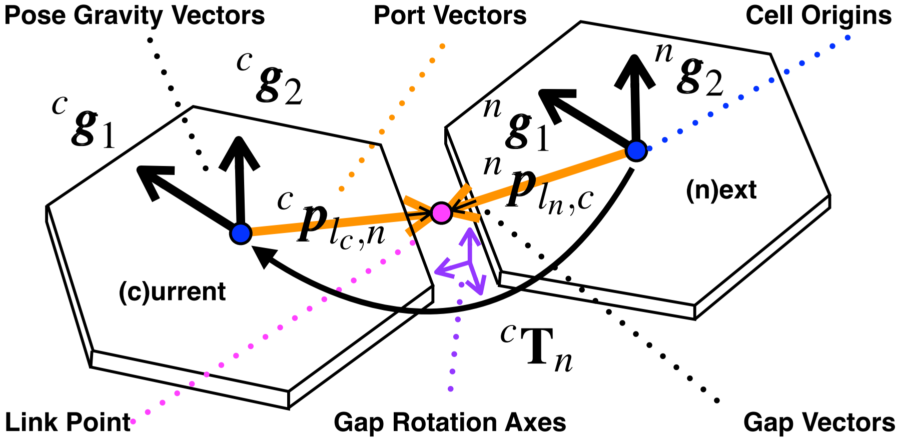

FIGURE 4.3. The figure shows the model of the elastomer gap in between two skin cells

As our artificial skin builds from an instantiation of the same thin rigid skin cell, homogeneous rigid body transformations, with a rotation ($^{c}\mathbf{R}_n$) and a translation ($^{c}\boldsymbol{t}_n$), adequately describe the connection in between two neighboring skin cells n and c (see Fig. 4.3). In approximation, no scaling, shearing, reflection or projection takes place:

$$^{c}\mathbf{T}_n = \begin{bmatrix} ^{c}\mathbf{R}_n & ^{c}\boldsymbol{t}_n \\ \mathbf{0} & 1 \end{bmatrix} \tag{4.1}$$

We further assume that the link in between two skin cells n and c, directly connected through port l_c and l_n, can be approximated by setting the link point of the extended port vectors $^{c}\boldsymbol{p}_{l_c,n}$ and $^{n}\boldsymbol{p}_{l_n,c}$ equal, in the current (c) cell coordinates:

$$^{c}\mathbf{T}_n \cdot {}^{n}\boldsymbol{p}_{l_n,c} = {}^{c}\boldsymbol{p}_{l_c,n} \tag{4.2}$$

This assumption is based on specific properties of our artificial skin: 1) artificial skin cells do not overlap; 2) a dense tessellation of thin hexagonal shaped skin cells on a surface, constrains the local placement and alignment of each cell; 3) ports have to be closely placed and initially aligned, to be directly connected; 4) the average gap size for a tessellation is known a-priori; 5) the translational component of a relatively small elastomer gap in between thin, rigid hexagonal cells can be neglected; 6) the point of rotation of the elastomer gap is approximately in its center. Based on these assumptions, we neglect the change of the small gap vectors (see Fig. 4.3) and add half of the known gap size directly to each port vector - forming the four static extended port vectors (${}^{u}\boldsymbol{p}_1, ..., {}^{u}\boldsymbol{p}_4$), defined in skin cell (u) coordinates. Combining Equation (4.1) and (4.2) leads to:

$$ {}^{c}\boldsymbol{t}_n = {}^{c}\boldsymbol{p}_{l_c,n} - {}^{c}\mathbf{R}_n \cdot {}^{n}\boldsymbol{p}_{l_n,c} \tag{4.3} $$

This shows that the relative translation (${}^{c}\boldsymbol{t}_n$) can be calculated from the relative rotation (${}^{c}\mathbf{R}_n$) and the knowledge of connected skin cells (n and c) and ports (l_n and l_c), replacing the port vectors variables (${}^{c}\boldsymbol{p}_{l_c,n}$ and ${}^{n}\boldsymbol{p}_{l_n,c}$) with the connected port vectors (${}^{u}\boldsymbol{p}_1, ..., {}^{u}\boldsymbol{p}_4$). We utilize the network exploration to find directly connected ports of skin cells and measurements of the skin cell gravity vectors to estimate the relative rotation. When all local transformations in a skin patch (s) are known, the orientation and position of every skin cell (u), relative to a chosen origin cell (o_s), are calculated as kinematic chain between u and o_s, with a variable number of cells (x) in between:

$$ {}^{o_s}\mathbf{T}_u = {}^{o_s}\mathbf{T}_x \cdot ... \cdot {}^{x}\mathbf{T}_u \tag{4.4} $$

An error estimate, allocated to every local transformation (${}^{c}e_n$), allows to calculate the inherently accumulated error (${}^{o_s}e_u$) between each skin cell (u) and its origin (o_s):

$$ {}^{o_s}e_u = {}^{o_s}e_x + ... + {}^{x}e_u \tag{4.5} $$

The overall error in a skin patch is minimized by choosing an optimal origin for every skin patch and calculation path for every skin cell in it (refer to Sec. 4.2.2). The shape and size of the skin cell, as well as the position and orientation of every sensor on a cell, are known in cell coordinates. With Equation (4.4), it is possible to transform these sensor coordinates into common skin patch coordinates. This allows the reconstruction of the partial shape of the carrier object, the surface of the skin patch and the orientation and location of every sensor in it, relative to the origin of each skin patch.

4.2.2. Representation as Graph

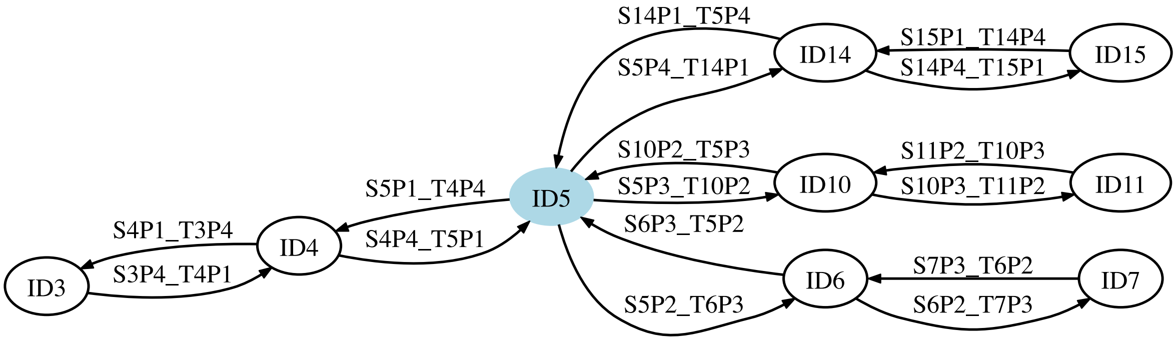

FIGURE 4.4. The figure shows a partial visualization of the X17 test patch network graph with GraphViz. The nomenclature for each edge is SxPz_TyPw, where x/y represent the source and sink skin cell IDs and z/w the source and sink port IDs.

Graph theory (here implemented with BGL[2]) provides an adequate representation for our artificial skin, and methods to efficiently handle arbitrary configurations of skin cells. We begin with parsing the result of the automatic network exploration into an empty graph (refer to Alg. 4.1), attaching a property map to the graph, with a variable for the number of skin patches and a vector to memorize the origin of each skin patch. For every skin cell we create a vertex, attaching a property map with its unique ID and placeholders for its skin patch ID, relative orientation matrix and position vector. For every neighbor, in the list of network neighbors, we create a directed edge, attaching a property map with the ID of the source and

Algorithm 4.1 3D Reconstruction of multiple skin patches

```
Detection of available skin cells ($U$)
Creation of a skin graph with ($U$) vertices
Exploration of skin cell network neighbors = neighbor list
Creation of directed port edges from neighbor list
Deletion of non-direct edges e.g. across body parts
Analysis of connected components = skin patches
while reconstruction loop do
    Sampling of gravity vectors in multiple poses ($P$)
    Estimation of rotations (${}^{c}\mathbf{R}_{n}$) between connected skin cells
    Calculation of edge weights from local estimation errors (${}^{c}e_{n}$)
    Find skin cell with shortest accumulated path for every patch
    Set these skin cells as patch origins ($o_s$) and memorize paths
    Default position (${}^{w}\boldsymbol{t}_{o_s}$) and orientation (${}^{w}\mathbf{R}_{o_s}$) of patch origins
    Update remaining skin cell orientations along calculation paths
    Update remaining skin cell positions (${}^{o_s}\boldsymbol{t}_{u}$) along calculation paths
```

---

[2] J. G. Siek and L. Q. Lee and A. Lumsdaine, “The Boost Graph Library”, Addison-Wesley, 2001, version 1.4.9

the target, as well as the source port and the target port, and placeholders for the relative rotation matrix and the weight related to the estimation error. As all available connections are bidirectional, each add two edges (see Fig. 4.4). For the 3D reconstruction of skin patches, only close connections are of interest. All others edges need to be deleted or muted. So far, we have implemented two methods: 1) we delete edges to computer interfaces, acting like skin cells with top of the range IDs; 2) we delete edges in between different body parts (refer to Sec. 5.2). In both cases spatial relations are lost, e.g. by long cables. For the next steps, the relative edge rotation estimation must be complete for all edges. First, we perform a connected components algorithm on the whole graph. This algorithm returns the number of skin patches (S) and assigns every skin cell to a patch (s). Next, we search the skin cell with the shortest accumulated path for every skin patch, based on a Dijkstra shortest path algorithm, and set it as origin (o_s) of the skin patch (s). As the positions (${}^{w}\boldsymbol{t}_{o_s}$) and orientations (${}^{w}\mathbf{R}_{o_s}$) of the skin patch origins are not yet defined, we default them to:

$$ {}^{w}\boldsymbol{t}_{o_s} = \mathbf{0} \text{ and } {}^{w}\mathbf{R}_{o_s} = \mathbf{I}\,,\; s \in \{1,...,S\} \tag{4.6} $$

Starting from each origin (o_s), we then propagate along the shortest paths and update all relative skin cell orientations (${}^{o_s}\mathbf{R}_u$) and positions (${}^{o_s}\boldsymbol{t}_u$) along the kinematic chain:

$$ {}^{o_s}\mathbf{R}_n = {}^{o_s}\mathbf{R}_c \cdot {}^{c}\mathbf{R}_n \tag{4.7a} $$

$$ {}^{o_s}\boldsymbol{t}_n = {}^{o_s}\boldsymbol{t}_c + {}^{o_s}\mathbf{R}_c \cdot {}^{c}\boldsymbol{t}_n \tag{4.7b} $$

4.2.3. Relative Rotation Estimation

The rotational component (${}^{c}\mathbf{R}_n$) of the transformation (${}^{c}\mathbf{T}_n$) in between two directly connected cells n and c combines two subcomponents: 1) the $\frac{2\pi}{6}$ repetitive initial port alignment of the hexagonal tessellation; 2) the deformation of the elastomer gap, simplified as rotation around the link point (see Fig. 4.3). Due to Equation (4.3) both can be estimated at the same time. We estimate the rotation between two neighboring skin cells (${}^{c}\mathbf{R}_n$) based on measurements of the time (t) dependent local gravity vectors (${}^{c}\boldsymbol{g}_c(t)$ and ${}^{n}\boldsymbol{g}_n(t)$) which are measured by the triaxial accelerometer on every cell. This is possible as the gravitational ($G = 6.7 \times 10^{-11}\,\frac{\mathrm{m}^3}{\mathrm{kg}\cdot\mathrm{s}^2}$) vector (${}^{w}\boldsymbol{g}({}^{w}\boldsymbol{r} + {}^{w}\boldsymbol{s})$) in world coordinates ($w$), for a robot on the comparably large (${}^{w}\boldsymbol{r} = 6371\,\mathrm{km}$) and heavy ($M = 5.9 \times 10^{24}\,\mathrm{kg}$) earth surface, is independent of the sample point vector (${}^{w}\boldsymbol{s}$):

$$ {}^{w}\boldsymbol{g}({}^{w}\boldsymbol{r} + {}^{w}\boldsymbol{s}) = -\frac{G(M+m)}{\|{}^{w}\boldsymbol{r} + {}^{w}\boldsymbol{s}\|^3}({}^{w}\boldsymbol{r} + {}^{w}\boldsymbol{s}) \approx {}^{w}\boldsymbol{g} \tag{4.8} $$

Thus the relative, time dependent rotation matrix (${}^{c}\mathbf{R}_{n}(t)$) directly links the two local gravity vectors (${}^{c}\boldsymbol{g}_{c}(t)$ and ${}^{n}\boldsymbol{g}_{n}(t)$):

$$ {}^{c}\mathbf{R}_{n}(t) \cdot {}^{n}\boldsymbol{g}_{n}(t) = {}^{c}\boldsymbol{g}_{c}(t) \tag{4.9} $$

As described in [Hoshi and Shinoda, 2007], a single measurement of the gravity vectors is not sufficient to estimate the relative orientation of rigid bodies. Here, we present a method to combine a variable number of measurements of the gravity vectors (${}^{c}\boldsymbol{g}_{c,p}$ and ${}^{n}\boldsymbol{g}_{n,p}$) in ($P$) different poses ($p$), to obtain the missing complementary information. Therefore, we actively or passively drive the skin patches to different poses between two measurements. *Active* means that the robot actuates a related, revolute joint axis itself. Whereas *passive* specifies that an operator inclines the whole robot or forces a related revolute joint axis to move. The method assumes that the relative rotation (${}^{c}\mathbf{R}_{n}(t)$) exhibits minimum changes over the lifetime (T) of the reconstruction:

$$ {}^{c}\mathbf{R}_{n}(t) \approx {}^{c}\mathbf{R}_{n} \ , \ t \in [0, T] \tag{4.10} $$

This (quasi) rigid body assumption makes it possible to continuously generate new sets of gravity vectors, changing in time (t) the orientation $\left({}^{b}\mathbf{R}_{w}(t)\right)$ of the body part (b) where the skin patch is mounted on:

$$ {}^{c}\mathbf{R}_{n} \cdot {}^{n}\mathbf{R}_{w}(t) {}^{w}\boldsymbol{g} = {}^{c}\mathbf{R}_{w}(t) \cdot {}^{w}\boldsymbol{g} \tag{4.11a} $$

$$ {}^{n}\mathbf{R}_{w}(t) \equiv {}^{c}\mathbf{R}_{w}(t) \equiv {}^{b}\mathbf{R}_{w}(t) \tag{4.11b} $$

The following equation system, relates all nine unknowns of the rotation matrix (${}^{c}\mathbf{R}_{n}$):

$$ {}^{c}\mathbf{R}_{n} \cdot {}^{n}\boldsymbol{g}_{n,p} = {}^{c}\boldsymbol{g}_{c,p} \qquad (3 \cdot P) \tag{4.12a} $$

$$ \det({}^{c}\mathbf{R}_{n}) = 1 \qquad (1) \tag{4.12b} $$

$$ {}^{c}\mathbf{R}_{n}^{T} = {}^{c}\mathbf{R}_{n}^{-1} \qquad (3) \tag{4.12c} $$

Equation (4.12a) provides up to 9 independent equations based on three 3-dimensional orthogonal vectors from ($P = 3$) orthogonal poses:

$$ {}^{u}\boldsymbol{g}_{u,1}^{T} \cdot {}^{u}\boldsymbol{g}_{u,2} = {}^{u}\boldsymbol{g}_{u,1}^{T} \cdot {}^{u}\boldsymbol{g}_{u,3} = {}^{u}\boldsymbol{g}_{u,2}^{T} \cdot {}^{u}\boldsymbol{g}_{u,3} \equiv 0, u \in \{n, c\} \tag{4.13} $$

Given the additional properties of the rotation matrix, defined in Equations (4.12b) and (4.12c), it is sufficient to provide a set of ($P = 2$) independent gravity measurements, to maintain an overdetermined system. Certain rotations of the body part, in order to reach new poses, are excluded to obtain independent equations in (4.12a). Rotations around the gravity vector itself or π repetitive rotations around any axis, provide linearly dependent equations. We utilize a constrained general solution of the procrustes problem[3], to find a rotation matrix (${}^{c}\mathbf{R}_{n}$) that closely maps a variable set (${}_{n}\mathbf{N}^{P\times 3}$) of ($P$) gravity vectors (${}^{n}\boldsymbol{g}_{n,p}$) to another variable set (${}_{c}\mathbf{C}^{P\times 3}$) of ($P$) gravity vectors (${}^{c}\boldsymbol{g}_{c,p}$). The actual solution of the mapping is thus shifted to a singular value decomposition (svd) of the two sample sets (${}_{n}\mathbf{N}$ and ${}_{c}\mathbf{C}$):

$$[{}_{nc}\mathbf{U}\ ,\ {}_{nc}\boldsymbol{\Sigma}\ ,\ {}_{nc}\mathbf{V}] = \mathrm{svd}\left({}_{n}\mathbf{N}^{T}\,{}_{c}\mathbf{C}\right) \tag{4.14}$$

The rotation matrix (${}^{c}\mathbf{R}_{n}$) builds from the left singular vectors in (${}_{nc}\mathbf{U}$), the right singular vectors in (${}_{nc}\mathbf{V}$) and the modified singular values (${}_{nc}\boldsymbol{\Sigma}'$):

$${}^{c}\mathbf{R}_{n} = {}_{nc}\mathbf{U}\cdot{}_{nc}\boldsymbol{\Sigma}'\cdot{}_{nc}\mathbf{V}^{T} \tag{4.15}$$

Sigma (${}_{nc}\boldsymbol{\Sigma}'$) is a 3×3 identity matrix ($\mathbf{I}^{3\times 3}$) with the location of the lowest singular value (matrix entry $(3,3)$) replaced with the determinant ($\det({}_{nc}\mathbf{U}\cdot{}_{nc}\mathbf{V}^{T})$), in order to enforce the rotation matrix (${}^{c}\mathbf{R}_{n}$) to be a special orthogonal matrix ($\det({}^{c}\mathbf{R}_{n}) = 1$):

$${}_{nc}\boldsymbol{\Sigma}' = \begin{pmatrix} 1 & 0 & 0 \\ 0 & 1 & 0 \\ 0 & 0 & \det({}_{nc}\mathbf{U}\cdot{}_{nc}\mathbf{V}^{T}) \end{pmatrix} \tag{4.16}$$

We only utilize the original singular values (${}_{nc}\sigma_1 \geq {}_{nc}\sigma_2 \geq {}_{nc}\sigma_3$ in ${}_{nc}\boldsymbol{\Sigma}$) in order to evaluate the quality of the estimation. In the following calculations we assume that all measured gravity vectors are normalized:

$$\|\boldsymbol{g}\| \equiv 1\mathrm{g} \tag{4.17}$$

---

[3] P. H. Schonemann, “A generalized solution of the orthogonal Procrustes problem”, Psychometrika 31, pp. 1-10, 1966

Deviations of gravity ($\boldsymbol{g}$) from the local constant ($\frac{GM}{r^2}$) indicate additional effects with the accelerometer (see Equ. (4.19)). With the normalization, we make our approach independent of the local constant. The estimation of the rotation matrix (${}^{c}\mathbf{R}_{n}$) itself is not affected by a normalization, as a rotation matrix preserves the length of a vector. Here, we only differentiate in four estimation qualities, with the following edge weights (${}_{nc}w$):

$$\text{un-defined} \qquad {}_{nc}\sigma_1 < 1, {}_{nc}\sigma_2 < 1 \qquad {}_{nc}w = \infty \tag{4.18a}$$

$$\text{partially-defined} \qquad {}_{nc}\sigma_1 \geq 1, {}_{nc}\sigma_2 < 1 \qquad {}_{nc}w = U \tag{4.18b}$$

$$\text{fully-defined} \qquad {}_{nc}\sigma_1 \geq 1, {}_{nc}\sigma_2 \geq 1, {}_{nc}\sigma_3 < 1 \qquad {}_{nc}w = 1 \tag{4.18c}$$

$$\text{over-defined} \qquad {}_{nc}\sigma_1 \geq 1, {}_{nc}\sigma_2 \geq 1, {}_{nc}\sigma_3 \geq 1 \qquad {}_{nc}w = 1 \tag{4.18d}$$

In case of an un-defined or only partially-defined estimation, it is not possible to completely estimate the rotational component around the link point in the elastomer gap. However, the alignment of the connected ports can still be enforced, appending a set of scaled (10% of unit length), correctly signed (incoming or outgoing) gap axes (see Fig. 4.3) to the data sets (${}_{n}\mathbf{N}$ and ${}_{c}\mathbf{C}$). The influence of the support axes vanishes when the gravity measurements (P vectors) are well defined, but help to stabilize the system output in un- or partially defined cases. Finally, we wish to describe the sampling of the gravity vectors. We measure the gravity vectors (${}^{u}\boldsymbol{g}_{u,p}$) of every skin cell ($u$) in a skin patch in ($P$) different poses ($p$) with an accelerometer aligned with the cell origin. The accelerometer does not only measure a rotated version of the world gravity vector (${}^{w}\boldsymbol{g}$), but also the second time derivative of position of the skin cell origin, transformed from world (${}^{w}\boldsymbol{o}_{u}(t)$) into skin cell (${}^{u}\boldsymbol{o}_{u}(t)$) coordinates ($u$) by the rigid body transformation (${}^{u}\mathbf{T}_{w,p}(t)$) of pose ($p$):

$${}^{u}\boldsymbol{a}_{u,p}(t) = \frac{\mathrm{d}^2}{\mathrm{d}t^2}\left({}^{u}\mathbf{R}_{w,p}(t) \cdot {}^{w}\boldsymbol{o}_{u,p}(t) + {}^{w}\boldsymbol{t}_{u,p}(t)\right) + {}^{u}\mathbf{R}_{w,p}(t) \cdot {}^{w}\boldsymbol{g} \tag{4.19}$$

This shows that, in order to extract the gravity vector from the accelerometer data, the skin patch has to maintain a static pose in world coordinates. We then average $N = 100$ subsequent samples at 1 kHz in every pose (p) to decrease the influence of noise and vibrations on the robot:

$${}^{u}\boldsymbol{g}_{u,p} = \frac{1}{N}\sum_{n=1}^{N} {}^{u}\boldsymbol{a}_{u,p}[n] \tag{4.20}$$

Thus sampling a pose (p) currently takes 100 ms.

4.2.4. Experiments

In this section, we provide experimental results on the 3D reconstruction quality.

4.2.4.1. Known Shape

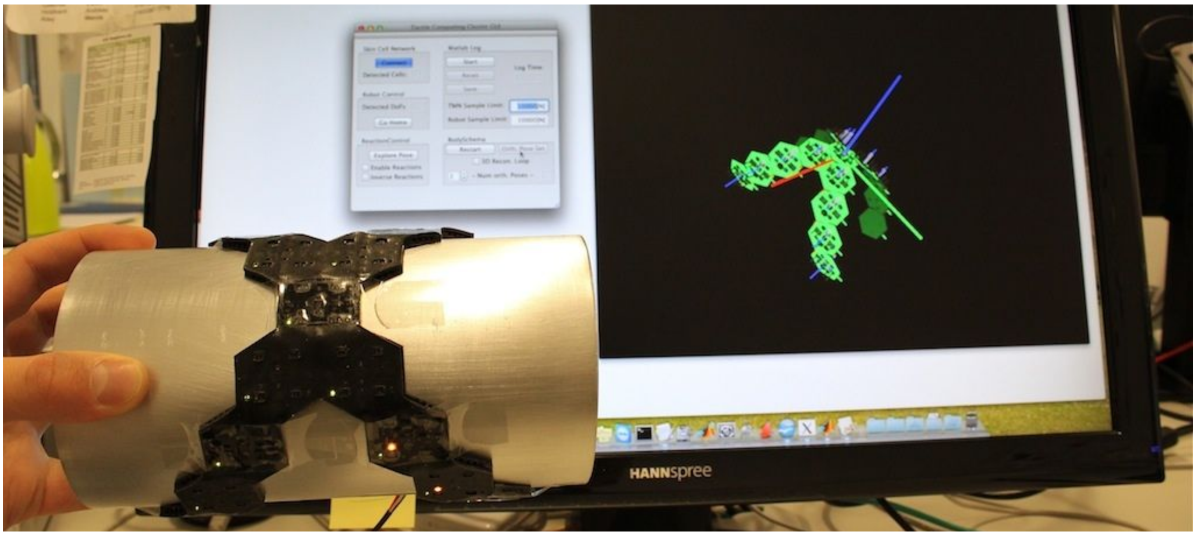

FIGURE 4.5. The figure shows the 3D surface reconstruction of a cylindrical test shape equipped with the X17 test patch.

In this experiment, we provide quantitative results on the reconstruction quality of a carrier object. To do this, we put a X-shaped skin patch, made from $U = 17$ skin cells (version 1.1, refer to Sec. A.4), on a geometrically known object, an aluminum cylinder with a measured radius of $r_{\text{real}} = 50.1\,\text{mm}$ (see Fig. 4.5). We sampled a minimal set of gravity vectors in $P = 2$ orthogonal poses. The first pose with the cylinder standing on a desk, the second held by hand as depicted in Fig. 4.5, to include vibrations as noise. We then compared the generated point cloud of the ($U = 17$) skin cell origins (${}^{o_s}\boldsymbol{t}_u$), with the ground truth – the parameterized cylinder surface. As we do neither exactly know the alignment of the x-shaped patch on the cylinder, nor its axis or a point on it, we started with a registration algorithm on the point cloud. We utilize the *fgcylinder* function of the LSGE[4] MATLAB library. Besides the point cloud, *fgcylinder* requires rough initial estimates on the cylinder axis (${}^{o_s}\boldsymbol{h}_{\text{init}} = [0;1;0]\text{mm}$), the radius ($r_{\text{init}} = 15\,\text{mm}$) and one point on the axis (${}^{o_s}\boldsymbol{b}_{\text{init}} = [0;0;-15]\text{mm}$), which we provided. Starting from this input, *fgcylinder* estimates the best fitting cylinder axis (${}^{o_s}\boldsymbol{h}_{\text{est}} = [-0.02;1.00;0.01]\text{mm}$), radius ($r_{\text{est}} = 49.80\,\text{mm}$) and one point on the axis (${}^{o_s}\boldsymbol{b}_{\text{est}} = [-3.11;1.21;-49.64]\text{mm}$), based on a least squares algorithm.

---

[4] "The least squares geometric elements library", EUROMET Repository of Software, version 0.7.6

Additionally, it provides an array of the minimal radial distances ($d_{\text{est},u}$), in between each of the skin cell origins and the parameterized surface model (see Fig. 4.6). We utilized this array, along with the difference in between the real (r_{real}) and estimated (r_{est}) cylinder radii, in order to build a quantitative reconstruction error ($\varepsilon_{\text{recon}}$) metric:

$$\triangle = r_{\text{est}} - r_{\text{real}} \tag{4.21}$$

$$\varepsilon_{\text{recon}} = \sqrt{\frac{1}{U}\sum_{u=1}^{U}(d_{\text{est},u} + \triangle)^2} \tag{4.22}$$

For the experiment shown in Fig. 4.5 we maintained a difference of $\triangle = -0.30\,\text{mm}$ and an error of $\varepsilon_{\text{recon}} = 1.62\,\text{mm}$. We have not yet taken the thickness $f \approx 3.4\,\text{mm}$ of the skin into account, statically modeled the elastomer gap as an extension of the according port vectors by half of the gap ($\frac{1.77}{2}$mm) and have not yet calibrated the triaxial accelerometers. We are aware that a selection of the skin cell origins, as sample points, is optimal for a concave surface like the cylinder, whereas points on the boundary of the rigid hexagonal shape are optimal for a convex surface. With a reduction of the skin cell size, in comparison to the curvature of the robotic part, this will no longer be relevant.

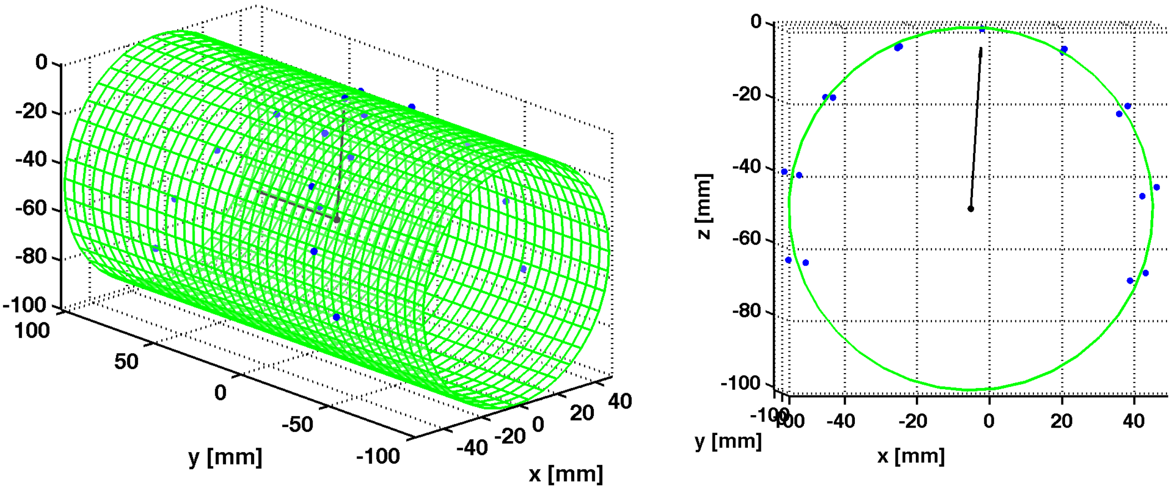

Cell ID	1	2	3	4	5	6	7	8	9	10	11	12	13	14	15	16	17
x	39.5	43.2	37.1	21.9	0	23.0	40.6	48.9	46.1	-23.0	-41.6	-51.2	-49.7	-23.0	-42.5	-53.6	-52.2
y	57.1	43.2	29.0	14.6	0	-13.4	-26.4	-39.3	-52.0	14.1	28.1	41.8	54.5	-13.5	-27.2	-40.3	-51.6
z	-69.0	-45.8	-23.2	-6.2	0	-5.7	-21.5	-44.0	-67.8	-4.7	-18.7	-40.0	-64.1	-5.4	-19.1	-39.7	-64.2
d	-1.77	-2.52	-1.32	0.36	-0.06	-1.27	1.83	1.71	1.50	-0.89	-0.99	-1.62	-1.97	-1.06	0.66	2.52	2.35

FIGURE 4.6. The figure shows the round truth comparison of the cylinder 3D reconstruction result. The best fitting cylinder is plotted in green, while the skin cell origins (${}^{o_s}\boldsymbol{t}_u$) are plotted in blue. The table denotes the relative skin cell positions towards the origin cell (o_s), here the skin cell with ID 5, and the radial distances (d_u) to the cylinder surface.

4.2.4.2. Closed Loop

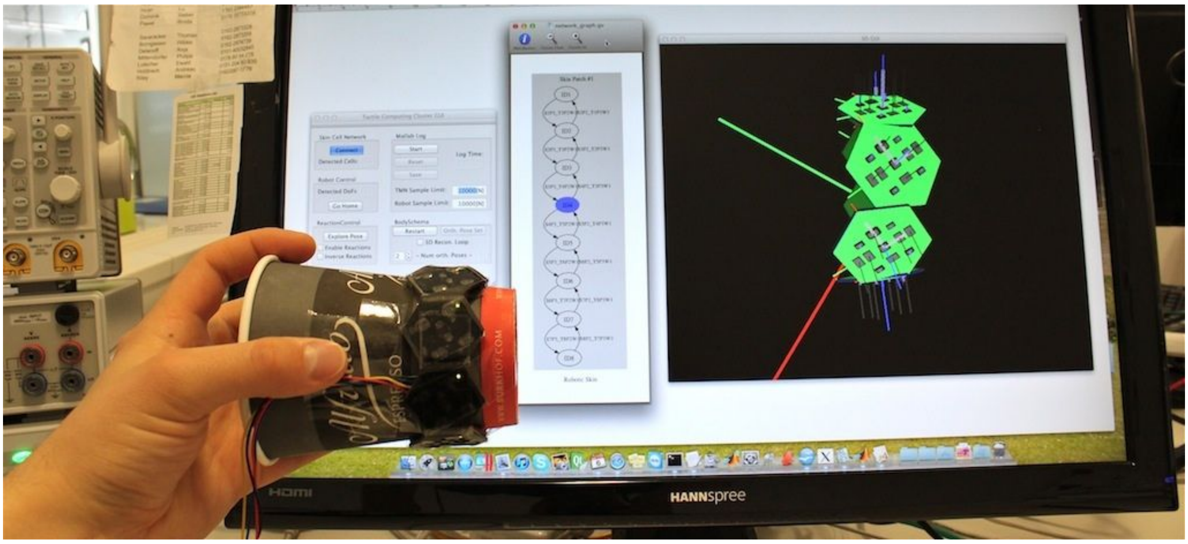

FIGURE 4.7. The figure shows the closed-loop 3D reconstruction result of a skin patch with 8 skin cells.

In this experiment, we provide quantitative results on the closed loop test case. To do this, we placed a patch of $U = 8$ skin cells (version 1.1, refer to Sec. A.4) in the longest configuration - a straight line. Then, we connected the two unconnected ends closely together, forming a ring (see Fig. 4.7). In order to stabilize the shape between poses, we fixed the patch on a paper cup. We then sampled $P = 2$ orthogonal poses, one with the cup standing on the table, the other holding the cup in the hand, to validate the robustness of the algorithm to vibrations. Fig. 4.8 depicts the difference between the link points ${}^{O_s}\boldsymbol{p}_{2,1}$ and ${}^{O_s}\boldsymbol{p}_{3,8}$ of the unconnected, but closely placed ports 2 and 3, in between the skin cells with ID 1 and ID 8. In the given experiment the difference vector $\boldsymbol{\delta} = [-6.10; -2.36; 8.16]$mm has a length of $||\boldsymbol{\delta}|| = 10.46\,\text{mm}$. Compared to the loop length $L = 222.28\,\text{mm}$ of the 16 accumulated port vectors, the error is 4.71%. The curvature of the skin, and thus also the error of the simplified gap model, is higher than in the previous experiment. Every gap is prone to a $360/8 = 45°$ rotation.

4.2.4.3. Large Skin Patch

In this experiment, we provide quantitative results on the reconstruction quality of a real robotic part and a large skin patch. To do this, we equipped the largest tube like body part of the UR-5 robotic arm (see Fig. 3.6) with $U = 143$ skin cells (version 2.0, refer to Sec. A.4). We then sampled a set of gravity vectors in $P = 3$ poses and compared the generated point

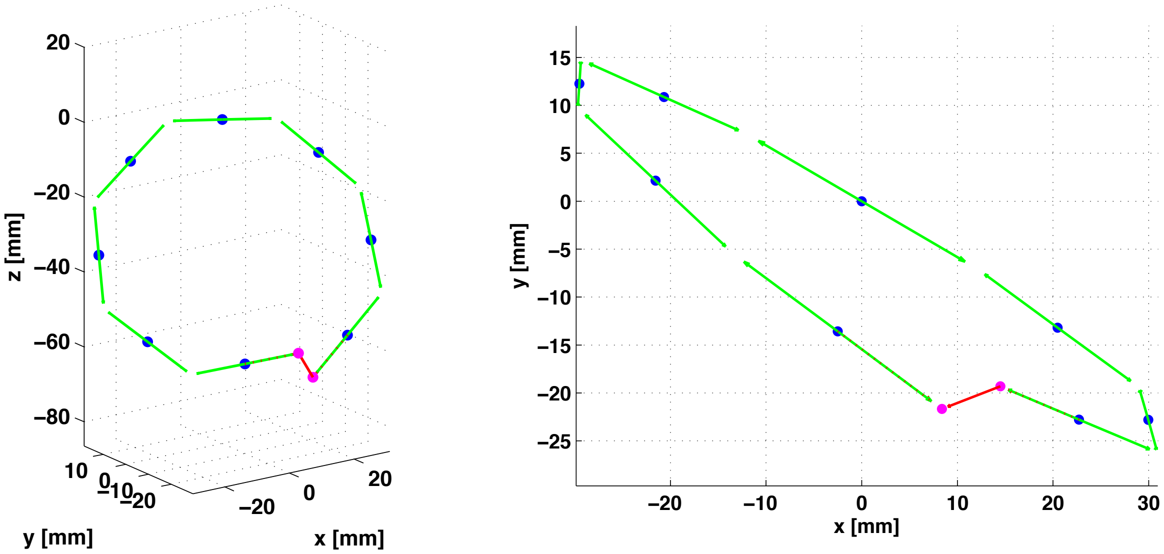

FIGURE 4.8. The figure shows the deviation (red) of the ideally connected link points (magenta) with the closed loop 3D reconstruction experiment. The skin cell origins are plotted in blue, while the utilized port vectors for the closed loop calculation are given in green.

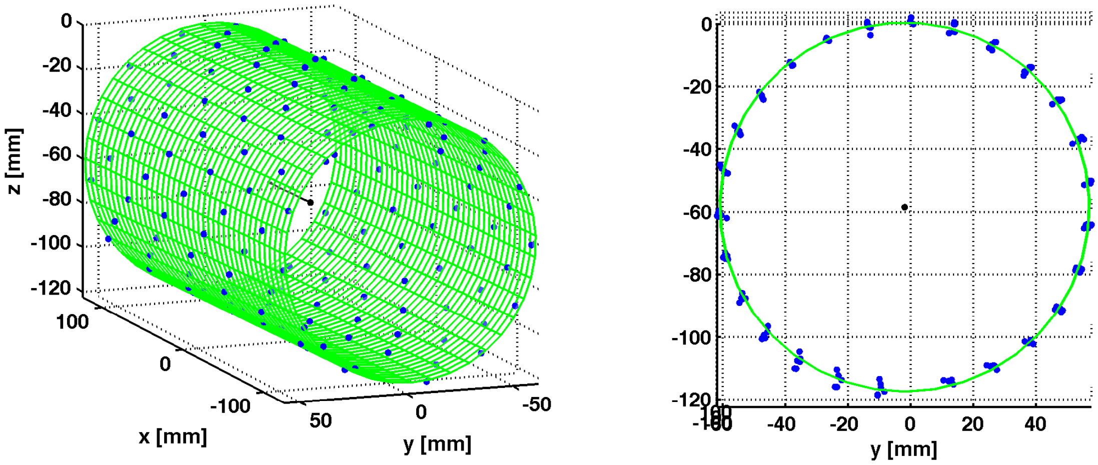

(A) 3D view

(B) y/z plane view

FIGURE 4.9. The figure shows the 3D point cloud of skin cell origins (blue) of a skin patch made from 143 skin cells, mounted on the largest tube of the UR-5 robot arm (see Fig. 4.1), in comparison to an optimal cylinder fitting (green).

cloud of the $U = 143$ skin cell origins (${}^{o_s}\boldsymbol{t}_u$), with ground truth – a parameterized cylinder surface. We utilized the same *fgcylinder* fitting function as in Sec. 4.2.4.1. In this experiment, the algorithm estimated a cylinder radius of $r_{\text{est}} = 58.96\,\text{mm}$, while we calculated a radius of $r_{\text{real}} = 60.16\,\text{mm}$ from a 378 mm circumference, measured at mid skin height. The radial distances ($d_{\text{est},u}$) in between each of the skin cell origins (${}^{o_s}\boldsymbol{t}_u$) and the parameterized cylinder model (see Fig. 4.9) are depicted in Fig. 4.10. The maximum radial distance is 3.5 mm with a standard deviation of 1.3 mm.

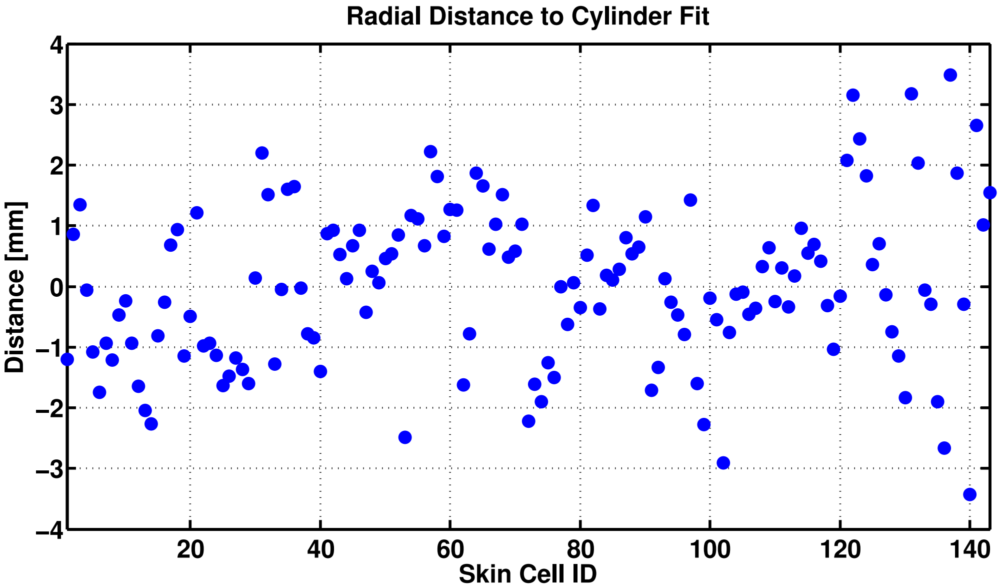

FIGURE 4.10. The figure shows the radial distance of the 3D reconstructed skin cell origins to an optimal cylinder fitting as depicted in Fig. 4.9

4.2.4.4. Influence of Accelerometer Calibration

In this experiment, we provide results on the influence of accelerometer calibration on the 3D reconstruction quality. Therefore, we performed a $P = 6$ pose calibration routine as described in Sec. 5.4.1.2. We then compared the results of our reconstruction algorithm for two different data sets: 1) directly running on the $P = 6$ complementary calibration poses; 2) running on a set of $P = 6$ poses generated by only rotating around one close to horizontal axis, but using offset and gain compensated accelerometer readings. In this experiment we utilized a straight line of of $U = 12$ skin cells (version 2.0, refer to Sec. A.4), conducting the closed loop test case as previously described in Sec. 4.2.4.2. Both experiment sets showed an accumulated loop error below 0.7% for a total loop length of $L = 333.42\,\text{mm}$. The link displacement was $\|\boldsymbol{\delta}\| = 2.22\,\text{mm}$ for set 1 and $\|\boldsymbol{\delta}\| = 2.09\,\text{mm}$ for set 2. One the one hand, those results show that the reconstruction quality can be largely improved (see Fig. 4.11) by an additional

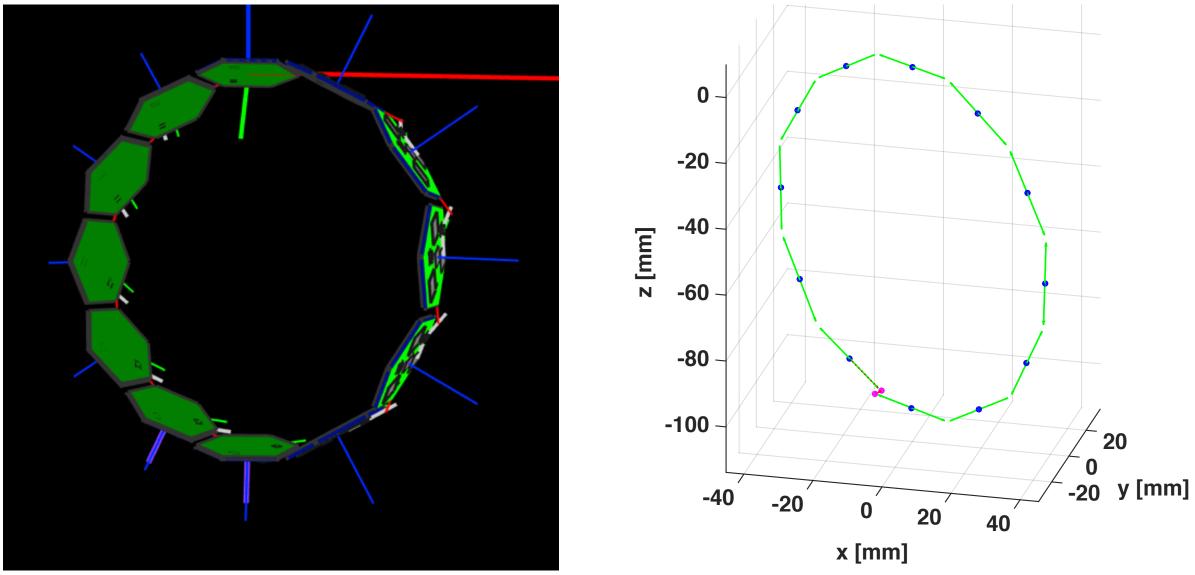

FIGURE 4.11. The figure shows the improved closed-loop 3D reconstruction result of a skin patch made of 12 skin cells. This was achieved by calibrating the skin cell accelerometers, reducing the loop error to 0.7%.

accelerometer calibration - either during production or in situ. On the other hand, we could show that our algorithm can implicitly handle this calibration, given an adequate pose set (like 6 gravity vectors spanning a sphere). This behavior is an intrinsic property of the constrained Procrustes rotation estimation that we apply.

4.2.5. Discussion on Scalability

Every time a new skin cell version has to be integrated, only the specific information of the skin cell must be updated. A smaller size of the skin cell naturally increases the number of consecutive transformations, which increases the probability of propagation errors. However, we think that the increasing the number of alternate pathways, the decreasing influence of a single (local) transformation and the denser sampling of the surface will finally decrease the overall error. A higher number of skin cells, and their subsequent connections, will also increase robustness due to the manifold of network redundancies. With flexible skin cells, a smaller cell size allows to neglect the cell deformation and to continue with the rigid body assumption. Relative rotations in between skin cells can be estimated with alternative sensors – e.g. strain gages in the elastomer gap. However, local strain sensors suffer when the incremental rotations between the elements become barely measurable. In our approach, utilizing accelerometers, the homogeneous field allows to measure relative rotations between arbitrary element pairs. Finding direct neighbors through the network exploration is a very fast method, it currently takes around 130 ms to power up and explore $U = 31$ skin cells – most of which is static waiting times. Nonetheless, we can generate edges with a different method, e.g. using spatial information distances (refer to Sec. 2.3.1). Regarding processing power, our approach is efficient. The rotation estimation is calculated numerically with a singular value decomposition, while the graph algorithms have known complexity. In order to save high level processing time, most of the relative computations can also be shifted to the skin cells.

4.3. Visual Transformation Estimation between Skin Patches

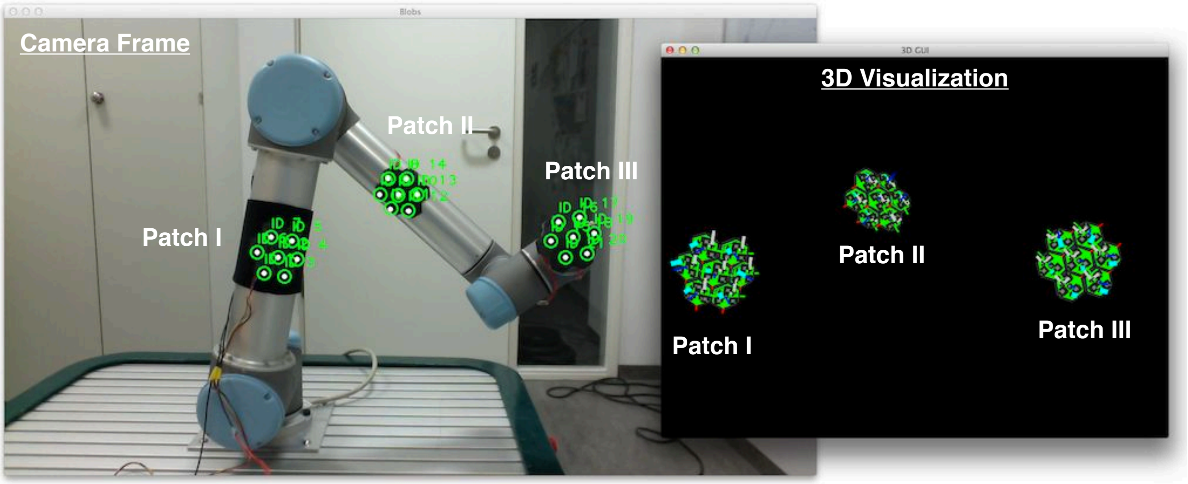

FIGURE 4.12. The figure shows three skin patches of a multi-modal, modular artificial skin (7 skin cells per patch) arbitrarily placed on a UR-5 robotic arm. All skin patches are individually 3D reconstructed, transformed into optical markers and visually joined into a single homogeneous body representation.

In this section, we present an approach to spatially self-organize a distributed modular artificial skin in 3D space[5]. With the help of a calibrated monocular camera we can then estimate a homogeneous transformation between the camera and every, at least partially visible, skin patch. When multiple skin patches are visible at the same time, we can utilize those camera transformations to calculate the missing transformations between skin patches (see Fig. 4.15). Here, we combine our 3D surface reconstruction algorithm for individual patches of artificial skin with a common active visual marker approach. Light emitting diodes, built into every cell of our modular artificial skin enable us to turn each reconstructed patch of skin into an absolute, active visual marker. Our approach allows to quickly combine distributed tactile and visual coordinate systems into one homogeneous body representation (see Fig. 4.12).

---

[5] Work in this section has been published in [Mittendorfer *et al.*, 2014a]

4.3.1. Visual Pose Estimation

In order to turn a skin patch into an absolute visual marker, and estimate its homogeneous transformation to a camera with a standard Perspective-n-Point (PnP) algorithm, we have to provide a set of ($N \geq 6$) independent point correspondences between the visual and 3D space.

Algorithm 4.2 Visual pose estimation for skin patches

```
calculate relative 3D LED positions for all skin patches
for localization of all (U) skin cells do
    turn all LEDs off
    capture background color frame ($\mathbf{BC}_u$)
    turn single LED (u) on
    capture foreground color frame ($\mathbf{FC}_u$)
    convert color images to gray scale ($\mathbf{BG}_u$ and $\mathbf{FG}_u$)
    subtract background from foreground ($\mathbf{D}_u$)
    blur difference frame ($\mathbf{DB}_u$)
    threshold to binary image ($\mathbf{B}_u$)
    run constrained blob detector
    check (single) and memorize blob coordinates (${}^{v}\boldsymbol{c}_u$)
solvePnP for all skin patches with $N \geq 6$ visible LEDs
```

4.3.1.1. Visual Marker Generation

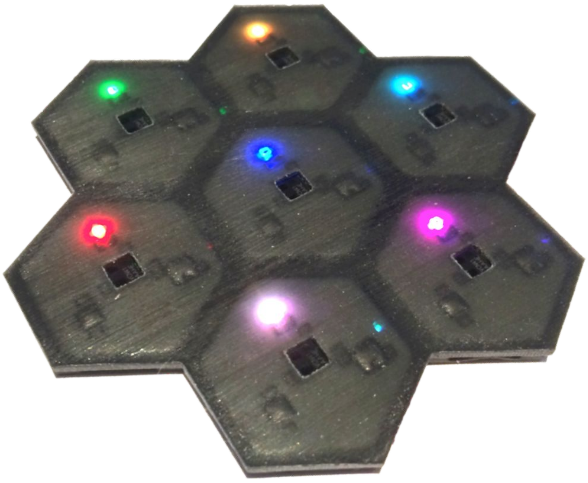

FIGURE 4.13. The figure shows a skin patch made from 7 skin cells, turned into an active visual color marker by the RGB LEDs integrated into every cell.

For the generation of known, locatable visual features in 3D space, we make use of the RGB LED integrated into every of our skin cells (see Fig. 4.13). As explained in the previous section (refer to Sec. 4.2), the position (${}^{o_s}\boldsymbol{t}_u$) and orientation (${}^{o_s}\mathbf{R}_u$) of every skin cell is known relative to its related patch origin (o_s). The allocation of skin cells to patches is known from our connected components algorithm. Since all LEDs have a static location (${}^{u}\boldsymbol{t}_{\mathrm{LED}} = (7.9, 0, 0)^T$ mm) in skin cell (u) coordinates, we directly calculate their feature positions (${}^{o_s}\boldsymbol{f}_u$):

$$ {}^{o_s}\boldsymbol{f}_u = {}^{o_s}\boldsymbol{t}_u + {}^{o_s}\mathbf{R}_u \cdot {}^{u}\boldsymbol{t}_{\mathrm{LED}} \tag{4.23} $$

As every LED is controlled (color and on/off) individually from the main system, we are able to generate salient visual features. Due to the similar characteristics of our small size LED (1x1mm, 120 degree visual angle) to a point light source, those features will be close to circular in visual space (see Fig. 4.14).

4.3.1.2. Visual Localization

In order to identify and localize the visual features (LEDs) in the camera frame (see Fig. 4.14), we actively control all LEDs and subtract foreground from background frames. Here, we make

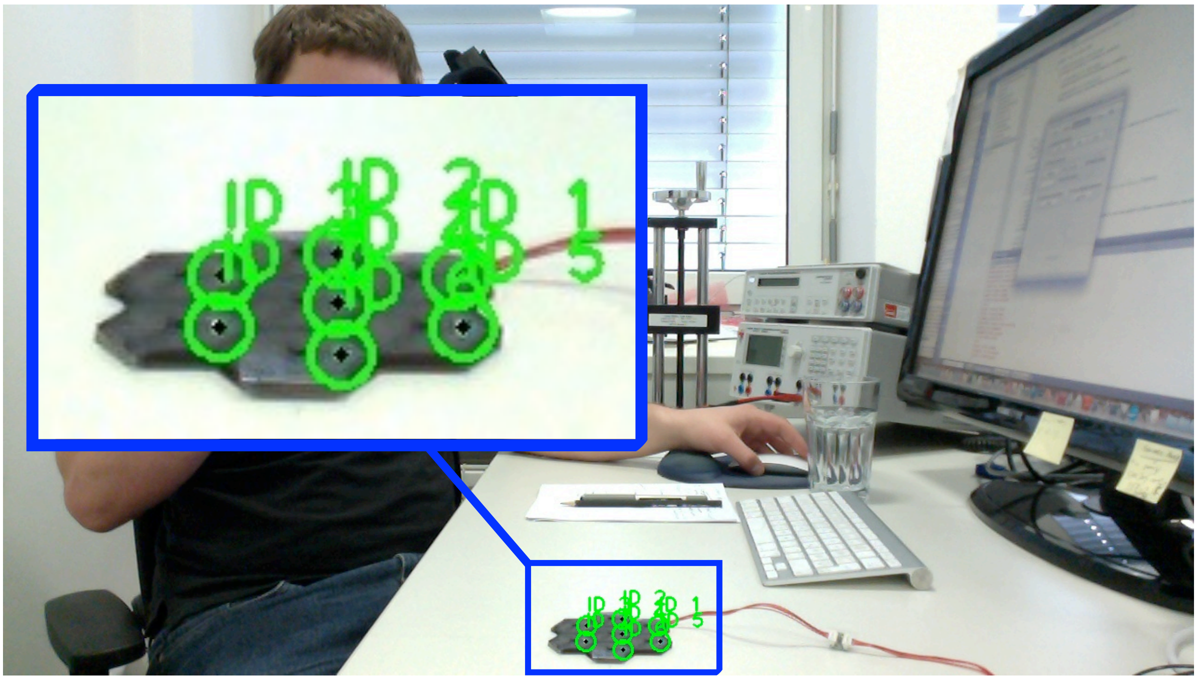

FIGURE 4.14. The figure (original resolution) shows a close-up (6.4x) of the visual localization for a skin patch with 7 skin cells, seen by a 720HD camera from 630 mm distance. The black dots in the center of the LED pixels symbolize the corresponding pixel coordinates.

use of OpenCV[6] for all image processing routines. Color features would allow to identify multiple LEDs at once and thus reduce the localization time. With the 7 basic RGB combinations (see Fig. 4.13), we would for example handle a complete skin patch transformation estimation ($N \geq 6$) with a single frame. However, the hue grade value of the LED blobs is strongly dependent on the viewing angle and distance. For a robust mapping only one LED (u) can be used at a time. The foreground ($\mathbf{FC}_u$) and background ($\mathbf{BC}_u$) color images are captured in close time vicinity to avoid large changes in the background. The images are then converted to gray scale ($\mathbf{FG}_u$ and $\mathbf{BG}_u$) and subtracted to calculate the local differences ($\mathbf{D}_u$):

$$\mathbf{D}_u = \mathbf{FG}_u - \mathbf{BG}_u \tag{4.24}$$

The difference image is then blurred and binary thresholded:

$$\mathbf{DB}_u = \text{GaussianBlur}(\mathbf{D}_u, size, sigma) \tag{4.25a}$$

$$\mathbf{B}_u = \text{Thresh}\left(\mathbf{DB}_u, thresh\right) \tag{4.25b}$$

This process is repeated and multiple (M) binary images are Hadamard-multiplied (element wise), in order to form an overlay image ($\mathbf{BO}_u$) that excludes uncorrelated changes in the background:

$$\mathbf{BO}_u = \mathbf{B}_u^{(1)} \circ \ldots \circ \mathbf{B}_u^{(M)} \tag{4.26}$$

This final image ($\mathbf{BO}_u$) is then fed to a constrained ($maxArea = 500$, $minArea = 1$) blob detector. When the current LED (u) is visible, the blob detector should return only one blob (0) with the blob point (pt) coordinates (${}^{v}\boldsymbol{c}_u = (x, y, 1)^T$) approximately at the visual (v) LED's center:

$${}^{v}\boldsymbol{c}_u = \text{BlobDetector}(\mathbf{BO}_u, maxArea, minArea)(0)\text{pt} \tag{4.27}$$

If none or more than one blob is returned, the visual feature is not available and excluded from the pose estimation.

---

[6] OpenCV Library, version 2.4.8

4.3.1.3. Pose Estimation

The LED camera (${}^{v}\boldsymbol{c}_u$) and relative 3D (${}^{o_s}\boldsymbol{f}_u$) coordinates are linked by the homogeneous transformation (${}^{v}\mathbf{T}_{o_s}$), between the camera and the skin patch coordinate system, and the camera projection matrix ($\mathbf{A}$):

$$ {}^{v}\boldsymbol{c}_u = \mathbf{A} \cdot {}^{v}\mathbf{T}_{o_s} \cdot {}^{o_s}\boldsymbol{f}_u \tag{4.28a} $$

$$ \mathbf{A} = \begin{bmatrix} f_x & 0 & c_x \\ 0 & f_y & c_y \\ 0 & 0 & 1 \end{bmatrix} \tag{4.28b} $$

$$ {}^{v}\mathbf{T}_{o_s} = \begin{bmatrix} {}^{v}\mathbf{R}_{o_s} & {}^{v}\boldsymbol{t}_{o_s} \\ \mathbf{0} & 1 \end{bmatrix} \tag{4.28c} $$

Given a calibrated (and undistorted) camera and $N \geq 6$ independent corresponding points, the homogeneous transformation (${}^{v}\mathbf{T}_{o_s}$) (see Fig. 4.15) can be uniquely estimated [Leng and Sun, 2009]. We utilize an OpenCV PnP algorithm to estimate this transformation if more than 6 corresponding points are available for each skin patch.

4.3.2. Homogeneous Rigid Body Representation

Once we have estimated all skin patch transformations (${}^{v}\mathbf{T}_{o_s}$), we are able to represent all simultaneously visible skin patches in a common visual (v) camera coordinate system (see Fig. 4.15). This allows us to combine local skin patch reconstructions of those patches, as well as their related multi-modal tactile stimuli, in a single homogeneous rigid body representation. Due to occlusions, and a constrained view of the camera, only a small set of skin patches will be visible at the same time. To be able to map the remaining skin patches, and an entire rigid body, we need to re-locate the camera. In order not to loose all existing estimations, we must set a common rigid body reference coordinate system (r). – e.g. to identity ($\mathbf{I}_4$) with the first utilized camera coordinates (v_1):

$$ {}^{r}\mathbf{T}_{v_1} = \mathbf{I}_4 \tag{4.29} $$

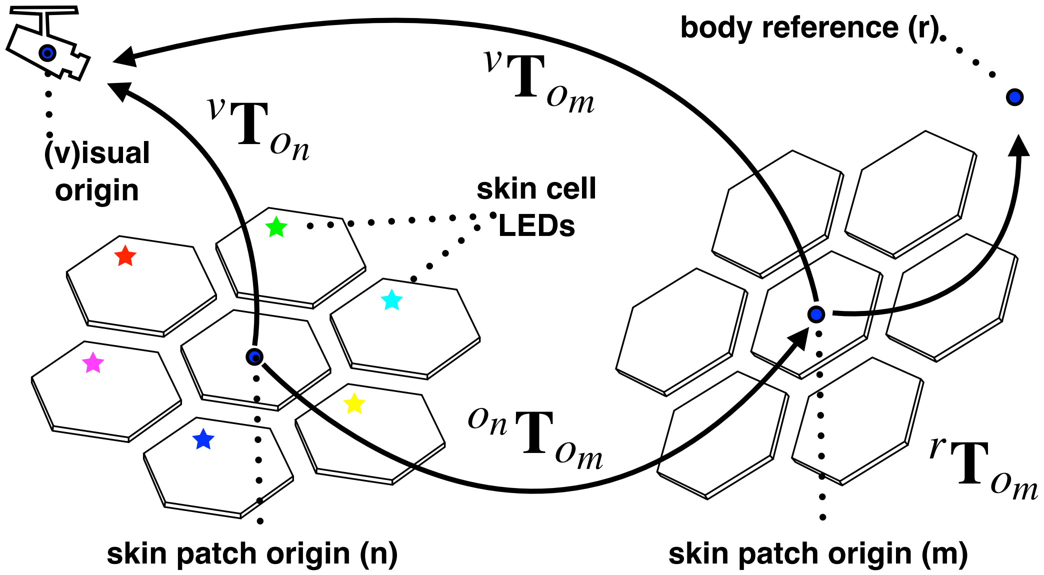

FIGURE 4.15. The figure shows the estimation of the transformation (${}^{o_m}\mathbf{T}_{o_n}$) between two individually 3D reconstructed, modular artificial skin patches (m) and (n), by the means of a camera pose estimation (${}^{v}\mathbf{T}_{o_n}$ and ${}^{v}\mathbf{T}_{o_m}$). If the position of one visible patch is memorized (m), a new patch (n) can be added/transformed to an existing homogeneous body representation (r).

New (n) patches are added to this existing homogeneous body representation (r), when they are simultaneously visible ($N \geq 6$) with at least one known patch in memory (m):

$$ {}^{r}\mathbf{T}_{o_n} = {}^{r}\mathbf{T}_{o_m} \cdot {}^{o_m}\mathbf{T}_{o_n} \tag{4.30a} $$

$$ {}^{o_m}\mathbf{T}_{o_n} = ({}^{v}\mathbf{T}_{o_m})^{-1} \cdot {}^{v}\mathbf{T}_{o_n} \tag{4.30b} $$

We can now estimate the relative position and orientation of all skin cells applied on the same rigid body – e.g. a robotic arm or a full sized humanoid robot in a (quasi-)static pose.

4.3.3. Experiments

In this section, we experimentally evaluate the performance of our approach by comparing it to ground truth. All visual tests have been performed with a calibrated MacBook Pro (2012) camera with a resolution of 1280x720 and $M = 3$ binary images. Due to the bright LED dot we found a blur in the pixel range ($size = 9 \times 9$, $sigma = 2 \times 2$) and a 50 % threshold ($thresh = \max(\mathbf{DB}_u)/2$) effective. Setting a heuristic minimum value (e.g. $minVal = 40$) for the thresholding excludes false detection when no LED is visible. In order to estimate the PnP transformations, we utilized the OpenCV *solvePnPRansac* algorithm ($iterationsCount = 100$, $reprojectionError = 8.0$, $minInliersCount = 6$) with the method CV_EPNP[7]. The proposed algorithms also effectively deal with outliers (see Fig. 4.17 or Fig. 4.1).

4.3.3.1. Single Skin Patch Pose Estimation Quality

In this subsection, we evaluate the pose estimation accuracy of a single skin patch. We chose the most compact setting of 7 skin cells as default test shape (see Fig. 4.13), due to its close to minimal (PnP algorithm requires $N \geq 6$ point correspondences) number of skin cells and its quite common appearance as sub-set in larger patches.

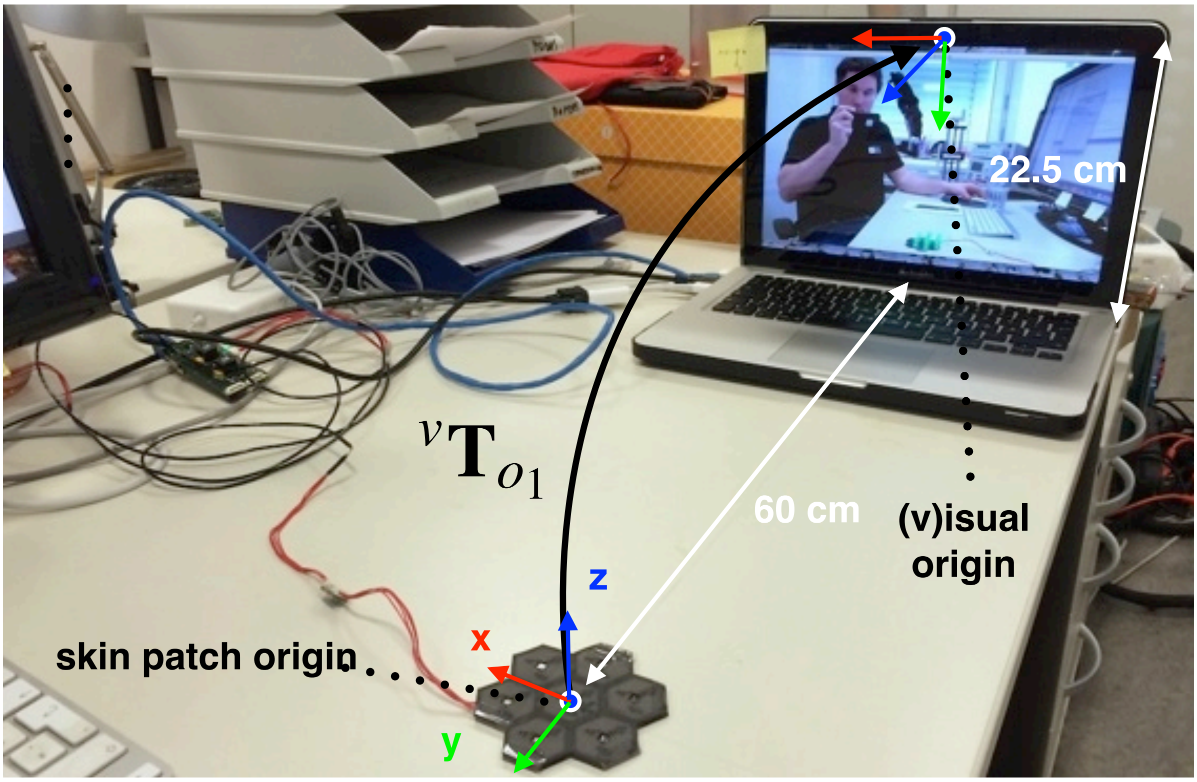

FIGURE 4.16. The figure shows the test setup for the plausibility check of the skin patch marker transformation estimation. The picture approximately shows the local camera and skin patch coordinates.

---

[7] F. Moreno-Noguer, V.Lepetit and P. Fua, “EPnP: Efficient Perspective-n-Point Camera Pose Estimation”, OpenCV 2.4.8

Absolute Accuracy: In this experiment, we compared the returned pose estimation to a manually measured homogeneous transformation between the camera and the skin patch. We would like to point out that our manual measurements are imprecise and the exact camera coordinates unknown. The difficulties to manually measure a relative transformation confirmed our initial motivation to replace manual with automated spatial calibration routines. For this test, we placed the skin patch flat on the table approximately 60 cm mid front of the laptop display, where the camera is integrated at a hight of approximately 22.5 cm, put the display into an exactly vertical position (using a water level) and aligned the skin patch y coordinate with the projection of the visual z-axis on the table (see Fig. 4.16). The pose (${}^{v}\mathbf{T}_{o_1}$) estimation algorithm returned a translation of ${}^{v}\boldsymbol{t}_{o_1} = (8.1, 193.4, 597.6)^T$mm and a rotation vector of ${}^{v}\boldsymbol{r}_{o_1} = (1.634, 0.015, -0.020)^T$radian. This is close to the expected 1.57 radian rotation around the $\boldsymbol{e}_x$ vector, while the patch origin is located 32 mm from the manually measured one $(0, 225, 600)^T$mm. The estimated distance of 628 mm is such 13 mm shorter than the manually measured value of 641 mm.

Relative Accuracy: In this experiment, we evaluated the pose estimation quality with known relative transformations in 3D space. For accurate translational displacements, we utilized a linear wheel stand with an integrated caliper. For rotational displacements, we utilized the last two revolute joints of a UR-5 robotic arm. We performed all tests with our default 7 skin cell test skin patch, one time flat and one time bent to the surface of a paper cylinder (radius 40 mm). Each time we located the patch into three different distances from the camera (≈60/100/140 cm) and translated/rotated it by a fixed value (20 mm and 0.175 rad), approximately around/along the visual coordinate vectors. The results in Table 4.1 indicate a relative translational accuracy below 1 cm and a relative rotational accuracy below 0.07 radian (4°) for tested camera to object distances up to 1.4 m.

4.3.3.2. Large Patches & Partial Occlusion

Our algorithm also handles large patches and partial occlusion. Here, we show a large 23 skin cell skin patch, placed on a shoe (see Fig. 4.17) or our latest implementation with 260 skin cells on the robot TOM (see Fig. 4.1). In order to measure the worst case effect of occlusion, we visually blocked the center cell of our default test patch, placed it on a cylinder (radius 40 mm) in a distance of 100 cm to the camera and shifted it 20 mm along the visual axis ${}^{v}\boldsymbol{e}_z$. The estimation result of 25.68 mm indicates that even a minimal ($N = 6$) worst case configurations will work.

	relative estimation results					
camera distance	60 cm		100 cm		140 cm	
marker shape	flat	bent	flat	bent	flat	bent
translation($^{v}\boldsymbol{e}_z$, 20 mm)	19.53	17.66	23.02	25.95	26.18	23.09
translation($^{v}\boldsymbol{e}_y$, 20 mm)	19.88	19.73	19.67	19.84	21.66	19.91
rotation($^{v}\boldsymbol{e}_z$, 0.175 rad)	-	0.172	-	0.178	-	0.182
rotation($^{v}\boldsymbol{e}_y$, 0.175 rad)	-	0.145	-	0.106	-	0.184

TABLE 4.1. The table shows the relative experimental accuracy of visual skin patch markers.

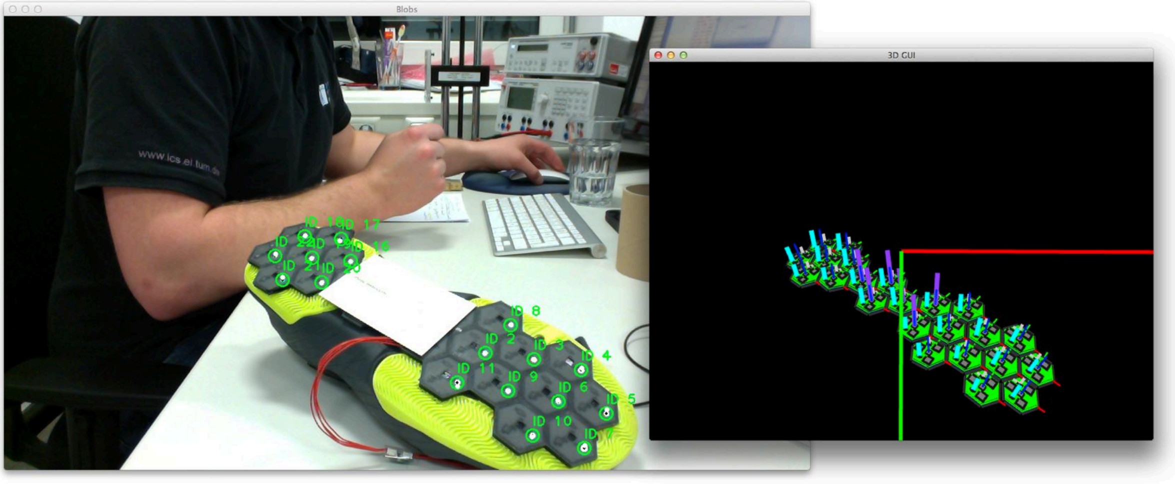

FIGURE 4.17. The figure shows the camera frame and absolute 3D visualization of a shoe sole, equipped with a skin patch of 23 skin cells. Six of the skin cells in the center are occluded by a business card.

4.3.3.3. Multi-Patch Pose Estimation Quality

In order to evaluate the relative pose estimation quality between two patches of skin, we put them physically next to each other on a cylinder (radius 50 mm) and measured the displacement between the ideally linked port vector pairs (see Fig. 4.18). In our experiment, placing the cylinder 100 cm in front of the camera, all three potential link points only had a distal mismatch of 3 mm.

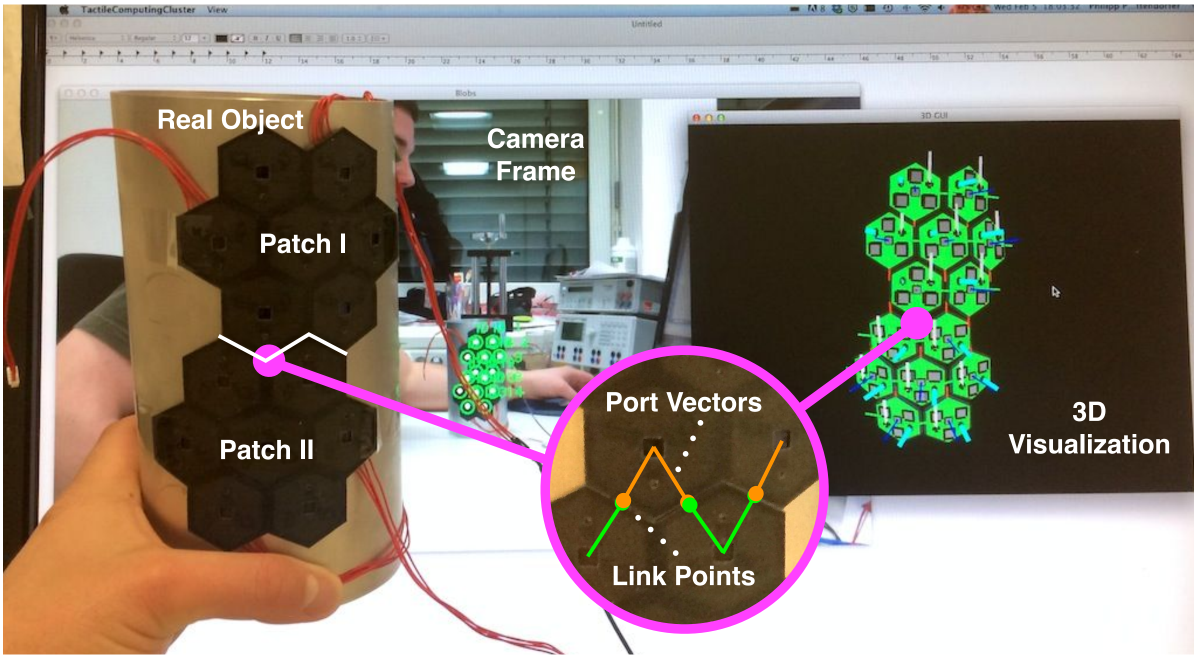

FIGURE 4.18. The figure shows two closely placed, but unconnected patches of skin on a cylinder, separately 3D reconstructed and joined into one body representation by our algorithm.

4.4. Summary

In this chapter, we introduced and quantitatively evaluated a new approach to quickly and automatically spatially self-organize an artificial skin. Distributed accelerometers, along with information on the network topology, have been utilized to reconstruct the 3D surface of patches of artificial skin. Light emitters, integrated into every skin cell, turn each skin patch into an active optical marker, in order to visually combine all distributed coordinate frames into one homogeneous body representation. Unlike point probing approaches, or even a manual calibration of tactile sensors, our approach is significantly faster, more precise and easy to apply. Our visual approach can work with external as well as internal cameras, e.g. the robots own eyes. In comparison to existing optical markers, e.g. for motion tracking, skin patch markers can have arbitrary shape, be bent to conform to a surface and partially occluded. The scalability of our approach to a high number of cells has been proven (see Fig. 4.1). Given full coverage, our algorithms quickly and robustly deliver a complete volumetric surface representation, along with the relative orientation and position of every tactile sensor, and a biologically inspired cross-modal fusion between tactile and visual space. Thus, the methods in this chapter enable the complete body schema for spatial representation to be realized.

CHAPTER 5

Body Schema for Sensory-motor Control

> Our own physical body possesses a wisdom which we, who inhabit the body, lack. We give it orders which make no sense.
>
> *(Henry Miller)*

In this chapter, we introduce methods to automatically acquire sensory-motor knowledge for robots equipped with our artificial skin. This knowledge is important to transfer sensory stimulations into motor actions. We first introduce an algorithm to self-explore the sequential dependencies of the kinematic tree of a multi-limb robot. Then, we present an algorithm to obtain a local, inverse Jacobian-like mapping in order to reactively transfer tactile stimulations into joint velocities and forces. Finally, we show an approach to automatically model and calibrate the kinematics of a robot manipulator.

5.1. Introduction

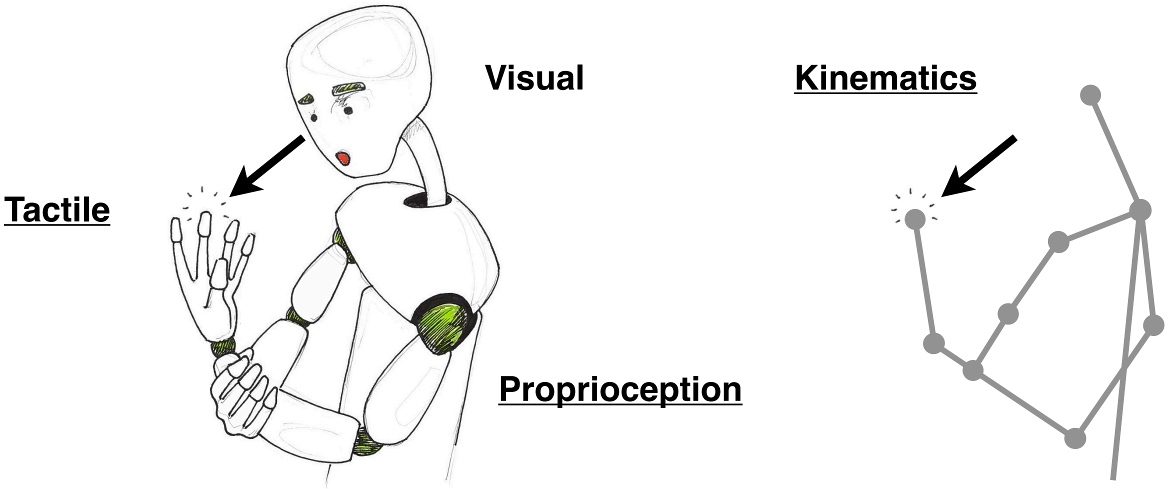

FIGURE 5.1. The figure shows the importance of acquiring kinematic knowledge for the integration of multiple modalities into a homogeneous, sensory-motor body representation.

It is important for our body to acquire the relationships between sensor and motor spaces (see Fig. 5.1), in order to react on stimulations, e.g. to support active tactile compliance or trigger protective reflexes. Manually providing those kinematic parameters is not effective, especially in case of a high number of motor and sensor units. Robots should utilize their own motion and sensing capabilities to explore and calibrate their own sensory-motor body schema. In comparison to human, robots are constrained in time to generate this knowledge and immediately exposed to a potentially harmful environment. Therefore, we introduce fast open-loop approaches, based on inertial sensors integrated into our artificial skin, that only require the robot to perform a set of safe, small-ranging motions. In this chapter we specifically introduce: 1) an approach to explore the structural dependencies of the kinematic tree in order to build kinematic models; 2) an approach to automatically acquire a local, inverse Jacobian-like mapping to immediately transfer tactile stimulations into joint motions; 3) an approach to calibrate the kinematic parameters for a global kinematic model. No *a-priory* knowledge regarding the kinematic structure and/or parameters is required. We specifically make use of accelerometers, since purely rotation dependent motion sensors, e.g. magnetometers or gyroscopes, are translation invariant. Although our approach might initially seem far off biological inspiration, human is most likely using differential information to acquire body knowledge as well, for example the resistance of movements in water as simulated in [Kuniyoshi *et al.*, 2004] or the acquisition of Jacobian mappings as in [Fuke *et al.*, 2007].

5.2. Self-exploration of the Kinematic Tree

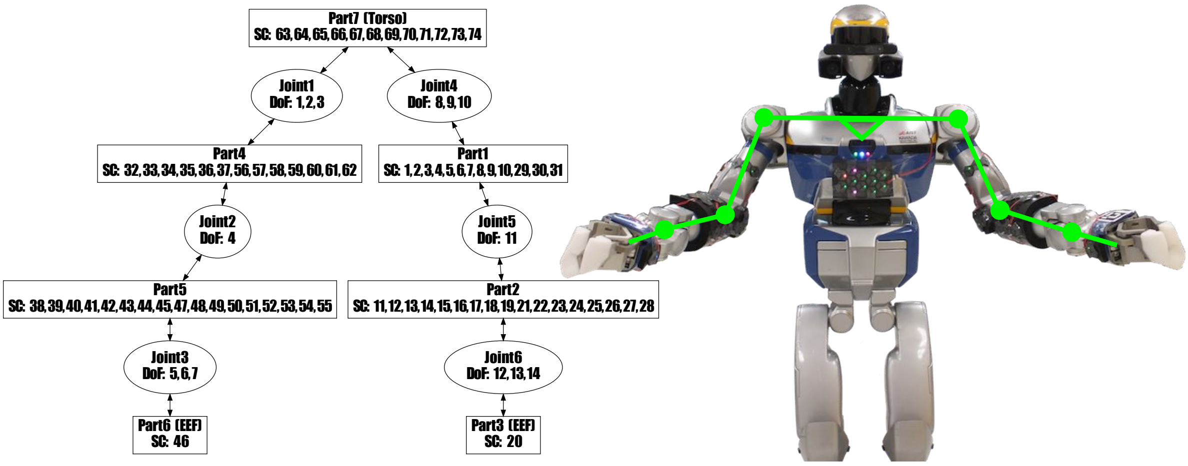

FIGURE 5.2. The figure shows the exploration result for the kinematic tree of HRP-2's upper body, visualizing the dependencies of joints (featuring one or multiple revolute degrees of freedom (DoF)) and body parts (featuring one or multiple skin cells (SCs)) towards the torso (root of the tree), in comparison to the real robot.

In this section, we introduce an algorithm (see Alg.5.1) to automatically explore the dependencies of the kinematic tree of a robot equipped with our artificial skin[1] (see Fig. 5.2). This information is necessary to identify individual manipulator limbs and build sequential kinematic models for them (refer to Sec. 5.4). Moreover, we utilize the result to suppress uncorrelated motions in the sensory-motor-map (refer to Sec. 5.3) and to detect connections between body parts in the neighbor graph of the 3D surface reconstruction (refer to Sec. 4.2). The algorithm provides information on about the number of body parts and which skin cells are allocated to which body part. It also defines how joints, composed of one or more revolute degrees of freedom (DoFs), connect the body parts. The algorithm identifies which body parts are end-effectors (located at the end of a serial kinematic chain) or root (located at the start of a serial kinematic chain). In order to achieve this, our method only utilizes information from the accelerometers built into every skin cell and small range, quasi-static, open loop motions of the robot. Our approach only requires control on joint axes and a quasi-static base/torso, e.g. humanoid fixed into a calibration stand or a stationary mobile base. We use an internal observer which is not limited by occlusions or any dependent on any external components. Due to the contact-less approach, our method is able to acquire its information in a very short time, even for a high number of distributed skin cells and revolute degrees of freedom.

---

[1] Work in this section has been published in [Mittendorfer and Cheng, 2012c], [Mittendorfer *et al.*, 2013] and [Mittendorfer *et al.*, 2015].

5.2.1. Theory of Operation

5.2.1.1. Constraints

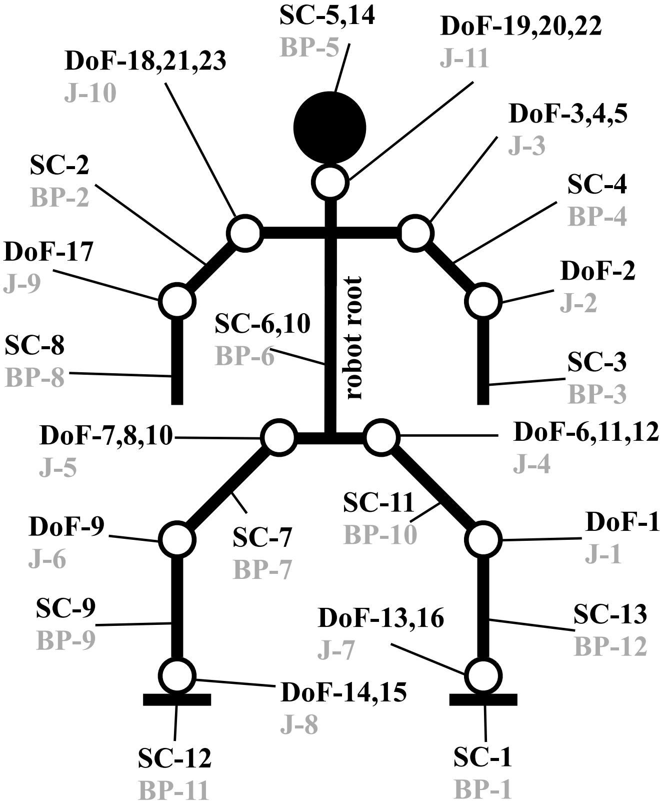

FIGURE 5.3. The figure shows an exemplary distribution of skin cells (SC) on body parts (BP) and revolute degrees of freedom (DoF) of Joints (J) for a stick-man model of a humanoid.

We assume rigid body kinematics, i.e. joints with one or more revolute degrees of freedom (DoF) are connected by non-deformable body parts. Furthermore, our approach requires a non-inertial base frame. This implies that during the whole calibration process one reference body part (root) of the robot has to remain static in world coordinates. With a robotic arm or wheeled robotic platform this constraint is naturally given by the base frame. For a humanoid robot the torso is considered the best option, as it is a casual point to fix a humanoid, is located close to the center of mass and is a relatively central point in the kinematic tree. It is necessary that every DoF can be actuated freely. Impacts with the DoF limits or on any objects surrounding the robot interfere with the motion generation and sensory sampling. This is no limitation as in general collisions during calibration procedures are usually avoided. Given full coverage, artificial skin can automatically detect any collision. The robot needs to be equipped with at least one skin cell per body part. Only then, it is possible to unambiguously discriminate the sequence of joints and body parts of the robot's kinematic tree (see Fig. 5.3). We currently only support revolute DoFs, which covers the grand majority of robots. However, an extension to include linear joints is possible.

5.2.1.2. Physical Formulation

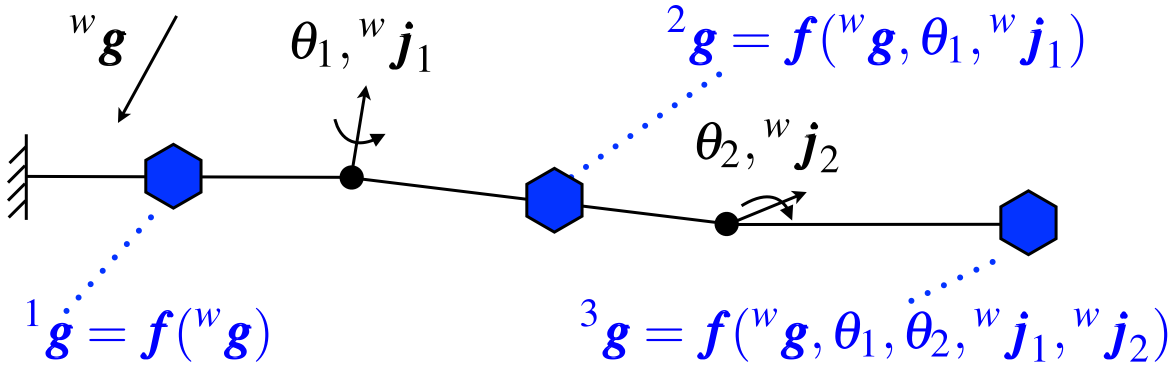

FIGURE 5.4. The figure shows an exemplary functional dependency between gravity measurements of distributed accelerometers (blue), the joint axes and joint position variables (black), towards the position of the accelerometers in the serial kinematic chain. The gravity measurement (${}^{3}\boldsymbol{g}$) on the end-effector is for example affected by both joint axes, while the one on the static body part (${}^{1}\boldsymbol{g}$) is independent of both.

Actuating one revolute degree of freedom (DoF) at a time generates two dynamic and one static contributor (refer to Sec. 5.4.2 or Sec. 5.3.1.2). Both dynamic effects (centripetal and tangential acceleration) vanish if the length of the radial vector between the joint axis (d) and the accelerometer (u) (${}^{u}\boldsymbol{r}_{u,d}$) is close to zero. For skin cells close to the axis of motion, it is difficult to extract an influence from noise. Here, we use the static component, the rotated gravity vector ${}^{u}\boldsymbol{g}[n]$, which is independent of translations. Rigid body kinematics enforce the same rotation for all accelerometers located on the same body part. All skin cell (u) gravity measurements (${}^{u}\boldsymbol{g}_{u,d}$) can be expressed as a function of the position variables (θ_d) of the joints between the static root and the body part carrying the skin cell (see Fig. 5.4). Whether a skin cell (u) is dependent on a DoF (d) or not, is detected by changing the position of one DoF after the other, while monitoring the gravity vectors measured before (${}^{u}\boldsymbol{g}_{u,d}(t)$) and after (${}^{u}\boldsymbol{g}_{u,d}(t+\triangle T)$) the incremental ($\triangle\theta_d$) motion around each joint axis (${}^{u}\boldsymbol{j}_d$):

$$ {}^{u}\boldsymbol{g}_{u,d}(t+\triangle T) = \mathrm{vrrotvec2mat}({}^{u}\boldsymbol{j}_d, \triangle\theta_d) \cdot {}^{u}\boldsymbol{g}_{u,d}(t) \tag{5.1} $$

If the distance between two normalized gravity vectors $\boldsymbol{g}_{u,d}$ is above a pre-defined limit (l_{th}), the correlation entry ($am_{u,d}$) in a binary table, called activity matrix (**A**), is set to *true*:

$$am_{u,d} = \left\| \frac{{}^{u}\boldsymbol{g}_{u,d}(t)}{\left\|{}^{u}\boldsymbol{g}_{u,d}(t)\right\|} - \frac{{}^{u}\boldsymbol{g}_{u,d}(t+\triangle T)}{\left\|{}^{u}\boldsymbol{g}_{u,d}(t+\triangle T)\right\|} \right\| > l_{\mathrm{th}}\ , \quad am_{u,d} \in \{0,1\} \tag{5.2}$$

Problems occur, whenever a joint axis is aligned to the gravity vector. In this case the gravity vector is the eigenvector of the rotation matrix, the measured gravity vectors do not change and matrix entries are falsely set to ‘0’:

$${}^{u}\boldsymbol{g}_{u,d}(t+\triangle T) = \mathrm{vrrotvec2mat}\left({}^{u}\boldsymbol{g}_{u,d}(t), \triangle\theta_d\right) \cdot {}^{u}\boldsymbol{g}_{u,d}(t) = {}^{u}\boldsymbol{g}_{u,d}(t) \tag{5.3}$$

Since every motion must produce an effect at least on one body part, we are able to detect this singular situation. To overcome it, multiple activity matrices of the same robot are combined with an element wise logical ‘or’. A secure approach to generate two complementary activity matrices is to rotate the static body part (root) of the robot around one of the horizontal axes, e.g. a ‘standing’ and a ‘lying’ humanoid. In cases where the joint axes directly connected to the root are not vertical, one position incremental and one position decremental sequence on every DoF is sufficient.

5.2.2. Algorithm

Algorithm 5.1 Exploration of the kinematic tree

```
1: Detect number of available skin cells (U) and revolute DoFs (D)
2: Move one DoF at a time, sampling all skin cell gravity vectors
3: Create activity matrix $\boldsymbol{A}_{U\times D}$, thresholding the samples
4: Merge skin cells with similar row vectors in $\boldsymbol{A}$ to body parts
5: Merge DoFs with similar column vectors in $\boldsymbol{A}$ to joints
6: Extract connection sequences from row vectors
7: Detect the reference body part (RS)
8: Determine available end-effectors
9: Assemble a serial sequence for a each robotic limb (manipulator)
```

For all further steps, we infer that a valid activity matrix has been acquired (refer to Sec. 5.2.1.2). In each step, the results are automatically evaluated for errors, e.g. DoFs must feature at least one positive entry in the activity matrix to exclude rotations around the gravity axis (refer to Equ. 5.3). This error detection is important for an autonomous system.

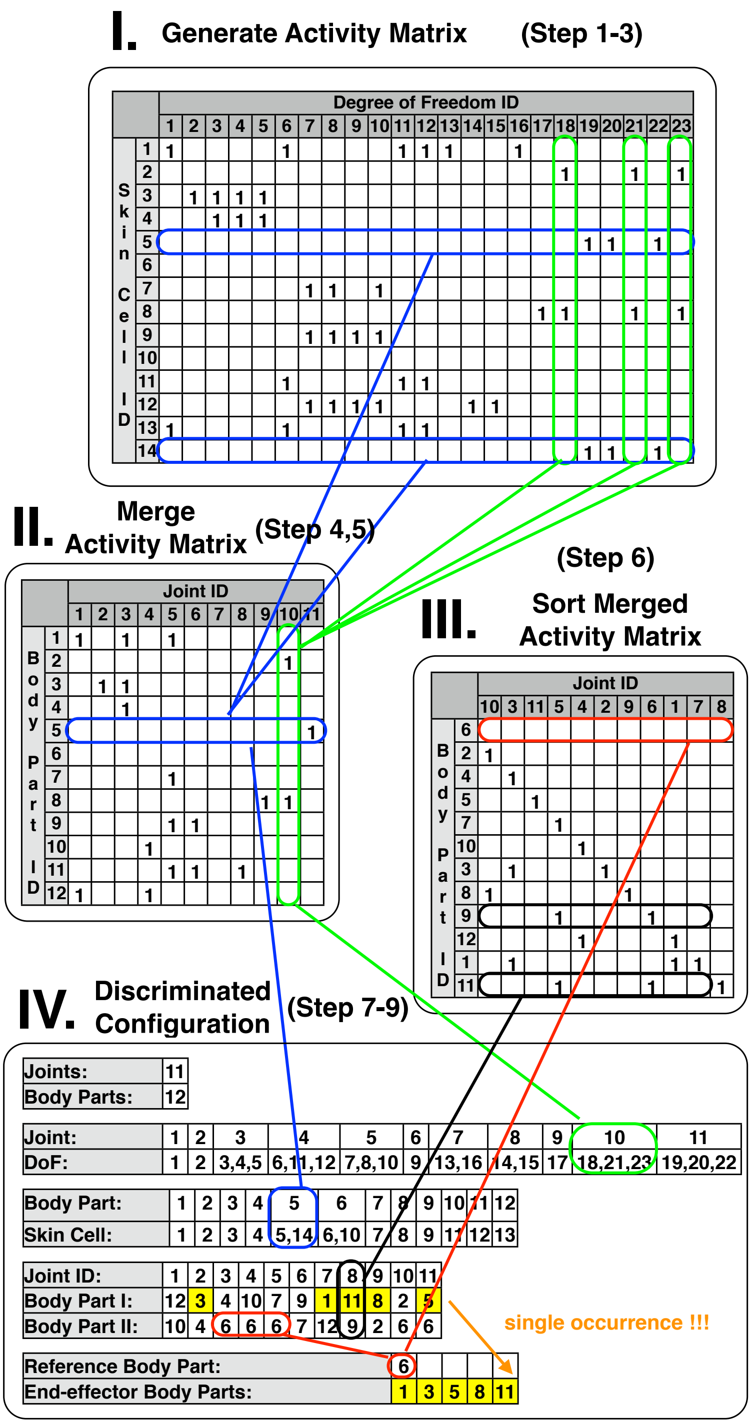

FIGURE 5.5. Steps of the kinematic tree exploration algorithm (refer to Alg. 5.1) for an activity matrix representing a "simulated" humanoid robot test case (see Fig. 5.3). Available skin cells and degrees of freedom (DoF), as well as detected body parts and joints are automatically labeled with consecutive identification numbers (IDs).

5.2.2.1. Segment and Joint Merging

Skin cells that are located on the same body part present the same motion ‘activity’ and are merged into body parts (see Fig. 5.5.III). Similarly, all DoFs between body parts are merged into its corresponding joints. This leads to a merged matrix, correlating joint and body part activities (see Fig. 5.5). The number of rows gives the number of detected body parts while the number of columns provides the number of joints. This is common for a tree like robotic structure, where the number of body parts (S) must be higher than the number of joints (J), i.e. $S = J + 1$.

5.2.2.2. Joint Segment Connectivity

The merged activity matrix must be sortable to a strictly lower triangular form (see Fig. 5.5). If this is not true, one of the given constraints has been violated (refer to Sec. 5.2.1.1), e.g. there are body parts without skin cells. Our algorithm progresses along the secondary lower diagonal. For each column of the secondary lower diagonal we perform a column wise search of common elements, excluding only the current diagonal element. For example in Fig. 5.5.III, we can see that joint 2 (column 6) connects body part 3 (row 7) with body part 4 (row 3).

5.2.2.3. Segments and Limbs

The extracted joint/body-part connectivity represents a hierarchical kinematic tree. The static reference body part (root) of the robot is the null row vector of the merged activity matrix. End effector body parts (leaves), like the finger tips of a humanoid, exactly connect to a single joint. Body parts that connect more than two joints, like the palm of a humanoid, are inner nodes and can serve as an intermediate reference for sub-manipulators. A limb is a kinematic chain, starting from a reference body part and ending at an end-effector or inner node.

5.2.3. Experiments

In order to verify our approach, we performed kinematic tree exploration experiments with three different robot platforms: 1) with a simulated model humanoid (i.e. fixed torso); 2) with a KUKA light weight robotic arm mounted on a horizontal stand (i.e. fixed base); 3) with the upper body of a HRP-2 humanoid robot while balancing (i.e. floating base). In all the cases we were able to reliably extract the kinematic tree. For the simulated humanoid, we manually extracted the activity matrix (see Fig. 5.5) from the stick-man model (see Fig. 5.3). In this thesis, we focus only on the most interesting experiment on the HRP-2. In this case, 74 skin cells have been distributed on the upper body of HRP-2 (see Fig. 5.2), while having control on 14 actuators (DoFs) of the left and right arm. All skin cell gravity vectors were measured 500 ms before and 500 ms after (to attenuate vibrations) each postural change by $\triangle\theta_d = 0.1\,\text{rad}$. We sampled each vector with an averaging window of 1.0 s length. The total exploration lasts approximately 70 seconds and can be easily sped up by tuning the previous parameters. A binarizing threshold of $l_{\text{th}} = 0.01\text{g}$ was applied (refer to Equ. 5.2), which is 10% of the maximum value caused by a 0.1 rad rotation around an axis orthonormal to gravity (refer to Alg. 5.1). The chosen threshold has proven to be sensitive enough, but is still robust enough against sensor noise and balancing motions of the robot. We did not detect any failure in all ($N \approx 10$) conducted experiments. The result of the exploration can been seen in detail in Fig. 5.2.

5.3. Self-acquisition of an Inverse Jacobian like Mapping

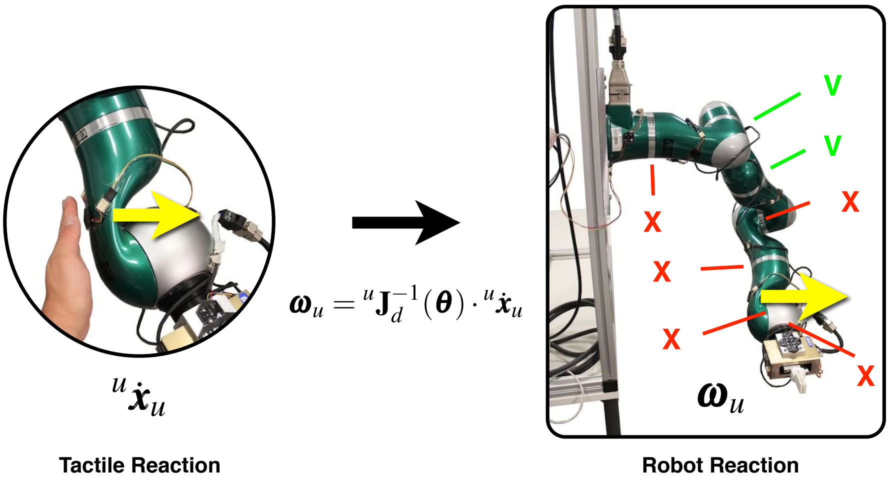

FIGURE 5.6. The figure shows the similarity of the sensory-motor map to an inverse Jacobian matrix (${}^u\mathbf{J}_d^{-1}(\boldsymbol{\theta})$), mapping tactile stimulations, generating desired contact point velocities (${}^u\dot{\boldsymbol{x}}_u$), into joint velocities ($\boldsymbol{\omega}_u$).

In this section, we introduce an inverse Jacobian like mapping – the sensory-motor map[2]. This self-acquired lookup table is used to map multi-modal tactile reactions into joint velocity reactions of the robot, like an inverse Jacobian matrix (see Fig. 5.6). It can be used when a full kinematic estimation is not possible or necessary. The sensory-motor map is organized in tiles, each directly linked to a pose of the robot. Tiles are generated during an initial phase to supply a set of key poses for the desired workspace. In operation (see Fig. 5.8), our algorithm automatically selects a tile with minimum euclidean distance (measured in the joint space) to the actual pose of the robot. Every tile contains a set of joint velocity vectors to directly transfer multi-modal tactile stimuli on the skin cells into joint motions. Currently, we only utilize one joint velocity vector, allocated to the motion along the surface normal of each cell, which is sufficient for a variety of multi-modal reactions, e.g. temperature or proximity. The two other sideways translational directions can be easily added by reformulating our weight extraction equation (see Equ. 5.12). Rotational components have not yet been implemented, however a similar approach can be implemented using gyroscopes, magnetometers or gravity samples. For most tactile applications, the three translational components will be sufficient.

---

[2] Work in this section has been published in [Mittendorfer and Cheng, 2011b] and [Mittendorfer *et al.*, 2015].

Our approach only requires control on the joint axes and a quasi-static base/torso. We use an internal observer and are not limited by occlusion or any external components. Due to the touch-less approach, our method is able to acquire its information in a very short time, even for a high number of distributed skin cells.

5.3.1. Theory of Operation

5.3.1.1. Working Principle

In order to acquire all weight values of a tile, our algorithm applies dynamic motion pattern to all actuated joint axes, one after the other. Our algorithm then evaluates the effects each motion had on our skin cells using the information from the built-in 3-axis accelerometer. A high acceleration in the desired direction returns a high score, while unwanted motions in the other directions are penalized with low scores. Only few constraints have to be taken into account during the acquisition of the map: 1) a fixed robot base frame; and 2) a sufficient unconstrained motion range around every robot pose for the exploration. In principle, our approach is based on three theorems: 1) Every sensor modality on our multi-modal skin cell has a preferred direction in which motion increases or decreases the sensor excitation, e.g. the proximity sensor along the local surface normal; 2) The robot has an explicit central point in the kinematic tree which grounds reflex like, immediate reactions; 3) Reactions from different sensor modalities and locations can be meaningfully super-imposed. The first theorem implies that we are able to use the motion sensor on every skin cell, in order to evaluate appropriate reactions and transfer these to other modalities. To achieve this, it is necessary to know the alignment between the new sensor modality and the motion sensor. In our case this information is available on each skin cell. The second theorem makes possible to reuse previously explored sensory-motor weights and apply them to generate reactions around the same or sufficiently close poses. Since we use a relative motion sensor, it is necessary that a reference point is quasi-static during the whole exploration phase. With a robotic arm, this central point is given by the base, while for a humanoid robot, we have to artificially provide this fixation, e.g. by fixing the torso or hip in a calibration stand. The third theorem sum reactions from different sensor modalities and skin cells before mapping this combined information into motor actions. Conflicts between reactions have to be solved at a higher level. Here, we only propose a standard interface per skin cell for a high level controller (refer to Sec. 5.3.3 and Sec. 6.2).

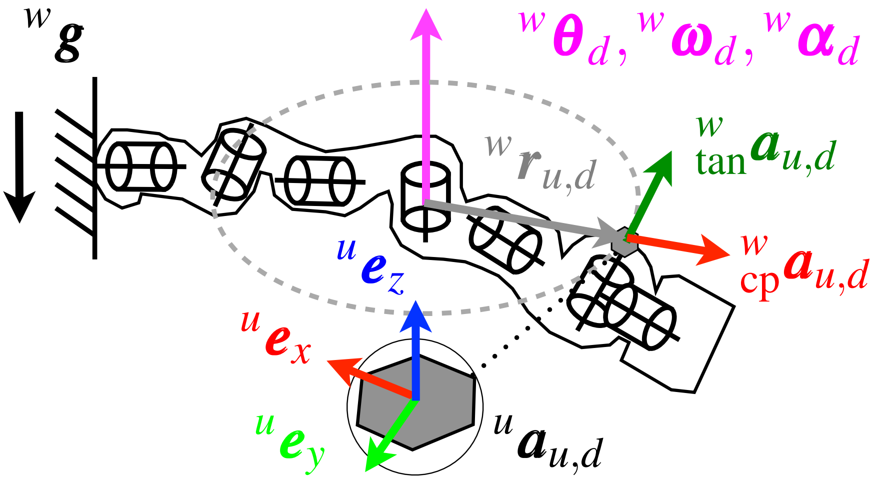

FIGURE 5.7. The figure shows the components of the accelerometer reading, when actuating one revolute joint at a time.

5.3.1.2. Physical Formulation

In this paragraph, we briefly describe the physical effects of an isolate revolute joint motion on accelerometers mounted on the actuated body parts (see Fig. 5.7). Neglecting skin deformations, every skin cell follows the acceleration of its mounting point. Given a single static reference body part (w), a change in velocity ($\frac{\mathrm{d}}{\mathrm{d}t}{}^{w}\omega_d(t) = {}^{w}\alpha_d(t)$) of a revolute DoF ($d$) has a direct influence on the acceleration ${}^{u}\boldsymbol{a}_{u,d}$ of skin cell (u), which measures three superposed effects:

(a) The tangential acceleration ${}^{w}_{\tan}\boldsymbol{a}_{u,d}$, which is dependent on the revolute acceleration ${}^{w}\boldsymbol{\alpha}_{\boldsymbol{d}}$ and the radial vector ${}^{w}\boldsymbol{r}_{u,d}$, in between DoF ($d$) and the accelerometer (u):

$$
{}^{w}_{\tan}\boldsymbol{a}_{u,d} = {}^{w}\boldsymbol{\alpha}_{\boldsymbol{d}} \times {}^{w}\boldsymbol{r}_{u,d} \tag{5.4}
$$

(b) The centripetal acceleration ${}^{w}_{\mathrm{cp}}\boldsymbol{a}_{u,d}$, which is dependent on the angular velocity ${}^{w}\boldsymbol{\omega}_{\boldsymbol{d}}$ as well as the vector ${}^{w}\boldsymbol{r}_{u,d}$:

$$
{}^{w}_{\mathrm{cp}}\boldsymbol{a}_{u,d} = {}^{w}\boldsymbol{\omega}_{\boldsymbol{d}} \times \left({}^{w}\boldsymbol{\omega}_{\boldsymbol{d}} \times {}^{w}\boldsymbol{r}_{u,d}\right) \tag{5.5}
$$

(c) And the gravity vector ${}^{w}\boldsymbol{g}$.

An accelerometer (u) senses all these effects at the same time, in its local coordinate system:

$$
{}^{u}\boldsymbol{a}_{u,d} = {}^{u}\mathbf{R}_{w} \cdot \left({}^{w}\boldsymbol{g} + {}^{w}_{\tan}\boldsymbol{a}_{u,d} + {}^{w}_{\mathrm{cp}}\boldsymbol{a}_{u,d}\right) \tag{5.6}
$$

The rotation matrix ${}^{u}\mathbf{R}_{w}$ between the static reference frame and the accelerometer, as well as the vector ${}^{w}\boldsymbol{r}_{u,d}$, are dependent on the unknown kinematics of the robot. Here, we exploit the fact that the tangential acceleration vector is co-linear with the angular motion vector.

5.3.2. Generation of a Sensory-Motor Map

The sensory motor map is a container for the explored weight values, acting as a lookup table for the mapping of tactile reactions (see Fig. 5.8). Each tile of the sensory motor map is explored in a pose ($p = [1,2,...,P]$), and features up to 3 sets of matrices, which are related to the 3 translational directions (${}^{u}\boldsymbol{e}_{z}$,${}^{u}\boldsymbol{e}_{y}$,${}^{u}\boldsymbol{e}_{z}$). The dimension of each matrix is defined by the available skin cells ($u = [1,2,...,U]$) and degrees of freedom ($d = [1,2,...,D]$), leading matrices of size ($U \times D$). Due to our current set of sensor modalities, we only use one matrix which is collinear to the surface normal (${}^{u}\boldsymbol{e}_{z}$), with the values ${}_{z}w_{u,d,p}$. Each tile also contains a vector of the robot pose that has been used for the exploration. This helps to recall the closest (e.g. quadratic distance) memorized pose when mapping tactile reactions into robot reactions.

5.3.2.1. Exploration Pattern

In order to evaluate the influence of each revolute degree of freedom (DoF) (d), on the translational motion of a skin cell (s), in a pose (p), the robot applies test pattern to one DoF after the other (see Fig. 5.9). For the translational components, only the tangential acceleration ${}^{u}_{\tan}\boldsymbol{a}_{u,d}$ can be utilized, since it is collinear with the local motion vector. The influence of the centripetal acceleration is minimized by keeping the angular velocity ω_d low. The rotated gravity vector is nearly constant, and thus subtract-able, when the DoF motion only covers a small angular range $\triangle\theta_d$. In order to maximize the tangential acceleration, the angular acceleration α_d has to be high. In order to maintain smooth accelerometer readings, it is necessary to control the angular velocity $\omega_d(t)$, the acceleration $\alpha_d(t)$ and the jerk $\zeta_d(t)$. It is desirable that the DoF returns to its initial position $\theta_d(0) = \theta_d(T)$ once the exploration pattern stops at time T. A velocity profile $\omega_d(t)$ that fulfills all the above requirement is a sine wave:

$$\theta_d(t) = \frac{A}{2\pi f}(1-\cos(2\pi f t)) \qquad \text{(position)} \tag{5.7}$$

$$\omega_d(t) = A\sin(2\pi f t) \qquad \text{(velocity)} \tag{5.8}$$

$$\alpha_d(t) = 2\pi f A\cos(2\pi f t) \qquad \text{(acceleration)} \tag{5.9}$$

$$\zeta_d(t) = -(2\pi f)^2 A\sin(2\pi f t) \qquad \text{(jerk)} \tag{5.10}$$

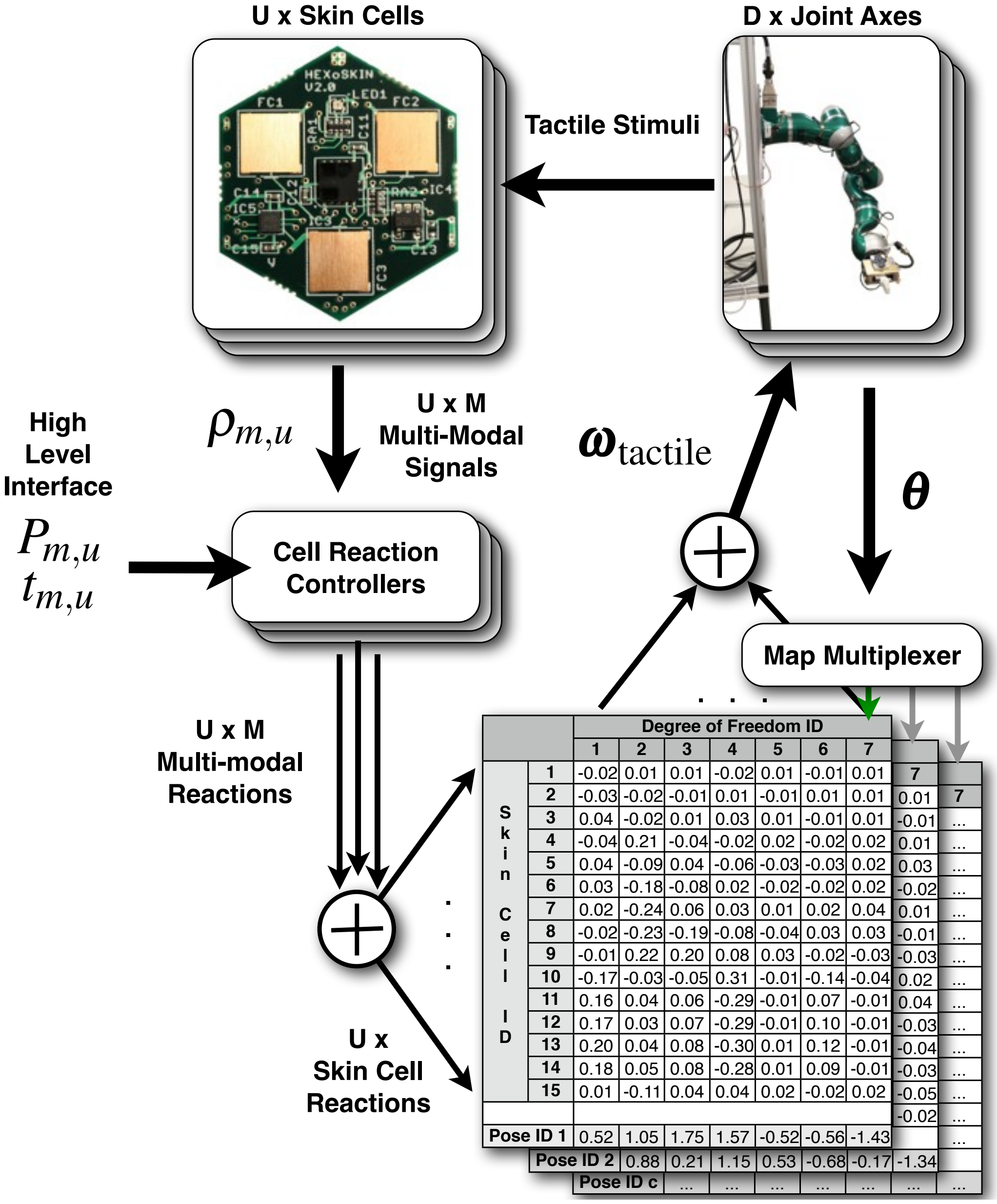

	Degree of Freedom ID						
	1	2	3	4	5	6	7
1	-0.02	0.01	0.01	-0.02	0.01	-0.01	0.01
2	-0.03	-0.02	-0.01	0.01	-0.01	0.01	0.01
3	0.04	-0.02	0.01	0.03	0.01	-0.01	0.01
4	-0.04	0.21	-0.04	-0.02	0.02	-0.02	0.02
5	0.04	-0.09	0.04	-0.06	-0.03	-0.03	0.02
6	0.03	-0.18	-0.08	0.02	-0.02	-0.02	0.02
7	0.02	-0.24	0.06	0.03	0.01	0.02	0.04
8	-0.02	-0.23	-0.19	-0.08	-0.04	0.03	0.03
9	-0.01	0.22	0.20	0.08	0.03	-0.02	-0.03
10	-0.17	-0.03	-0.05	0.31	-0.01	-0.14	-0.04
11	0.16	0.04	0.06	-0.29	-0.01	0.07	-0.01
12	0.17	0.03	0.07	-0.29	-0.01	0.10	-0.01
13	0.20	0.04	0.08	-0.30	0.01	0.12	-0.01
14	0.18	0.05	0.08	-0.28	0.01	0.09	-0.01
15	0.01	-0.11	0.04	0.04	0.02	-0.02	0.02
Pose ID 1	0.52	1.05	1.75	1.57	-0.52	-0.56	-1.43

FIGURE 5.8. The figure shows the control loop of the tactile reaction control system using a sensory-motor map – Tactile stimulations are sensed by the multi-modal skin cells. A low-level reaction controller evaluates the sensor input and provides an interface for a higher level controller. All reactions for a single skin cell are super imposed and then multiplied by the according row of the current sensory-motor map tile. A multiplexer automatically selects a tile of the sensory motor map with the minimal euclidean distance to the current pose of the robot. Finally, all generated velocity commands are super imposed and sent to the robot.

These equations help us to dimension the DoF exploration pattern. The selection of A is limited by the maximum DoF velocity and the tolerable influence of the centripetal acceleration. $2\pi f A$ has to be lower than the maximum DoF acceleration and below a value that shows undesired dynamic side effects, e.g. base motions. $\frac{A}{2\pi f}$ has to be small enough to be able to neglect

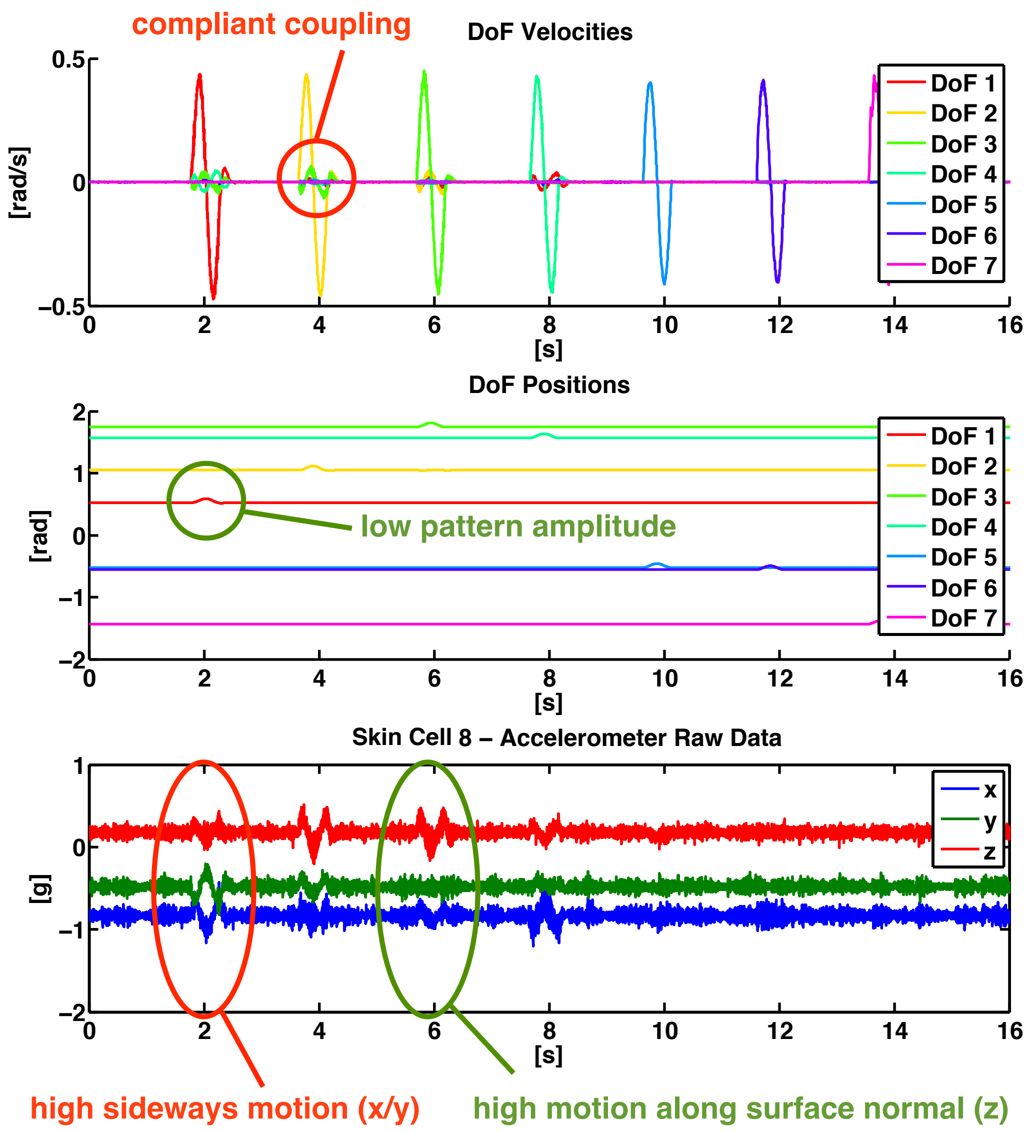

FIGURE 5.9. The figure shows data recorded during the sensory-motor map exploration of pose I, shown in Fig. 5.12, with a Kuka LWR robotic arm – The first graph shows the velocity pattern the robot performs on every revolute degree of freedom (DoF), one after the other. The highlighted area shows compliant coupling of DoFs due to the dynamics of the distributed mass. The second graph shows the angular DoF positions during exploration of pose I. The pattern amplitude is low and every DoF returns to its initial position. The last graph shows unfiltered accelerometer data from skin cell with ID 8. The highlighted accelerometer readings explain the generation of a high normal weight for DoF with ID 3, but a low one for DoF with ID 1. The readings show high z and low x/y activity for DoF with ID 3 and lower z and high x/y activity for DoF with ID 1. The surface normal of every skin cell is aligned with the z axis of the accelerometer.

the influence of the rotating gravity vector and the postural change of the robot. However $2\pi f A$, has to be sufficiently large that the measurement of the accelerometer ${}^{u}\boldsymbol{a}_{u,d}$ of skin cell (u) stands out from its intrinsic sensor noise. A windowing function $W(t)$ is necessary to cut the executed pattern in time $\omega_{\mathrm{ex},d}(t)$ and stop the robot at its initial posture:

$$\omega_{\mathrm{ex},d}(t) = W(t) \cdot \omega_d(t) \tag{5.11}$$

We currently utilize a rectangular function, cutting the oscillation after one period ($T = 1/f$). In general, we use the same empirical values across different robots: $A = 0.4\,\mathrm{rad\,s^{-1}}$, $f = 2\,\mathrm{Hz}$ and $T = 0.5\,\mathrm{s}$, e.g. tested on UR-5, HRP-2 and the KUKA LWR.

5.3.2.2. Weight Extraction

A distinct value quantifies the contribution of a DoF (d), to the desired motion of a skin cell (u) in the current robot pose (p). We first subtract the mean value from all accelerometer axes, in order to eliminate constant sensor offsets and the gravity vector ${}^{u}\boldsymbol{g}$. Then, we apply a digital low pass filter, with a bandwidth B larger than 10 times the pattern frequency f, to eliminate noise and vibrations. Finding the minimum and maximum, we calculate the amplitude for every axis (see Fig. 5.10), here along the z-axis ${}^{u}\boldsymbol{e}_{\mathrm{z}}$ of the accelerometer ${}_{\mathrm{z}}A_{u,d,p}$:

$${}_{\mathrm{z}}A_{u,d,p} = \max({}_{\mathrm{z}}a_{u,d,p}) - \min({}_{\mathrm{z}}a_{u,d,p}) \tag{5.12}$$

In order to discriminate if the desired motion is in-phase or anti-phase, we evaluate if half of the minimum or the maximum is located first in time (MATLAB terminology, see Fig. 5.10):

$$\begin{aligned} {}_{\mathrm{z}}s_{u,d,p} = \operatorname{sign}\Big(&\operatorname{find}\left({}_{\mathrm{z}}a_{u,d,p} == \max({}_{\mathrm{z}}a_{u,d,p})/2, \text{‘first’}\right) - \\ &\operatorname{find}\left({}_{\mathrm{z}}a_{u,d,p} == \min({}_{\mathrm{z}}a_{u,d,p})/2, \text{‘first’}\right)\Big) \end{aligned} \tag{5.13}$$

The weight ${}_{\mathrm{z}}w_{u,d,p}$, in the local skin cell surface normal direction ${}^{u}\boldsymbol{e}_{\mathrm{z}}$, is now computed as:

$${}_{\mathrm{z}}w_{u,d,p} = {}_{\mathrm{z}}s_{u,d,p} \cdot \frac{{}_{\mathrm{z}}A_{u,d,p}}{{}_{\mathrm{x}}A_{u,d,p} + {}_{\mathrm{y}}A_{u,d,p} + {}_{\mathrm{z}}A_{u,d,p}} \tag{5.14}$$

Weights have values between $[-1;1]$, being close to ± 1 if the DoF motion fully correlates with the desired translational motion, while being 0 in orthogonal cases. Weights in the shear directions ${}^{u}\boldsymbol{e}_{\mathrm{x}}$ and ${}^{u}\boldsymbol{e}_{\mathrm{y}}$, are calculated by replacing the numerator with ${}_{\mathrm{x}}A_{u,d,p}$ and ${}_{\mathrm{y}}A_{u,d,p}$.

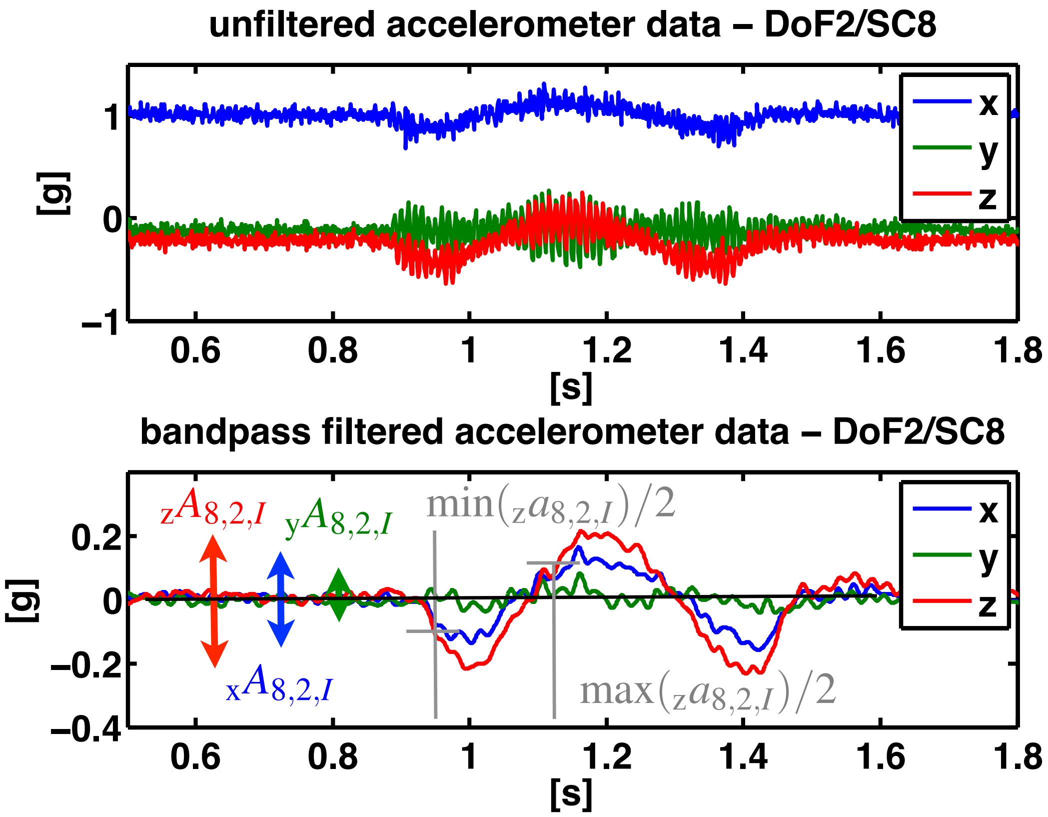

FIGURE 5.10. The figure shows the weight extraction from accelerometer data – The plots show unfiltered and bandpass-filtered data from skin cell with ID 8 on a pattern generated by the revolute degree of freedom with ID 2 in pose I (see Fig. 5.12). ${}_{\mathrm{x}}A_{8,2,I}$, ${}_{\mathrm{y}}A_{8,2,I}$ and ${}_{\mathrm{z}}A_{8,2,I}$ ideally constitute of the maximal amplitude of the tangential acceleration ${}_{\mathrm{tan}}\boldsymbol{a}_{8,2,I}$ (see Fig. 5.7). The first occurrence of the half of the minimum ($\min({}_{\mathrm{z}}a_{8,2,I})/2$) and the half of the maximum ($\max({}_{\mathrm{z}}a_{8,2,I})/2$) is a measure of the sign (out of phase/in phase) in between motion generation and sensation.

5.3.3. Mapping of Multi-Modal Tactile Stimuli

The sense of touch allows to implement meaningful direct reactions on multi-modal tactile stimulation – e.g. to avoid self- or environment collisions or to let users kinesthetically guide the robot. The advantage of instantiating one multi-modal reaction controller for every skin cell (u) is the scalability of this approach – tactile behavior is programmed for the smallest piece of skin and expanded to the whole robot surface. Since all cellular parameters ($t_{m,u}$, $P_{m,u}$) are accessible by the high level control system, spatial reactions are set up for a specific task. Here, we compute a proportional ($P_{m,u}$) gain motor reaction for every multi-modal (m) sensor value ($\rho_{m,u}$) of a skin cell (u) above a pre-defined threshold ($t_{m,u}$). All (M) multi-modal reactions on a cell are then accumulated and mapped to a desired cellular velocity reaction vector, via the sensory-motor map. Super-imposing the resulting velocity vectors from all (U)

skin cells, leads to a global tactile robot joint velocity reaction ($\boldsymbol{\omega}_{\text{tactile}}$):

$$\boldsymbol{\omega}_{\text{tactile}} = \sum_{u=1}^{U} \left(\boldsymbol{w}_{u,p} \cdot \sum_{m=1}^{M} (\rho_{m,u} > t_{m,u}) \cdot (\rho_{m,u} - t_{m,u}) \cdot P_{m,u} \right) \tag{5.15}$$

Modalities are be inhibited, promoted or inverted by setting their gain ($P_{m,u}$), please see examples in Sec. 6.2. The threshold ($t_{m,u}$) determines the activation level and is important to suppress sensor noise and offsets. In general, we act directly on persistent sensor data (e.g. force or proximity), omitting additional reaction delays and computational efforts. In case smoother reactions are desired, either the stimuli or the executed response can be extended/filtered in time, damping the whole system. With time singular tactile stimulations, e.g. the detection of impacts via vibrational cues like in [Mittendorfer and Cheng, 2011a], an elongated temporal response is inevitable.

5.3.4. Experiments

In this subsection, we show results from our initial experiments on a KUKA LWR arm. Further results can be seen in Chapter 6, where the sensory-motor map is used for tactile kinesthetic guidance and a reactive grasping approach on a full-sized humanoid.

5.3.4.1. Setup

In order to validate our approach, we distributed 15 of our skin cells (version 1.1, refer to Sec. A.4) on a KUKA light weight robotic arm. Fig. 5.11 illustrates the distribution of skin cells and revolute degrees of freedom (DoF) along the serial kinematic chain. The generator for the sinusoidal DoF velocity pattern was set to an amplitude of $A = 0.4\,\text{rad}\,\text{s}^{-1}$ with a frequency of $f = 2\,\text{Hz}$ and a length of a single wave of 500 ms, cut by a rectangular window function. The acceleration recording was started 500 ms before a DoF pattern was launched and stopped 500 ms after the pattern has finished. We then detected touch by applying a threshold of 0.3 on the proximity sensor raw data. This represents a human hand being closer than 2 mm with skin cell version 1.1 (refer to Sec. A.4). The exited modality reaction strength was set to $0.4\,\text{rad}\,\text{s}^{-1}$ with a binary controller.

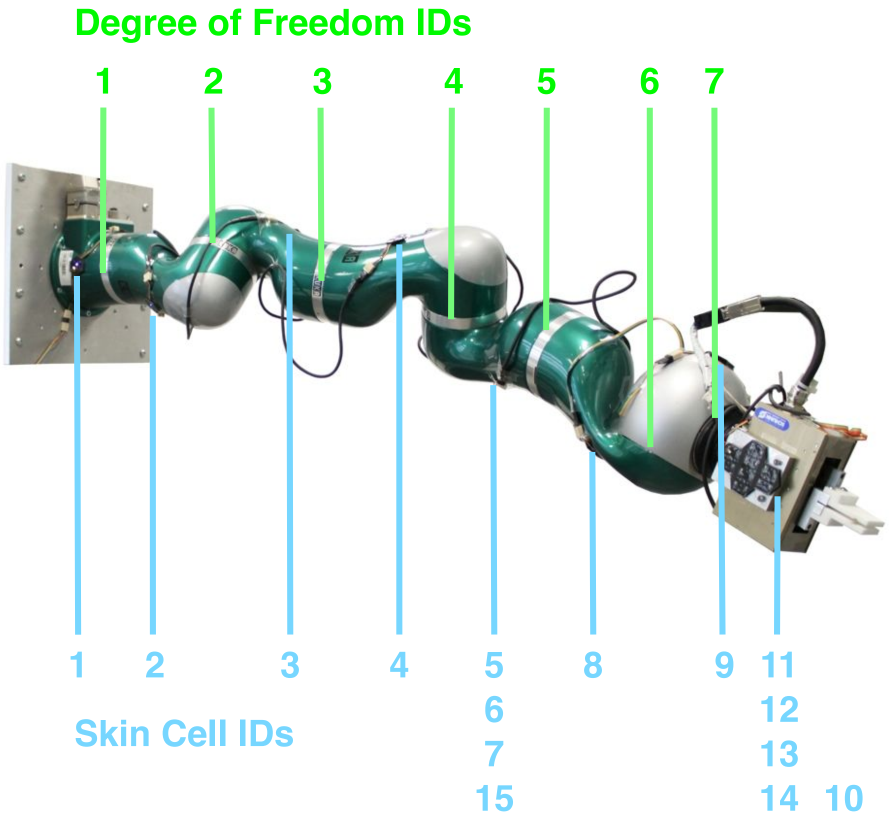

FIGURE 5.11. The figure shows the experimental setup for testing the acquisition of the sensory-motor map. Multiple skin cells (blue) and revolute degrees of freedom (green) have been distributed along the entire serial kinematic robotic chain.

5.3.4.2. Results

Fig. 5.12 shows two out of many poses we tested. The skin cells with ID 11-14 always show similar weights, as they are located closely and exhibit the same orientation. Skin cell ID 10 always shows similar amplitudes, compared to ID 11-14, but with opposite sign. This is correct as the skin cell has been mounted on the opposite side of the box like gripper. Touching the robot at skin cell with ID 11-14 makes the robot evade the contact along the surface normal (${}^{u}\boldsymbol{e}_{z}$), the more skin cells are simultaneously touched, the stronger is the reaction. This is due to the super imposing behavior of the reaction controller. Touching two opposite cells, e.g. skin cells with ID 10 and 11, the reaction is nearly canceled. There is minor motion left, due to inherent sensor noise, small alignment mismatches and coupled motions during exploration. Changing from pose I to II, the weights of DoF with ID 4 remain similar, while in the second pose the weights of DoF with ID 2 gain a significant influence for skin cells with ID 11-14. A touch reaction in pose II is also stronger than in pose I. This shows the demand to normalize reactions and the influence postural changes have on the sensory motor map. Our approach can

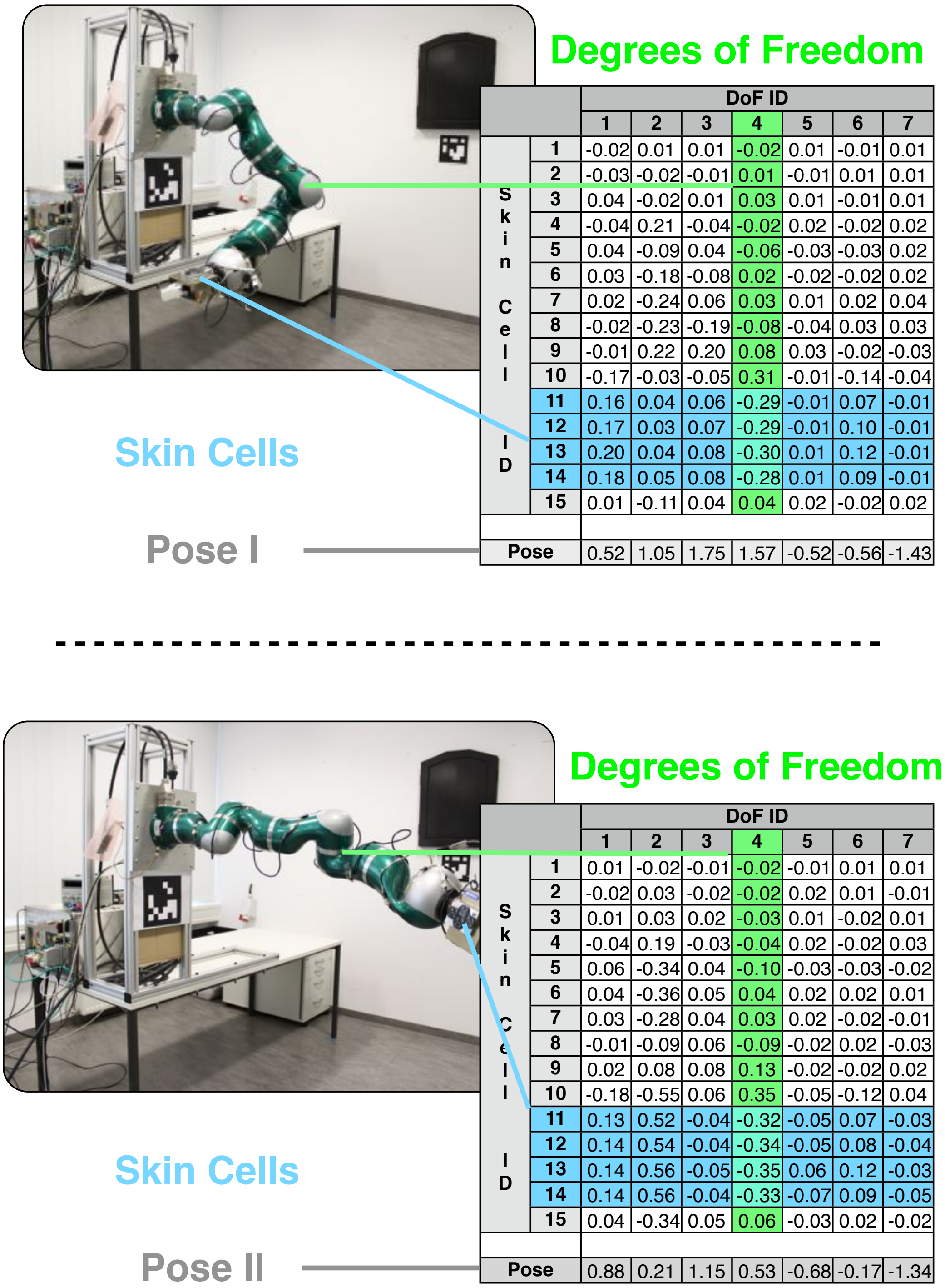

	DoF ID						
Skin Cell ID	1	2	3	4	5	6	7
1	-0.02	0.01	0.01	-0.02	0.01	-0.01	0.01
2	-0.03	-0.02	-0.01	0.01	-0.01	0.01	0.01
3	0.04	-0.02	0.01	0.03	0.01	-0.01	0.01
4	-0.04	0.21	-0.04	-0.02	0.02	-0.02	0.02
5	0.04	-0.09	0.04	-0.06	-0.03	-0.03	0.02
6	0.03	-0.18	-0.08	0.02	-0.02	-0.02	0.02
7	0.02	-0.24	0.06	0.03	0.01	0.02	0.04
8	-0.02	-0.23	-0.19	-0.08	-0.04	0.03	0.03
9	-0.01	0.22	0.20	0.08	0.03	-0.02	-0.03
10	-0.17	-0.03	-0.05	0.31	-0.01	-0.14	-0.04
11	0.16	0.04	0.06	-0.29	-0.01	0.07	-0.01
12	0.17	0.03	0.07	-0.29	-0.01	0.10	-0.01
13	0.20	0.04	0.08	-0.30	0.01	0.12	-0.01
14	0.18	0.05	0.08	-0.28	0.01	0.09	-0.01
15	0.01	-0.11	0.04	0.04	0.02	-0.02	0.02
Pose	0.52	1.05	1.75	1.57	-0.52	-0.56	-1.43

	DoF ID						
Skin Cell ID	1	2	3	4	5	6	7
1	0.01	-0.02	-0.01	-0.02	-0.01	0.01	0.01
2	-0.02	0.03	-0.02	-0.02	0.02	0.01	-0.01
3	0.01	0.03	0.02	-0.03	0.01	-0.02	0.01
4	-0.04	0.19	-0.03	-0.04	0.02	-0.02	0.03
5	0.06	-0.34	0.04	-0.10	-0.03	-0.03	-0.02
6	0.04	-0.36	0.05	0.04	0.02	0.02	0.01
7	0.03	-0.28	0.04	0.03	0.02	-0.02	-0.01
8	-0.01	-0.09	0.06	-0.09	-0.02	0.02	-0.03
9	0.02	0.08	0.08	0.13	-0.02	-0.02	0.02
10	-0.18	-0.55	0.06	0.35	-0.05	-0.12	0.04
11	0.13	0.52	-0.04	-0.32	-0.05	0.07	-0.03
12	0.14	0.54	-0.04	-0.34	-0.05	0.08	-0.04
13	0.14	0.56	-0.05	-0.35	0.06	0.12	-0.03
14	0.14	0.56	-0.04	-0.33	-0.07	0.09	-0.05
15	0.04	-0.34	0.05	0.06	-0.03	0.02	-0.02
Pose	0.88	0.21	1.15	0.53	-0.68	-0.17	-1.34

FIGURE 5.12. The figure shows two sensory-motor map tiles for two different poses of a Kuka LWR arm equipped with 15 skin cells. Here, we only show weight values for the mapping of reactions along the local surface normal (${}^{u}\boldsymbol{e}_z$) of each skin cell (u).

also be applied to motion constrained skin cell locations, e.g. close to the kinematic reference. An example is skin cell ID 4, which is located on the 4th body part with only 3 DoFs before the robot base. Our algorithm found a high weight for DoF ID 2, which we verified by touching the skin cell. As our approach is singularity free, it does not exhibit fast motions that scare people.

5.4. Automatic Kinematic Modeling of Manipulators

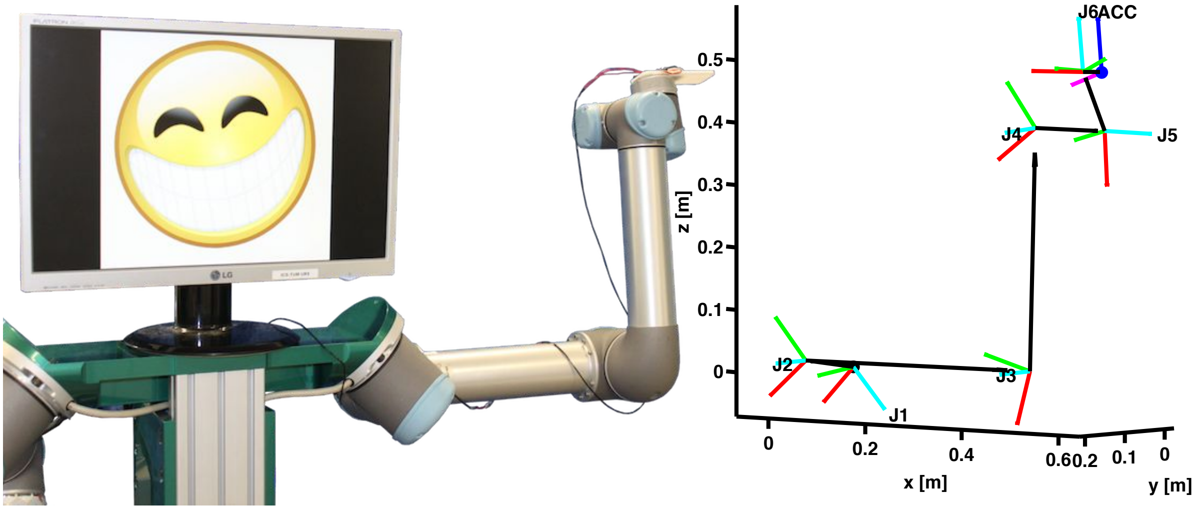

FIGURE 5.13. The figure shows the result of our method, acquiring the kinematic model of the left arm of TOM (Tactile Omni-directional Mobile Manipulator), with an accelerometer mounted on the end effector frame.

In this section, we present an approach to automatically acquire the kinematic model of a robot equipped with a multi-modal, modular artificial skin[3]. Here, we use the tri-axial accelerometer built into every cell of our artificial skin, along with a set of static and dynamic open-loop test motions performed by the robot. With a circle point analysis we extract the relevant vectors to assemble a forward kinematic model. In comparison to existing approaches, our method builds and calibrates a kinematic model with minimal motions around the initial workspace, does not require any external metrology system and works with low-grade motion sensors. A similar kinematic estimation approach by Canepa *et al.* [Canepa *et al.*, 1994] was not able to handle our low-grade accelerometer and safe minimal motions. We demonstrate the robustness of our approach by estimating the kinematic parameters of an industrial Universal Robots' UR-5 robotic arm mounted on an inertial dual arm platform (see Fig. 5.13).

---

[3] The work in this section has been published in [Mittendorfer *et al.*, 2014b].

5.4.1. Robotic System

5.4.1.1. Robot Requirements

In order to cover a broad hardware spectrum, minimum requirements are needed from the robot platform. The robot has to accept (emulated) velocity control signals and has to return position feedback that is differentiable (2 times) to joint accelerations. In this first stage, our approach only handles revolute joints, which is the most common joint used for robots (i.e. humanoids). At least one reference body frame, like the torso of a humanoid or base of a mobile manipulator, has to remain stationary during the whole process.

5.4.1.2. Accelerometer Calibration

The utilized BMA250 tri-axial accelerometer is a very small-scale (2x2x1mm) and low-cost sensor. This has benefits, e.g. a close to common center for all axes, but also drawbacks. Although calibrated by the manufacturer, the accelerometer shows significant offsets and some gain differences. The given ±0.08g offset on each axis contributes to a vector estimation misalignment of up to ±5°. We developed a quick calibration routine that estimates all three gains (${}^{u}\boldsymbol{G}$) and offsets (${}^{u}\boldsymbol{O}$) by forcing the norm of gravity samples (${}^{u}\boldsymbol{g}_p$) in (P=6) complementary poses (p) on the unit sphere:

$$[{}^{u}\boldsymbol{G}, {}^{u}\boldsymbol{O}] = \min_{{}^{u}\boldsymbol{G}, {}^{u}\boldsymbol{O}} \sum_{p=1}^{P} \left(\|{}^{u}\boldsymbol{g}_p\| - 1 \right)^2 \tag{5.16}$$

In comparison to other approaches, our method does not need exact alignments or special calibration equipment. Performing two runs after each other, the offset corrections for each axis in the second run drop to $\leq \pm 0.001$g.

5.4.2. Accelerometer Circle Point Analysis

In the following, we show how to extract the circle point vectors (${}^{u}\boldsymbol{j}_d$, ${}^{u}\boldsymbol{r}_{u,d}$) for each joint (d), from accelerometer (u) measurements (${}^{u}\boldsymbol{a}_{u,d}[n]$) during quasi-static and dynamic test motions performed on one joint axis (d) after the other. For an angular motion around a joint axis (${}^{u}\boldsymbol{j}_d$) (see Fig. 5.14) the accelerometer is subject to the sum of three accelerations:

$${}^{u}\boldsymbol{a}_{u,d}[n] = {}^{u}_{\mathrm{tan}}\boldsymbol{a}_{u,d}[n] + {}^{u}_{\mathrm{cp}}\boldsymbol{a}_{u,d}[n] + {}^{u}\boldsymbol{g}_{u,d}[n] \tag{5.17}$$

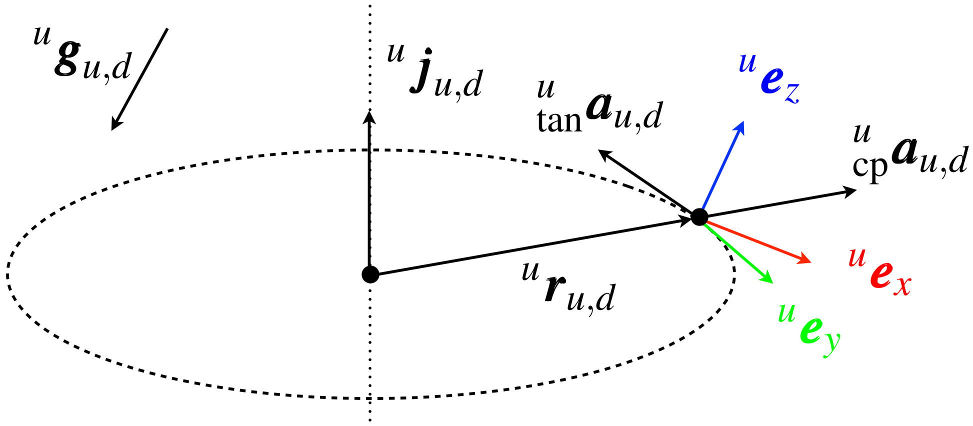

FIGURE 5.14. The figure shows the circle point vectors (${}^{u}\boldsymbol{j}_d$ and ${}^{u}\boldsymbol{r}_{u,d}$) along with the acceleration components (${}^{u}\boldsymbol{g}$,${}^{u}_{\tan}\boldsymbol{a}_{u,d}$,${}^{u}_{\mathrm{cp}}\boldsymbol{a}_{u,d}$) an accelerometer (u) is subject to on a revolute joint axis (d) motion.

All components depend on one of the joint variables (θ_d, $\omega_d = \dot{\theta}_d$, $\alpha_d = \dot{\omega}_d$) and the circle point vectors (${}^{u}\boldsymbol{j}_d$, ${}^{u}\boldsymbol{r}_{u,d}$):

$$ {}^{u}\boldsymbol{g}_{u,d}[n] = \mathrm{vrrotvec2mat}\left({}^{u}\boldsymbol{j}_d, \theta_d[n] - \theta_d[0]\right) \cdot {}^{u}\boldsymbol{g}_{u,d}[0] \tag{5.18} $$

$$ {}^{u}_{\tan}\boldsymbol{a}_{u,d}[n] = \alpha_d[n] \cdot \|{}^{u}\boldsymbol{r}_{u,d}\| \cdot \left({}^{u}\boldsymbol{j}_d \times \frac{{}^{u}\boldsymbol{r}_{u,d}}{\|{}^{u}\boldsymbol{r}_{u,d}\|}\right) \tag{5.19} $$

$$ {}^{u}_{\mathrm{cp}}\boldsymbol{a}_{u,d}[n] = \omega_d[n]^2 \cdot \|{}^{u}\boldsymbol{r}_{u,d}\| \cdot \left({}^{u}\boldsymbol{j}_d \times \left({}^{u}\boldsymbol{j}_d \times \frac{{}^{u}\boldsymbol{r}_{u,d}}{\|{}^{u}\boldsymbol{r}_{u,d}\|}\right)\right) \tag{5.20} $$

In the following we utilize three features: 1) the two dynamic components, the tangential (${}^{u}_{\tan}\boldsymbol{a}_{u,d}[n]$) and centripetal (${}^{u}_{\mathrm{cp}}\boldsymbol{a}_{u,d}[n]$) acceleration, which are orthogonal to each other; 2) the directions of the dynamic components are stationary in accelerometer (u) coordinates; 3) each component in Equ. 5.18 depends on another joint variable (θ_d, ω_d, α_d). This enables us to design specific motion patterns and algorithms for each circle point vector.

5.4.2.1. Exploration Motions

Similar to [Canepa *et al.*, 1994], we execute static and dynamic motions on one revolute joint axis (d) after the other. These designed motions are:

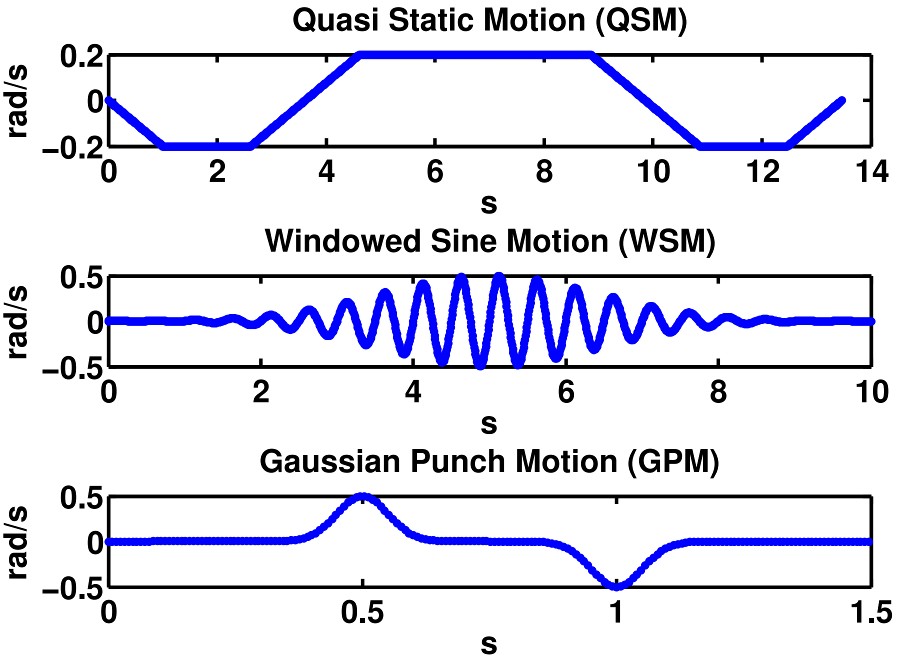

FIGURE 5.15. The figure shows the three special test motions we utilize for the CPA.

The quasi-static motion (QSM) is a three step trapezoid velocity function (see Fig. 5.15). The joint travels both directions and stops at the initial position ($\theta_d[0]$). The QSM is designed to quickly generate gravity vector measurements, while minimizing other motion influences. We commonly use a trapezoid function with the following heuristic parameters: $max(|\omega_d|) = 0.2\,\mathrm{rad\,s^{-1}}$, $\triangle\theta_d \leq \pm 0.53\,\mathrm{rad}$ and $T_{\mathrm{ramp}} = 1\,\mathrm{s}$.

The windowed sine motion (WSM) is a sinusoidal velocity control function with a Gaussian window function (see Fig. 5.15):

$$\omega_{d,\mathrm{WSM}}(t) = e^{-\frac{(t-T_m)^2}{2T_\sigma{}^2}} \left(A \cdot \sin\left(2\pi f t\right)\right) \tag{5.21}$$

The WSM is designed to repeatedly generate high joint accelerations with a varying amplitude, while minimizing position changes, joint velocity and jerk. This is necessary to robustly estimate the direction of the tangential acceleration vector. We commonly use the following heuristic values: $A = 0.5\,\mathrm{rad\,s^{-1}}$, $f = 2\,\mathrm{Hz}$, $T_m = 2.5\,\mathrm{s}$, $T_\sigma = 0.7\,\mathrm{s}$.

The Gaussian punch motion (GPM) is a velocity function, combining a positive and a negative Gaussian pulse (see Fig. 5.15):

$$\omega_{d,\mathrm{GPM}}(t) = A \cdot \left(e^{-\frac{(t-T_m)^2}{2T_\sigma{}^2}} - e^{-\frac{(t-2T_m)^2}{2T_\sigma{}^2}} \right) \tag{5.22}$$

The GPM generates a smooth, traceable polarity in joint accelerations, while minimizing position changes, joint velocity and jerk. This is necessary to correct the sign of the tangential acceleration vector, which can not be extracted from the symmetric envelope of the WSM. We commonly use the following heuristic values: $A = 0.5\,\mathrm{rad\,s^{-1}}$, $T_m = 0.5\,\mathrm{s}$, $T_\sigma = 0.05\,\mathrm{s}$
In general, at least a quasi-static and a dynamic motion primitive are required to separate the static and dynamic measurements from the accelerometer (refer to Equ. 5.17). The further separation of the dynamic primitive into the WSM and GPM supports the robust estimation of the direction and polarity of the tangential motion vector.

5.4.2.2. Joint Axis Unit Vector Estimation

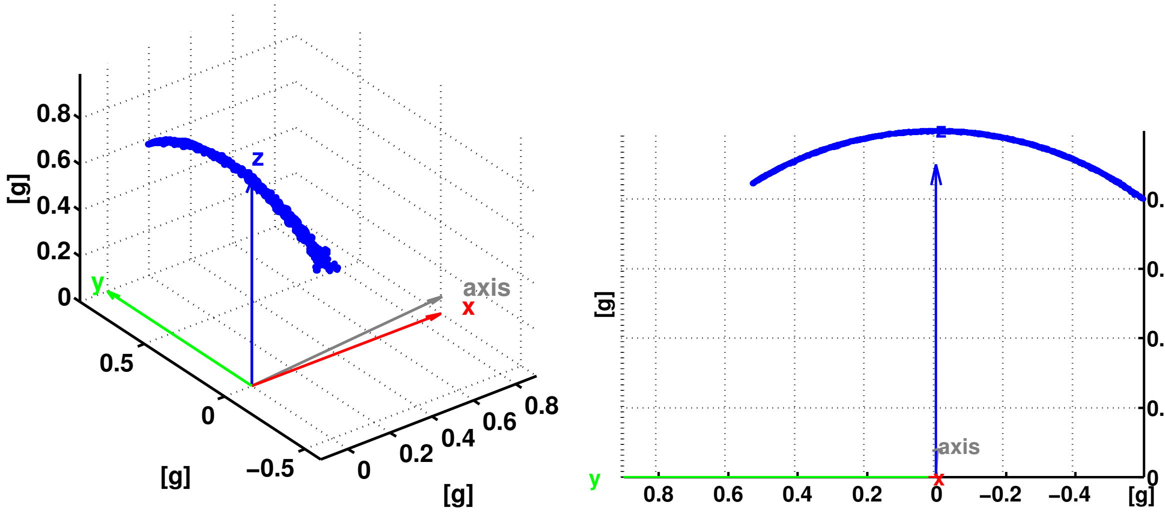

(A) 3D view (B) y/z plane view

FIGURE 5.16. The figure shows accelerometer samples for the joint axis estimation of the second UR-5 joint, sampled during QSM, along with the estimated joint axis.

The joint axis unit vector (${}^{u}\boldsymbol{j}_d$, $\|{}^{u}\boldsymbol{j}_d\| = 1$) are estimated in accelerometer coordinates (u) from the gravity vector samples recorded during QSM (see Fig. 5.16). We first tried to reproduce the result by Canepa *et al.* [Canepa *et al.*, 1994], enforcing a constant dot product between the joint axis and the gravity samples. Alas this approach was not successful since

Algorithm 5.2 Estimation of joint axis vector

```
for $d = 1$ to $D$ do
    Sample ${}^{u}\boldsymbol{a}_{u,d}[n]$, $\theta_d[n]$ while QSM on joint (d)
    Solve ${}^{u}\boldsymbol{j}_d = \min_{{}^{u}\boldsymbol{j}_d}(e_{u,d})$
```

it is not explained how to reliably maintain the unknown value of the constant dot product. Sensor noise and a small angular motion prevent the accurate estimation of the dot product, especially close to the singular case where the joint axis is collinear with gravity. We finally solved the estimation problem minimizing an enhanced three component error function towards the unknown joint axis:

$$ {}^{u}\boldsymbol{j}_d = \min_{{}^{u}\boldsymbol{j}_d}\left(\sum_{i=1}^{3}\left(W_i \cdot e_{u,d,i}\right)\right) \tag{5.23} $$

The first error component is a high priority (e.g. $W_1 = 1000$) embedded constraint and enforces the unit length of the axis:

$$ e_{u,d,1} = (\|{}^{u}\boldsymbol{j}_d\| - 1)^2 \tag{5.24} $$

The second mid priority (e.g. $W_2 = 10$) error component minimizes the variance of the dot product for all (N) samples:

$$ e_{u,d,2} = \sum_{n=1}^{N}\left({}^{u}\boldsymbol{g}_{u,d}[n]^T \cdot {}^{u}\boldsymbol{j}_d - \frac{1}{N}\sum_{n=1}^{N}{}^{u}\boldsymbol{g}_{u,d}[n]^T \cdot {}^{u}\boldsymbol{j}_d\right)^2 \tag{5.25} $$

The third soft (e.g. $W_3 = 1$) error is the squared length of the difference between the measured gravity samples and vectors predicted by an angle axis rotation (vrrotvec2mat$(axis, angle)$) from the initial gravity vector (${}^{u}\boldsymbol{g}_{u,d}[0]$) and joint position ($\theta_d[0]$):

$$ e_{u,d,3} = \sum_{n=1}^{N}\|\text{vrrotvec2mat}\left({}^{u}\boldsymbol{j}_d, \theta_d[n] - \theta_d[0]\right) \cdot {}^{u}\boldsymbol{g}_{u,d}[0] - {}^{u}\boldsymbol{g}_{u,d}[n]\|^2 \tag{5.26} $$

This last component serves as a stabilization term around singular cases and provides correct axis polarity in non-singular cases. The global minimization problem is solved with a derivative free local minimizer (GNU Scientific Library, Nelder and Mead Simplex, nmsimplex2rand) and multiple starting points on the unit sphere (e.g. $\pm\boldsymbol{e}_\text{x}, \pm\boldsymbol{e}_\text{y}, \pm\boldsymbol{e}_\text{z}$). We commonly use the following heuristic parameters: an initial step size of 0.01 and a termination size of 1e-9 or 2000 iterations. Gravity samples are normalized and Gaussian filtered (size=11, sigma=2.83) before utilization.

5.4.2.3. Tangential Unit Vector Estimation

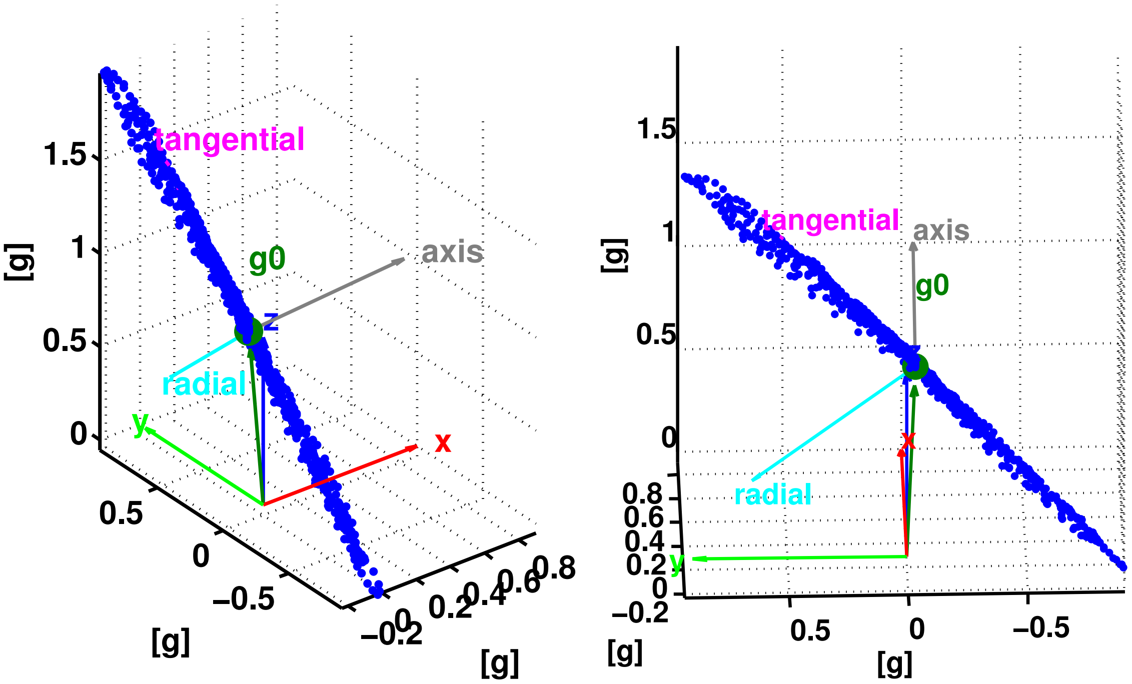

FIGURE 5.17. The figure shows an example of the filtered raw data for the tangential unit vector estimation of the 2nd UR-5 joint, sampled during WSM, along with the estimated tangential, joint and radial unit vector axes and gravity.

The direction of the tangential unit vector (${}^{u}\boldsymbol{n}_{u,d}$) is estimated in accelerometer coordinates (u) from the dynamic acceleration samples recorded during WSM, while its polarity is corrected by the samples recorded during GPM. In order to maintain the dynamic acceleration components (${}^{u}_{\text{dyn}}\boldsymbol{a}_{u,d}[n]$), we first subtract gravity (see Equ. 5.18) from the raw data:

$${}^{u}_{\text{dyn}}\boldsymbol{a}_{u,d}[n] = {}^{u}\boldsymbol{a}_{u,d}[n] - {}^{u}\boldsymbol{g}_{u,d}[n] \tag{5.27}$$

Algorithm 5.3 Estimation of tangential vector

```
for $d = 1$ to $D$ do
    Sample ${}^{u}\boldsymbol{a}_{u,d}[n]$, $\theta_d[n]$ while WSM on joint (d)
    Subtract gravity from samples $\Rightarrow {}^{u}_{\text{dyn}}\boldsymbol{a}_{u,d}[n]$
    Subtract accelerations along joint axis $\Rightarrow {}^{u}_{\text{dyn}}\hat{\boldsymbol{a}}_{u,d}[n]$
    Assemble sample matrix $\Rightarrow {}^{u}\mathbf{A}_d$
    SVD of sample matrix $\Rightarrow [{}^{u}\mathbf{U}_d, {}^{u}\mathbf{S}_d, {}^{u}\mathbf{V}_d]$
    Extract largest eigenvector $\Rightarrow {}^{u}\boldsymbol{n}_{u,d}$
    Correct sign of tangential unit vector with GPM $\Rightarrow {}^{u}\hat{\boldsymbol{n}}_{u,d}$
```

Next, we subtract uncorrelated dynamic motions along the known joint axis (${}^{u}\boldsymbol{j}_d$):

$$
{}^{u}_{\text{dyn}}\hat{\boldsymbol{a}}_{u,d}[n] = {}^{u}_{\text{dyn}}\boldsymbol{a}_{u,d}[n] - \left(({}^{u}\boldsymbol{j}_d)^T \cdot {}^{u}_{\text{dyn}}\boldsymbol{a}_{u,d}[n]\right) \cdot {}^{u}\boldsymbol{j}_d \tag{5.28}
$$

We also subtract the remaining mean value in order to prevent that an incomplete gravity subtraction interferes with the following singular value decomposition:

$$
{}^{u}_{\text{dyn}}\tilde{\boldsymbol{a}}_{u,d}[n] = {}^{u}_{\text{dyn}}\hat{\boldsymbol{a}}_{u,d}[n] - \frac{1}{N}\sum_{n=1}^{N} {}^{u}_{\text{dyn}}\hat{\boldsymbol{a}}_{u,d}[n] \tag{5.29}
$$

We then assemble a matrix (${}^{u}\mathbf{A}_{u,d}$) from all samples:

$$
{}^{u}\mathbf{A}_{u,d} = \left[{}^{u}_{\text{dyn}}\tilde{\boldsymbol{a}}_{u,d}[1], \ldots, {}^{u}_{\text{dyn}}\tilde{\boldsymbol{a}}_{u,d}[N]\right]^T \tag{5.30}
$$

And perform a singular value decomposition (SVD) on this sample matrix :

$$
[{}^{u}\mathbf{U}_{u,d}, {}^{u}\mathbf{S}_{u,d}, {}^{u}\mathbf{V}_{u,d}] = \text{svd}({}^{u}\mathbf{A}_{u,d}) \tag{5.31}
$$

For a sinusoidal velocity control function the relation between the maximum amplitude of the tangential and centripetal acceleration is given by the parameters (f and A):

$$
\frac{\max({}_{\tan}a_{u,d})}{\max({}_{\text{cp}}a_{u,d})} = \frac{\max(\alpha_d)}{\max(\omega_d^2)} = \frac{2\pi f}{A} \tag{5.32}
$$

Due to the orthogonality of the tangential and centripetal acceleration, and the dominance in case of the chosen sinusoidal parameters ($A = 0.5\,\text{rad}\,\text{s}^{-1}$, $f = 2\,\text{Hz}$), the tangential unit vector is the largest/first eigenvector of the SVD (see Fig. 5.17):

$$
{}^{u}\boldsymbol{n}_{u,d} = [V_{11} V_{21} V_{31}]^T \tag{5.33}
$$

Due to the line symmetry of the Gaussian window function, the polarity of the tangential vector can not be extracted from the WSM. Therefore we have developed the point symmetric GPM. Again, we subtract the gravity vectors from the raw accelerometer data. We then calculate the tangential amplitude by multiplying the dynamic acceleration samples with the previously extracted tangential vector:

$$_{\tan}a_{u,d}[n] = ({}^{u}\boldsymbol{n}_{u,d})^{T} \cdot {}^{u}_{\text{dyn}}\boldsymbol{a}_{u,d}[n] \tag{5.34}$$

This tangential amplitude ($_{\tan}a_{u,d}[n]$) is then correlated with the joint acceleration ($\alpha_d[n]$) to determine the phase:

$${}^{u}C_d[m] = \sum_{n=-\infty}^{+\infty} {}_{\tan}a_{u,d}[n] \cdot \alpha_d[n+m] \tag{5.35}$$

In case the vector is anti-phase, we correct its polarity (${}^{u}\hat{\boldsymbol{n}}_{u,d}$):

$${}^{u}\hat{\boldsymbol{n}}_{u,d} = \text{copysign}(1, |\max({}^{u}C_d)| - |\min({}^{u}C_d)|) \cdot {}^{u}\boldsymbol{n}_{u,d} \tag{5.36}$$

5.4.2.4. Radial Distance Estimation

The radial distance ($r_{u,d}$) is estimated from the linear relation:

$$_{\tan}a_{u,d}[n] = \alpha_d[n] \cdot r_{u,d} \tag{5.37}$$

Here, we apply a least squares linear fitting on the data set recorded during WSM:

$$r_{u,d} = \min_{r_{u,d}} \sum_{n=1}^{N} \left({}_{\tan}a_{u,d}[n] - (r_{u,d} \cdot \alpha_d[n])\right)^2 \tag{5.38}$$

It is important that the sensor samples in Equ. 5.37 (but also Equ. 5.27) have the similar sampling rates and do not exhibit mutual delays. Signals with different sample rates are up/down sampled to a common frequency. Delays are e.g. introduced by signal filters (up sampling, noise reduction, differentiation), the utilization of a non real-time OS or communication delays. We compensate delays (${}^{u}\triangle_d$) detected with a correlation of the off-line samples:

$${}^{u}\triangle_d = \max_{{}^{u}\triangle_d} \sum_{n=-\infty}^{+\infty} \left(({}_{\tan}a_{u,d}[n]) \cdot \alpha_d[n + {}^{u}\triangle_d]\right) \tag{5.39}$$

Algorithm 5.4 Estimation of radial distance

```
for $d = 1$ to $D$ do
    Sample ${}^{u}\boldsymbol{a}_{u,d}[n]$, $\theta_d[n]$, $\alpha_d[n]$ while WSM on joint $d$
    Subtract gravity from samples $\Rightarrow {}^{u}_{\mathrm{dyn}}\boldsymbol{a}_{u,d}[n]$
    Calculate tangential amplitude $\Rightarrow {}_{\tan}a_{u,d}[n]$
    Compensate mutual delays between $\alpha_d[n]$ and ${}_{\tan}a_{u,d}[n]$
    Fit least squares linear model $\Rightarrow r_{u,d}$
```

5.4.2.5. Calculation of Radial Vector

Finally, we compute the radial vector (${}^{u}\boldsymbol{r}_{u,d}$), pointing from the closest point on the joint axis to the accelerometer origin:

$$ {}^{u}\boldsymbol{r}_{u,d} = r_{u,d} \cdot \left({}^{u}\hat{\boldsymbol{n}}_{u,d} \times {}^{u}\boldsymbol{j}_{u,d} \right) \tag{5.40} $$

5.4.2.6. Constraints

Our CPA algorithm has two important constraints: 1) joint axes may not be aligned with gravity in order to discriminate their polarity; 2) a minimal radial distance is required to estimate the tangential vector. The first constraint only affects the first axis, as subsequent joints axes are automatically put into a different pose. For the first axis, either the base frame has to change orientation or an additional method (e.g. visual observation) has to help with the binary decision. We are able to handle the second constraint in the common case that a whole skin patch is mounted on the end-effector. If a too small radial distance is detected, another skin cell can be chosen for the estimation.

5.4.3. Kinematic Model Extraction

In this subsection, we extract a kinematic model from the previously estimated circle point vectors and a known sequence of joints (see Fig. 5.18). Two algorithmically complex methods to extract minimal Denavit-Hartenberg (DH) parameters from a CPA are presented in [Mooring *et al.*, 1991]. In our case, we apply an algorithm that is simple and robust, and intrinsically deals with the last transformation to the free accelerometer coordinate frame. The algorithm first estimates all accelerometer-2-joint transformations from the circle point vectors. It then assembles the forward kinematic model using those transformations and revolute joint models.

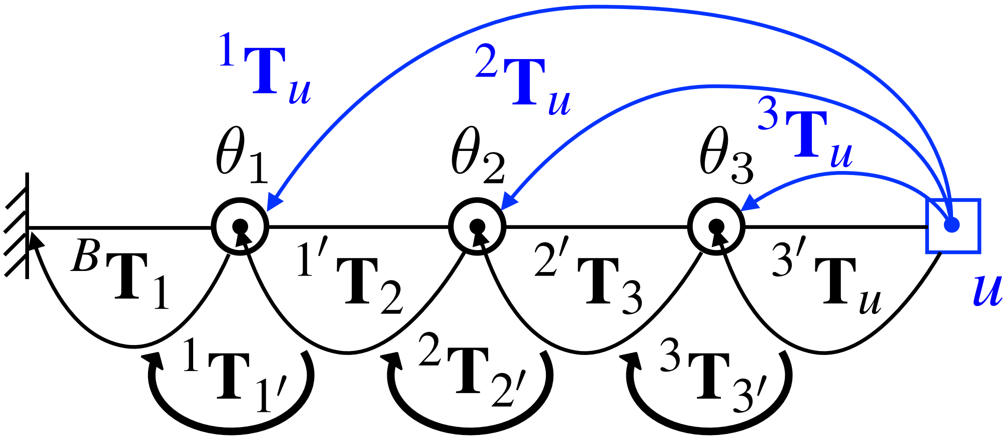

FIGURE 5.18. The figure shows the transformations of an exemplary kinematic chain model for $D = 3$ single DoF joints. The accelerometer-2-joint transformations (blue) are estimated by the CPA. The joint-2-joint transformations are then calculated in the initial pose and multiplied with the joint rotation transformations to form a serial kinematic chain.

5.4.3.1. Accelerometer-2-Joint Transformations

In a first step, we calculate the homogeneous transformation (${}^{d}\mathbf{T}_u$) from the accelerometer coordinate frame (u) to each newly defined joint coordinate frame (d). Similar to DH coordinates we align the joint axis (${}^{u}\boldsymbol{j}_d$) with the z-axis ($\boldsymbol{e}_\mathrm{z}$). Furthermore, we define that the x-axis is aligned with the radial vector (${}^{u}\boldsymbol{r}_{u,d}$) and the joint origin is located at the intersection of the joint axis and the radial vector. The rotation matrix between both coordinate systems is calculated with a Procrustes algorithm[4]. The two related vector sets ($\mathbf{N}$ and $\mathbf{M}_d$) that need to be mapped are the corresponding axes of the coordinate frames (u and d):

$$\mathbf{N} = [\boldsymbol{e}_\mathrm{x}, \boldsymbol{e}_\mathrm{z}]; \qquad \mathbf{M}_d = [\frac{{}^{u}\boldsymbol{r}_{u,d}}{||{}^{u}\boldsymbol{r}_{u,d}||}, {}^{u}\boldsymbol{j}_d]; \tag{5.41a}$$

The Procrustes algorithm solves this mapping using a SVD (also refer to Sec. 4.2.3):

$$[\mathbf{U}_d \,,\, \boldsymbol{\Sigma}_d \,,\, \mathbf{V}_d] = \mathrm{svd}\left(\mathbf{N} \cdot \mathbf{M}_d^T\right) \tag{5.41b}$$

$${}^{d}\mathbf{R}_u = \mathbf{U}_d \cdot \hat{\boldsymbol{\Sigma}}_d \cdot \mathbf{V}_d^T \tag{5.41c}$$

---

[4] P. H. Schonemann, “A generalized solution of the orthogonal Procrustes problem”, Psychometrika 31, pp. 1-10, 1966

$$\hat{\boldsymbol{\Sigma}}_d = \begin{pmatrix} 1 & 0 & 0 \\ 0 & 1 & 0 \\ 0 & 0 & \det(\mathbf{U}_d \cdot \mathbf{V}_d^T) \end{pmatrix} \tag{5.41d}$$

The homogeneous transformation is given as:

$${}^d\mathbf{T}_u = \begin{pmatrix} {}^d\mathbf{R}_u & {}^d\mathbf{R}_u \cdot {}^u\boldsymbol{r}_{u,d} \\ \mathbf{0}^T & 1 \end{pmatrix} \tag{5.42}$$

5.4.3.2. Joint-2-Joint Transformations

In order to compute the joint-2-joint transformations in the initial pose, we require information about the sequence of joints from the structural exploration. Here, we infer linearly increasing joint IDs from the base to the accelerometer frame. The transformation between two consecutive joints (${}^d\mathbf{T}_{d+1}$) is calculated from the accelerometer-2-joint transformations:

$${}^d\mathbf{T}_{d+1} = {}^d\mathbf{T}_u \cdot {}^{d+1}\mathbf{T}_u^{-1} \tag{5.43}$$

5.4.3.3. Full Kinematic Chain Model

Now, we assemble the kinematic forward model from the base to the accelerometer on the end effector frame, taking the joint positions (θ_d) into account. Each revolute joint (${}^d\mathbf{T}_{d'}(\theta_d)$) is modeled with a rotation (vrrotvec2mat($axis, angle$)) around the z-axis ($\boldsymbol{e}_z$):

$${}^d\mathbf{T}_{d'}(\theta_d) = \begin{pmatrix} \text{vrrotvec2mat}(\boldsymbol{e}_z, \theta_d[n] - \theta_d[0]) & \mathbf{0} \\ \mathbf{0}^T & 1 \end{pmatrix} \tag{5.44}$$

The kinematic chain (${}^B\mathbf{T}_u(\boldsymbol{\theta})$) is then calculated from a concatenation of the known homogeneous transformations:

$${}^B\mathbf{T}_u(\boldsymbol{\theta}) = {}^B\mathbf{T}_1 \cdot \prod_{d=1}^{D-1} \left({}^d\mathbf{T}_{d'}(\theta_d) \cdot {}^{d'}\mathbf{T}_{d+1} \right) \cdot {}^D\mathbf{T}_{D'}(\theta_D) \cdot {}^{D'}\mathbf{T}_u \tag{5.45}$$

Hereby the transformation from the first joint to the base frame (${}^B\mathbf{T}_1$) can be freely chosen (e.g. ${}^B\mathbf{T}_1 = \mathbf{I}_4$).

5.4.4. Experiments

In this section, we experimentally evaluate the performance of our approach by comparing it to ground truth. All measurements have been performed with a 6-axis UR-5 robotic arm (Universal Robots), mounted on our custom built "Tactile Omni-directional Mobile Manipulator" (TOM) robot (see Fig. 5.13). The sampling rate of the accelerometer is 250 Hz, the robot control frequency is 62.5 Hz (interpolated to 125 Hz on the robot) and the robot sample rate is 125 Hz. All signals are converted to a common 250 Hz sample rate and run through Gaussian filters ($size = 11$, $sigma = 2.83$). One complete estimation run approximately lasts for 180 s.

5.4.4.1. Ground Truth Circle Point Analysis

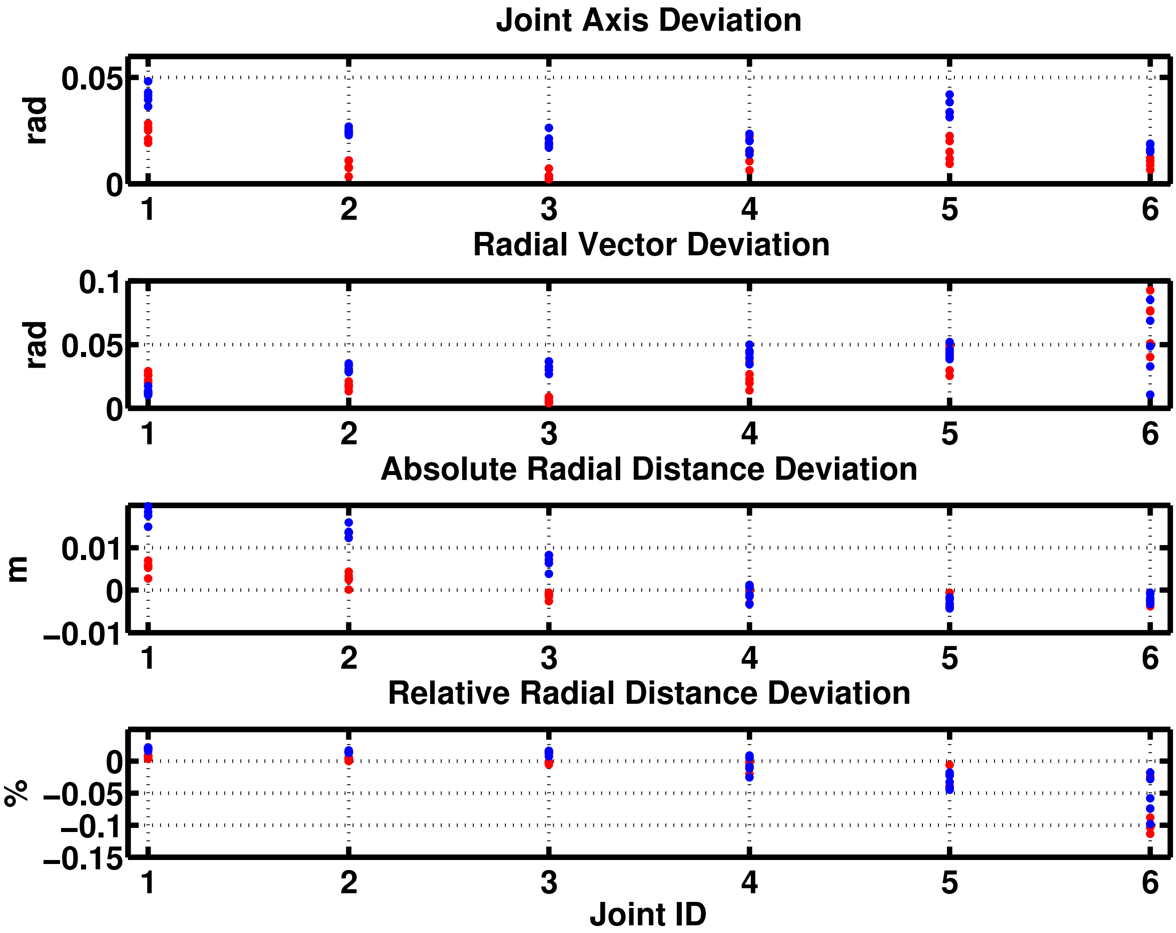

FIGURE 5.19. The figure shows the deviation of the estimated CPA vectors to CPA vectors extracted from an ideal kinematic model, in two different initial poses of the robot (red, blue) with 5 trials in each pose.

In this experiment, we compare the circle point vectors (${}^{u}\boldsymbol{j}_{d}$, ${}^{u}\boldsymbol{r}_{u,d}$) estimated with our algorithm, to the ground truth vectors extracted from an ideal kinematic model of the robot, computed with the DH parameters of the robot and a known accelerometer placement. The results in Fig. 5.19 show an angular deviation of $\leq 0.05\,\mathrm{rad}$ for the joint axis and $\leq 0.09\,\mathrm{rad}$ for the radial vector, and a radial displacement of $\leq 0.02\,\mathrm{m}$ or $\leq 11\,\%$, for 10 trials in two different poses of the robot. The accuracy and precision of the radial vector alignment drops with the decreasing distance (see Fig. 5.19, radial vector deviation), while the joint axis estimation is independent of the localization (see Fig. 5.19, joint axis deviation). The radial distance deviation absolutely increases and relatively decreases with the distance (Fig. 5.19, radial distance deviation). Especially with small radial distances ($\ll 3\,\mathrm{cm}$), motion (e.g. jerk and structure vibrations) and sensor noise render the extraction of small tangential effects challenging. With large radial distances, e.g. a fully extended robot arm, induced base motions are challenging. Our heuristic motion parameter set is a good compromise for both.

5.4.4.2. Ground Truth Kinematic Model

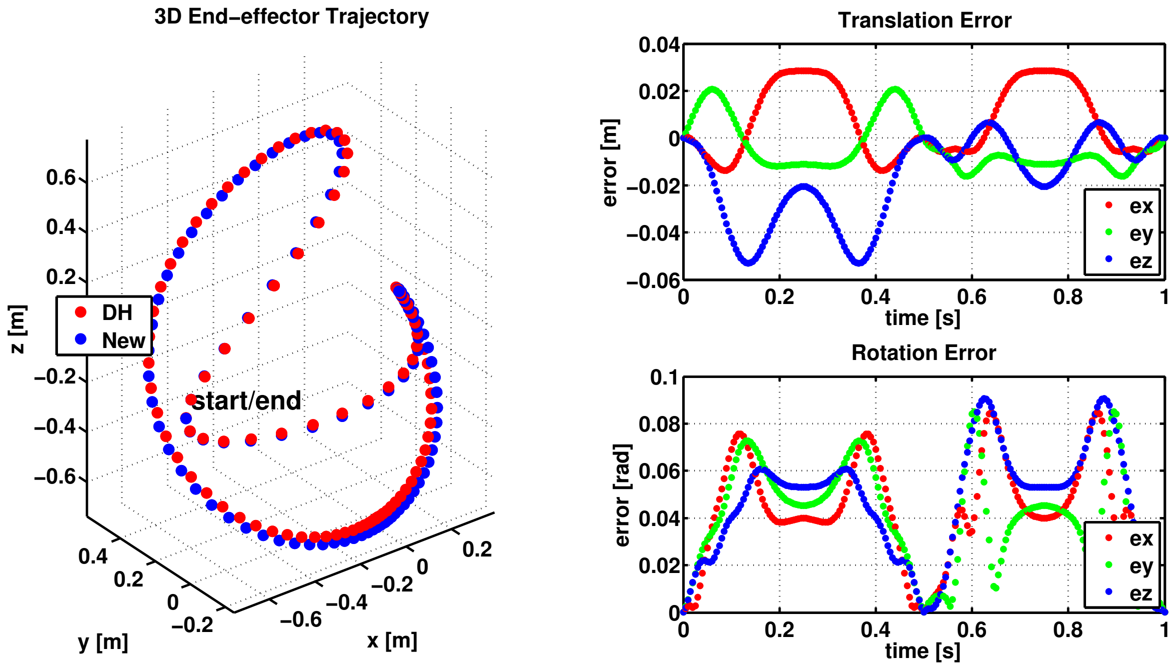

FIGURE 5.20. The figure shows the deviation of a kinematic model extracted with our method, in comparison to an ideal kinematic model (calculated by Emmanuel Dean) with the DH parameters of the robot and a known accelerometer placement.

In this experiment, we compare our kinematic extraction algorithm to an ideal kinematic model of the robot, computed with the optimal DH parameters of the robot and a measured (visual alignment) accelerometer placement (see Fig. 5.13). Here, we take one set of the previously estimated CPA vectors. Due to the free placement of the base frame, we need to first register (${}^{B_{\text{new}}}\mathbf{T}_{B_{\text{dh}}}$) both kinematic models in the initial pose. We then compare the global end-effector transformation (${}^{B}\mathbf{T}_{u}(\boldsymbol{\theta})$) of both models, executing large sinusoidal motions on all (D) joints ($f = 1\,\text{Hz}$, $\triangle\theta_d = \pm\pi$). The results in Fig. 5.20 show a translation error of $\leq 0.05\,\text{m}$ and a rotational displacement of the ideally aligned end effector coordinates (${}^{u}\boldsymbol{e}_{\text{x}}$,${}^{u}\boldsymbol{e}_{\text{y}}$,${}^{u}\boldsymbol{e}_{\text{z}}$) of $\leq 0.09\,\text{rad}$.

5.5. Summary

In this chapter, we introduced three methods to acquire sensory-motor control knowledge with open-loop motions of the robot and feedback from the accelerometers integrated in every of our multi-modal skin cells: 1) an algorithm to explore the kinematic dependencies of the kinematic tree of a robot; and 2) an algorithm to acquire an inverse Jacobian like mapping between tactile stimulations and robot reactions; 3) an algorithm to model and calibrate the kinematic models of articulated robot manipulators. Using minimalistic static and dynamic motions on one revolute joint axis after the other, we can acquire those parts of the body schema in a very short time and without the need for potentially dangerous fast and large ranging robot motions. First implementations on the upper body of a humanoid robot and multiple industrial robotic arms show the transferability, scalability and robustness of our approaches.

CHAPTER 6

Integration/Applications

> Few things are impracticable in themselves; and it is for want of application, rather than of means, that men fail to succeed.
>
> *(Francois de La Rochefoucauld)*

In this chapter, we show exemplary applications of the artificial skin system. We first introduce a novel approach to grasp unknown objects with a full-sized, position controlled humanoid robot only via tactile feedback and a self-explored body schema. We then provide additional use cases, e.g. the exoskeleton robot that has been used during the opening-ceremony of FIFA world championship 2014 or the two different industrial robot arms that have been enhanced with multi-modal tactile sensitivity.

6.1. Introduction

FIGURE 6.1. The figure shows different integrations and applications of CellulARSkin.

In this chapter, we show exemplary applications (e.g. grasping, collision avoidance, human-robot interaction, tactile feedback) of our artificial skin system with implementations on more than 3 different robots, e.g. Kuka's LWR, Universal Robots' UR-5 and Kawada Industry's HRP-2. In the first section, we introduce a novel approach to grasp unknown objects with a full-sized, position controlled humanoid robot only via tactile feedback and a self-explored body schema. This implementation demonstrates the transferability of our artificial skin to new robotic systems in a short time[1]. We then introduce multiple use cases, on an exoskeleton robot that has been used during the opening ceremony of the FIFA world championship 2014 and on two industrial robot arms that have been enhanced with multi-modal tactile sensitivity. The latest implementation on our robot TOM shows the scalability of our modular approach to a higher number of skin cells, while the robustness of our artificial skin has been proven with demonstrators on international conferences and fairs (e.g. Automatica 2014 or Robots on Tour 2013).

---

[1] In this case a 3 month research visit at AIST

6.2. Grasping Unknown Objects with a Humanoid

FIGURE 6.2. The figure shows HRP-2 holding objects that have been grasped only with tactile feedback and a self-explored body model. Key poses for the trajectory generation and expected contact points have been taught with a novel method of tactile human-robot interaction.

In this section we introduce a new approach to grasp unknown objects with the complete upper body of a position controlled humanoid robot (HRP-2) and tactile feedback [2]. Our work has been motivated by the demand to handle unknown, large and/or heavy objects with the whole robot body, instead of grasping them only with the end-effectors. Being able to efficiently handle those objects would have a large impact in households, care giving or industrial scenarios – e.g. robots could help to (un-)load airplanes, handle bags of clothes in an industrial laundry or deliver parcels in an office. For such tasks, multi-modal, large-area surface sensation seems predestined, as it provides a rich and direct feedback from numerous simultaneous contact points from a potentially large area of contact. In order to omit manual calibration with a high number of sensor and actuators, we use our kinematic self-organizing features – here the sensory-motor map and the structural exploration method. Additional task-related knowledge, e.g. the expected contact points or grasping trajectories, were taught through direct physical human-robot tactile interaction. This direct, interactive method to transfer knowledge to the robot includes non-specialists.

---

[2] The work in this section has been published in [Mittendorfer *et al.*, 2013].

6.2.1. Integration on HRP-2

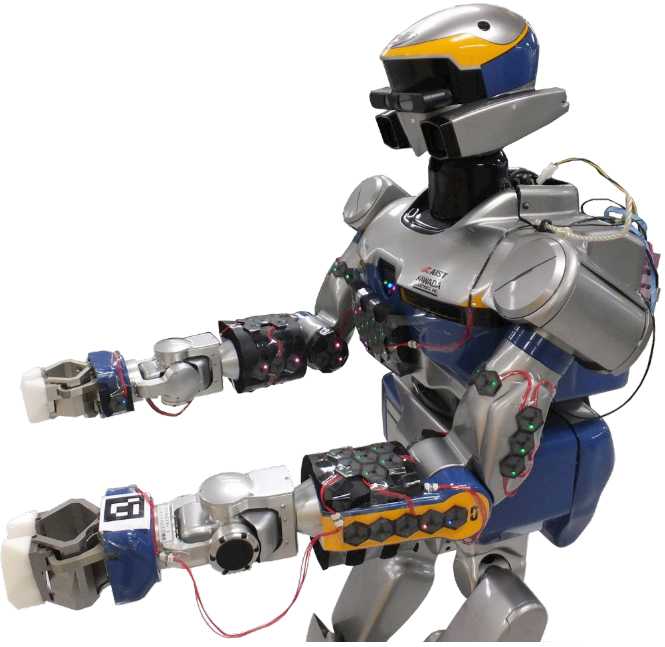

FIGURE 6.3. The figure shows the distribution of skin on the humanoid robot HRP-2. The interface box to the on board computer can be seen on the back side. A foam layer between the skin and the robot's surface provides compliance and smooths out the irregular surface.

In this experiment setup, 74 skin cells have been distributed on the whole upper body of HRP-2, covering parts of the chest and both arms (see Fig. 6.3). A foam layer between the skin and the robot's surface provides compliance (lowering control constraints), smooths out the irregular surface of the the robot and ensures that contact is made on the elevated skin. In order to minimize delays, we utilized the second on board computer (i686, 1.6 GHz, 2 cores, 3 MB L2, 32 GB RAM, Ubuntu 10.04) of HRP-2. The primary computer executes the 200 Hz real-time control loop – the stack of tasks (SoT). A stable central body part, like the torso of a humanoid robot or the platform of a mobile robot, is required during self-organization. This base frame will be the reference of actions for the motion primitives. With a humanoid robot like HRP-2, a stable balancing controller is required. This is not a constraint, as our algorithm currently only takes a subset of the available DoFs into account - namely those related to both arms. The HRP-2 controller generates actuator commands by resolving, in real-time, a set of prioritized tasks. In our experiments, equilibrium is achieved by fixing feet and center of mass position to a static position. Redundancy allows the HRP-2 to realize whole-body manipulation while satisfying the equilibrium tasks. To generate grasping motions with the robot upper-body, a low-priority task is added to the SoT, enforcing both arm velocities.

6.2.2. Tactile Teaching

This section is devoted to the explanation of transfer of knowledge from human to robot through tactile interaction.

6.2.2.1. Tactile Guidance

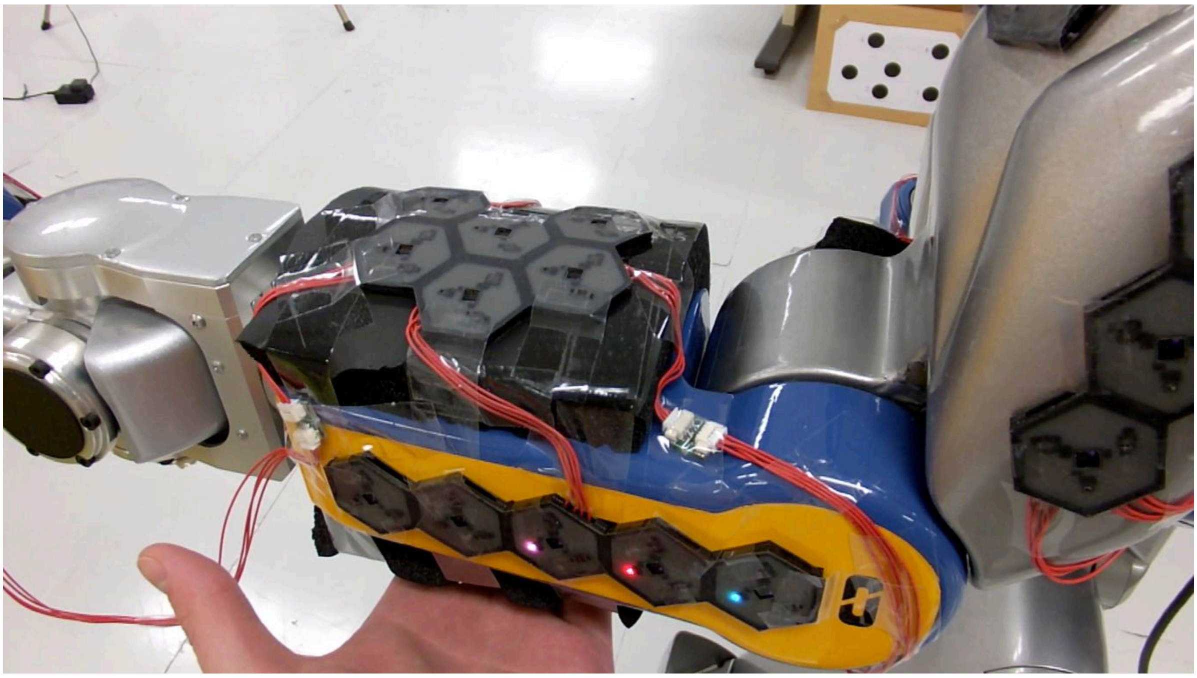

FIGURE 6.4. The figure shows an example of tactile guidance with HRP-2.

Tactile guidance (see Fig. 6.4) is a direct evasive reaction of body parts on multi-modal tactile stimulation, with the purpose to follow the motion of a teacher. Utilizing simultaneous or sequential contacts, the robot is driven into different meaningful configurations – here the key poses. We currently provide two different modes: (i) force guidance; (ii) proximity guidance. Force guidance takes the force modality into account and thus requires physical contact with the robot and a sufficiently high force to safely detect the stimulus from background noise. With the proximity sensor, and thus proximity guidance, the robot will start to react before the teacher touches the robot (here $\sim 5\,\text{cm}$ before).

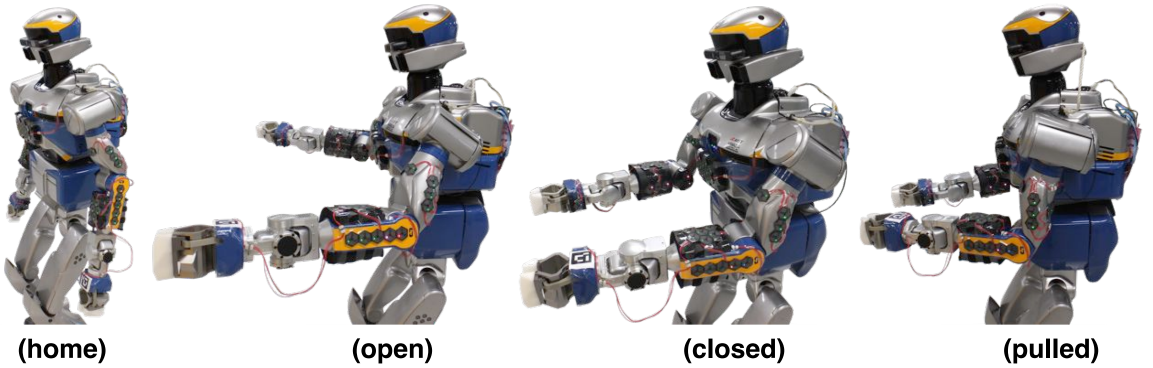

FIGURE 6.5. The figure shows key poses that are taught to the robot via tactile guidance and serve for the generation of grasping trajectories.

6.2.2.2. Key Poses

Tactile guidance is used to interactively drive the robot into different key poses (see Fig. 6.5). For example, the robot starts from an initial 'home' key pose, which the robot remembers and uses as a safe home configuration. In the 'open' key pose, both arms are opened widely to allow an object in between. The 'closed' key pose brings both arms together, therefore an object between is clamped and makes contact with the robot. In the 'pulled' key pose both arms are still together, but the arms are pulled closer to the chest. In this form, any object between the arms will be in contact with the chest. All key poses are added to the sensory-motor map and serve for grasping trajectory generation.

6.2.2.3. Touch Areas

Tactile sensing allows to define areas of special interest – the touch areas (see Fig. 6.6). For example, we activate the grasping sequence by touching the robot in a 'pat' area (PA) (see Fig. 6.11). Teaching touch areas is done by selecting a label, activating the attention of the robot (e.g. pushing a button), brushing over the desired area and deactivating attention. While paying attention, the robot evaluates the incoming event stream for new (close) contact events and stores the related unit IDs in a binary vector. For the grasping approach, the operator needs to define the expected contact areas (CA), while the remaining IDs are automatically allocated to the non-contact area (NCA). Both areas are allocated with different reaction primitives and their events lead to different state changes while grasping objects. The chest area (CHA) serves as a third explicit contact point, besides the left and right arm, which is necessary for a globally stable grasp.

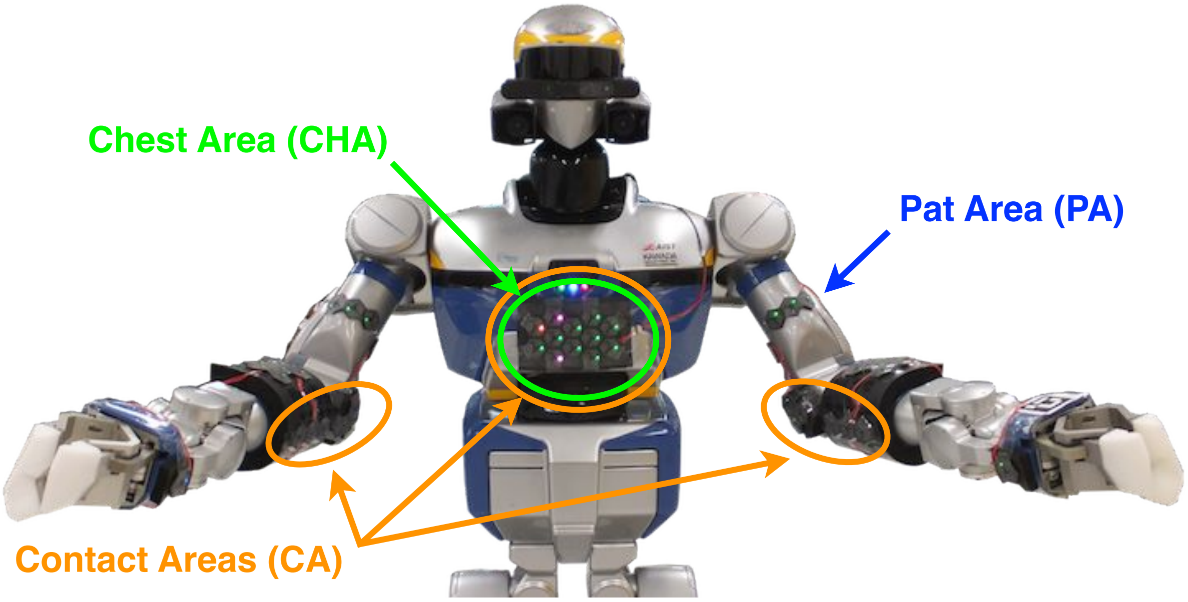

FIGURE 6.6. The figure shows the touch areas that allow the generation of specialized tactile events and a differentiation of touch reactions with specific parameters (see Table 6.2).

6.2.3. Control Strategies

In this section, we describe the low and high level control (see Fig. 6.7) used with HRP-2.

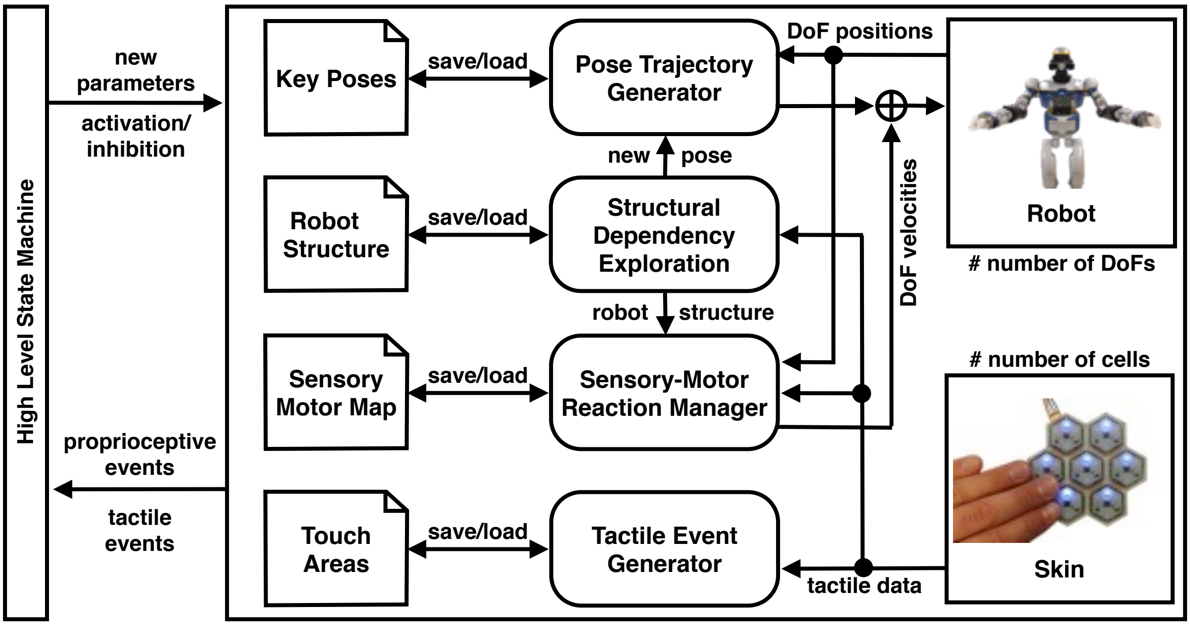

FIGURE 6.7. The figure shows the data exchange between the robot, the artificial skin, the long term memory and the controller sub-blocks during our grasping approach. The state machine controls sub-block activity and parameter distribution.

6.2.3.1. Tactile Reaction Primitives

The sense of touch allows to implement meaningful direct reactions on multi-modal tactile stimulation – e.g. to avoid self- or environment collisions or to let users kinesthetically guide the robot. The advantage of instantiating one multi-modal reaction controller for every skin cell (u) is the scalability of this approach – tactile behavior is programmed for the smallest piece of skin and expanded to the whole robot surface. Since all cellular parameters, are accessible by the high level control system, spatial reactions can be set up for a specific task. We compute a proportional motor reaction for every multi-modal (m) sensor value (ρ_m) above a pre-defined threshold (t_m) (refer to Sec. 5.3.3). All (M) multi-modal reactions on a cell are accumulated and mapped to a desired cellular velocity reaction vector, via the sensory-motor map vectors ($\boldsymbol{w}_{u,p}$) of the current pose (p). Super-imposing the resulting velocity vectors from all ($u = [1,...,U]$) skin cells, leads to a global tactile robot joint velocity reaction ($\boldsymbol{\omega}_{\text{tactile}}$) (see Equ. 5.15). Modalities are inhibited, promoted or inverted by setting their gain ($P_{m,u}$) and threshold ($t_{m,u}$) (refer to Table 6.2). The threshold determines the activation level and is important to suppress sensor noise and offsets.

6.2.3.2. Postural Trajectory Generation

The trajectory generator calculates velocity commands to transfer the robot in joint space from the current pose ($\boldsymbol{\theta}_{\text{cur}}$) to a desired ($\boldsymbol{\theta}_{\text{des}}$) key pose:

$$\boldsymbol{\omega}_{\text{traject}} = \frac{\omega_{\text{max}} \cdot (\boldsymbol{\theta}_{\text{des}} - \boldsymbol{\theta}_{\text{cur}})}{\max\left(\max(\text{abs}(\boldsymbol{\theta}_{\text{des}} - \boldsymbol{\theta}_{\text{cur}})), \theta_{\text{acc}}\right)} \tag{6.1}$$

Control parameters define the maximum joint velocity (ω_{max}), the desired postural accuracy (θ_{acc}), the name of the pose and a flag if the robot should stop once the desired key pose has been reached. Once the desired pose has been reached, an event is sent to the control system. For the overall reaction of the robot, the tactile reaction velocity vector ($\boldsymbol{\omega}_{\text{tactile}}$) and trajectory velocity vector ($\boldsymbol{\omega}_{\text{traject}}$) are super-imposed:

$$\boldsymbol{\omega}_{\text{robot}} = \boldsymbol{\omega}_{\text{traject}} + \boldsymbol{\omega}_{\text{tactile}} \tag{6.2}$$

This is the reason why tactile reactions have to be dominant in comparison to the trajectory speed and/or cancel the current trajectory execution in case of detected ‘pain’ levels, e.g. a high force applied on a single force sensor (see Table 6.1).

6.2.3.3. Tactile Events

Force Cells		Proximity Sensor	
pain force	0.45	close contact	0.80
high force	0.30	low proximity	0.10
medium force	0.10	medium proximity	0.02
low force	0.04	high proximity	0.01
no force	0.00	no proximity	0.00

TABLE 6.1. The table shows the heuristic, normalized thresholds for the generation of multi-modal tactile events with the proximity and force sensors.

Centrally monitoring a growing number of tactile sensors generates high computational and network overloads. Since most skin areas are not (or in constant) contact, this effort is not efficient. To prevent this scalability bottleneck, we pre-process tactile signals into events. Currently this is still done on the computer, as we wish to log all raw experimental data. However, the design of CellulARSkin$^{\text{TM}}$ allows to locally process tactile signals in every skin cell, extracting information at the earliest stage. New data packets should only be generated if sensor values deviate significantly from sensor noise and recently transmitted samples. Therefore all our high level algorithms use abstract tactile events, while our low level control algorithms can deal with varying update rates. For our grasping approach on HRP-2, we utilized force and proximity events, with a coarse separation into heuristically pre-defined thresholds (refer to Table 6.1). A new tactile event is only emitted on changes between those levels, with a small hysteresis to prevent repetitive triggers. Due to the direct localization of touch, tactile events in specific areas can trigger robot behaviors or state changes, e.g. launch a grasping sequence when patted on the shoulder.

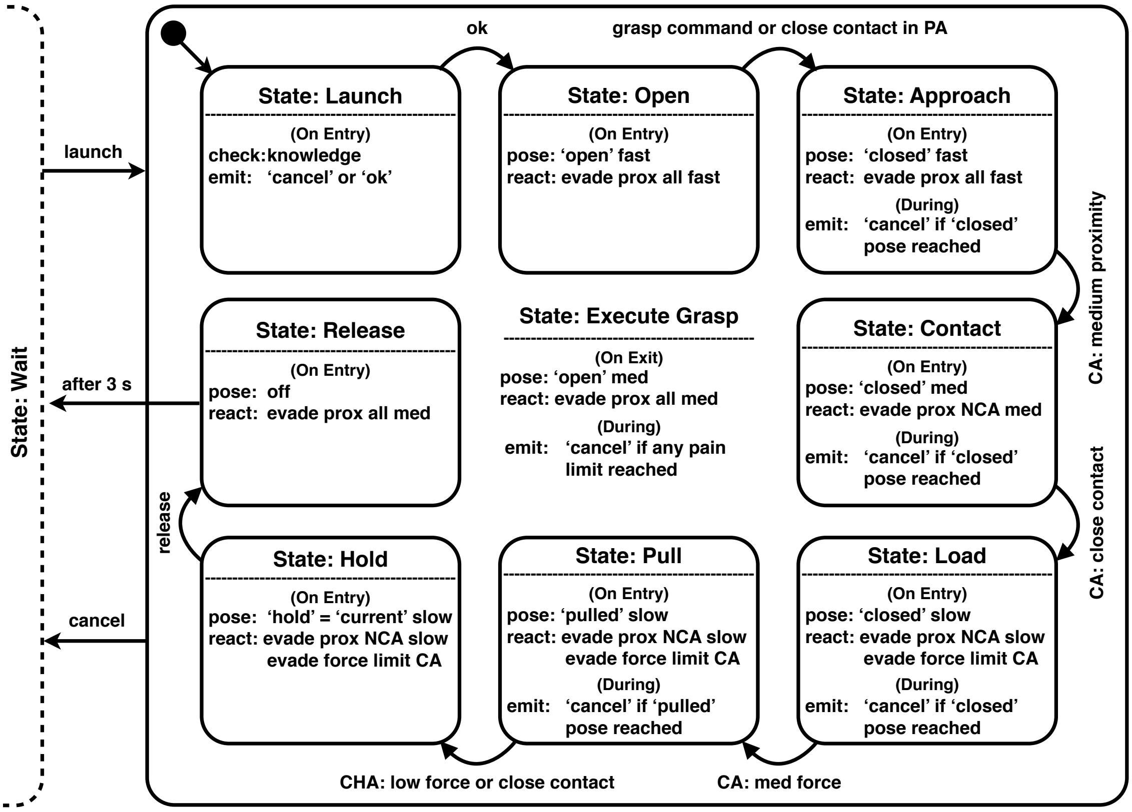

FIGURE 6.8. The figure shows the high-level control state-machine of our grasping approach. Tactile events or high level commands trigger transitions between the discrete grasping states. Entry or exit actions of the states send new parameters to the low-level postural trajectory (see Equ. 6.1) or tactile reaction controllers (see Equ. 5.15 and Fig. 5.8).

6.2.3.4. Grasp State Machine

The whole grasping sequence is split into multiple states of a sequential state machine (see Fig. 6.8). As an entry action, every state sends a set of area specific control directives to the low-level tactile controllers. Changes between states are triggered by events from the trajectory generator or tactile events. Emergency situations, e.g. pain level forces, drive the robot into a safe state. The safest action is not to stop all upper body motions, but to slowly evade all contacts. States with contact as main objective (e.g. the approach, contact, load or pull state), fail if the set key pose is reached without receiving the desired tactile events. In the 'approach' state, the object needs to come close to the expected contact area (CA), while forces have to be applicable in the 'load' state. In general, the interaction speed is reduced the closer the robot and the object come together. Here, we specifically use the proximity sensor modality to safely increase the speed in the approach and contact phase (refer to Table 6.2). Purely relying on the force sensors, forces can ramp up quicker than the reaction time of the robot, damaging the robot or the object. With HRP-2 and CellulARSkin$^{\text{TM}}$ we solved this issue by: (i) using the on-board computer to minimize delays; (ii) adding a foam layer between the robot and the skin to provide (sensor) hysteresis free compliance; and (iii) using proximity sensors to slow down motion before contact.

6.2.4. Experiments

In this section, we explain results from our grasping experiments, showing the main features obtained using the skin.

6.2.4.1. Tactile Guidance

The effectiveness of tactile reactions, and their transfer to motor actions through the sensory-motor map, are best evaluated on tactile guidance. Fig. 6.9 shows a plot of force guidance with both arms, first the left and then the right arm. The activation threshold of $t_{\mathrm{F},u} = 0.05$ force sensor readings, approximately relates to 0.6 N, the chosen force gain is $P_{\mathrm{F},u} = 1.0$. A single force reading of $\rho_{\mathrm{F},u} = 0.14$, relating to a force of 1.0 N, leads to commanded velocity of $\boldsymbol{\omega}_{re} = 0.09\,\mathrm{rad\,s^{-1}}$ on a single DoF – which is approximately what we observe in Fig. 6.9 between 75 s and 85 s with DoF ID 1 and SC ID 52. All key poses in Fig. 6.5 have been taught without touching the robot, via the proximity sensor. As the sensory-motor map builds on the fly, it operates as an extrapolation of the closest explored pose – starting from the initial home key pose (see Fig. 6.5). Due to the lack of the two shear sensing directions on the current SC version, the rotation of some DoFs require a postural change first – which is unintuitive.

6.2.4.2. Grasping of Unknown Objects

In Fig. 6.10, we show a set of 5 objects with different weight, size, shape and compliance, which we successfully tested our approach on (see Fig. 6.2). We applied the same set of heuristic control parameters for all objects (refer to Table 6.2). A grasp succeeded, when the robot was able to make contact with the object, apply forces on it and pull it to its chest. Our approach infers that the graspable object is in between both arms when receiving the launch command. If there is no object, or the object can not be pulled, the robot automatically cancels the grasp. The plastic cover on the wrist does not support force and is allocated to the non-contact areas, where applied forces intentionally cancel the grasp. Naturally this limits our success rate when grasping big objects, e.g. the trash bin or the big moving box, as big objects are likely to touch the wrist. We wish to emphasize that no object has been damaged during all experiments. To demonstrate the reliability of our system, we let the robot 'hug' human

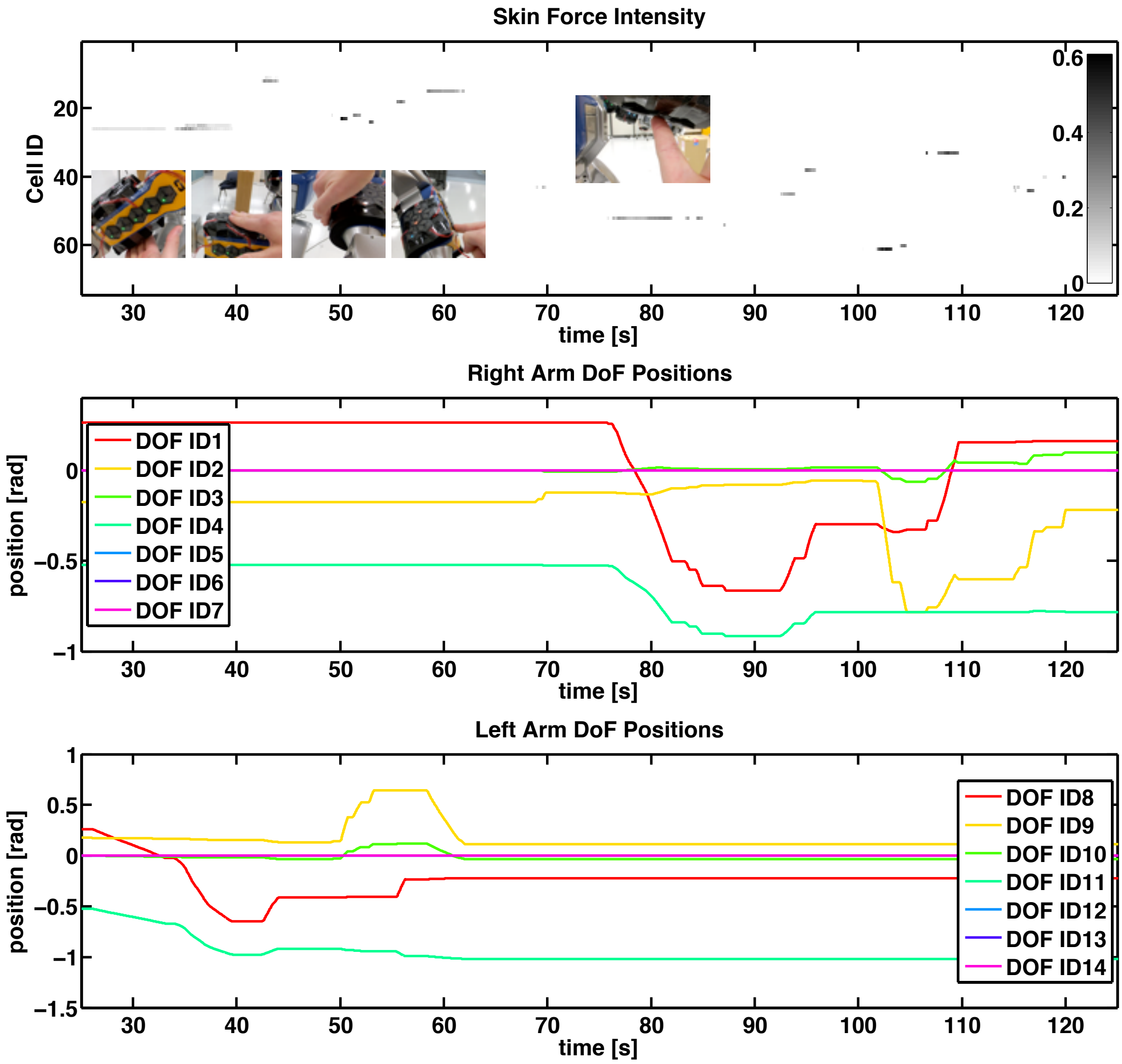

FIGURE 6.9. The figure shows a force guidance experiment – Tactile stimulations are directly mapped to evasive motor reactions via the sensory-motor map. The first graph shows the force stimulation intensity (grayscale value, white is sub-threshold) of all sensor cells over time. The two other graphs show the resulting joint positions of the left and right arm.

multiple times (first author). The proximity sensor modality allows to speed up motions prior to contact and robustly detects when the object touches the chest, which is sufficient to prevent the rotation of grasped objects. The advantages of our multi-modal approach, triggering and controlling phases of the grasping approach with different sensor modalities, can be seen in Fig. 6.11. As a consequence of the similar size, both objects (B and E) are first contacted after nearly the same time. First light contact forces also build up in a similar time frame. However, it is already visible in the proximity intensity, that object E has a symmetric surface, while object B is asymmetric. This observation continues within the force profile, where object E

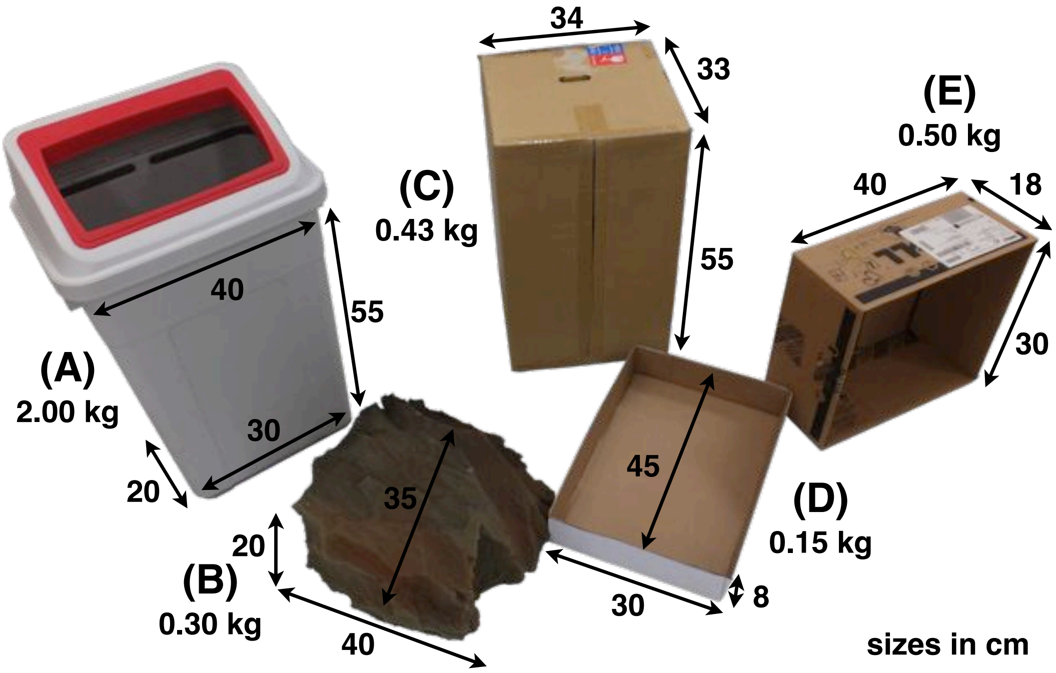

FIGURE 6.10. The figure shows the objects utilized to test the graping approach: (A) plastic trash bin; (B) sponge rock; (C) moving box; (D) lid of a paper box; (E) computer delivery box. The objects have different weights, shape, hardness and size.

develops and maintains a clear and symmetric contact force intensity on both arms, while object B remains squishy. Due to the conformation of object B to the robot's surface, and the incomplete coverage with skin, forces for object B are in parts grounded on insensitive spots, which is visible in the remaining sensational asymmetry. Both grasps are finalized with a close contact on the chest, but after a significantly different time span. This can be explained, as Object B had to be pulled over a longer distance and compressed for a longer time to maintain 'satisfying' contact pressure.

6.2.5. Application Notes

In this section, we presented a general tactile approach to grasp unknown objects with a position controlled humanoid robot. We demonstrated that even a coarse, self-explored sensory-motor mapping is sufficient to achieve the task. Additionally, we showed how knowledge is transfered from human to robots using tactile interaction. For the first time, we apply our multi-modal artificial skin, and its self-organizing features, on a full-sized humanoid robot. A general tactile approach for grasping unknown objects is introduced, which efficiently takes advantage of a distributed, multi-modal sense of touch. In comparison to existing approaches, our novel grasping algorithm requires minimum knowledge on the robot it controls (no kine-

Control State	**Control Parameters**							**Touch Areas**
	Force		**Proximity**		**Pose**			
	$t_{\mathrm{F},u}$	$P_{\mathrm{F},u}$	$t_{\mathrm{P},u}$	$P_{\mathrm{P},u}$	hash	$\omega_{\max}$	θ_{acc}	
F-guide	0.05	1.0	-	-	-	-	-	all
open	-	-	0.01	0.4	open	0.4	0.01	all
approach	-	-	0.01	0.4	closed	0.4	0.01	all
contact	-	-	- 0.01	- 0.4	closed	0.1	0.01	NCA CA
load	- -	- -	0.01 -	0.01 -	closed	0.05	0.01	NCA CA
pull	- 0.10	- 0.80	0.01 -	0.01 -	pulled	0.05	0.01	NCA CA
hold	- 0.10	- 0.80	0.01 -	0.01 -	-	-	-	NCA CA
release	-	-	0.01	0.2	-	-	-	all

TABLE 6.2. The table shows the heuristic parameters of the grasping experiment. Every high level state of the state machine (see Fig. 6.8) features its own set of parameters for the contact (CA) and non-contact (NCA) areas (see Fig. 6.6). Here, we utilize normalized threshold and gain values for the force ($t_{\mathrm{F},u}$ and $P_{\mathrm{F},u}$) and proximity ($t_{\mathrm{P},u}$ and $P_{\mathrm{P},u}$) sensor mappings (see Equ. 5.15). The trajectory generator takes a pose hash, a leading joint velocity ($\omega_{\max}$) and postural accuracy (θ_{acc}) as an input (see Equ. 6.1).

matic/dynamic model) and the object it handles (no object model). Utilizing proximity sensors as a novel method of teaching behaviors through direct tactile interaction, it is not necessary to apply force on the robot or even touch it – making heavy or position controlled robots featherlight to interact with. Relying on artificial skin, no joint level force sensing is required. Our approach provides a new and complementary level of direct physical interaction.

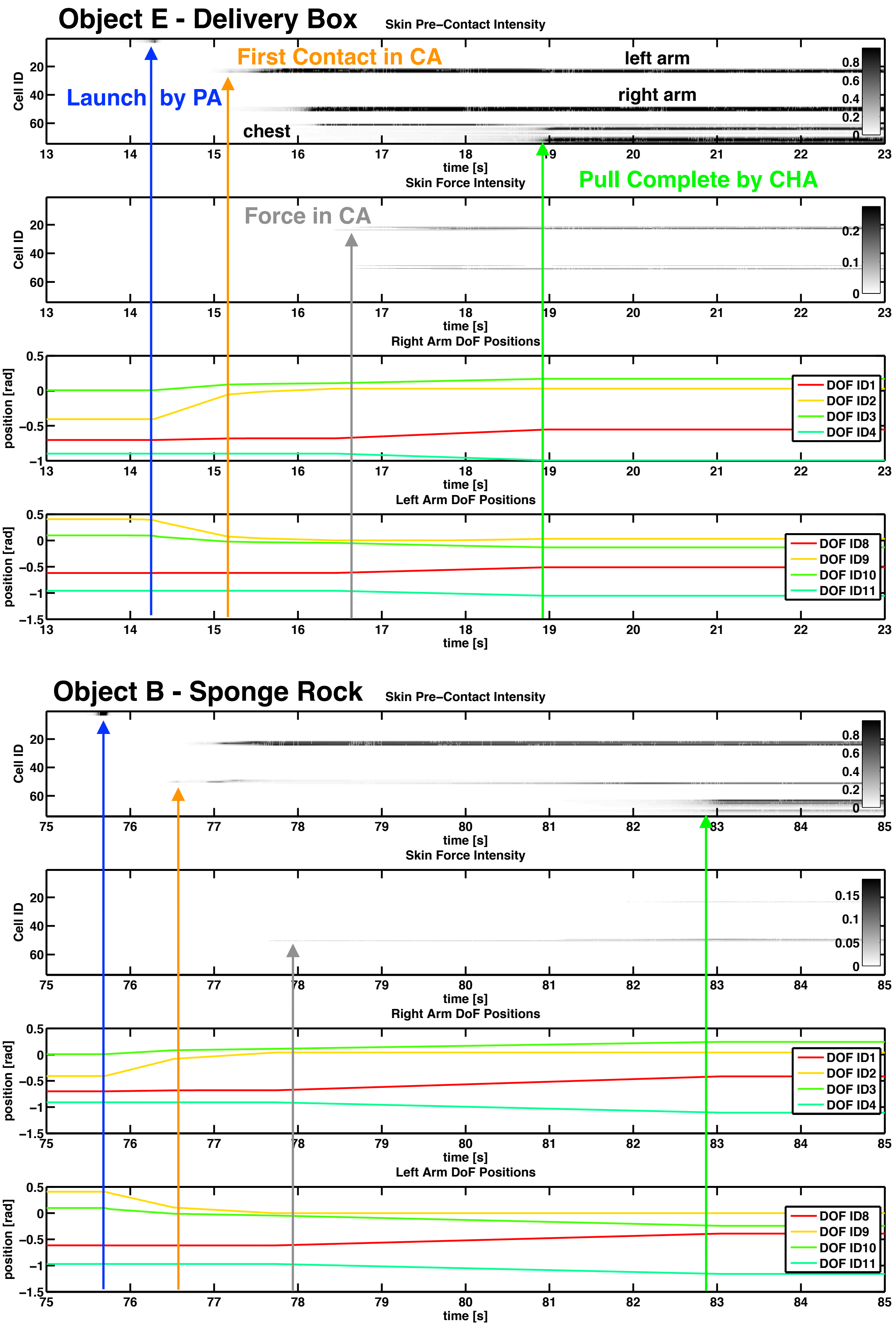

FIGURE 6.11. The figure shows the proprioceptive and tactile feedback while grasping two objects (E/B) with different compliance (hard/soft) and shape (regular/irregular), please also see Fig. 6.10.

6.3. Walk Again Project

FIGURE 6.12. The figure shows the kick-off with the Walk Again Project exoskeleton robot at the FIFA world cup in Brazil 2014. [source: https://twitter.com/walkagainproject]

In the Walk Again Project an international team of researchers and a company (BIA), enabled a paralyzed teenager to do the ceremonial kick-off at the FIFA world championship 2014 (see Fig. 6.12). The vision was to control the powerful exoskeleton only with a EEG brain machine interface and to provide the exoskeleton and the user with tactile feedback in order to sympathize human robot interaction. One key contribution of TUM in this project was to provide the artificial skin system for the exoskeleton and training facilities.

6.3.1. Skin Applications

Multiple applications have been discussed regarding the application of artificial skin on the exoskeleton. With an exoskeleton, the artificial skin can be used to measure the interaction with the external world, as well as with the internal user. External sensors can also provide feedback to the user – e.g. provide paralyzed patients with a feeling of their feet. For the final demonstration, only two of the potential applications have been applied, namely: 1) the tactile feedback about the time of ground contact; and 2) sensors on the arm wrist as a safety measure for the EEG control. In the following, we will give a concise overview on all potential applications.

6.3.1.1. Ground Contact

The exoskeleton needs to detect the ground contact time to synchronize the walking motion patterns, while force distributions can provide feedback about the center of mass for balancing. For the patient, it is important to synchronize his upper body motions with the exoskeleton, like a passenger on a motorcycle, in order to avoid antagonistic behavior with the stabilization algorithm. The detection of the time of contact with the ground is thus important for the exoskeleton, as well as for the patient which is carried by the robot. Prior to our involvement in the Walk Again Project (WAP), we already tested the capability of our artificial skin to measure ground contacts. To do this, we installed 4 skin cells on the foot of an HRP-2 robot and recorded the data while the robot was performing cyclic steps. We obtained the result that all four implemented sensor modalities can be used to detect ground contact (see Fig. 6.13). We also developed a tactile feedback shoe (see Fig. 6.14) that maps the magnitude of the proximity and force into a PWM signal for vibrational motors that can be mounted on other parts of the body. For the WAP, we manufactured a high range version of our custom force sensor, in order to avoid saturation with the expected weight of the exoskeleton. Multiple skin cells were then implemented (by BIA) into the shoe sole of the exoskeleton (see Fig. 6.15). The tactile shoe is able to measure the weight of a person standing on it ($\approx 86\,\mathrm{kg}$) with an approximate accuracy of $\pm 2\,\mathrm{kg}$. Due to constant re-designs of the exoskeleton shoes, an additional stand-alone skin cell was provided. This stand-alone version is able to detect ground contact via the proximity sensor and provides a binary interface for an external tactile display (developed by EPFL). This combination of tactile sensor and tactile display has for example been utilized for patient training on the Locomat (see Fig. 6.16).

6.3.1.2. Shot Contact

Similar to ground contact, the contact with the soccer ball can be detected with the multi-modal sensors (see Fig. 6.17).

6.3.1.3. Contact Surface between the Exoskeleton and the Patient

The exoskeleton developed during the Walk Again Project is very powerful. At the same time the patients wearing it are fragile and can exhibit involuntary spastic movements. When the exoskeleton is forcing against those spastic movements, the patient may be harmed. One idea was to equip the exoskeleton braces, fixing the patient to the robot, with surface sensation (see Fig. 6.18 and Fig. 6.19) and monitor spasticity. Three problems finally prohibited utilization

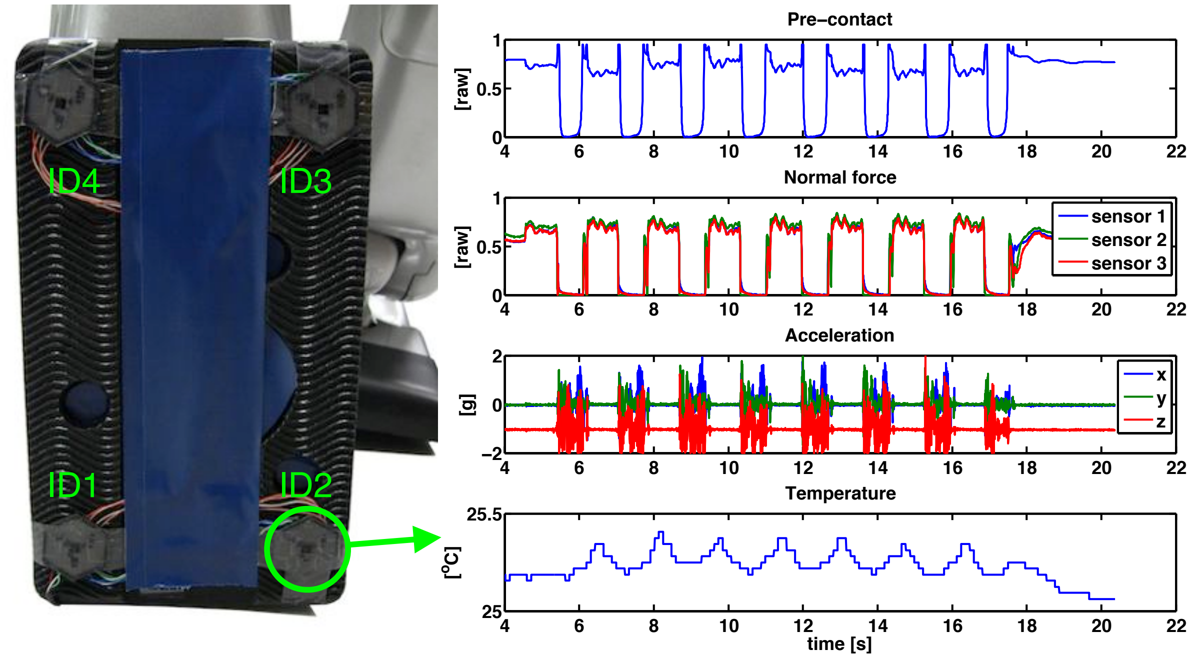

FIGURE 6.13. The figure shows four skin cells mounted on the right foot of HRP-2 and a plot with the reaction of all four sensor modalities, while the robot walks eight steps. The plots show the complete relaxation of the normal force sensor, the clean measurement of foot motion phase by the accelerometer, the contact phases by the proximity sensor and the slightly delayed thermal transfer on ground contact.

in the current state: 1) the flexible braces are closed with a high compressive load, causing high offsets; 2) the braces were always mounted differently, causing varying feedback; 3) the discrimination of normal vs spastic motions was difficult. Those three issues must be solved before brace inlets can be utilized for patient monitoring.

6.3.2. Application Notes

CellulARSkin$^{\mathrm{TM}}$ provided reliable feedback to the patients during walking with the exoskeleton and training on the Locomat. Some of the potential applications of skin on an exoskeleton have been utilized in the final demonstration of the exoskeleton during the FIFA world championship opening ceremony. Those applications have only been possible due to the ease of integration of our modular artificial skin and the reliable multi-modal sensor feedback it delivers. Further applications like the integration into the shoe or into the braces have been tested. The self-organizing features developed in this thesis can also be applied to an exoskeleton (see Fig. 6.19).

FIGURE 6.14. The figure shows the tactile feedback shoe developed at ICS.

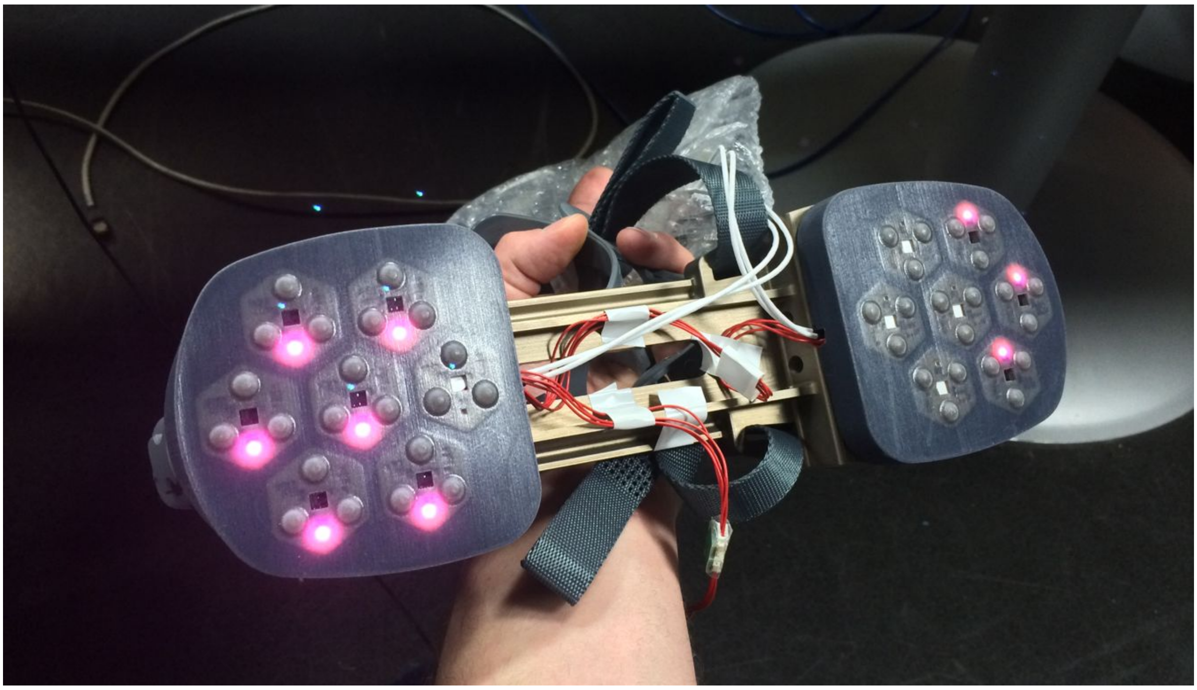

FIGURE 6.15. The figure shows the shoe sole of the exoskeleton, equipped with CellulARSkin^{TM}.

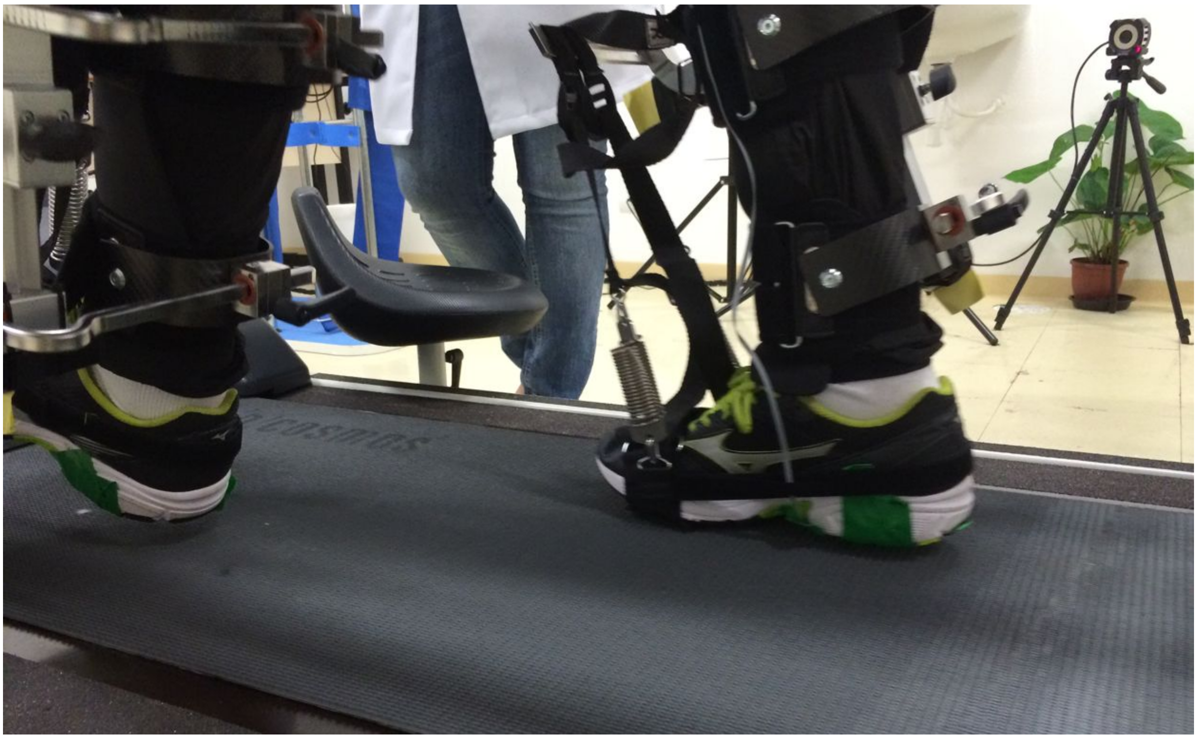

FIGURE 6.16. The figure shows a patient training on Locomat with tactile feedback from the shoe sole.

FIGURE 6.17. The figure shows a skin cell of CellulARSkin^{TM} mounted on the tip of the exoskeleton shoe for contact detection with the soccer ball.

FIGURE 6.18. The figure shows a brace inlet of the exoskeleton for patient monitoring.

FIGURE 6.19. The figure shows the 3D reconstruction results of the brace inlet in Fig. 6.18.

6.4. Multi-modal Interaction with a Kuka LWR

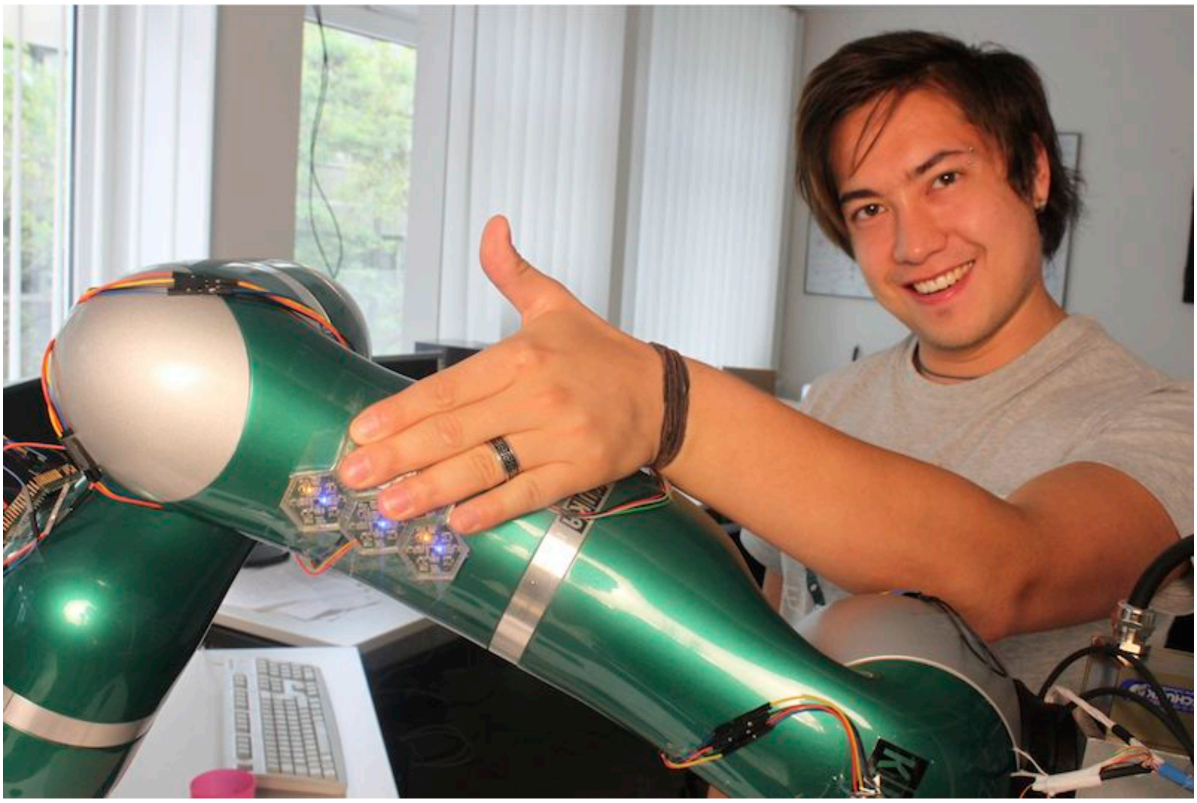

FIGURE 6.20. The figure shows the Kuka Light Weight Robot (LWR) arm equipped with a couple of skin cells version 1.1 (refer to Sec. A.4).

In this subsection, we present results from our initial experiments towards multi-modal tactile interactions with an industrial robot arm [3]. We therefore distributed 8 cells of the previous version 1.1 of our skin cell (refer to Sec. A.4) on the whole body of our Kuka Light Weight Robot (LWR) arm (see Fig. 6.20). Version 1.1 only features four low ranging proximity sensors (1-2mm), a 3-axis accelerometer and six temperature sensors – therefor no force experiments have been conducted, as this sensor has been introduced with version 2.0 of our skin cells (refer to Sec. A.4).

---

[3] The work in this section has been published in [Mittendorfer and Cheng, 2011a].

6.4.1. Control Framework

6.4.1.1. Multi-Modal, Multi-Touch Controller

Multi-modal touch stimuli can be directly mapped to reactive motions of the robot. Therefore a local reaction of a skin cell adds a rotational or translational velocity to the relative mounting point of its body part. To do this, it is necessary to provide the tactile controller with the body part, and the relative location and orientation of every skin cell in local body part coordinates. In this sub-section, we manually provide this information. The overall reaction of a single body part is then superimposed from the local reactions of the skin cells on it.

6.4.1.2. Robot controller

An inverse kinematic chain algorithm per body part, calculates the desired joint velocities from the desired Cartesian velocities of all super-imposed tactile reactions on it. To do this, the kinematic parameters of the robot, as well as the homogeneous mapping between tactile and kinematic coordinates, have to be known. For the results in this subsection, we manually calibrated those parameters. The joint control values of all body parts are then superposed, along with an optional global task. This global task can for example be a weak 'return to a home position' as in our experiments.

6.4.2. Experiments

6.4.2.1. Proximity - Multi-touch Reactions

Fig. 6.21 shows the robot reaction to multiple touch places detected by the proximity sensor. In version 1.1, this sensor only had a range of 1-2mm, whereas it has been extended up to 200 mm in version 2.0 (refer to Sec. A.4). For version 1.1, a binary controller evaluating the offset-adjusted signals of all proximity sensors was enough. When a threshold of 200 raw sensor reading was reached a constant velocity excitation of -0.05 m/s was added to the lateral velocity of the body part where the skin cell was located on. Since we also super-impose the reactions of multiple proximity sensors on a single skin cell, this fairly simple controller already shows desired tactile reactions. It reacts faster when the touched surface is increasing, while touching two opposite Tactile Modules neutralize the reaction (see Fig. 6.21 at 13 s).

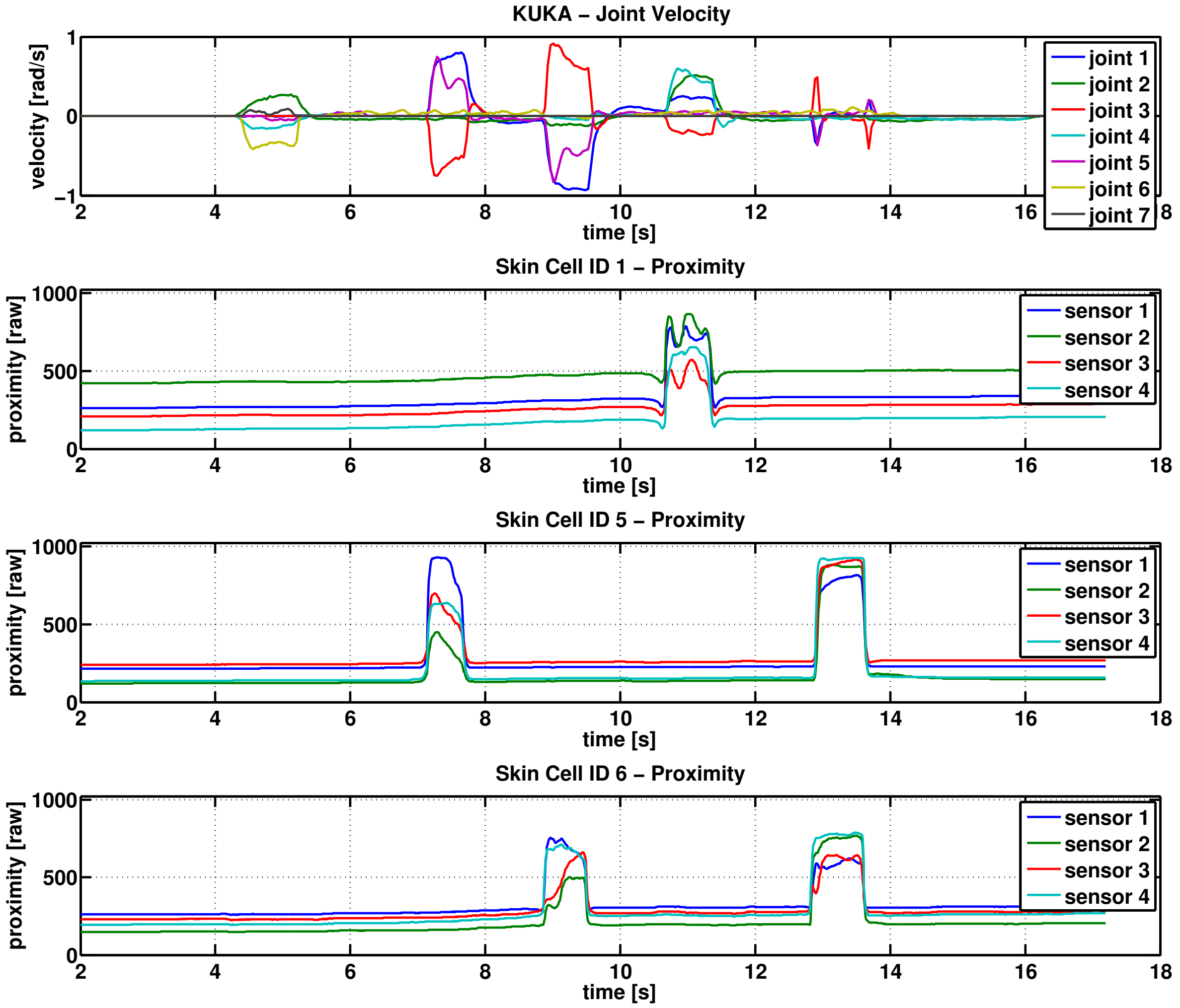

FIGURE 6.21. The figure shows the reactions of the Kuka LWR arm, towards tactile stimulations on the proximity sensors, with isolated or simultaneous stimulations on different skin cell locations.

6.4.2.2. Temperature - Air Draft Reaction

The power dissipation of the micro-controller and the robot are generating an over temperature of the artificial skin towards common environments (e.g. office rooms). The cooling effect of an air flow (see Fig. 6.23) or human touch can thus be used to trigger actions, e.g. evasive movements. We implemented this reaction with a constant threshold on a low pass filtered signal, such that the robot is reacting either on the cooling effect of touching it with a human hand or by blowing at it (see Fig. 6.22) .

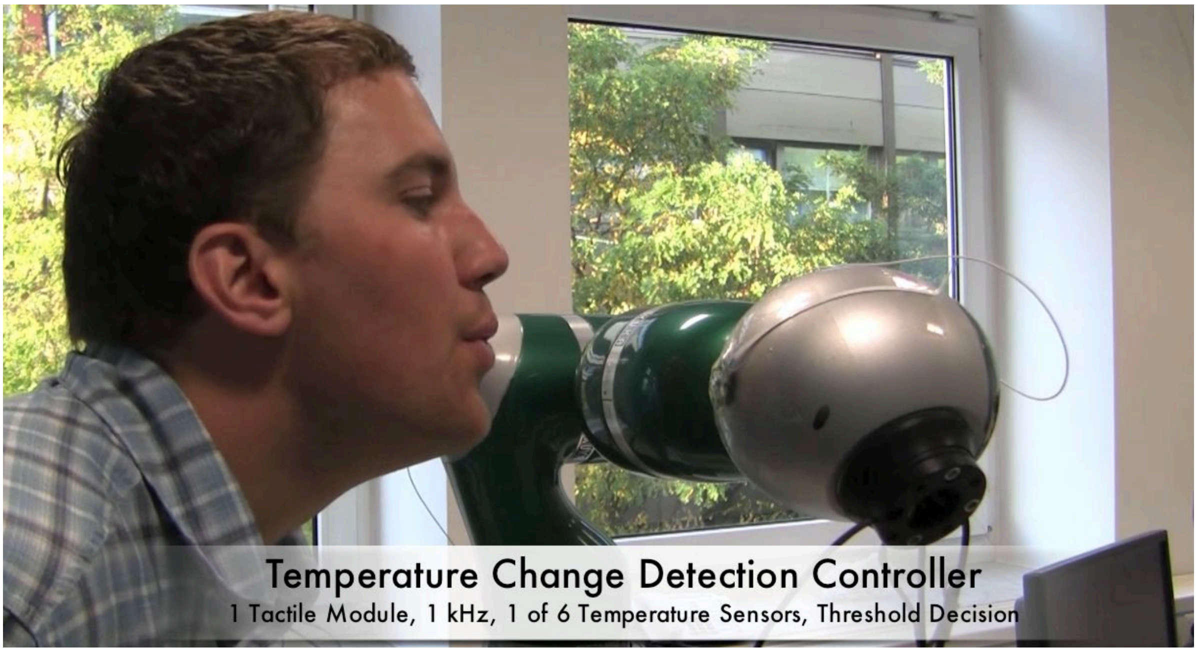

FIGURE 6.22. The figure shows the author, gently blowing on a cell of the artificial skin. In the video this picture is captured from, the robot evades next.

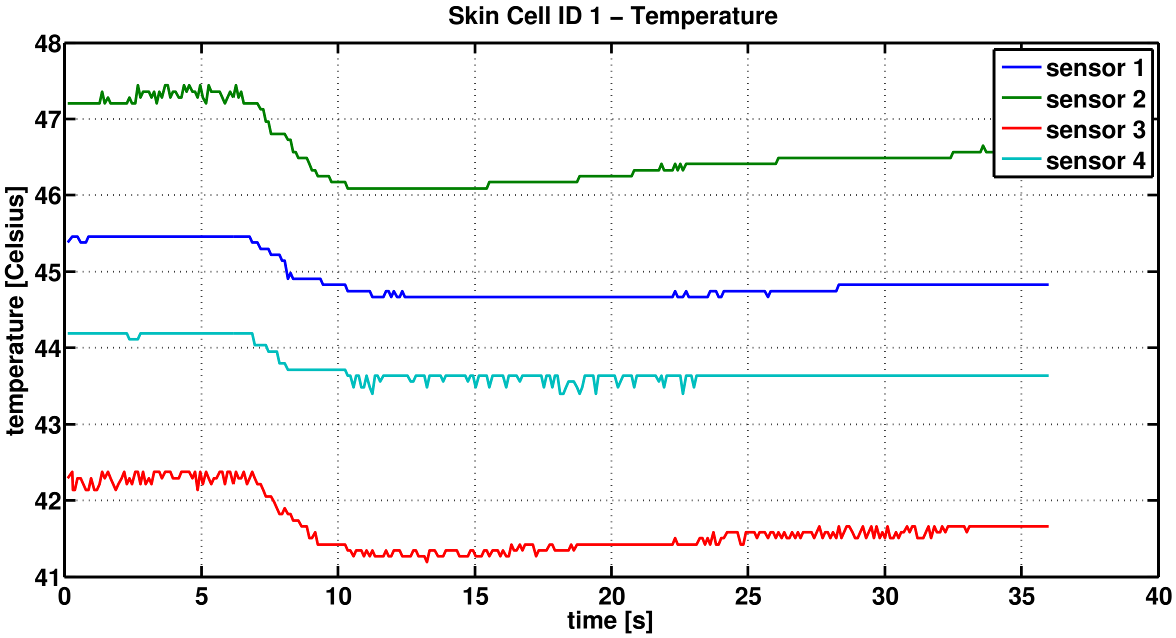

FIGURE 6.23. The figure shows the thermal cooling effect either by gently blowing on a skin cell of the artificial skin. 95 % of the response value is reached after 2.4 s. Setting adequate thresholds, the robot reacts approximately after 500 ms.

FIGURE 6.24. The figure shows the tip-tap controller reacting on impacts on the fingers by changing the direction – the robot is trapped between the fingers.

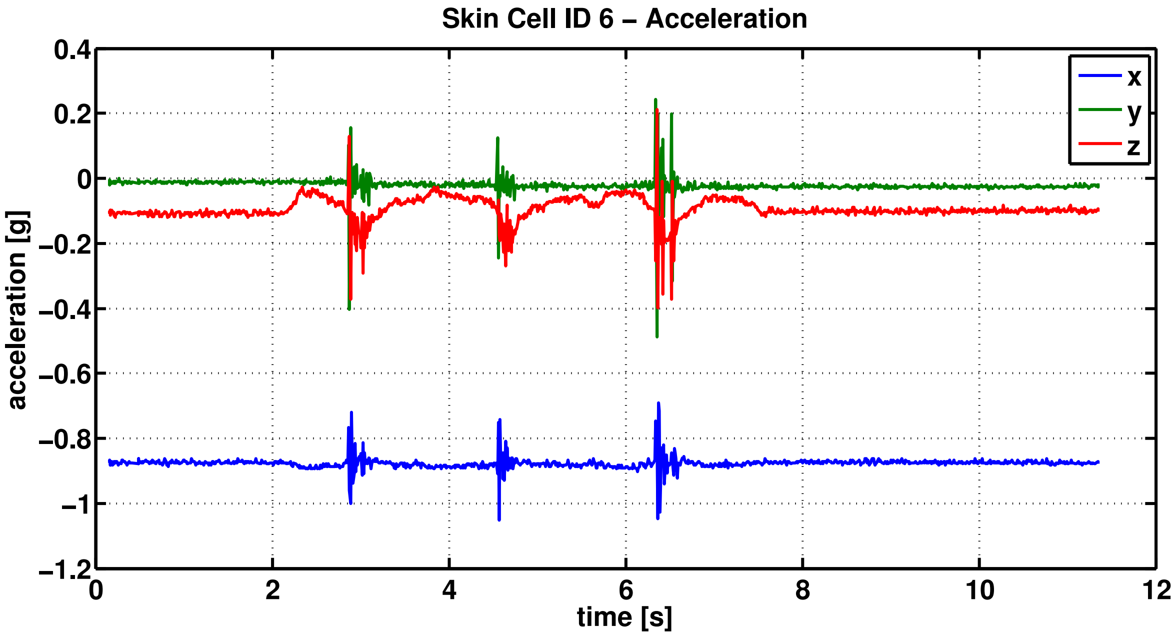

FIGURE 6.25. The figure shows exemplary signals from one skin cell accelerometer when impacts (similar to Fig. 6.24) occur on a KUKA LWR arm.

6.4.2.3. Acceleration - Impact Reaction

Safety is very important when a robot interacts with people or the environment. Independent of the robot force sensors (tactile or joint) we need to detect self- or environment impacts. As a robot body normally moves smoothly, we discriminate unexpected impacts with objects from the rate of change of acceleration (see Fig. 6.25). To demonstrate this effect, we programmed the robot to go in the opposite direction whenever a constant magnitude threshold was detected on the accelerometer axis normal to a skin cell (see Fig. 6.24). As an impact has influence on the acceleration of a whole body part, and the exited vibrations are partially conducted by the frame, we were able to use a single accelerometer to detect impacts at various body part locations and even across body parts.

6.4.2.4. Acceleration - End Effector Orientation Control

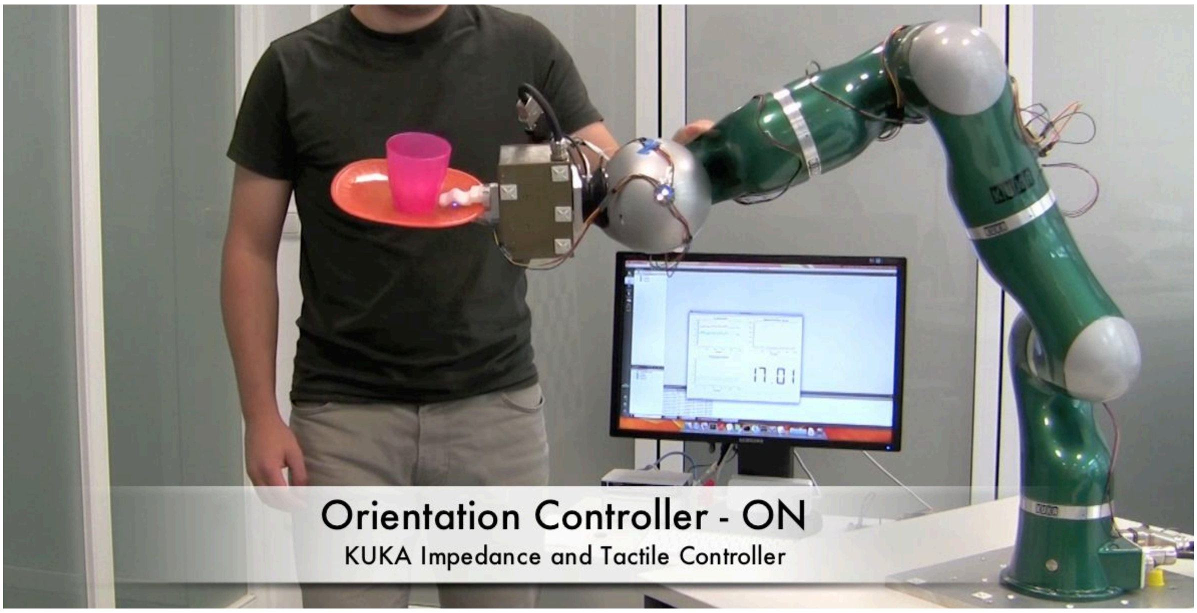

FIGURE 6.26. The figure shows the Kka LWR arm balancing a cup with orientation control based on an accelerometer below the tablet.

In this experiment, we implemented an orientation controller for the robot end effector, with one local accelerometer of a skin cell on it (see Fig. 6.26). Two proportional controllers for the pitch and roll axes stabilize the orientation based on the measured acceleration vector. As the accelerometer measures a superposition of the gravity and movement acceleration vector, we normalized the axes values before we calculated the two orientations angles. We are not stabilizing towards the world coordinates, but towards the normal vector of the current superposition of both acceleration values. This enables us to stabilize a loosely placed cup on a plate that is held by the end effector even when the rest of the robot is moving. If necessary, we detect additional acceleration by movements, by a deviation of the norm from 1 g. A data log of the experiment is given in Fig. 6.27. This test also shows the sufficiently low latency of our system for dynamic control.

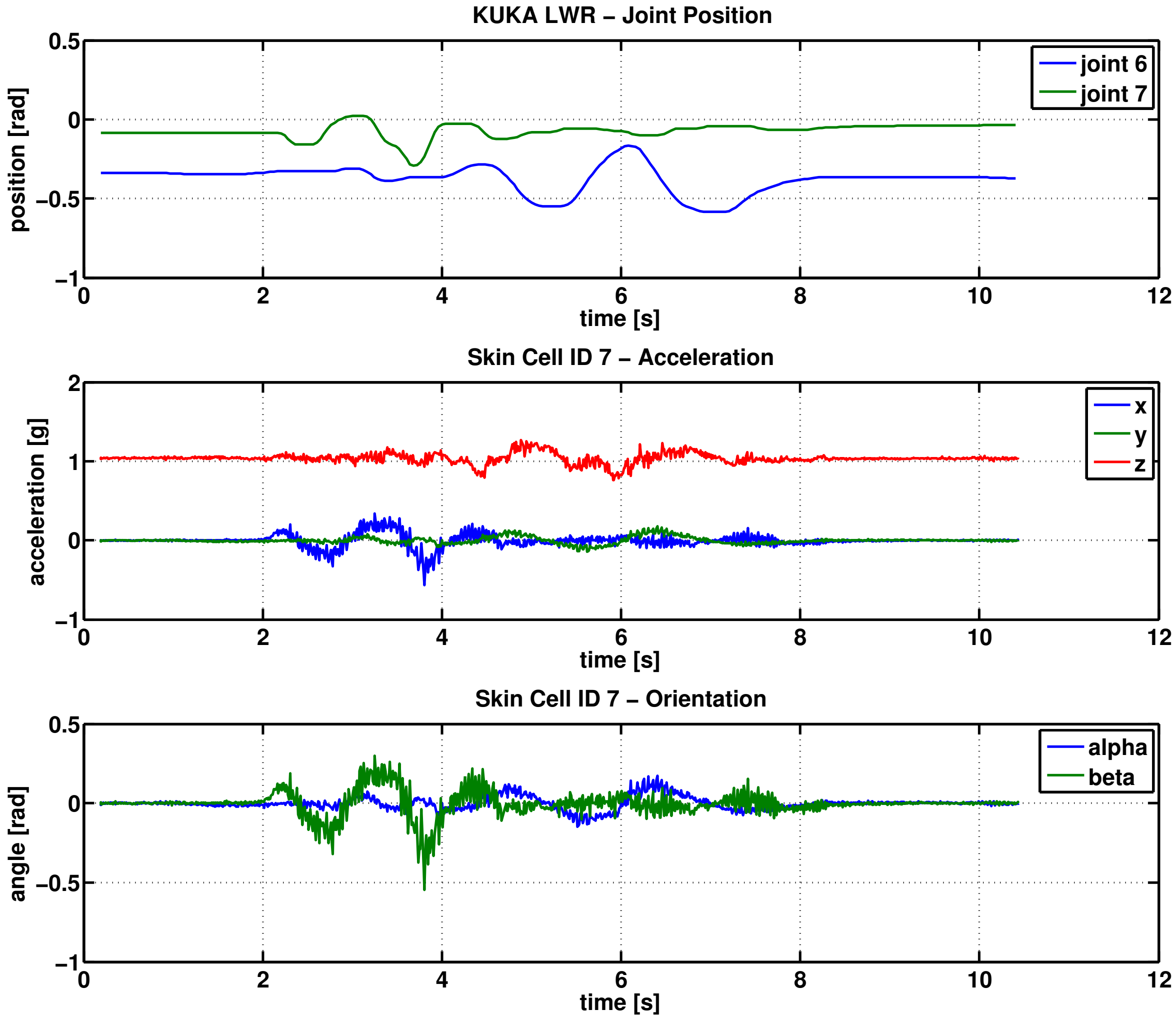

FIGURE 6.27. The figure shows signal plots from the end-effector orientation controller.

6.4.3. Application Note

We demonstrated that multi-modal tactile sensors can be utilized for a variety of tactile interactions with industrial robots. Standard non-compliant robots can be provided with compliance and compliant robots can be enhanced with multi-modal and multi-touch features. For example, we showed that impacts of the robot with the environment can be detected with vibrations measured by the accelerometer, even if the impact was not directly on the skin cell. This feature allows skin cells to be placed at higher spatial distances, while still being able to monitor safety critical impacts. Pre-contact sensors allowed a feather light interaction with the robot, on multiple-simultaneous contact points. We especially showed that antagonistic touch reactions cancel out, like with joint level sensing, but can still be detected and e.g. used to react differently. One of the essential findings we made during those first experiments was that manual calibration is cumbersome and erroneous. We thus identified self-calibration as one of the key challenges to efficiently use artificial skin. Amongst others, this highly complex challenge has been solved in this thesis.

6.5. Factory-in-a-Day

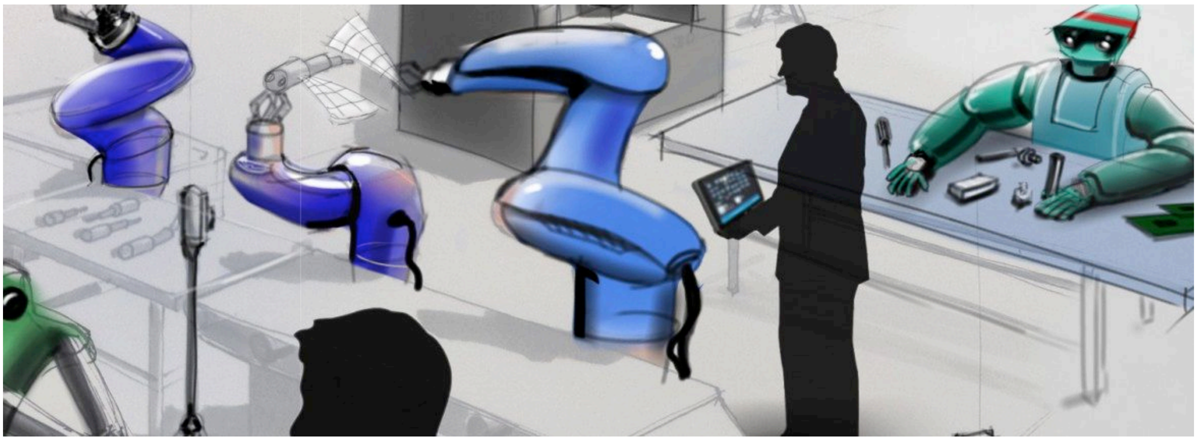

FIGURE 6.28. The figure shows a futuristic factory layout using collaborative robots at small and medium enterprises (SMEs). [Source: www.factory-in-a-day.eu]

"*The project Factory-in-a-day aims at improving the competitiveness of European manufacturing SMEs by removing the primary obstacle for robot automation: installation time and installation cost.*"[`www.factory-in-a-day.eu`]. The EU FP-7 project Factory-in-a-day (FiaD), which we participate in, aims to reduce the installation time of hybrid human-robot production lines, from weeks/months to a single day. The FiaD robots will be able to operate without safety fences due to the utilization of intrinsically safe robots (e.g. Universal Robots' UR-5), dynamic contact avoidance and intention-projection showing the robots' motion plans to the human coworkers [FiaD]. As stated by [Harmon, 1982] (please also refer to Sec. 2.2), artificial skin plays a major role in this context. Enhancing robots with a proximity-sensitive skin, dynamic collision avoidance can be implemented. A set of multi-modal sensors (e.g. force and acceleration) provides safety redundancy in the case collision avoidance fails, e.g. via multi-modal collision detection (refer to Sec. 6.4) or contact force control. At the same time artificial skin provides a large and user friendly human-robot interface. In the framework of FiaD, we intend to utilize this feature to speed up the teach-in process at the installation site and to enable non-expert users to directly interact with the robot, e.g. with gestures or tactile kinesthetic teaching – removing the necessity for complicated teach-pendants. Part of the intention-projection, showing the robots' motion plans, will be projected on the surface of the robot (e.g. LEDs with CellulARSkin). As stated by [Harmon, 1982] users and manufacturers are unwilling and/or unable to cope with specialized installations. The artificial skin system must be able to self-organizing/calibrate and provide a standard software framework that embeds all features. In the context of FiaD, self-organization is especially required to speed up initial integration and to support autonomous failure recovery at the customer.

6.5.1. Research Platform TOM

FIGURE 6.29. The figure shows the robot TOM on the trade fair Automatica 2014, visually displaying the contact states detected on its surface.

TOM (Tactile Omni-directional Mobile Manipulator) is a robot that has been developed at ICS under the umbrella of the Factory-in-a-Day project and has been first introduced at the Automatica trade fair 2014 (see Fig. 6.29). The aim was to show the differences between a standard UR-5 robotic arm and an arm equipped with artificial skin. For this demonstration, we equipped one of the UR-5 robotic arms with 260 skin cells. We then combined the artificial skin framework with a new virtual dynamics control framework developed at ICS (by Emmanuel Dean). With his framework the robot can for example be enhanced with virtual tactile compliance (see Fig. 6.30). We specifically made use of the 3D reconstruction capability of the artificial skin in order to match the skin to the existing robot model. Therefore, we individually 3D reconstructed the three patches of artificial skin. We then imported the resulting 3D skin patch models into ROS. In a quick manual calibration step, the 3 missing transformations of the skin root cells were matched to the RViz (ROS Visualization, see Fig. 6.31) model of the robot. This process sped up the integration of the artificial skin, as it reduced the required number of homogeneous transformations (one for each of the three patches, instead

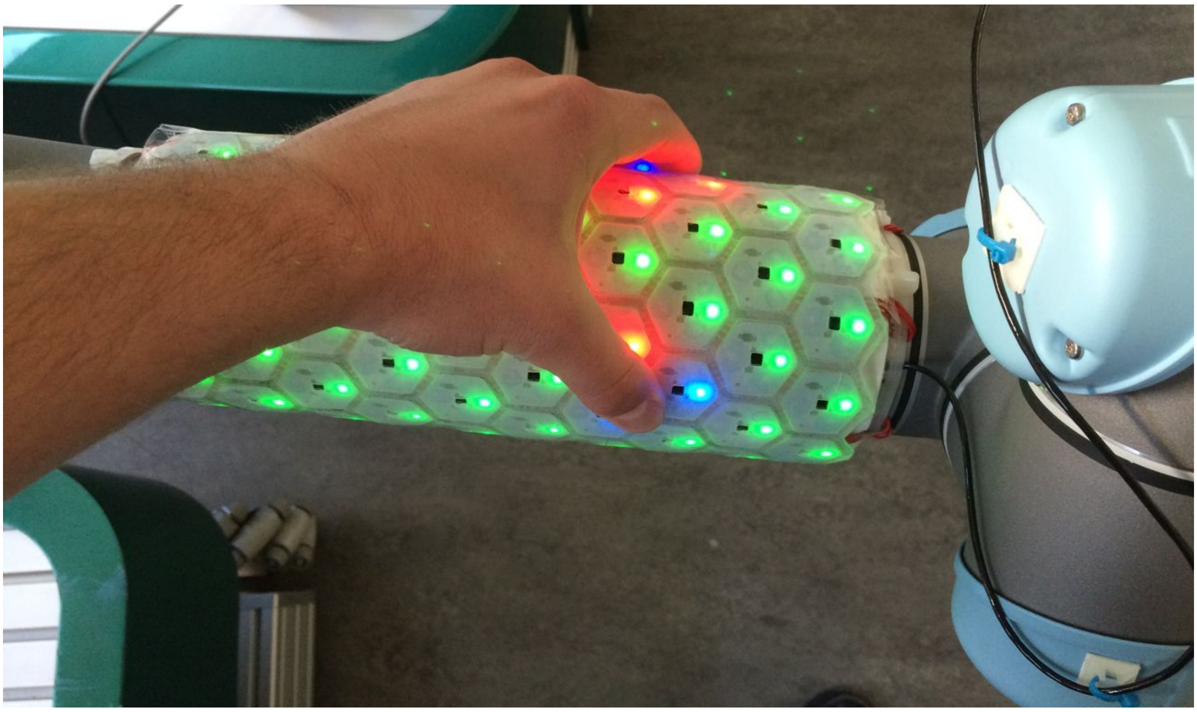

FIGURE 6.30. The figure shows the robot TOM in compliance mode, detecting the approach of a human hand with the proximity sensors (red), while compliant motions are canceled out due to the antagonistic forces (blue) applied to the skin surface.

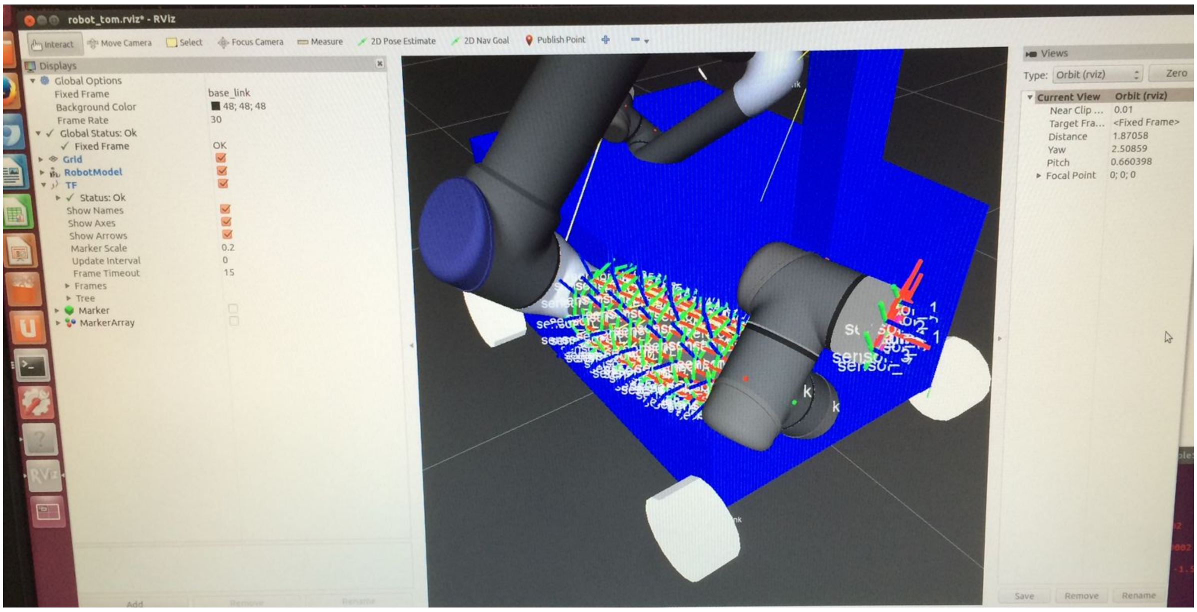

Global Options
Fixed Frame base_link
Background Color 48; 48; 48
Frame Rate 30
✓ Global Status: Ok
✓ Fixed Frame OK
Grid ☑
RobotModel ☑
TF ☑
✓ Status: Ok
Show Names ☑
Show Axes ☑
Show Arrows ☑
Marker Scale 0.2
Update Interval 0
Frame Timeout 15
Frames
Tree
Marker ☐
MarkerArray ☐

Type: Orbit (rviz)
Current View Orbit (rviz)
Near Clip ... 0.01
Target Fra... <Fixed Frame>
Distance 1.87058
Yaw 2.50859
Pitch 0.660398
Focal Point 0; 0; 0

FIGURE 6.31. The figure shows the RViz model of the robot TOM along with the 3D models of the last two patches of artificial skin.

of one for each of the 260 skin cells). Additionally, we were able to utilize a method that we call heuristic visual matching, finding the relative transformation between two CAD models by their best visual alignment. Given the final results of this thesis, this matching could also be performed fully automatically. The algorithm then automatically calculates a Jacobian for each skin cell and implements an impedance like controller to map multi-modal stimulations into joint motions (similar to the controllers in this thesis). Two of the modalities, force and proximity, have been utilized to interact with the robot. A first implementation of a distributed visual feedback utilized the RGB LEDs in every skin cell to display current contact states, e.g. red for pre-contact (see Fig. 6.32), blue for force (see Fig. 6.30) and green for no touch.

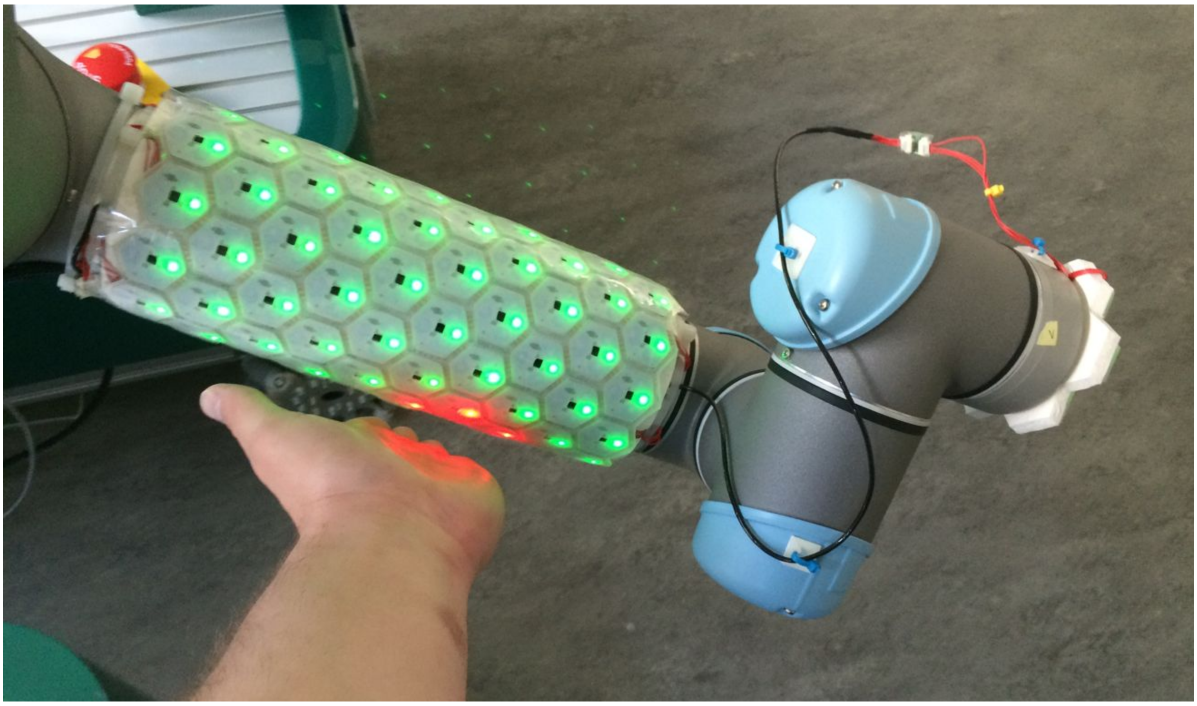

FIGURE 6.32. The figure shows the contact state display of the robot TOM, detecting the approach of a human hand with the proximity sensors (red).

6.5.2. Application Notes

With TOM, we demonstrated our currently largest deployment of artificial skin on a robot (260 skin cells). Large surface areas of the robot arm UR-5 have been enhanced with multi-modal tactile sensitivity. We have shown that our 3D reconstruction algorithm can be utilized to quickly map our skin to existing robot models. We also demonstrated that our artificial skin can be integrated into other control frameworks. Unlike the KUKA LWR, UR-5 is a low-cost industrial robot that is used in industry and does not feature advanced joint level torque sensing. With our artificial skin, we still achieved to render this non-compliant robot compliant.

6.6. Summary

In this chapter, we demonstrated the feasibility of our new artificial skin system. We applied our skin on more than three different robots (e.g. Kuka's LWR, Universal Robots' UR-5 and Kawada Industry's HRP-2), showing that our design is transferable. Our latest implementation on the robot TOM (see Fig. 6.29) supports the scalability of our approach to a high number of skin cells and large areas. We demonstrated that our self-organization features are applicable to complex robots, such as a HRP-2, and can largely speed up the integration time on industrial robots, such as TOM. We showed exemplary applications of our artificial skin: such as grasping, collision avoidance and human-robot interaction. With demonstrators on international conferences and trade fairs, e.g. Automatica 2014, we have proven the reliability of our system. First internal (TOM) and external (Walk Again Project, Factory-in-a-Day) projects, provided us with feedback on the usability and on the remaining technical challenges.

CHAPTER 7

Conclusion

> In literature and in life we ultimately pursue, not conclusions,
> but beginnings.
>
> *(Sam Tanenhaus:* Literature Unbound*)*

In this chapter, we first summarize the content of this thesis. We then state our contribution on top of the related works. Finally, we give a brief overview of potential future works.

7.1. Summary

In this thesis, we presented new approaches to design, self-organize and utilize artificial skin. In Chapter 1 we introduced our motivation to develop a self-organizing artificial skin. We denoted potential impacts in the field of robotics and beyond, e.g. in health care or industry. We summarized challenges involved in the design and organization of a large area artificial skin, along with our contributions to solve these issues. In Chapter 2, we gave an overview on the related work. Starting from biological skin and the development of human body schema, we introduced multiple approaches to develop electronic sensitive skins and the notion of body schema in robotics, for the development of spatial embeddings and kinematic modeling/calibration. In Chapter 3, we introduced a new approach to create artificial skin from multi-modal skin cells. With our biologically inspired, modular approach, we solved common challenges like wiring efforts, failure tolerance, processing efforts and scalability. The self-organizing network of skin cells automatically initializes and adapts to changes in the topology, e.g. recovers from wiring failures using redundant cell-2-cell connections. Our modular approach can be easily transfered to other robots or applications. In Chapter 4, we introduced a new approach to automatically reconstruct the 3D surface of body parts equipped with our artificial skin and a new method to visually combine distributed tactile representations. This method allows us to quickly and automatically acquire the location and orientation of all distributed tactile sensors, relative to an egocentric coordinate system and only using internal sensors. At the same time internal visual and tactile frames of reference are combined. In Chapter 5, we introduced novel approaches to acquire kinematic knowledge for robots equipped with our skin system, from the acquisition of an inverse-Jacobian like mapping, via the exploration of the kinematic tree, to a full kinematic model estimation. Altogether, this allows us to fuse visual, tactile and proprioceptive sensations in a single self-centered body representation. In Chapter 6, we finally showed exemplary applications of our artificial skin system, enhancing the interaction capabilities of industrial robots or enabling a full-sized humanoid to grasp unknown objects only with tactile feedback. Therefore, we introduced a new framework to map multi-modal stimulations into motor actions, taking the location of tactile stimuli and tactile events into account. All-in-all this thesis contributes a complete approach to design, organize and utilize a multi-modal, modular artificial skin system.

7.2. Contribution

This thesis extends the state of the art (refer to Sec. 2) in the following aspects.

Modular skin: We presented a novel modular approach to create artificial skin from a multi-modal, self-contained skin cell. Our design supports the acquisition and transfer of multi-modal tactile signals, along with distributed processing capabilities. Digital cell-2-cell transmissions reduce wiring efforts and provide robustness against interferences and failure. Due to the high modularity, the system can be easily applied to different robots and applications.

Force Sensor: We developed a low-cost, capacitive force sensor. Due to our novel design, based on a metal spring, outstanding sensor performance has been achieved. The sensor is scalable to a variety of force sensing ranges. Its robustness against mechanical abuse, due to an intrinsic overload mode, has been proven. In order to reduce production offsets, a patented self-alignment method has been invented.

Multi-modal integration: A biological inspired set of multi-modal tactile sensors has been chosen. All multi-modal sensors have been integrated in a single skin cell. The cell supports the acquisition, preprocessing and transfer of all its multi-modal sensor signals. A composite, micro-structured coating has been developed to support and protect all discrete sensors.

Artificial skin network: We developed methods to support a scalable surface sensor network, with a high flexibility in the network topology. Our system supports a fast and automatic network self-exploration and can forward acquired sensor data in real-time. Failure in the network connections can be quickly and automatically handled with a re-exploration, supporting an enhanced life-time of the artificial skin.

3D surface reconstruction: Our 3D surface reconstruction method allows to precisely acquire the surface model of robotic body parts and the location/orientation of each sensor on it. Utilizing network connectivities and embedded motion sensors, we can acquire the required local information within a very short time. Our algorithm can deal with different topologies, is scalable and can be enhanced with additional information, e.g. local and global transformations as has been shown with the visual marker approach.

Visual markers: In combination with our 3D surface reconstruction algorithm, we are able to turn every patch of the artificial skin into an absolute, active visual marker. This enables us to estimate a homogeneous transformation between visual and tactile coordinate frames in a short time. In comparison to common visual markers, our skin patch markers can conform to arbitrary surfaces and can be largely occluded.

Kinematic calibration: We contribute new methods to explore, model and calibrate an egocentric kinematic model of a robot. Therefore, we only utilize motion sensors distributed on the robot and low-ranging, open-loop motions of the robot. Along with our 3D reconstruction and visual marker method, we can acquire a complete robotic body schema, across visual, tactile and proprioceptive space, within a short time.

Application of artificial skin: In order to proof the effectiveness of our system, we provide exemplary applications: 1) a control framework to adaptively grasp objects with the upper-body of a humanoid robot and multi-modal tactile feedback only; 2) a control framework to enhance multi-modal tactile interactions with industrial robots.

Modular framework: We contribute a complete and scalable framework to support the utilization of a modular artificial skin. The modular nature of the framework allows a quick and easy expansion and/or improvement using extra modules. With our framework new robots and applications can be easily enhanced with an otherwise complex artificial skin technology.

Dissemination: The presented work lead to 2 international journal papers and 9 international conference papers (first author). One European patent has been filed and one international workshop (ICRA13) has been organized. A scientific audience has been addressed with presentations at workshops, a summer school and several invited talks. The work has been disseminated to a general audience with press-releases, interviews to mass media (TV, radio, print) and demonstrations on scientific and trade fairs. The novel skin technology has led to a participation in two ongoing European projects (CONTEST and Factory-in-a-Day).

7.3. Outlook

Although the presented work is complete in itself, a self-organizing modular artificial skin, it is only a starting point on which future work can build:

New technologies: System on chips and flexible printed organic electronics could be utilized to improve the mechanical flexibility and the spatial resolution of the existing sensor system. New mechanical or biomedical sensors, e.g. shear sensors or hormone receptors, would broaden the potential area of application. In order to satisfy diverse needs with a common hardware and framework, a generalized surface sensor chip should be developed. This chip could be the processing and communication center of a variety of hybrid (organic/silicon) skin cells in different application scenarios. First approaches in the direction of flexible and printable sensors are made in the CONTEST project, which we participate in.

Technology transfer: In order to create innovation, we must bring our technology to the market. Building on the first prototype system, this technology transfer could be started soon. Our artificial skin can deliver two key contributions to robotics industry: 1) it can enhance human robot interaction in close contact collaboration; 2) it can provide contact safety and tactile compliance as a flexible add-on solution, even for heavy robots. In order to satisfy industrial needs, the software and hardware framework must be adapted and evaluated according to industrial standards. First approaches towards industrial robots are made under the umbrella of the Factor-in-a-Day project, which we participate in.

Event based system: An early and efficient encoding of spatio-temporal tactile data into events is important for a large scale integration of artificial skin. Sensor signals should be encoded into events as early as possible in order to reduce the required communication and processing bandwidth. The transition to an event based system does not only affect the low-level encoding, but also the real-time communication pathways and low/high level control algorithms. The multi-modal skin cells and framework that have been developed in this thesis, can be extended with this functionality.

Spatio-temporal analysis: Spatio-temporal analysis of tactile data would give way to new applications and enhance the capability of existing robots. A multi-modal artificial skin, as presented in this thesis, could passively or actively classify materials and objects, discriminate human touch from other contacts and distinguish contact states based on past experience. New methods need to be developed, in order to automatically generate and robustly extract spatio-temporal features. Frameworks to support dynamic and transfer learning with (event based) tactile data need to be developed.

Utilizing close encounters: Taking advantage of distributed contacts is a key aspect for future robots, in order to efficiently deal with complex manipulation tasks (e.g. lifting large and heavy objects) and to be able to handle everyday environments (e.g. sitting on a chair while doing handcraft). In this thesis, we presented a first framework to react on multi-modal tactile stimulation and to coordinate these tactile behaviors into primitive tasks. This framework should now be extended. Sensor prediction would allow to suppress expected sensory feedback and to focus attention on unexpected sensations. New control paradigms should be developed, to learn task requirements and to resolve competing low-level reactions. The utilization of close encounters also requires the effective modeling and controlling of contact dynamics.

APPENDIX A

Appendix

> Appendix usually means "small outgrowth from large intestine," but in this case it means "additional information accompanying main text." Or are those really the same things? Think carefully before you insult this book.
>
> *(Pseudonymous Bosch:* The Name of This Book Is Secret*)*

The appendix introduces additional technical details on our artificial skin that did not fit in the main document. In A.1, we show different interfaces for the skin. An exemplary manufacturing process of the current skin prototype is shown in A.2. In A.3 we introduce the demokit that has been developed for the Factory-in-a-Day project. A.4 gives an overview of the skin cell versions we have developed during the thesis. The same is done in A.5 for the elastomer encapsulation. In A.6 we show the scalability of our force sensor to higher force ranges. And finally, in A.7, we consider bandwidth and latency constraints of our current communication system.

A.1. Skin Interfaces

In order to power and communicate with the artificial skin, we developed a variety of interfaces.

The FPGA based Gigabit Ethernet interface (see Fig. A.1) is the most powerful interface. It can currently handle up to 335 skin cells at full speed (250 Hz) on 5 ports (refer to Sec. A.7). The same limit in numbers applies for powering the connected skin cells. The interface provides a DC/DC converted 5 V output voltage, with up to 6 A current output, from a wide range (7-35 V) input voltage. In order to simultaneously reset all skin cells, the supply voltage can be switched on/off from central control. The utilization of Gigabit Ethernet UDP packets causes minimal transmission delays and computational overhead on the control PC. At the same time Ethernet allows to easily interface to a great variety of robotic hardware. Due to the parallel processing in the FPGA, this interface can be easily extended to support more skin cells. With up to 87 ports on a single interface, 5829 skin cells could be handled at full speed (250 Hz).

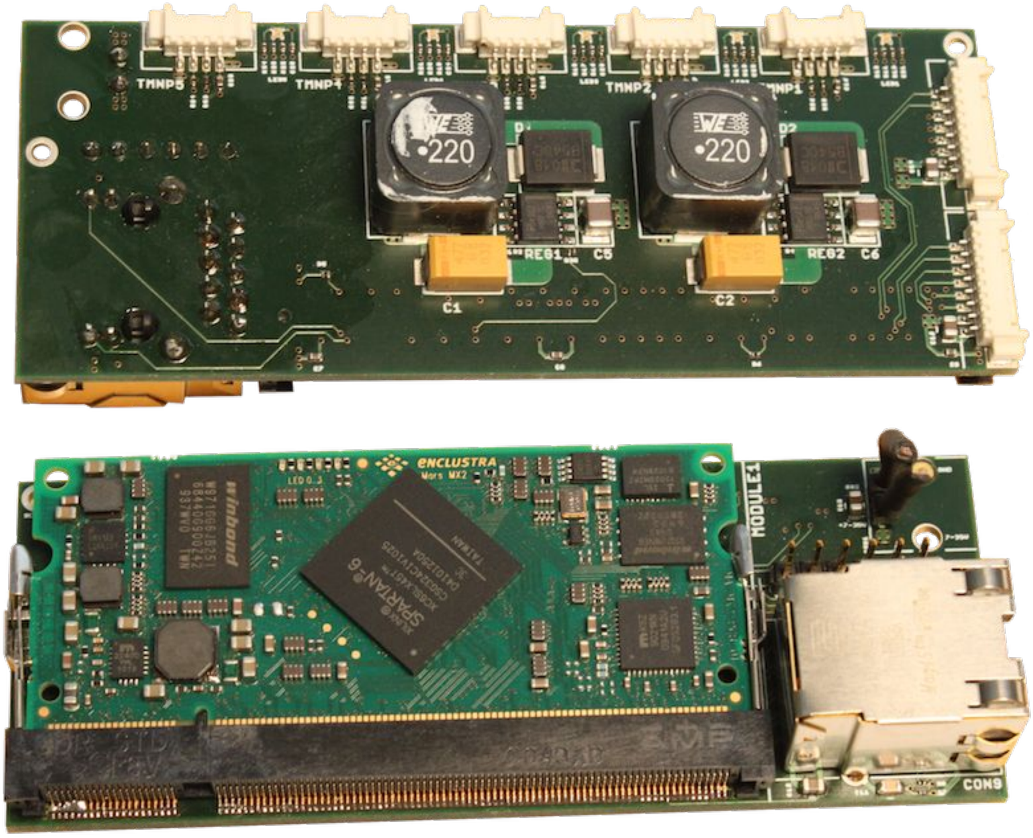

FIGURE A.1. The figure shows the Gigabit Ethernet interface board.

The Bluetooth interface (see Fig. A.2) is the only wireless interface we currently support. Bluetooth was preferred over WiFi, due to the lower power consumption, low cost and simplified setup. High performance WiFi connections can also be realized by interfacing our Gigabit Ethernet interface with wireless switches. The Bluetooth interface's transmission capability is limited by the Bluetooth standard, as well as the utilization of the serial SPP protocol. The maximum throughput of our module, an OBS421 from connectBlue, is $1.3\,\mathrm{Mbit\,s^{-1}}$. With 20 byte data messages, theoretically up to 32 skin cells could be served at full speed (250 Hz). Practically this number is further limited. Due to the conversion of skin cell packets to a serial stream, the package structure is lost, causing additional delay and re-packing issues on the PC side. The same issue applies to common serial to USB converters. Due to the increasing transmission loop delay, with an increasing number of Bluetooth modules, the maximum number of modules is reduced from 7 to 3. Each module only features a single interface port.

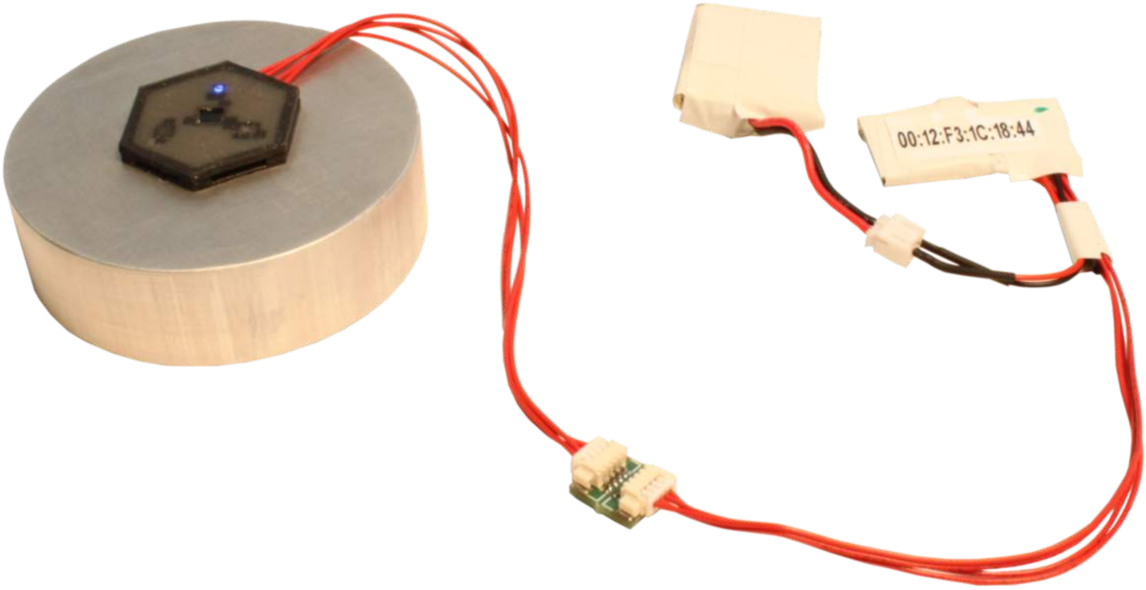

FIGURE A.2. The figure show the Bluetooth interface, along with a skin cell and the battery.

The standalone CAN interface (see Fig. A.3) has been developed to interface the skin without a PC in the 'Walk-Again-Project'. Therefore, it incorporates all necessary code for the skin network exploration that is commonly handled by the PC. Its transmission capabilities are limited due to the maximum $1\,\mathrm{Mbit\,s^{-1}}$ bandwidth of the CAN bus. Skin cell package IDs are mapped to CAN bus message IDs. The advantage of this board is its low cost and its stand-alone capabilities. The interface can also be enhanced with $10/100\mathrm{Mbit\,s^{-1}}$ Ethernet or USB 2.0 (full speed) connections. Due to the utilization of a micro-controller, instead of an

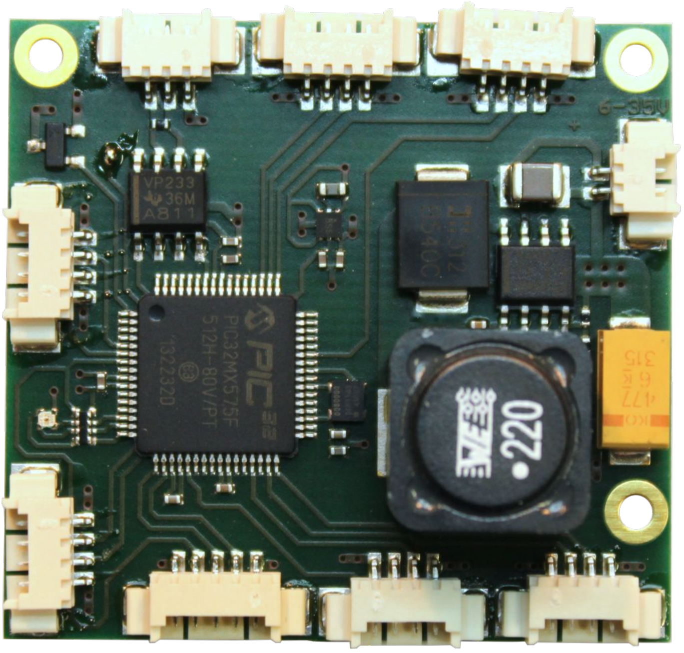

FIGURE A.3. The figure shows the CAN interface we developed to operate the skin stand-alone and interface it e.g. with the exoskeleton robot of the 'WalkAgainProject'.

FPGA, the number of cells that can be connected is limited by the re-packing capabilities of the micro-controller. First experiments (PIC32 Ethernet Starter Kit) indicate a limitation of about 17000 UDP packets per second, relating approximately to 80 skin cells at 250 Hz update rate.

A.2. Skin Assembly

Currently the assembly of a skin patch with standard electronics is split into the following steps: We first buy discrete components and the printed circuit boards. Those are then sent to a pick&place company that mounts the components for us (see Fig. A.4). In a first step, we program all cells with the micro-controller software (boot loader and application code). We then separate the production trays into single skin cells (see Fig. A.5). Afterwards, the skin cells are pick & placed into templates, according to the specific dimension of the skin patch we wish to produce (see Fig. A.6). We then dispense the solder paste on the ports of the skin cells (see Fig. A.7). and place the flexible PCBs on the guidances of the solder template (see Fig. A.8). The cell-2-cell connections can now be soldered in a reflow or hot air process (see Fig. A.9). We also mount the cables to interface the skin at the desired boundary ports (see Fig. A.10). After this step, we perform a final test before encapsulation (see Fig. A.11). The bottom and top mold are either printed with a rapid prototyping printer or molded with silicon and molding templates (see Fig. A.12). The electronic boards are finally put in between the bottom and the top elastomer and both molds are glued together (see Fig. A.13). Currently, this

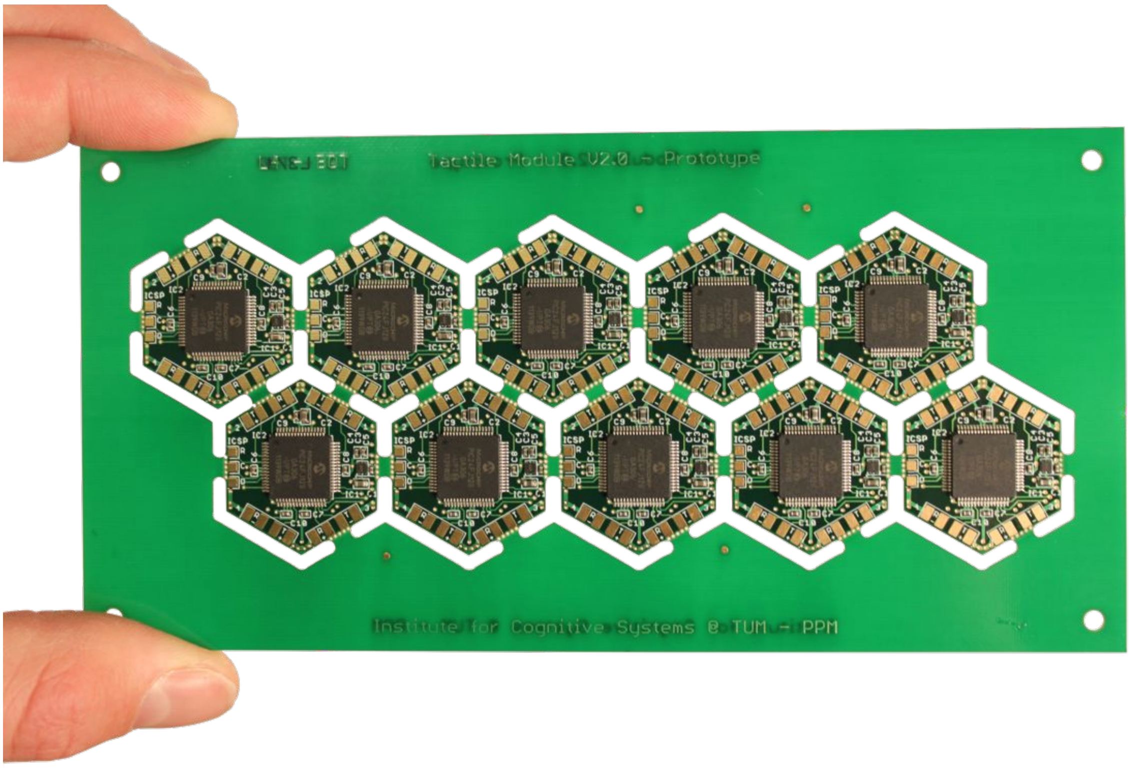

FIGURE A.4. The figure shows a production panel, holding 10 skin cells, as returned from the component pick & place company.

FIGURE A.5. The figure shows the skin cells separated from the production panel.

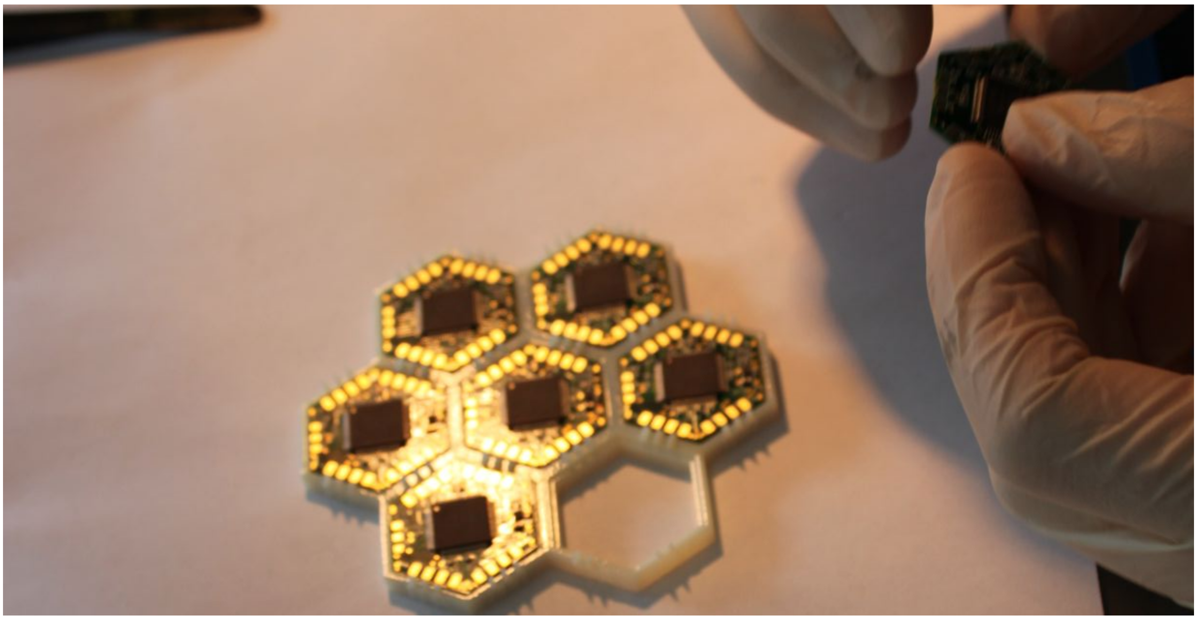

FIGURE A.6. The figure shows the skin cell pick&place process into a soldering template.

production process still involves a lot of costly manual labor. This is why we are looking into options to automate the entire process. Especially the handling of flexible materials, e.g. the interfacing cables (see Fig. A.10) and elastomer covers (see Fig. A.13), is challenging. In the framework of the Factory-in-a-Day project, we would like to develop a shared human/robot workspace for the collaborative assembly of artificial skin by and for robots.

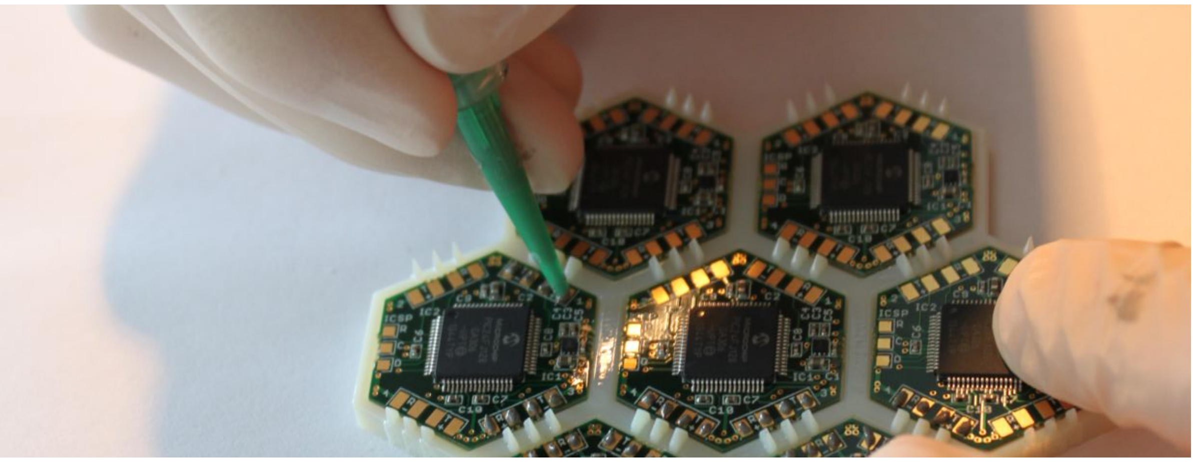

FIGURE A.7. The figure shows the solder paste dispensing process for the flexible cell-2-cell interconnects.

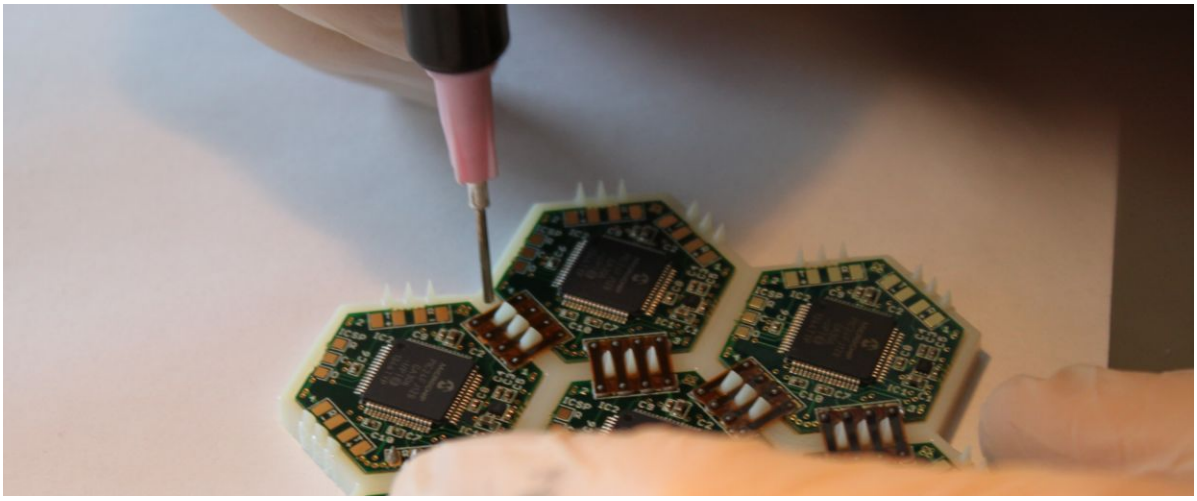

FIGURE A.8. The figure shows the pick&place process of the flexible cell-2-cell connection into the solder template.

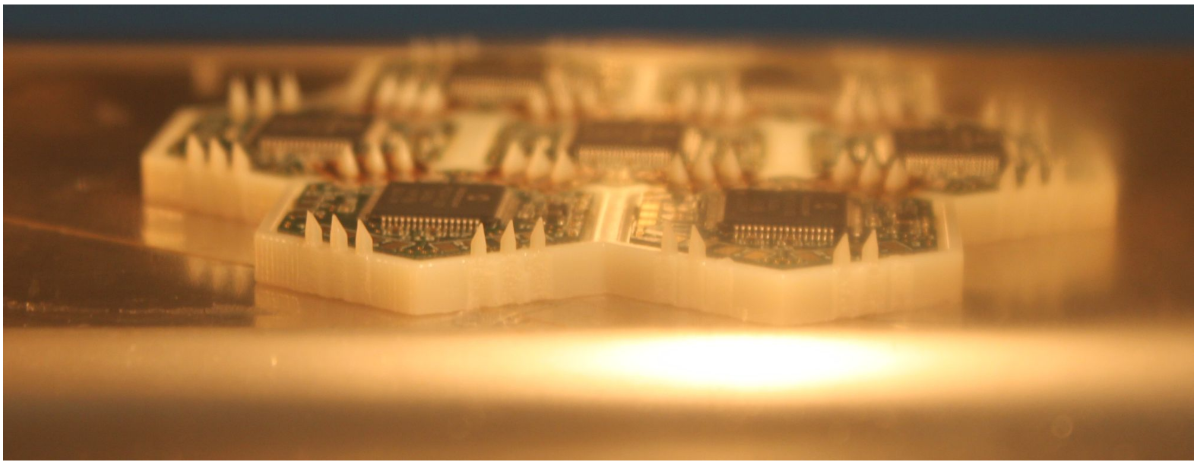

FIGURE A.9. The figure shows the re-flow soldering of the flexible cell-2-cell connections.

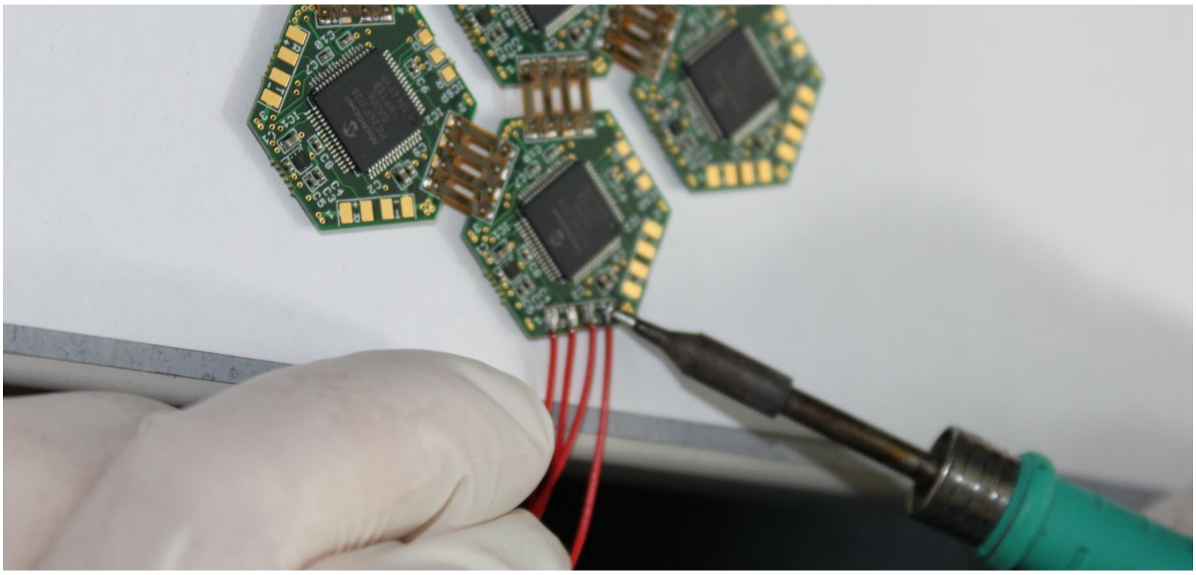

FIGURE A.10. The figure shows the process of soldering interface cables to the skin patches.

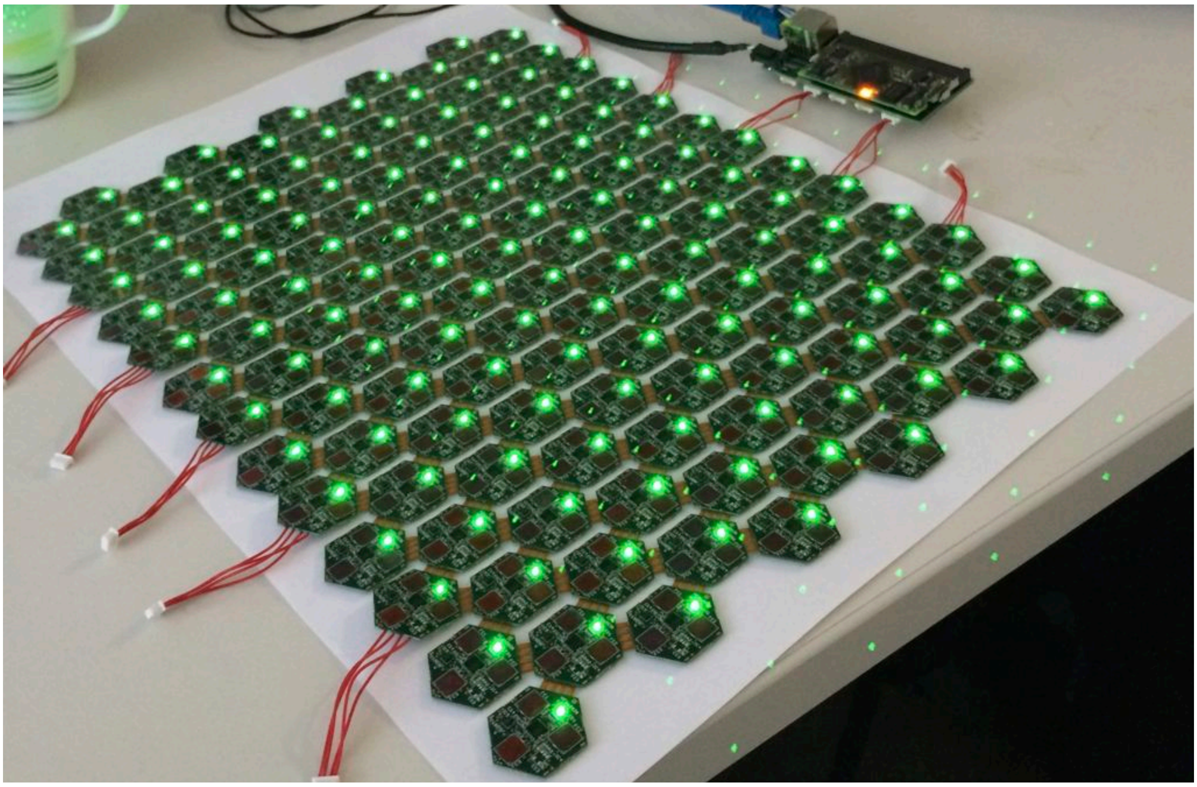

FIGURE A.11. The figure shows an active skin patch with 110 skin cells before the elastomer encapsulation.

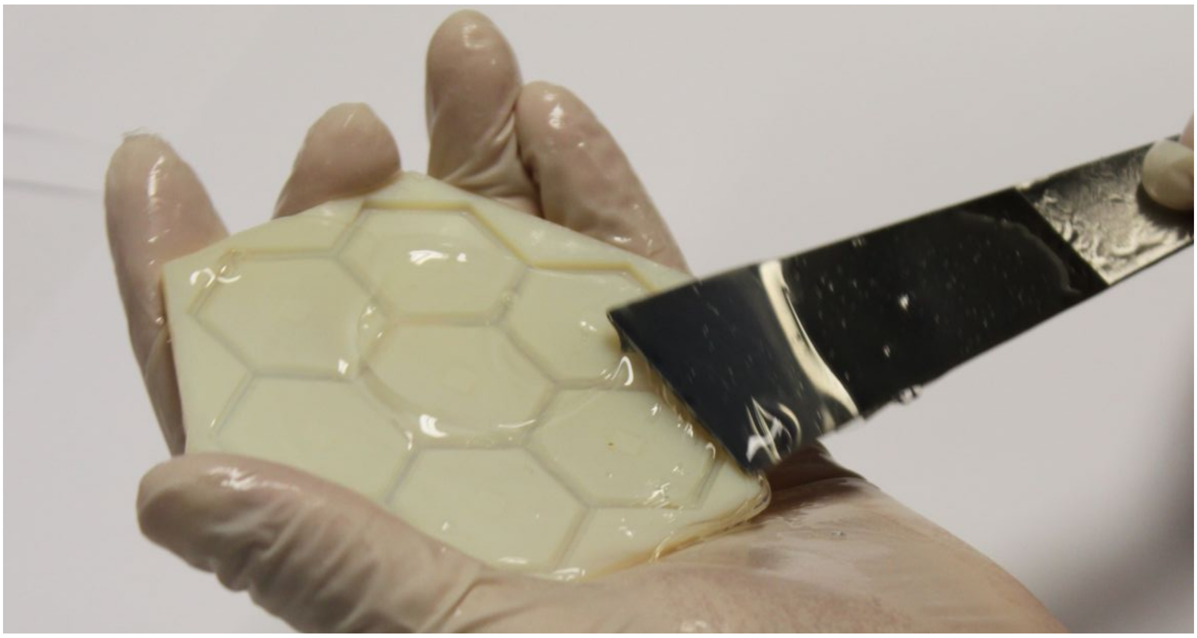

FIGURE A.12. The figure shows the filling of the top mold for a silicone forming process to produce the skin elastomer.

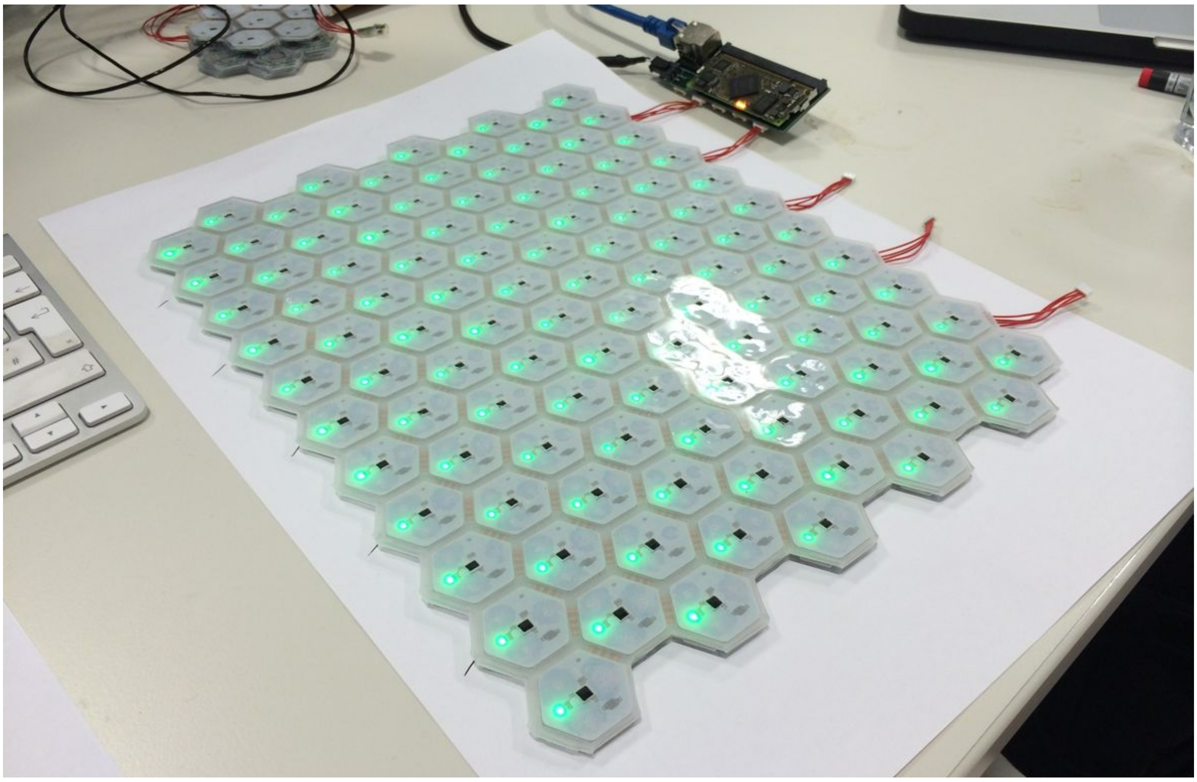

FIGURE A.13. The figure shows an active skin patch with 110 skin cells after the elastomer encapsulation.

A.3. Demo Kit

FIGURE A.14. The figure shows the demo kit delivered to partners in the European Union FP-7 project 'Factory-in-a-Day'.

In order to disseminate our work to a broader community, and in order to collect feedback for a potential spin-off company, we created a demo kit within the framework of the EU FP-7 project 'Factory-in-a-day'. The demo kit contains the required hardware (see Fig. A.14) to operate CellulARSkin^{TM} with an additional PC. All algorithms have been ported to ROS, by Emmanuel Dean, and provided as ROS drivers. In a basic tutorial, the user can control the classical ROS turtle via multi-modal tactile input (see Fig. A.15).

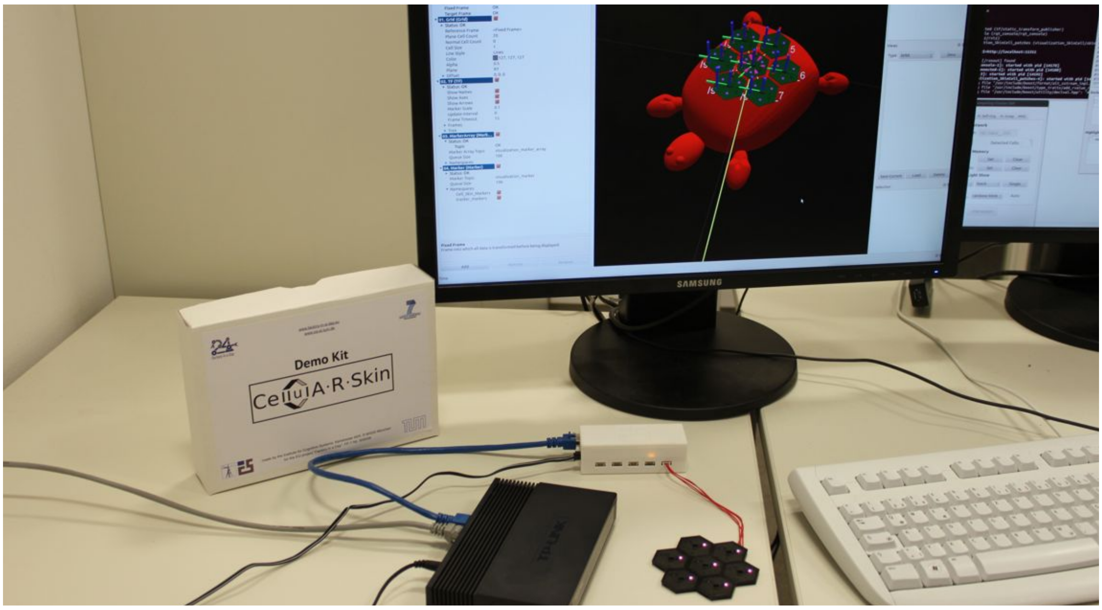

FIGURE A.15. The figure shows the visualization of the demo-kit's ROS tutorial, where the user can experience tactile interaction with a simulated turtle.

A.4. Skin Cell Versions

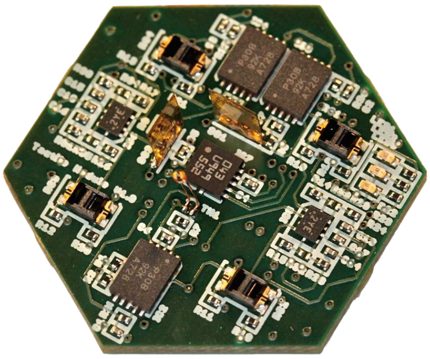

FIGURE A.16. The figure shows a skin cell version 1.0.

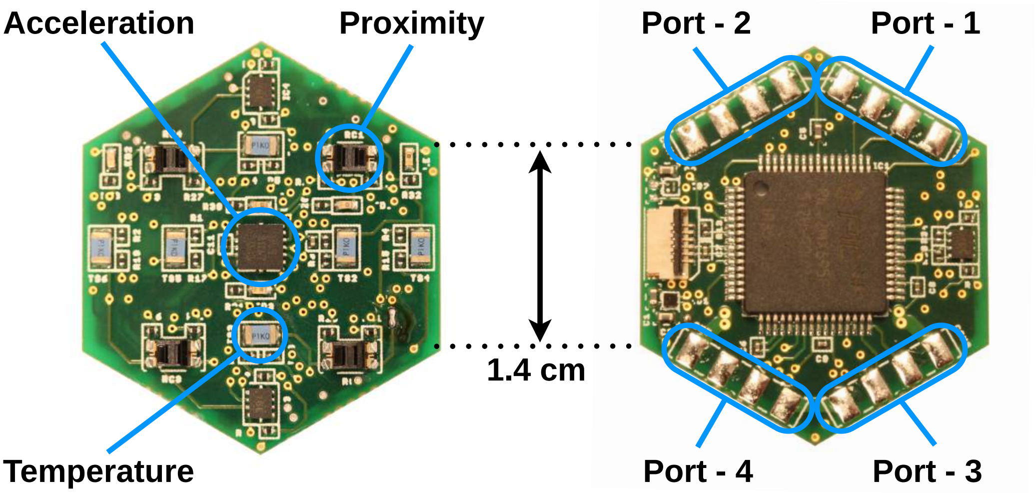

FIGURE A.17. The figure shows a skin cell version 1.1.

Most of the work in this thesis has been performed with version 2.0 of our multi-modal skin cell (see Fig. A.18). In this section, we would like to shortly introduce the differences between the multiple versions of our skin cells. The dimension of the cells are equal between all versions. Both first generation versions operated with a PIC32MX695F micro-controller. In comparison to the current PIC24FJ128GA306 the serial communication speed of this chip (12 $\mathrm{Mbit\,s^{-1}}$) was three times higher than the current 4 $\mathrm{Mbit\,s^{-1}}$. Alas, it's power consumption with 60 mA, instead of now 7 mA, was also more than 8 times higher. For an artificial skin, the differences between 32 and 16 bit architecture are negligible – commonly 16 bit is a better business choice. Only 3 pieces have been manufactured of version 1.0 (see Fig. A.16),

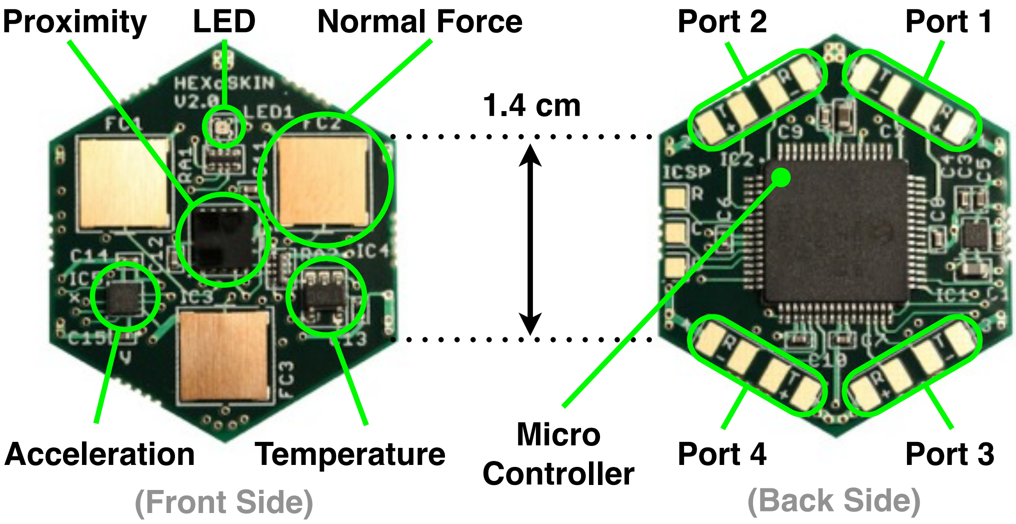

FIGURE A.18. The figure shows a skin cell version 2.0.

about 140 pieces of version 1.1 (see Fig. A.17) and more than 1500 pieces of version 2.0 (see Fig. A.18). Therefore production costs had to be optimized and reduced, simplifying the design and reducing components. Version 2.0 for example only requires a 4 layer board, instead of 6 layers with the previous versions. In order to reduce cost and space, the programming connector was shifted to test pads and analog circuitry was reduced to the available components in the micro-controller. Most changes have been made on the sensor side. From version 1.0 to version 1.1, we removed all non-SMD components, e.g. the strain gages and the thermistor. From version 1.1 to version 2.0, we largely introduced digital sensors, in order to improve performance (e.g. noise and resolution) and get rid of analog circuitry. Version 2.0 is also the first version with a customized sensor – the normal force sensor. The elastomer covers that are protecting the skin from both sides, have been introduced from version 1.1 on. Large efforts have been made, to integrate multiple discrete sensor modalities into the constrained common space. We tried to keep the skin thin, while maintaining the performance constraints for all sensor modalities, explicitly making use of the 3D placement of the sensors (refer to Sec. 3.2.2.2).

A.5. Elastomer Cover Versions

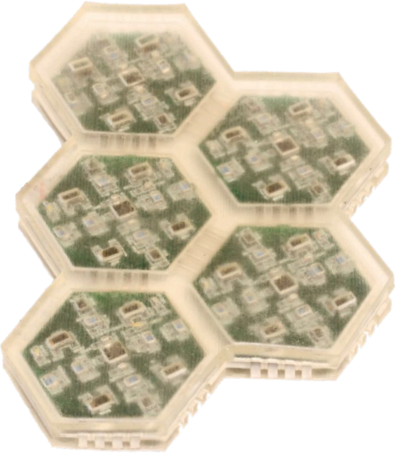

FIGURE A.19. The figure shows the elastomer cover version 1.1.

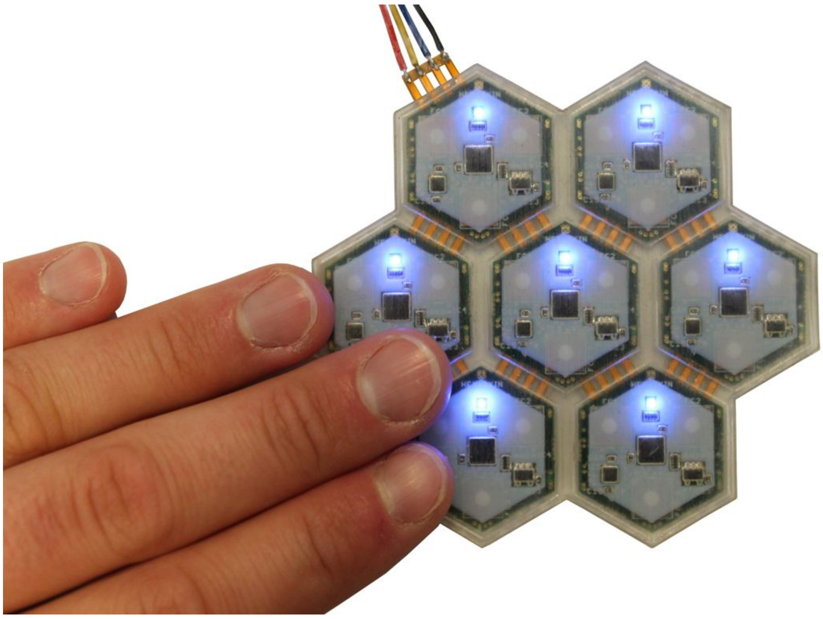

FIGURE A.20. The figure shows the elastomer cover version 2.0.

Multiple elastomer covers have been developed for the artificial skin. Fig. A.19 shows the initial single material version for version 1.1 of the skin cells. With version 2.0 (refer to Sec. A.4) of the skin cells, we introduced the first composite material for the top elastomer cover (see Fig. A.20). The harder material is necessary to collect and focus forces onto the discrete force sensors. With the first cover version, we experienced some problems with the low infrared transparency of the 3D printed material and insufficient receptive fields with the

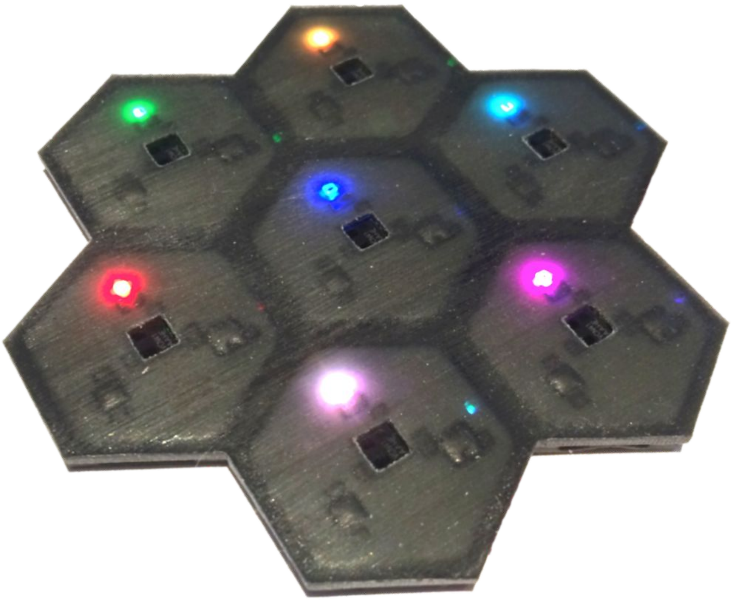

FIGURE A.21. The figure shows the elastomer cover version 2.1.

force sensors. The next cover version (see Fig. A.21) provided a cut-out for the proximity sensor and the LED, and a thicker hard epidermal layer to better collect contact forces applied to the surface. As this removed the need for an opaque material, we switched to the more frequently used black material color (cheaper). Fig. A.22 shows a special version of the cover for the Walk Again Project which has been enhanced with domes. Amongst others, this serves to ensure contact is made on a surface close to the location of the discrete force sensors. Fig. A.23, finally shows the latest version of the skin cover, made from silicon molding and plastic inserts. Molding the skin has two major benefits: 1) molding can dramatically lower the cost in mass production; 2) more durable materials, e.g. silicon, can be utilized. Difficulties to glue the dirt-repelling, high energetic surface of the silicon material have been solved with priming chemicals.

FIGURE A.22. The figure shows the elastomer cover version 2.S.

FIGURE A.23. The figure shows the elastomer cover version 2.2.

A.6. Force Sensor - Extended Range

In section 3.3 we stated that our custom force sensor can be easily scaled to support higher forces. In the following, we present results for extending the force sensitive range of our custom made force sensor. Therefore, we manufactured two additional versions of the CuBe2 cap, deviating from the common 100 µm thick substrate and 50 µm deep cavity. One version is etched from a 150 um thick substrate, etching only a 50 um cavity into the material. This 1/3 to 2/3 etching process is more complicated for the manufacturer, but gives higher capacitive changes due to lower initial distance. The other version is etched from a 300 um thick substrate, etching a 150 um cavity into the material. We manufactured skin cells with both versions and tested them with the flat tip of an Imada DS2-50 force gauge on a PCE-FTS 50 linear test stand. The resulting plots (see Fig. A.24 and Fig. A.25) support our sigmoid function approximation in Sec. 3.3 and demonstrate the scalability of our approach to higher force ranges. We cover forces ranges of one to several hundreds of Newtons with a similar cap design and the same skin cell design. This allows us to manufacture skin cells with different force ranges, e.g. for different body parts like arms and feet, in the same production run.

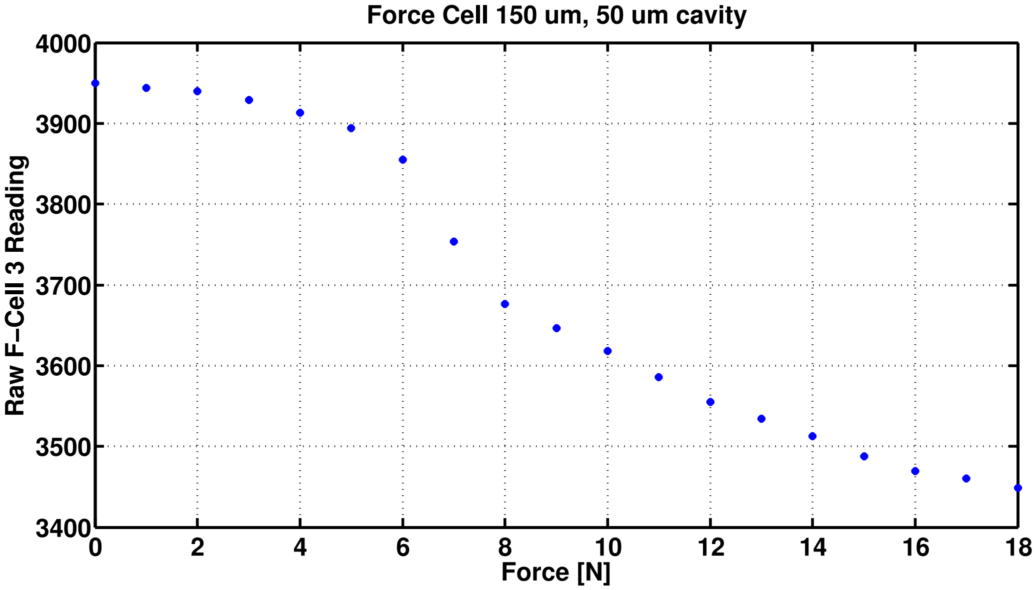

FIGURE A.24. The figure shows the force/response plot of an extended range force sensor with 150 µm material thickness and 50 µm cavity.

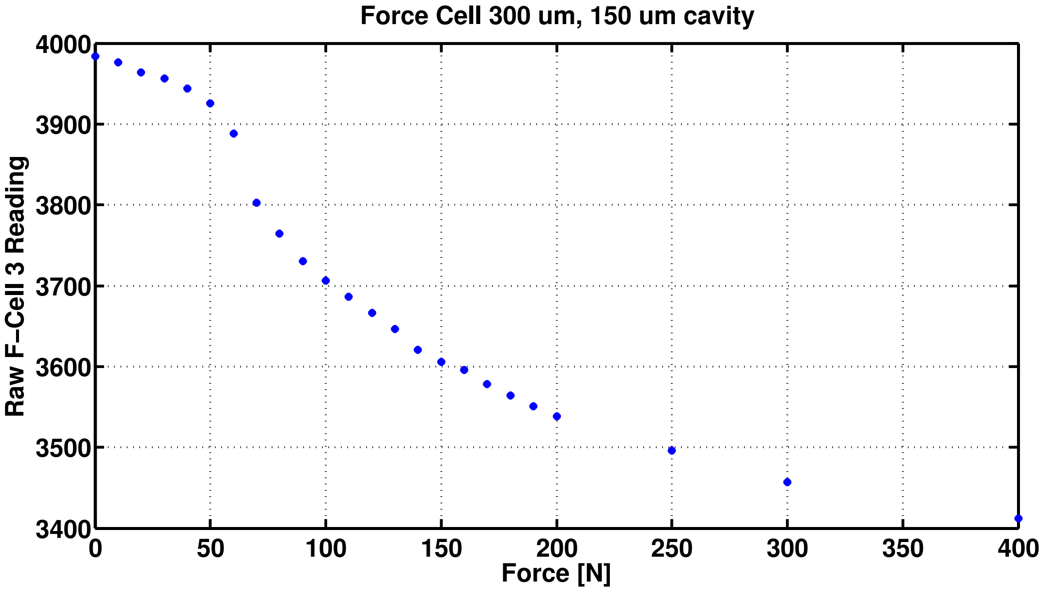

FIGURE A.25. The figure shows the force/response plot of an extended range force sensor with 300 µm material thickness and 150 µm cavity.

A.7. Communication Bandwidth and Latency

Bandwidth: Each port of skin cell version 2.0 (refer to Sec. A.4) utilizes a 4 Mbit s^{-1} UART with an 8b/10b encoding. Each 20 byte long sensor data packet (see Fig. 3.16) is such 200 bit long and its transfer takes about 50 µs. As every skin cell is sending updates with 250 Hz, 50 kbit s^{-1} data are generated. The theoretical limit is such 80 skin cells per port. The practical limit is lower than 67, as an additional 10 µs inter-frame gap is necessary to give interrupt routines time to react. With 5 ports per Gigabit Ethernet interface board (see Fig. A.1), up to 335 skin cells can be handled at full speed (250 Hz). In order to further increase the number of skin cells, additional interface boards have to be provided or the number of ports per interface have to be increased. The maximum number of ports on an interface is limited by the network connection. With one UDP packet, we transfer 20 bytes payload. The UDP, IPv4 and Ethernet layer add an additional 66 bytes overhead on top of the 20 data bytes. This leads to a total amount of 86 bytes that are approximately transmitted in 688 ns on the 1 Gbit s^{-1} line. As a single data packet transfer on the gigabit Ethernet line takes 688 ns, but data packets on the ports are coming in at most every 60 µs (see previous calculation), up to 87 interface ports are theoretically possible. One Gigabit Ethernet interface can consequently handle up to 5829 skin cells of version 2.0 at full speed (250 Hz).

Latency: As calculated in the last paragraph, the transfer of a single 20 byte data packet in the inter-cell network takes less than 60 µs. In a cell-2-cell routing, this is the minimum delay for one step upwards in the communication tree. With this minimum delay of 60 µs and an update time of 4 ms, the depth of a communication tree must not be higher than 66 cells. The worst case routing delay of a skin cell is dependent on the filling level of the local communication buffers (see Fig. 3.15). With every full round robin scheduling cycle a packet must wait, another $4 \cdot 60 = 240$ µs delay are added. With an update rate of 4 ms, the sensor data expires after 16 full waiting cycles. In comparison to the skin cell network, the UDP Gigabit Ethernet transfer adds a marginal latency of 688 ns per utilized interface port.

With a high number off skin cells, sophisticated networking and local data reduction algorithms are required to guarantee that those bandwidth and latency constraints are met.

Bibliography

[Alirezaei *et al.*, 2009] H. Alirezaei, A. Nagakubo and Y. Kuniyoshi. “A tactile distribution sensor which enables stable measurement under high and dynamic stretch”. In *IEEE Symposium on 3D User Interfaces*, pp. 87–93. March 2009. (Cited on page 19.)

[Argall and Billard, 2010] B. D. Argall and A. G. Billard. “A survey of tactile human robot interactions”. *Robotics and Autonomous Systems*, vol. 58, pp. 1159–1176, October 2010. (Cited on page 25.)

[Argall *et al.*, 2010a] B. D. Argall, E. L. Sauser and A. G. Billard. “Policy adaptation through tactile correction”. In *Proceedings of the 2nd International Symposium on New Frontiers in Human-Robot Interaction - A Symposium at the AISB 2010 Convention*, pp. 1–8. March 2010a. (Cited on page 25.)

[Argall *et al.*, 2010b] B. D. Argall, E. L. Sauser and A. G. Billard. “Tactile guidance for policy refinement and reuse”. In *IEEE International Conference on Development and Learning (ICDL)*, pp. 7–12. Ann Arbor, MI, USA, August 2010b. (Cited on page 25.)

[Ascari *et al.*, 2007] L. Ascari, P. Corradi, L. Beccai and C. Laschi. “A miniaturized and flexible optoelectronic sensing system for tactile skin”. *Journal of Micromechanics and Microengineering*, vol. 17(11), pp. 2288–2298, 2007. (Cited on page 18.)

[Battaglia *et al.*, 2009] M. Battaglia, L. Blanchet, A. Kheddar, S. Kajita and K. Yokoi. “Combining haptic sensing with safe interaction”. In *IEEE/RSJ International Conference on Intelligent Robots and Systems (IROS)*, pp. 231–236. St. Louis, MO, USA, October 2009. (Cited on page 25.)

[Beccai *et al.*, 2009] L. Beccai, C. M. Oddo, C. Cipriani and M. C. Carrozza. “A biorobotic approach for artificial touch: from the development of a mems sensor to the tactile array integration into an actuated finger”. In *IEEE-RAS International Conference on Humanoid Robots (Humanoids)*, Workshop on Tactile Sensing in Humanoids, pp. 38–41. Paris, France, December 2009. (Cited on page 18.)

[Bell and Holmes, 1992] J. Bell and M. Holmes. “Model of the dynamics of receptor potential in a mechanoreceptor”. *Mathematical Biosciences*, vol. 110, pp. 139–174, October 1992. (Cited on page 13.)

[Bennett *et al.*, 1992] D. J. Bennett, J. M. Hollerbach and P. D. Henri. “Kinematic calibration by direct estimation of the jacobian matrix”. In *IEEE-RAS International Conference on Robotics and Automation (ICRA)*, pp. 351–357. Nice, France, May 1992. (Cited on page 23.)

[Biggio *et al.*, 2010] A. Biggio, P. Maiolino and G. Cannata. “Towards a skin-like embedded tactile sensor for robotic hands”. In *Proceedings of the 2nd International Symposium on New Frontiers in Human-Robot Interaction - A Symposium at the AISB 2010 Convention*, pp. 16–21. March 2010. (Cited on page 18.)

[Bongard *et al.*, 2006a] J. Bongard, V. Zykov and H. Lipson. “Automated synthesis of body schema using multiple sensor modalities”. In *International Conference on the Simulation and Synthesis of Living Systems (ALIFEX)*, pp. 220–226. 2006a. (Cited on page 24.)

[Bongard *et al.*, 2006b] J. Bongard, V. Zykov and H. Lipson. “Resilient machines through continuous self-modeling”. *Science*, vol. 314(5802), pp. 1118–1121, November 2006b. (Cited on page 24.)

[Buescher *et al.*, 2012] G. Buescher, R. K. C. Schuermann, R. Haschke and H. J. Ritter. “Tactile dataglove with fabric-based sensors”. In *IEEE-RAS International Conference on Humanoid Robots (Humanoids)*, pp. 204–209. Osaka, Japan, November 2012. (Cited on page 17.)

[Camazine *et al.*, 2001] S. Camazine, J.-L. Deneubourg, N. R. Franks, J. Sneyd, G. Theraulaz and E. Bonabeau. *Self-organization in Biological Systems*. Princeton University Press, 2001. (Cited on page 11.)

[Canepa *et al.*, 1994] G. Canepa, J. M. Hollerbach and A. J. M. A. Boelen. “Kinematic calibration by means of a triaxial accelerometer”. In *IEEE-RAS International Conference on Robotics and Automation (ICRA)*, pp. 2776–2782. San Diego, CA, USA, May 1994. (Cited on pages 23, 115, 117, and 119.)

[Cannata *et al.*, 2010a] G. Cannata, S. Denei and F. Mastrogiovanni. “Contact based robot control through tactile maps”. In *IEEE Conference on Decision and Control (CDC)*, pp. 3578–3583. Atlanta, GA, USA, December 2010a. (Cited on page 24.)

[Cannata *et al.*, 2010b] G. Cannata, S. Denei and F. Mastrogiovanni. "On internal models for representing tactile information". In *IEEE/RSJ International Conference on Intelligent Robots and Systems (IROS)*, pp. 1108–1113. Taipei, Taiwan, October 2010b. (Cited on page 20.)

[Cannata *et al.*, 2010c] G. Cannata, S. Denei and F. Mastrogiovanni. "Towards automated self-calibration of robot skin". In *IEEE-RAS International Conference on Robotics and Automation (ICRA)*, pp. 4849–4854. Anchorage, AK, USA, May 2010c. (Cited on page 20.)

[Cannata *et al.*, 2008] G. Cannata, M. Maggiali, G. Metta and G. Sandini. "An embedded artificial skin for humanoid robots". In *IEEE International Conference on Multisensor Fusion and Integration for Intelligent Systems (MFI)*, pp. 434–438. Seoul, South Korea, August 2008. (Cited on pages 17, 18, and 19.)

[Cartaa *et al.*, 2009] R. Cartaa, P. Jouranda, B. Hermansa, J. Thonéa, D. Brosteauxb, T. Vervust, F. Bossuyt, F. Axisab, J. Vanfleterenb and R. Puersa. "Design and implementation of advanced systems in a flexible-stretchable technology for biomedical applications". *Sensors and Actuators A: Physical*, vol. 156, pp. 79–87, November 2009. (Cited on page 19.)

[Castelli, 2002] F. Castelli. "An integrated tactile-thermal robot sensor with capacitive tactile array". *IEEE Transactions on Industry Applications*, vol. 38(1), pp. 85–90, 2002. (Cited on page 18.)

[Cauna, 1954] N. Cauna. "Nature and functions of the papillary ridges of the digital skin". *The Anatomical Record*, vol. 119(4), pp. 449–468, 1954. (Cited on pages 12 and 35.)

[Chigusa *et al.*, 2007] H. Chigusa, Y. Makino and H. Shinoda. "Large area sensor skin based on two-dimensional signal transmission technology". In *Symposium on Haptic Interfaces for Virtual Environment and Teleoperator Systems*, pp. 151–156. 2007. (Cited on page 19.)

[Choi *et al.*, 2005] B. Choi, H. R. Choi and S. Kang. "Development of tactile sensor for detecting contact force and slip". In *IEEE/RSJ International Conference on Intelligent Robots and Systems (IROS)*, pp. 2638–2643. Edmonton, Canada, August 2005. (Cited on page 18.)

[Chorley *et al.*, 2009] C. Chorley, C. Melhuish, T. Pipe and Jonathan. “Development of a tactile sensor based on biologically inspired edge encoding”. In *IEEE International Conference on Advanced Robotics (ICAR)*, pp. 1–6. Munich, Germany, June 2009. (Cited on page 17.)

[Cutkosky *et al.*, 1987] M. R. Cutkosky, J. Jourdain and P. Wright. “Skin materials for robotic fingers”. In *IEEE-RAS International Conference on Robotics and Automation (ICRA)*, pp. 1649–1654. Raleigh, NC, USA, March 1987. (Cited on page 19.)

[Dahiya *et al.*, 2010] R. S. Dahiya, G. Metta, M. Valle and G. Sandini. “Tactile sensing-from humans to humanoids”. *IEEE Transactions on Robotics (T-RO)*, vol. 26, pp. 1–20, February 2010. (Cited on pages 17 and 45.)

[Dahiya *et al.*, 2013] R. S. Dahiya, P. Mittendorfer, M. Valle, G. Cheng and V. J. Lumelsky. “Directions toward effective utilization of tactile skin: A review”. *IEEE Sensors Journal*, vol. 13(11), pp. 4121–4138, November 2013. (Cited on pages ix, 17, and 20.)

[Dahiya and Valle, 2013] R. S. Dahiya and M. Valle. *Robotic Tactile Sensing*. Springer, 2013. (Cited on page 17.)

[Dahiya *et al.*, 2008] R. S. Dahiya, M. Valle and G. Metta. “System approach: A paradigm for robotic tactile sensing”. In *IEEE International Workshop on Advanced Motion Control*, pp. 110–115. March 2008. (Cited on page 17.)

[Dahl and Palmer, 2010] T. S. Dahl and A. Palmer. “Touch-triggered protective reflexes for safer robots”. In *Proceedings of the International Symposium on New Frontiers in Human-Robot Interaction*, pp. 27–33. 2010. (Cited on pages 20 and 25.)

[Dandekar *et al.*, 2003] K. Dandekar, B. I. Raju and M. A. Srinivasan. “3-d finite-element models of human and monkey fingertips to investigate the mechanics of tactile sense”. *Journal of Biomechanical Engineering*, vol. 125, pp. 682–691, 2003. (Cited on page 12.)

[Davison, 2010] B. Davison. “Techniques for robust touch sensing design”. AN1334 Microchip Technology Inc., 2010. (Cited on pages 53 and 56.)

[de Vignemont, 2010] F. de Vignemont. “Body schema and body image—pros and cons”. *Neuropsychologia*, vol. 48(3), pp. 669–680, 2010. (Cited on pages 13 and 15.)

[Edin, 2004] B. B. Edin. “Quantitative analyses of dynamic strain sensitivity in human skin mechanoreceptors”. *Journal of Neurophysiology*, vol. 92(6), pp. 3233–3243, 2004. (Cited on page 13.)

[Edwards *et al.*, 2008] J. Edwards, J. Lawry, J. Rossiter and C. Melhuish. “Extracting textural features from tactile sensors”. *Bioinspiration and Biomimetics*, vol. 3(3), June 2008. (Cited on pages 17 and 20.)

[Fearing, 1990] R. S. Fearing. “Tactile sensing mechanisms”. *The International Journal of Robotics Research*, vol. 9(3), pp. 3–23, June 1990. (Cited on page 17.)

[Fishel *et al.*, 2009] J. A. Fishel, V. J. Santos and G. E. Loeb. “Signal processing and fabrication of a biomimetic tactile sensor array with thermal, force and microvibration modalities”. In *IEEE International Conference on Robotics and Biomimetics (ROBIO)*, pp. 129–134. Guilin, China, December 2009. (Cited on pages 17 and 18.)

[Fritzsche *et al.*, 2011] M. Fritzsche, N. Elkmann and E. Schulenburg. “Tactile sensing: A key technology for safe physical human robot interaction”. In *ACM/IEEE International Conference on Human-Robot Interaction (HRI)*, pp. 139–140. Lausanne, Switzerland, March 2011. (Cited on page 19.)

[Fujimori *et al.*, 2009] Y. Fujimori, Y. Ohmura, T. Harada and Y. Kuniyoshi. “Wearable motion capture suit with full-body tactile sensors”. In *IEEE International Conference on Robotics and Automation (ICRA)*, pp. 3652–3659. Kobe, Japan, May 2009. (Cited on pages 18 and 19.)

[Fuke *et al.*, 2007] S. Fuke, M. Ogino and M. Asada. “Body image constructed from motor and tactile images with visual information”. *International Journal of Humanoid Robotics*, vol. 4(2), pp. 347–364, March 2007. (Cited on pages 21 and 95.)

[Gerling and Thomas, 2005] G. J. Gerling and G. W. Thomas. “The effect of fingertip microstructures on tactile edge perception”. In *Symposium on Haptic Interfaces for Virtual Environment and Teleoperator Systems*, pp. 63–72. March 2005. (Cited on page 19.)

[Göger *et al.*, 2009] D. Göger, N. Gorges and H. Wörn. “Tactile sensing for an anthropomorphic robotic hand - hardware and signal processing”. In *IEEE-RAS International Conference on Robotics and Automation (ICRA)*, pp. 895–901. Kobe, Japan, May 2009. (Cited on pages 17, 20, and 25.)

[Göger *et al.*, 2006] D. Göger, K. Weiß, C. Burghart and H. Wörn. “Sensitive skin for a humanoid robot”. International Workshop on Human-Centered Robotic Systems, 2006. (Cited on page 18.)

[Hakozaki *et al.*, 2001] M. Hakozaki, A. HATORI and H. Shinoda. “A sensitive skin using wireless tactile sensing elements”. In *Technical Digest of the 18th Sensor Symposium*, pp. 147–150. 2001. (Cited on page 20.)

[Harmon, 1982] L. D. Harmon. “Automated tactile sensing”. *The International Journal of Robotics Research*, vol. 1(2), pp. 3–31, June 1982. (Cited on pages 15, 16, and 161.)

[Hasegawa *et al.*, 2008] Y. Hasegawa, M. Shikida, D. Ogura, Y. Suzuki and K. Sato. “Fabrication of a wearable fabric tactile sensor produced by artificial hollow fiber”. *Journal of Micromechanics and Microengineering*, vol. 18(8), pp. 1–8, 2008. (Cited on page 18.)

[He and Jia, 2005] X. He and W. Jia. “Hexagonal structure for intelligent vision”. In *International Conference on Information and Communication Technologies (ICICT)*, pp. 52–64. Karachi, Pakistan, August 2005. (Cited on page 33.)

[Hellard and Russell, 2002] G. Hellard and R. A. Russell. “A robust, sensitive and economical tactile sensor for a robotic manipulator”. In *Australasian Conference on Robotics and Automation*, pp. 100–104. Auckland, New Zealand, November 2002. (Cited on page 18.)

[Hendriks, 2005] F. M. Hendriks. “Mechanical behaviour of human epidermal and dermal layers in vivo”. Ph.D. thesis, Technische Universiteit Eindhoven, 2005. (Cited on page 13.)

[Heo *et al.*, 2005] J.-S. Heo, J.-H. Chung and J.-J. Lee. “Tactile sensor arrays using fiber bragg grating sensors”. *Sensors and Actuators A: Physical*, vol. 126, pp. 312–327, February 2005. (Cited on page 19.)

[Hersch *et al.*, 2008] M. Hersch, E. Sauser and A. Billard. “Online learning of the body schema”. *International Journal of Humanoid Robotics*, vol. 5(2), pp. 161–181, 2008. (Cited on page 23.)

[Hoffmann *et al.*, 2010] M. Hoffmann, H. G. Marques, A. H. Arieta, H. Sumioka, M. Lungarella and R. Pfeifer. “Body schema in robotics: A review”. *IEEE Transactions on Autonomous Mental Development*, vol. 2(4), pp. 304–324, December 2010. (Cited on pages 13, 20, and 22.)

[Hollerbach and Wampler, 1996] J. M. Hollerbach and C. W. Wampler. “The calibration index and taxonomy for robot kinematic calibration methods”. *The International Journal of Robotics Research*, vol. 15(6), pp. 573–591, December 1996. (Cited on page 23.)

[Holmes and Spence, 2004] N. P. Holmes and C. Spence. “The body schema and the multisensory representation(s) of peripersonal space”. *Cognitive Processing*, vol. 5(2), pp. 94–105, June 2004. (Cited on pages 14 and 15.)

[Hoshi and Shinoda, 2007] T. Hoshi and H. Shinoda. “Gravity-based 3d shape measuring sheet”. In *SICE Annual Conference*, pp. 2126–2131. Kagawa, Japan, September 2007. (Cited on pages 22, 68, and 73.)

[Hoshi and Shinoda, 2008] T. Hoshi and H. Shinoda. “3d shape measuring sheet utilizing gravitational and geomagnetic fields”. In *SICE Annual Conference*, pp. 915–920. Tokyo, Japan, August 2008. (Cited on pages 18 and 22.)

[Hou *et al.*, 2013] C. Hou, T. Huang, H. Wang, H. Yu, Q. Zhang and Y. Li. “A strong and stretchable self-healing film with self-activated pressure sensitivity for potential artificial skin applications”. *Scientific Reports*, vol. 3, 2013. (Cited on page 19.)

[Howe, 1994] R. D. Howe. “Tactile sensing and control of robotic manipulation”. *Journal of Advanced Robotics*, vol. 8(3), pp. 245–261, 1994. (Cited on page 17.)

[Hsiao *et al.*, 2009] K. Hsiao, P. Nangeroni, M. Huber, A. Saxena and A. Y. Ng. “Reactive grasping using optical proximity sensors”. In *IEEE-RAS International Conference on Robotics and Automation (ICRA)*, pp. 2098–2105. Kobe, Japan, May 2009. (Cited on page 24.)

[Hubbard, 1974] J. I. Hubbard. *The Peripheral Nervous System*. Springer, 1974. (Cited on page 11.)

[Iwata and Sugano, 2006] H. Iwata and S. Sugano. “Human–robot-contact-state identification based on tactile recognition”. *IEEE Transactions on Industrial Electronics*, vol. 52(6), pp. 1468–1477, December 2006. (Cited on page 25.)

[Iwata and Sugano, 2009] H. Iwata and S. Sugano. “Design of human symbiotic robot twendy-one”. In *IEEE-RAS International Conference on Robotics and Automation (ICRA)*, pp. 580–586. Kobe, Japan, May 2009. (Cited on page 18.)

[Johansson and Flanagan, 2009] R. S. Johansson and J. R. Flanagan. “Coding and use of tactile signals from the fingertips in object manipulation tasks”. *Nature Reviews Neuroscience*, vol. 10, pp. 345–359, May 2009. (Cited on pages 13 and 17.)

[Johnson, 2001] K. O. Johnson. “The roles and functions of cutaneous mechanoreceptors”. *Current Opinion in Neurobiology*, vol. 11(4), pp. 455–461, August 2001. (Cited on page 13.)

[Kaboli *et al.*, 2014] M. Kaboli, P. Mittendorfer, V. Hugel and G. Cheng. “Humanoids learn object properties from robust tactile feature descriptors via multi-modal artificial skin”. In *IEEE-RAS International Conference on Humanoid Robots (Humanoids)*, pp. 187–192. Madrid, Spain, November 2014. (Cited on page ix.)

[Kadowaki *et al.*, 2009] A. Kadowaki, T. Yoshikai, M. Hayashi and Masayuki. “Development of soft sensor exterior embedded with multi-axis deformable tactile sensor system”. In *IEEE International Symposium on Robot and Human Interactive Communication*, pp. 1093–1098. September 2009. (Cited on page 18.)

[Kandel *et al.*, 2012] E. R. Kandel, J. H. Schwartz, T. M. Jessell, S. a. Siegelbaum and A. J. Hudspeth. *Principles of Neural Science*. Mcgraw-Hill Professional, 5th edition, 2012. (Cited on pages 11, 12, 13, 14, and 15.)

[Kim *et al.*, 2008] D.-H. Kim, J.-H. Ahn, W. M. Choi, H.-S. Kim, T.-H. Kim, J. Song, Y. Y. Huang, Z. Liu, C. Lu and J. A. Roger. “Stretchable and foldable silicon integrated circuits”. *Science Express*, vol. 320, March 2008. (Cited on page 19.)

[Kojima *et al.*, 2013] K. Kojima, T. Sato, A. Schmitz, H. Arie, H. Iwata and S. Sugano. “Sensor prediction and grasp stability evaluation for in-hand manipulation”. In *IEEE/RSJ International Conference on Intelligent Robots and Systems (IROS)*, pp. 2479–2484. Tokyo, Japan, November 2013. (Cited on page 25.)

[Kuniyoshi *et al.*, 2004] Y. Kuniyoshi, Y. Yorozu, Y. Ohmura, K. Terada, T. Otani, A. Nagakubo and T. Yamamoto. *Embodied Artificial Intelligence*, vol. 3139 of *Lecture Notes in Computer Science*, chapter From Humanoid Embodiment to Theory of Mind, pp. 202–218. Springer, 2004. (Cited on pages 21 and 95.)

[Lacour *et al.*, 2005] S. P. Lacour, J. Jones, S. Wagner, T. Li and Z. Suo. “Stretchable interconnects for elastic electronic surfaces”. *Proceedings of the IEEE*, vol. 93(8), pp. 1459–1467, 2005. (Cited on page 19.)

[Lai *et al.*, 2011] Y.-T. Lai, W.-C. Kuo and Y.-J. Yang. “A tactile sensing array with tunable sensing ranges using liquid crystal and carbon nanotubes composites”. In *IEEE International Conference on Micro Electro Mechanical Systems (MEMS)*, pp. 553–556. Cancun, Mexico, January 2011. (Cited on page 18.)

[Lee, 2000] M. H. Lee. “Tactile sensing: New directions, new challenges”. *Journal of Robotics Research*, vol. 19(7), pp. 636–643, July 2000. (Cited on page 17.)

[Lee and Nicholls, 1999] M. H. Lee and H. R. Nicholls. “Review article tactile sensing for mechatronics - a state of the art survey”. *Mechatronics*, vol. 9(1), pp. 1–31, 1999. (Cited on page 17.)

[Leng and Sun, 2009] D. Leng and W. Sun. “Finding all the solutions of pnp problem”. International Workshop on Imaging Systems and Techniques, May 2009. (Cited on page 87.)

[Lin and Jain, 2009] K. L. Lin and K. Jain. “Design and fabrication of stretchable multilayer self-aligned interconnects for flexible electronics and large-area sensor arrays using excimer laser photoablation”. *IEEE Electron Device Letters*, vol. 30(1), pp. 14–17, December 2009. (Cited on page 19.)

[Llinas, 2002] R. R. Llinas. *I of the Vortex*. A Bradford Book, March 2002. (Cited on page 11.)

[lori Kumagai *et al.*, 2012] lori Kumagai, K. Kobayashi, S. Nozawa, Y. Kakiuchi, T. Yoshikai, K. Okada and M. lnaba. “Development of a full body multi-axis soft tactile sensor suit for life sized humanoid robot and an algorithm to detect contact states”. In *IEEE-RAS International Conference on Humanoid Robots (Humanoids)*, pp. 526–531. Osaka, Japan, November 2012. (Cited on pages 18 and 25.)

[Lucarotti *et al.*, 2013] C. Lucarotti, C. M. Oddo, N. Vitiello and M. C. Carrozza. “Synthetic and bio-artificial tactile sensing: A review”. *Sensors*, vol. 13, pp. 1435–1466, January 2013. (Cited on page 17.)

[Lumelsky *et al.*, 2001] V. J. Lumelsky, M. S. Shur and S. Wagner. “Sensitive skin”. *IEEE Sensors Journal*, vol. 1, pp. 41–51, 2001. (Cited on pages 17, 18, and 25.)

[Macaluso and Maravita, 2010] E. Macaluso and A. Maravita. “The representation of space near the body through touch and vision”. *Neuropsychologia*, vol. 48, pp. 782–795, 2010. (Cited on page 13.)

[Maeno *et al.*, 1998] T. Maeno, K. Kobayashi and N. Yamazaki. “Relationship between the structure of human finger tissue and the location of tactile receptors”. *Journal of the Japan Society of Mechanical Engineers*, vol. 41(1), pp. 94–100, 1998. (Cited on page 12.)

[Maheshwari and Saraf, 2006] V. Maheshwari and R. F. Saraf. “High-resolution thin-film device to sense texture by touch”. *Science*, vol. 312, pp. 1501–1504, June 2006. (Cited on page 17.)

[Maiolino *et al.*, 2013] P. Maiolino, M. Maggiali, G. Cannata, G. Metta and L. Natale. “A flexible and robust large scale capacitive tactile system for robots”. In *IEEE-RAS International Conference on Robotics and Automation (ICRA)*, Workshop on Electronic Skin. Karlsruhe, Germany, May 2013. (Cited on page 17.)

[McGlone and Reilly, 2010] F. McGlone and D. Reilly. “The cutaneous sensory system”. *Neuroscience and Biobehavioral Reviews*, vol. 34(2), pp. 148–159, 2010. (Cited on pages 11 and 13.)

[Medina and Coslett, 2010] J. Medina and H. B. Coslett. “From maps to form to space: Touch and the body schema”. *Neuropsychologia*, vol. 48(3), pp. 645–654, February 2010. (Cited on page 14.)

[Mittendorfer, 2013] P. Mittendorfer. “Capacitive force sensor and fabrication method”. European Patent EP 12172602.0, December 2013. (Cited on pages x, 49, and 52.)

[Mittendorfer and Cheng, 2011a] P. Mittendorfer and G. Cheng. “Humanoid multi-modal tactile sensing modules”. *IEEE Transactions on Robotics (T-RO)*, vol. 27(3), pp. 401–410, June 2011a. (Cited on pages x, 30, 111, and 153.)

[Mittendorfer and Cheng, 2011b] P. Mittendorfer and G. Cheng. “Self-organizing sensory-motor map for low-level touch reactions”. In *IEEE-RAS International Conference on Humanoid Robots (Humanoids)*, pp. 59–66. Bled, Slovenia, October 2011b. (Cited on pages x and 103.)

[Mittendorfer and Cheng, 2012a] P. Mittendorfer and G. Cheng. “3d surface reconstruction for robotic body parts with artificial skins”. In *IEEE/RSJ International Conference on Intelligent Robots and Systems (IROS)*, pp. 4505–4510. Vilamoura, Algarve, Portugal, October 2012a. (Cited on pages x and 68.)

[Mittendorfer and Cheng, 2012b] P. Mittendorfer and G. Cheng. “Integrating discrete force cells into multi-modal artificial skin”. In *IEEE-RAS International Conference on Humanoid Robots (Humanoids)*, pp. 847–852. Osaka, Japan, November 2012b. (Cited on pages x and 49.)

[Mittendorfer and Cheng, 2012c] P. Mittendorfer and G. Cheng. “Open-loop self-calibration of articulated robots with artificial skins”. In *IEEE-RAS International Conference on Robotics and Automation (ICRA)*, pp. 4539–4545. Minneapolis, MN, USA, May 2012c. (Cited on pages x and 96.)

[Mittendorfer and Cheng, 2012d] P. Mittendorfer and G. Cheng. “Uniform cellular design of artificial robotic skin”. In *7th German Conference on Robotics*, pp. 145–149. Munich, Germany, May 2012d. (Cited on pages x and 30.)

[Mittendorfer and Cheng, 2013] P. Mittendorfer and G. Cheng. “From a multi-modal intelligent cell to a self-organizing robotic skin”. In *IEEE-RAS International Conference on Robotics and Automation (ICRA)*, Workshop on Electronic Skin. Karlsruhe, Germany, May 2013. (Cited on pages x and 30.)

[Mittendorfer *et al.*, 2014a] P. Mittendorfer, E. Dean and G. Cheng. “3d spatial self-organization of a modular artificial skin”. In *IEEE/RSJ International Conference on Intelligent Robots and Systems (IROS)*, pp. 3969–3974. Chicago, Illinois, U.S.A, September 2014a. (Cited on pages ix and 83.)

[Mittendorfer *et al.*, 2014b] P. Mittendorfer, E. Dean and G. Cheng. “Automatic robot kinematic modeling with a modular artificial skin”. In *IEEE-RAS International Conference on Humanoid Robots (Humanoids)*, pp. 749–754. Madrid, Spain, November 2014b. (Cited on pages ix and 115.)

[Mittendorfer *et al.*, 2015] P. Mittendorfer, E. Yoshida and G. Cheng. “Realizing whole-body tactile interactions with a self-organizing, multi-modal articial skin on a humanoid robot”. *Advanced Robotics*, vol. 29(1), pp. 51–67, 2015. (Cited on pages ix, 96, and 103.)

[Mittendorfer *et al.*, 2013] P. Mittendorfer, E. Yoshida, T. Moulard and G. Cheng. “A general tactile approach for grasping unknown objects with a humanoid robot”. In *IEEE/RSJ International Conference on Intelligent Robots and Systems (IROS)*, pp. 4747–4752. Tokyo, Japan, November 2013. (Cited on pages ix, 96, and 134.)

[Modayil, 2010] J. Modayil. “Discovering sensor space: Constructing spatial embeddings that explain sensor correlations”. In *IEEE International Conference on Development and Learning (ICDL)*, pp. 120–125. Ann Arbor, MI, USA, August 2010. (Cited on page 22.)

[Mooring *et al.*, 1991] B. Mooring, M. Driels and Z. Roth. *Fundamentals of Manipulator Calibration*. John Wiley and Sons Inc., April 1991. (Cited on pages 23 and 124.)

[Mukai *et al.*, 2011] T. Mukai, S. Hirano, M. Yoshida, H. Nakashima, S. Guo and Y. Hayakawa. “Whole-body contact manipulation using tactile information for the nursing-care assistant robot riba”. In *IEEE/RSJ International Conference on Intelligent Robots and Systems (IROS)*, pp. 2445–2451. San Francisco, CA, USA, September 2011. (Cited on page 24.)

[Mukai *et al.*, 2008] T. Mukai, M. Onishi, T. Odashima, S. Hirano and Z. Luo. “Development of the tactile sensor system of a human-interactive robot “ri-man””. *IEEE Transactions on Robotics (T-RO)*, vol. 24(2), pp. 505–512, April 2008. (Cited on page 18.)

[Myles and Binseel, 2007] K. Myles and M. S. Binseel. “The tactile modality: A review of tactile sensitivity and human tactile interfaces”. Army Reasearch Laboratory, May 2007. (Cited on page 11.)

[Navarro *et al.*, 2012] S. E. Navarro, N. Gorges, H. Woern, J. Schill, T. Asfour and R. Dillmann. “Haptic object recognition for multi-fingered robot hands”. In *IEEE Haptics Symposium (HAPTICS)*. Vancouver, BC, Canada, March 2012. (Cited on page 25.)

[Noda *et al.*, 2010] K. Noda, E. Iwase, K. Matsumoto and I. Shimoyama. “Stretchable liquid tactile sensor for robot-joints”. In *IEEE-RAS International Conference on Robotics and Automation (ICRA)*, pp. 4212–4217. Anchorage, AK, USA, May 2010. (Cited on page 18.)

[Noda *et al.*, 2007] T. Noda, T. Miyashita, H. Ishiguro and N. Hagita. “Map acquisition and classification of haptic interaction using cross correlation between distributed tactile sensors on the whole body surface”. In *IEEE/RSJ International Conference on Intelligent Robots and Systems (IROS)*, pp. 1099–1105. San Diego, CA, USA, October 2007. (Cited on page 25.)

[O'Brien *et al.*, 2000] J. F. O'Brien, R. E. Bodenheimer, G. J. Brostow and J. K. Hodgins. "Automatic joint parameter estimation from magnetic motion capture data". In *Graphics Interface Conference*, pp. 53–60. Montréal, Québec, Canada, May 2000. (Cited on page 23.)

[Oddo *et al.*, 2009] C. M. Oddo, L. Beccai, M. Felder, F. Giovacchini and M. C. Carrozza. "Artificial roughness encoding with a bio-inspired mems-based tactile sensor array". *Sensors*, vol. 9, pp. 3161–3183, April 2009. (Cited on page 19.)

[Ohmura and Kuniyoshi, 2007] Y. Ohmura and Y. Kuniyoshi. "Humanoid robot which can lift a 30kg box by whole body contact and tactile feedback". In *IEEE/RSJ International Conference on Intelligent Robots and Systems (IROS)*, pp. 1136–1141. San Diego, CA, USA, October 2007. (Cited on page 24.)

[Ohmura *et al.*, 2006] Y. Ohmura, Y. Kuniyoshi and A. Nagakubo. "Conformable and scalable tactile sensor skin for curved surfaces". In *IEEE-RAS International Conference on Robotics and Automation (ICRA)*, pp. 1348–1353. Orlando, Florida, May 2006. (Cited on pages 18 and 19.)

[Papakostas *et al.*, 2002] T. V. Papakostas, J. Lima and M. Lowe. "A large area force sensor for smart skin applications". *Proceedings of IEEE Sensors*, vol. 2, pp. 1620–1624, 2002. (Cited on page 17.)

[Park *et al.*, 2011] J.-J. Park, S. Haddadin, J.-B. Song and A. Albu-Schaeffer. "Designing optimally safe robot surface properties for minimizing the stress characteristics of human-robot collisions". In *IEEE-RAS International Conference on Robotics and Automation (ICRA)*, pp. 5413–5420. Shanghai, China, May 2011. (Cited on page 19.)

[Park *et al.*, 2010] Y.-L. Park, C. Majidi, R. Kramer, P. Berard and R. J. Wood. "Hyperelastic pressure sensing with a liquid-embedded elastomer". *Journal of Micromechanics and Microengineering*, vol. 20(12), pp. 1–6, 2010. (Cited on page 18.)

[Perez, 2006] G. B. Perez. "S.n.a.k.e.: A dynamically reconfigurable artificial sensate skin". Master's thesis, Massachusetts Institute of Technology, September 2006. (Cited on pages 19 and 20.)

[Persichetti *et al.*, 2009] A. Persichetti, F. Vecchi, N. Vitiello, T. Lenzi and M. C. Carrozza. "Skilsens: conformant and robust sensing skin". In *IEEE-RAS International Conference on Humanoid Robots (Humanoids)*, Workshop on Tactile Sensing in Humanoids. Paris, France, December 2009. (Cited on pages 17 and 19.)

[Petersen, 1962] D. P. Petersen. “Sampling and reconstruction of wave-number-limited functions in n-dimensional euclidean spaces”. *Information and Control*, vol. 5, pp. 279–323, 1962. (Cited on page 33.)

[Petrovskaya and Khatib, 2011] A. Petrovskaya and O. Khatib. “Global localization of objects via touch”. *IEEE Transactions on Robotics (T-RO)*, vol. 27(3), pp. 569–585, June 2011. (Cited on page 25.)

[Prete *et al.*, 2011] A. D. Prete, S. Denei, L. Natale, F. Mastrogiovanni, F. Nori, G. Cannata and G. Metta. “Skin spatial calibration using force/torque measurements”. In *IEEE/RSJ International Conference on Intelligent Robots and Systems (IROS)*, pp. 3694–3700. San Francisco, CA, USA, September 2011. (Cited on page 21.)

[Richardson *et al.*, 2004] B. Richardson, K. Leydon, M. Fernström and J. A. Paradiso. “Z-tiles: Building blocks for modular, pressure-sensing floorspaces”. In *Conference on Human Factors in Computing Systems (CHI)*, pp. 1529–1532. Vienna, Austria, April 2004. (Cited on page 20.)

[Rocha *et al.*, 2006] J. G. Rocha, C. Santos, J. M. Cabral and S. Lanceros-Mendez. “3 axis capacitive tactile sensor and readout electronics”. In *IEEE International Symposium on Industrial Electronics*, pp. 2767–2772. July 2006. (Cited on page 17.)

[Rochat, 1998] P. Rochat. “Self-perception and action in infancy”. *Experimental Brain Research*, vol. 123, pp. 102–109, 1998. (Cited on pages 14 and 15.)

[Roetenberg *et al.*, 2008] D. Roetenberg, H. Luinge and P. Slycke. “Moven: Full 6dof human motion tracking using miniature inertial sensors”. Technical report, Xsens Technologies, 2008. (Cited on page 23.)

[Romano *et al.*, 2011] J. M. Romano, K. Hsiao, G. Niemeyer, S. Chitta and K. J. Kuchenbecker. “Human-inspired robotic grasp control with tactile sensing”. *IEEE Transactions on Robotics (T-RO)*, vol. 27(6), pp. 1067–1079, December 2011. (Cited on page 24.)

[Rothmaier *et al.*, 2008] M. Rothmaier, M. P. Luong and F. Clemens. “Textile pressure sensor made of flexible plastic optical fibers”. *Sensors*, vol. 8, pp. 4318–4329, July 2008. (Cited on page 19.)

[Sagisaka *et al.*, 2011] T. Sagisaka, Y. Ohmura, T. Sagisaka, Y. Ohmura, Y. Kuniyoshi, A. Nagakubo and K. Ozaki. “High-density conformable tactile sensing glove”. In *IEEE-RAS International Conference on Humanoid Robots (Humanoids)*, pp. 537–542. Bled, Slovenia, October 2011. (Cited on page 18.)

[Sato *et al.*, 2012] M. Sato, I. Poupyrev and C. Harrison. “Touché: Enhancing touch interaction on humans, screens, liquids, and everyday objects”. In *Conference on Human Factors in Computing Systems (CHI)*, pp. 483–492. Austin, Texas, USA, May 2012. (Cited on page 17.)

[Scheibert *et al.*, 2009] J. Scheibert, S. Leurent, A. Prevost and G. Debrégeas. “The role of fingerprints in the coding of tactile information probed with a biomimetic sensor”. *Science*, vol. 323, pp. 1503–1506, 2009. (Cited on page 18.)

[Schmid *et al.*, 2008] A. J. Schmid, N. Gorges, D. Goeger and H. Woern. “Opening a door with a humanoid robot using multi-sensory tactile feedback”. In *IEEE-RAS International Conference on Robotics and Automation (ICRA)*, pp. 285–291. Pasadena, CA, USA, May 2008. (Cited on page 25.)

[Schmidt *et al.*, 2006] P. A. Schmidt, E. Mael and R. P. Wuertz. “A sensor for dynamic tactile information with applications in human-robot interaction and object exploration”. *Robotics and Autonomous Systems*, vol. 54, pp. 1005–1014, December 2006. (Cited on page 25.)

[Schmitz, 2011] A. Schmitz. “A distributed tactile system for humanoid robot hands”. Ph.D. thesis, University of Sheffield, 2011. (Cited on page 18.)

[Schmitz *et al.*, 2014] A. Schmitz, Y. Bansho, K. Noda, H. Iwata, T. Ogata and S. Sugano. “Tactile object recognition using deep learning and dropout”. In *IEEE-RAS International Conference on Humanoid Robots (Humanoids)*, p. (accepted). Madrid, Spain, November 2014. (Cited on page 25.)

[Schmitz *et al.*, 2010] A. Schmitz, M. Maggiali, L. Natale, B. Bonino and G. Metta. “A tactile sensor for the fingertips of the humanoid robot icub”. In *IEEE/RSJ International Conference on Intelligent Robots and Systems (IROS)*, pp. 2212–2217. Taipei, Taiwan, October 2010. (Cited on page 18.)

[Shimizu *et al.*, 2002] T. Shimizu, M. Shikida, K. Sato and K. Itoigawa. “A new type of tactile sensor detecting contact force and hardness of an object”. In *IEEE International Conference on Micro Electro Mechanical Systems (MEMS)*, pp. 344–347. Las Vegas, USA, January 2002. (Cited on page 18.)

[Shimojo, 1997] M. Shimojo. “Mechanical filtering effect of elastic cover for tactile sensor”. *IEEE Transactions on Robotics and Automation*, vol. 13(1), pp. 128–132, 1997. (Cited on pages 19 and 35.)

[Shimojo *et al.*, 2004] M. Shimojo, A. Namiki, M. Ishikawa, R. Makino and K. Mabuchi. “A tactile sensor sheet using pressure conductive rubber with electrical-wires stitched method”. *IEEE Sensors Journal*, vol. 4, pp. 589–596, 2004. (Cited on page 17.)

[Someya *et al.*, 2005] T. Someya, Y. Kato, T. Sekitani, S. Iba, Y. Noguchi, Y. Murase, H. Kawaguchi and T. Sakurai. “Conformable, flexible, large-area networks of pressure and thermal sensors with organic transistor active matrixes”. *Proceedings of the National Academy of Science of the United States of America*, vol. 102(35), pp. 12321–12325, August 2005. (Cited on page 19.)

[Someya *et al.*, 2004] T. Someya, T. Sekitani, S. Iba, Y. Kato, H. Kawaguchi and T. Sakurai. “A large-area, flexible pressure sensor matrix with organic field-effect transistors for artificial skin applications”. *Proceedings of the National Academy of Science of the United States of America*, vol. 101(27), pp. 9966–9970, July 2004. (Cited on page 19.)

[Stiehl and Breazeal, 2006] W. D. Stiehl and C. Breazeal. “A sensitive skin for robotic companions featuring temperature, force and electric field sensors”. In *IEEE/RSJ International Conference on Intelligent Robots and Systems (IROS)*, pp. 1952–1959. Beijing, China, October 2006. (Cited on page 17.)

[Strohmayr, 2012] M. Strohmayr. “Artificial skin in robotics”. Ph.D. thesis, Karlsruher Institut fuer Technologie, June 2012. (Cited on page 19.)

[Sturm *et al.*, 2008] J. Sturm, C. Plagemann and W. Burgard. “Adaptive body scheme models for robust robotic manipulation”. In *International Conference on Robotics: Science and Systems IV*. Zurich, Switzerland, June 2008. (Cited on page 23.)

[Sugaiwa *et al.*, 2008] T. Sugaiwa, H. Iwata and S. Sugano. “Shock absorbing skin design for human-symbiotic robot at the worst case collision”. In *IEEE-RAS International Conference on Humanoid Robots (Humanoids)*, pp. 481–486. Daejeon, Korea, December 2008. (Cited on page 19.)

[Sukhoy *et al.*, 2009] V. Sukhoy, R. Sahai, J. Sinapov and A. Stoytchev. “Vibrotactile recognition of surface textures by a humanoid robot”. In *IEEE-RAS International Conference on Humanoid Robots (Humanoids)*, Workshop on Tactile Sensing in Humanoids, pp. 57–60. Paris, France, December 2009. (Cited on pages 18, 20, and 24.)

[Tawil *et al.*, 2009] D. Tawil, D. Rye and M. Velonaki. “Artificial skin for human-robot interaction”. In *IEEE-RAS International Conference on Humanoid Robots (Humanoids)*, Workshop on Tactile Sensing in Humanoids, pp. 51–54. Paris, France, December 2009. (Cited on page 17.)

[Toohey *et al.*, 2007] K. S. Toohey, N. R. Sottos, J. A. Lewis, J. S. Moore and S. R. White. “Self-healing materials with microvascular networks”. *Nature Materials*, vol. 6, pp. 581–585, June 2007. (Cited on page 19.)

[Tseng *et al.*, 2008] W.-Y. Tseng, J. S. Fisher, K. Rinaldi and A. P. Lee. “A slow-adapting microfluidic based tactile sensor”. In *IEEE International Conference on Micro Electro Mechanical Systems (MEMS)*, pp. 912–915. Tucson, AZ, USA, January 2008. (Cited on pages 18 and 19.)

[Ude *et al.*, 2000] A. Ude, C. Man, M. Riley and C. G. Atkeson. “Automatic generation of kinematic models for the conversion of human motion capture data into humanoid robot motion”. In *IEEE-RAS International Conference on Humanoid Robots (Humanoids)*. Cambridge, Massachusetts, USA, September 2000. (Cited on page 23.)

[Ulmen and Cutkosky, 2010] J. Ulmen and M. Cutkosky. “A robust, low-cost and low-noise artificial skin for human-friendly robots”. In *IEEE-RAS International Conference on Robotics and Automation (ICRA)*, pp. 4836–4841. Anchorage, AK, USA, May 2010. (Cited on pages 17 and 18.)

[Vasarhelyi *et al.*, 2006] G. Vasarhelyi, M. Adam, E. Vazsonyi, I. Barsony and C. Duecso. “Effects of the elastic cover on tactile sensor arrays”. *Sensors and Actuators A: Physical*, vol. 132, pp. 245–251, November 2006. (Cited on page 19.)

[Vogt *et al.*, 2013] D. M. Vogt, Y. Menguc, Y.-L. Park, M. Wehner, R. Kramer, C. Majidi, L. Jentoft, Y. Tenzer, R. Howe and R. J. Wood. “Progress in soft, flexible, and stretchable sensing systems”. In *IEEE-RAS International Conference on Robotics and Automation (ICRA)*, Workshop on Electronic Skin. Karlsruhe, Germany, May 2013. (Cited on page 17.)

[Wakuda and Suganuma, 2011] D. Wakuda and K. Suganuma. “Stretchable fine fiber with high conductivity fabricated by injection forming”. *Applied Physics Letters*, vol. 98, pp. 1–3, February 2011. (Cited on page 19.)

[Weiss and Woern, 2004] K. Weiss and H. Woern. “Tactile sensor system for an anthropomorphic robotic hand”. In *IEEE International Conference on Manipulation and Grasping (IMG)*. Genova, Italy, 2004. (Cited on page 17.)

[Weiß and Woern, 2005] K. Weiß and H. Woern. “The working principle of resistive tactile sensor cells”. In *IEEE International Conference on Mechatronics and Automation (ICMA)*, pp. 471–476. Niagara Falls, Canada, July 2005. (Cited on page 17.)

[Wieser *et al.*, 2011] E. Wieser, P. Mittendorfer and G. Cheng. “Accelerometer based robotic joint orientation estimation”. In *IEEE-RAS International Conference on Humanoid Robots (Humanoids)*, pp. 67–74. Bled, Slovenia, October 2011. (Cited on page x.)

[Yamada *et al.*, 2002a] K. Yamada, K. Goto, Y. Nakajima, N. Koshida and H. Shinoda. “A sensor skin using wire-free tactile sensing elements based on optical connection”. In *SICE Annual Conference*, pp. 131–134. Osaka, Japan, August 2002a. (Cited on page 19.)

[Yamada *et al.*, 2002b] Y. Yamada, T. Maeno, I. Fujimoto, T. Morizono and Y. Umetani. “Identification of incipient slip phenomena based on the circuit output signals of pvdf film strips embedded in artificial finger ridges”. *Transactions of the Society of Instrument and Control Engineers*, vol. 40(6), pp. 648–655, 2002b. (Cited on pages 18 and 19.)

[Yan and Pollefeys, 2006] J. Yan and M. Pollefeys. “Automatic kinematic chain building from feature trajectories of articulated objects”. In *IEEE Computer Society Conference on Computer Vision and Pattern Recognition (CVPR)*, pp. 712–719. New York, USA, July 2006. (Cited on page 23.)

[Yang *et al.*, 2008] Y.-J. Yang, M.-Y. Cheng, W.-Y. Chang, L.-C. Tsao, S.-A. Yang, W.-P. Shih, F.-Y. Chang, S.-H. Chang and K.-C. Fan. “An integrated flexible temperature and tactile sensing array using pi-copper films”. *Sensors and Actuators A: Physical*, vol. 143, pp. 143–153, May 2008. (Cited on pages 18 and 19.)

[Yang *et al.*, 2010] Y. J. Yang, M. Y. Cheng, S. C. Shih, X. H. Huang, C. M. Tsao, F. Y. Chang and K. C. Fan. “A 32x32 temperature and tactile sensing array using pi-copper films”. *The International Journal of Advanced Manufacturing Technology*, vol. 46, pp. 945–956, 2010. (Cited on page 19.)

[Yoshikai *et al.*, 2007] T. Yoshikai, M. Hayashi, Y. Ishizaka, T. Sagisaka and M. Inaba. “Development of functional whole-body flesh with distributed three-axis force sensors to enable close interaction by humanoids”. In *IEEE/RSJ International Conference on Intelligent Robots and Systems (IROS)*, pp. 3610–3615. San Diego, CA, USA, October 2007. (Cited on page 19.)

[Yoshikawa *et al.*, 2002] Y. Yoshikawa, H. Kawanishi, M. Asada and K. Hosoda. “Body scheme acquisition by cross modal map learning among tactile, visual, and proprioceptive spaces”. In *Proceedings of the Second International Workshop on Epigenetic Robotics*. Edinburgh, Scotland, August 2002. (Cited on page 21.)

[Yousef *et al.*, 2011] H. Yousef, M. Boukallel and K. Althoefer. “Tactile sensing for dexterous in-hand manipulation in robotics–a review”. *Sensors and Actuators A: Physical*, vol. 167, pp. 171–187, June 2011. (Cited on page 17.)